JOHANNES GUTENBERG-UNIVERSITÄT MAINZ
DEPARTMENT OF PHYSICS, MATHEMATICS AND COMPUTER SCIENCE
INSTITUTE OF PHYSICS

A journey through nonlinear magneto-optics

by

Dimitra Kanta

A thesis submitted for the degree of
Doctor of natural sciences

JUNE 2024

Declaration of Authorship

I, Dimitra Kanta, declare that the thesis entitled *A journey through nonlinear magneto-optical effects* and the work presented in the thesis are both my own, and have been generated by me as the result of my own original research. I confirm that:

- this work was done wholly or mainly while in candidature for a research degree at this University;
- where any part of this thesis has previously been submitted for a degree or any other qualification at this University or any other institution, this has been clearly stated;
- where I have consulted the published work of others, this is always clearly attributed;
- where I have quoted from the work of others, the source is always given. With the exception of such quotations, this thesis is entirely my own work;
- with the oversight of my main supervisor, editorial advice has been sought. No changes of intellectual content were made as a result of this advice;
- I have acknowledged all main sources of help;
- where the thesis is based on work done by myself jointly with others, I have made clear exactly what was done by others and what I have contributed myself;

Signed:

Date: *18st October 2024*

Supervisor:

Examiner 1:
Examiner 2:
Examiner 3:

Abstract

This thesis contributes to the research on nonlinear magneto-optical effects, specifically focusing on atomic magnetometry based on nonlinear magneto-optical rotation and mirrorless lasing (based on amplified spontaneous emission) – while encountering also other nonlinear effects, such as the Kerr effect.

Measuring magnetic fields has been of great importance since the bronze age and has been crucial to the development of the human civilization [1]: the first magnetometer was the compass, a magnetometer that measures only the direction of the earth's magnetic field and is so important that it has a place amongst the four great inventions of ancient China. Measuring the magnitude of a magnetic field is a more modern story that starts with Carl Friedrich Gauss measuring the Earth's magnetic field in 1833 [2].

Among the techniques existing nowadays, for precisely measuring magnetic fields, optically pumped magnetometry (OPM) stands out for it's sensitivity, size, robustness and low cost [3], [4], [5]. After the pioneers set the foundations more than half a century ago [6], [7], [8], diode laser technology allowed optical magnetometers to become a workhorse for magnetometry. OPM magnetometers are potentially as sensitive [9] as SQUIDs (Superconducting Quantum Interference Device) [10] and do not require cryogenics. Applications span over a wide range of fields: geophysics [11], bio-magnetic measurements [12] and fundamental physics [13]. OPM research in recent years has shifted from working in the laboratory to applications in the field and a useful step towards commercialization is the self-oscillating configuration. The basic operation principle is based on using the detected signal to sustain continuous oscillation at the resonant frequency [14] [15]. Such systems have a broad dynamic range, can follow field fluctuations and are simple.
Although OPMs and especially SERF (spin exchange relaxation-free) type magnetometers are highly sensitive, they need to operate in low fields and hence require magnetic shielding from the Earth's field and other noise sources. Being able to measure in the geophysical field range or earth field with high sensitivity could open the path to low-cost bio-magnetic measurements [16], space-magnetometry [17], non-destructive testing and imaging [18] and magnetometry on rapidly moving platforms [19]. This thesis focuses on Earth-field optical magnetometry and addresses challenges arising from the Earth's magnetic field by using techniques like spin locking or creating a device free of classic Earth-field magnetometry issues, such as heading error.

The second part of this thesis is dedicated to mirrorless lasing. Since their invention in the 60s, lasers (light amplification by stimulated emission of radiation) have played a huge role in many areas of scientific research, industry, and everyday life and continue to grow. There are three principal components usually attributed to a laser: a gain medium, a pumping process and a feedback loop [20], although there is a debate over whether a feedback loop is always required. Lasing is often distinguished from processes such as Amplified Spontaneous Emission (ASE), Superradiance (SR) and Superflouorescence (SF) [21,22], but this is not the case for the work presented here. Typically, lasers follow a conventional structure that includes an optical resonator setup. This setup uses mirrors to amplify light over multiple round trips in the gain medium [20]. In mirrorless laser setups, the gain

medium serves as the resonator, and the feedback loop would typically happen through multiple scattering processes in systems with varying degrees of disorder [21]. Optical feedback through scattering can also create random lasers [23]. The system we are studying does not involve scattering mechanisms and we use the term lasing interchangeably with Amplified Spontaneous Emission (ASE). We define mirrorless lasing as as directed monochromatic emission from an ensemble of atoms or molecules pumped with a laser light. Experiments in alkali metal vapor have shown gain through the phenomenon of amplified spontaneous emission (ASE), see, e.g, [24]. This thesis focuses on the phenomenon of amplification of spontaneous emission and degenerate mirrorless lasing in alkali atoms with magnetically degenerate hyperfine states.

Contents

List of Figures

List of Tables

List of Abbreviations

Abbreviation	**Description**	**Chapter**
AOM	**A**cousto-**O**ptical **M**odulator	§3.3.2, §3.5
ASE	**A**mplified **S**pontaneous **E**mission	§2.4.3
ECDL	**E**xternal-**C**avity **D**iode **L**aser	§3.5.3
EOM	**E**lectro-**O**ptic **M**odulator	§3.3.2, §3.5
FWHM	**F**ull **W**idth at **H**alf **M**aximum	§4.4, §6.3.5
LASER	**L**ight **A**mplification by **S**timulated **E**mission of **R**adiation	§3.5.3
LIA	**L**ock-**I**n **A**mplifier	§3.5.2
NLZ	**N**on**L**inear **Z**eeman	§1.4.4, §3.4.1
NMOR	**N**onlinear **M**agneto-**O**ptic **R**otation	§3.3.3
OPM	**O**ptically-**P**umped **M**agnetometer	§3.1, §4.1
PC	**P**ersonal **C**omputer	§5.3.3
PD	**P**hoto**D**etector	§4.3, §6.3.4
QM	**Q**uantum **M**echanics	§1.4.3
RF	**R**adio**F**requency	§3.3.1, §4.1
PN	**P**rojection**N**oise	§3.1.6
PSN	**P**hoton**S**hot**N**oise	§3.1.6
VLS	**V**ector**L**ight **S**hift	§4.2
PM	**P**olarization **M**oments	§3.2

List of Symbols

Symbol	Description	Notes	Chapter
$\vec{\mu}$	magnetic moment		§1.2.1
J_z	total angular momentum on quantization axis		§1.2.1
γ	gyromagnetic ratio		§1.3.1
ψ_i	the atomic wave function of an atom i		§1.4.1
ρ_{mn}	density matrix		§1.4.1
$\mathbf{D}$	electric displacement		§2.2.1
χ	electric susceptibility		§2.2.1
η	refractive index		§2.2.1
$\mathbf{P}$	polarization of a medium		§2.2.1, §2.2.2
$\mathbf{d}$	electric-dipole operator		§2.2.2
Ω_R	Rabi frequency		§2.3
Ω_L	Larmor frequency		§2.3, §3.1.4
κ_1, κ_2	saturation parameters		§2.4.2
Γ	linewidth of a transition		§2.3.2
t_2	spin-coherence time		§3.1.6
$\rho^{\kappa q}$	polarization moments		§3.2

Acknowledgements

Alongside my journey into nonlinear magneto-optics, another journey was unfolding: my journey as a new researcher in a foreign country. The list of names is extensive, and I apologize if I forgot to mention anyone. One way or another, you all supported me through tough times, provided comfort and advice, inspired me with ideas, and made this journey fun and, as a result, possible.

First, I would like to thank my advisor and professor **Dima**, for not only being an exceptional scientist, but also a compassionate and patient mentor. His unwavering support and the freedom he granted me to explore my own path have been truly invaluable. It was a pleasure to have worked with you– and of course also make music with you and the spontaneous emission.

Following a loose chronological order I would like to start by thanking my friends **Vasilis** and **Natalia** who introduced me to the academic possibilities in Mainz, they let me stay at their place for as long as I needed and we eventually developed a deep friendship. It always makes me smile when I think of you. I am also grateful to all my colleagues and friends in MPIP who were part of my first community in Mainz and always made me feel welcome. Shout out to **Christoph, Jan, Malte** and **Maksim** for the most amusing coffee breaks. Thank you **Simon** and **Phillip** for all our fantastic tabletop quests. A big thanks from the bottom of my heart to my late friend **Eduard, Alexandra, Yu-Jen** and especially **Marco** who supported me through thick and thin. Marco, you have been a great friend and I wish you all the best in Spain.

Moving on, I would like to thank **Arne**, for all the discussions and supervision as well as his tasty group dinners. Your efforts to manage and bond this diverse group are really impressive and valued. **Lykourgos**, thank you for introducing me to the group and for always offering aid when I needed it. I want to thank **Hector** for our very interesting talks spanning from optical magnetometry to determinism and remember: your crippling awareness of the self brings all the existential doubt to the yard! **Roman** thank you for your friendship, for bringing always a good mood with you and for leaving your ukulele sometimes back home. And of course I cannot forget to thank **Marina** for her upbeat attitude and **Joey** for his helpful explanations on theoretical physics and on how on earth the US election system works. **Antoine** thank you for being so special, you give Paris an even better name.

For his wry humor and his solidarity I am thankful to **Jim**: I know you have deep down a big heart, an essential skill if you work in the penguin-lifting business. A big thank you to **James** for always listening and giving the most entertaining input: you are smart and a team player; science could only benefit from people like you. I am also indebted to **Giorgos** for being the person that I know I can always count on to help solve any kind of challenge I face. Giorgo thank you for all the tea and gym sessions, and generally for motivating me when things got tough. Thank you **Till** for your grounding and relaxed presence and for reminding me– way too often –to write my thesis. **Garry** thank you for the fascinating science-communication discussions, **Anna** for our philosophical pen and paper sessions and **Erik** for your always calming presence and composed demeanor.

Thank you **Lei** for being a great office mate. I can't thank you enough **Yinan** for being the best lab mate I could have wished for. Hu is the best? We had such a delightful time together in the lab: singing Greek and Chinese music, improvising games and smashing batteries!

I would also like to thank **Anne, Peter, Nate, Pavel, Alex, Felipe, Xue, Zhiyin** as well as the newer members **Olympia, Dani, Razmik, Alexander** and many more, for forming an eclectic and diverse group of people that has been a joy to be part of every day. A huge thank you to **Derek**, a truly inspiring physicist and friend whose love for physics and life is contagious. We are lucky to have you Derek!

Next, I would like to express my appreciation to the backbone of the group, postdocs that had my back, all exceptionally skilled and capable: to **John, Dionysis, Hendrik, Emmanuel, Geoffrey, Kirill, Oleg** thank you for your practical guidance in the lab and your creative input. And thank you for the fun times as well!

With deep gratitude, I thank **Alexander** for the opportunity to learn from him about mirrorless lasers and optics. Your guidance in the lab was very crucial in these first steps I was making in science. Thank you **Guzhi** for sharing your expertise with me, for working together on several projects and for letting me bombard you with questions on a daily basis. Of course, I need to say a big thank you to **Rui** for our excellence collaboration and for instilling in my methodology love for detail, planing and diligently optimizing a scientific project. I would also like to thank our collaborators in Armenia and **Aram's group** who gave me the opportunity to sleuth out the creation of degenerate mirrorless lasing and visit and work in Armenia.

Finally a special thanks goes to all the behind-the-scenes people: **Evi** for dealing with the huge amounts of administrative work required so often, the administrative staff of HIM and, of course, **Lars**, who keeps the building running and who had been trying to fix the cold air draft behind my back in the lab for quite some time. The draft's origins remain unknown, but thank you regardless for trying to deal with this and so many other issues.

Many of the already mentioned people have also become my friends. And since scientific research is similar to any other creative job in that it entails extensive work hours, inevitable setbacks, disagreements, and a continuous creative process that extends beyond regular working hours, friends are a crucial part of the PhD equation. This is why I need to thank also my friends outside the research group for filling my after-work life with laughter and ease. A heartfelt thank you to **Nora** who is the bravest researcher I have met, thank you for being there since week one. **Eleftheria** who I love chatting with, thank you for empathizing with my troubles every time and of course I have to thank Eleftheria's dog Lexy who is– literally –the best dog and **Felix** who is always so easy to be around. A big thank you to **Jonathan, Michi**, and **Tim** for the great company, especially during the dark times of COVID and for always being up for doing something spontaneous! Thank you Dr(yeah!) **Malte P.** for being one of the two people on this Earth wanting to play Anno Domini with me, **Kiera** and **Rebecca** for all the cosy get-togethers in Mainz, **Shamitha** for all the loud laughs and **Oriane** for the most joyful times we had during your last months in Mainz!

A big thank you goes also to my designer friends who might not understand physics, but understand the efforts I had to make being a physicist: **Eva, Meike, Fede, Juliet, Ranim**. I would also like to thank all those I befriended in Stuttgart while juggling thesis and work, you gave me perspective and daily serenity and I will honestly miss you. Thank you, **Melina, Anta** and **Dialechti**, for making Thessaloniki still feel like home.

Strange as it may seem, I would like to express my gratitude to my daily radio show, **Ellinofreneia**, which I listened to every day during the last 6-7 years. In the windowless, chilly, noisy lab, it kept me grounded and connected to the outside world.

To my close friends who I met in Athens, but are now spread all over the world: thank you **Aggelos** for all the humor, conversations, affection and crepe sharing, **Andreas** for all our adventures both real and imaginary, **Antonis** for being my kind tall souidos friend, **Giannis** for being hilarious, tolerant and supportive, **Grigoris** for all the games, music and discovering Athens with you, **Nikos** for having shared our best times together and we keep sharing more, **Karim** for caring for me since my bob-cut days until now as we stand at the threshold of our second youth and for still putting up with me– also for being the other person who wants to play Anno Domini, **Vaggelis** for all the great trips with you and your daily help with python and **Vaso** for the awesome times we have when you don't drink coffee. For all the precious moments, for shaping and forming one another, for our daily chats and rants, for helping each other while studying at the SEMFE, for roaming and loving the best city in the world: I would do it all over again with you!

To my parents: thank you for the love, support and parenting that did not perpetuate stereotypes, allowing me to always feel confident and free to discover myself. Mom, dad, thank you for everything! *Σας ευχαριστὼ*!

To Stela: thank you for your big heart, for living next to me so that not a day passes without talking, for meticulously listening to my daily happenings and for believing in me when I don't. I do not speak as an owl when I say: Thank you for being the best sister!

To Martin: I thank luck (and maybe also Dima) for you moving to the GNOME lab with me and I thank you for bringing all your wit, kindness, and humor to my life. Thank you for your moral, emotional and scientific support, and for always knowing how to cheer me up. Thank you for choosing to be my partner in this journey and many other journeys in the years to come.

Dimitra Kanta

Mainz June 2024

Happiness can be found even in the darkest of times, when one only remembers to turn on the light.

Albus Percival Wulfric Brian Dumbledore

It looks strange and it looks strange and it looks very strange; and then suddenly it doesn't look strange at all and you can't understand what made it look strange in the first place.

Gertrude Stein

1

Light-atom interactions 101

1.1 A brief history of light-matter interactions

Light-matter interactions cover a substantially wider range of phenomena than light-atom interactions, from the macroscopic world of black holes to the mesoscopic environment of nanophotonics to the tiniest matter possible in the realm of quantum mechanics. The expression light-matter interaction implies that these two entities are different and interact through some intermediate agent [26]. Interestingly enough though, the two were not considered separately until the 17^{th} century AD. In Figure 1.1 one can see some important landmarks of light-matter-interaction theories from ancient Greece to modern times. Of course the theories in antiquity are not using the scientific method and were part of a philosophical discourse, although it is quite impressive how close some of them came to our modern understanding of nature without experimental confirmation. During the Golden Ages of science in Islam, the *Book of Optics* by Ibn al-Haytham studied properties of light and came to conclusions that heavily influenced the scholars during the Renaissance in western and central Europe. Galileo, Fermat, Hooke, Descartes and Newton set important milestones in this journey and by the $1700s$ light and matter had been studied extensively –and separately– for two centuries. In one faction matter was studied by researchers such as Boyle, who working on the laws of gasses and Dalton, calculating atomic masses, while Lavoisier realized that mass is conserved in chemical reactions and Mendeleev organizing the different elements in the periodic table. The other side was in parallel studying light, with Fresnel and Young demonstrating the wave properties of light, disputing Newton's by-that-time established theory that light consists of particles{II} and culminating with Maxwell's equations of electromagnetism. By the end of the 19^{th} century, the black-body radiation

---

{II}What a fascinating journey this has been!

and Michelson-Morley experiments made clear that the picture of light and matter was not accurate and new theories were needed to explain nature [26]. The 20^{th} century established modern-physics theories of quantum mechanics, special and general relativity and returned to a more unified picture of light and matter. We will concern ourselves with light-atom interactions, since this thesis belongs to the realm of atomic physics. What is interesting to note at this point is that so far we understand light-micro-world interactions and light-macro-world interactions (through electromagnetism and general relativity), but we have not managed to connect the two worlds together. Connecting quantum mechanics to gravity is arguably the holy Grail of modern physics.

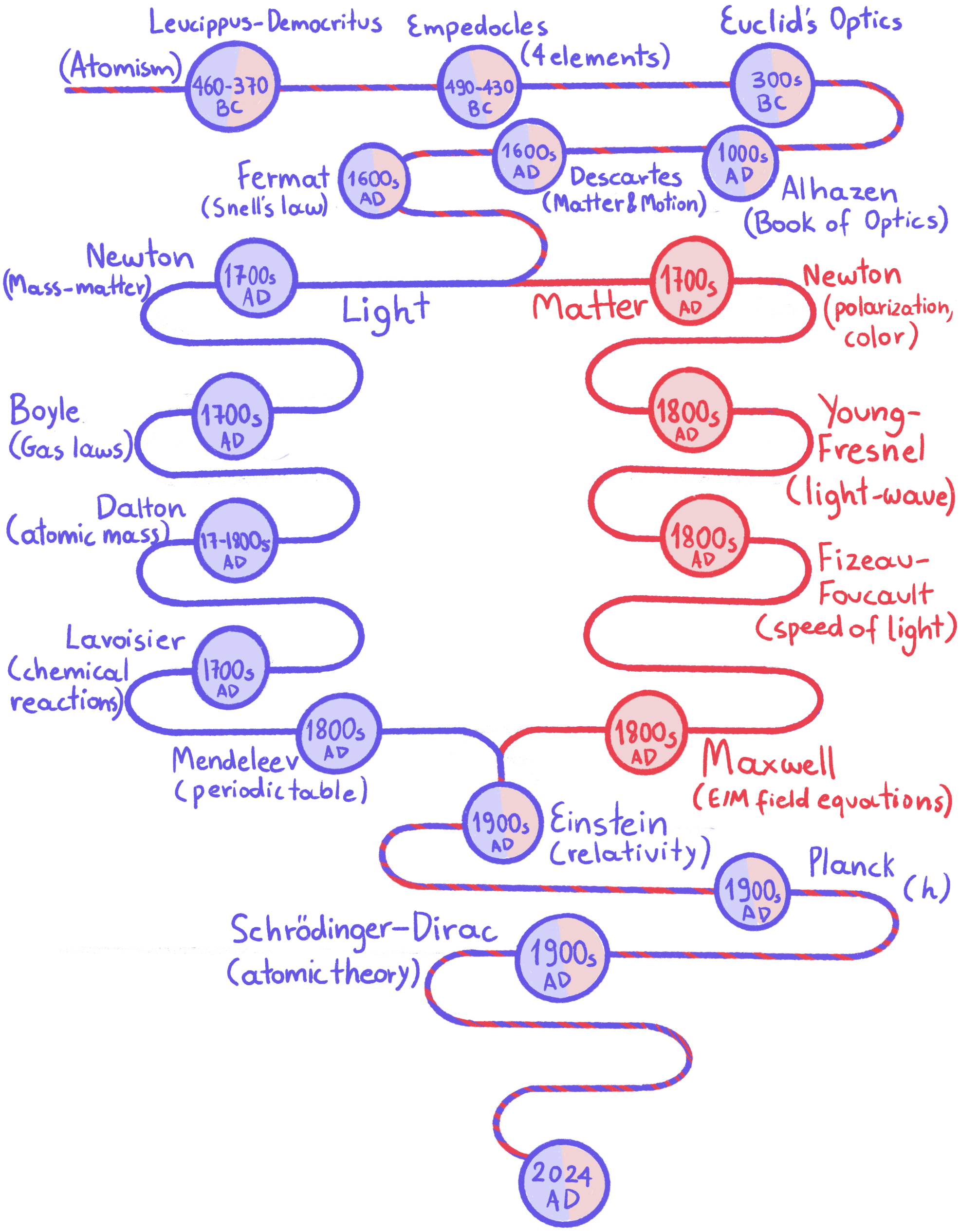

FIGURE 1.1: A brief history of light-matter theories.

1.2 Atoms and their structure

When it comes down to it, our experiments are all interactions between light and atoms. Therefore, this thesis could not begin without properly introducing to the reader the basic properties of atoms and how these interact with electromagnetic waves. The atoms that interest us in this thesis, belong to group 1 of the periodic table which includes hydrogen (H), lithium (Li), sodium (Na), potassium (K), rubidium (Rb), cesium (Cs), and francium (Fr). Since I worked only with Rb and Cs, these will be the atoms more referred to throughout the next Chapters.

One of the basic principles of quantum mechanics states that electrons are distributed not randomly around the nucleus of an atom, but in discrete, allowed energy levels. What alkali atoms have in common is their ground-state **{I}** electronic configuration: they all have one electron in the outermost layer, the layer being an *s*-orbital. This electron has a low binding energy and can be manipulated with lower energies **{II}** and visible light.

The simplest atom is the hydrogen atom, which consists of a proton and a singe electron. Hence, the properties and energy levels of the outermost electron of the alkali atoms can be closely described by the formalism of the hydrogen atom. By solving the Schrödinger equation for the hydrogen atom in spherical coordinates, we get the solution of the equation: the **spherical harmonics** for the angular part and the **radial functions** for the radial part. These functions describe how the electron moves around the nucleus and are characterized by the integers n, l, and m which are called quantum numbers (See Table 1.1 and 1.2).

Spherical harmonics $Y_l^m(\theta, \phi)$		
$l = 0$	$m = 0$	$Y_0^0 = 1/(\sqrt{4\pi})$
$l = 1$	$m = +1$	$Y_1^{1,-1} = \pm 1/2\sqrt{3/2\pi}\ sin\theta\ e^{\pm i\phi}$
$l = 1$	m=0	$Y_1^0 = 1/2\sqrt{3/\pi}\ cos\theta$

TABLE 1.1: Hydrogenic wavefunctions: spherical-harmonics part.

Radial functions $R_{nl}(r)$		
$n = 1$	$l = 0$	$R_{10}(r) = 2\exp\{-r/a_0\}/a_0^{3/2}$
$n = 2$	$l = 0$	$R_{20}(r) = 2(1 - r/2a_0)\exp\{-r/2a_0\}/(2a_0)^{3/2}$
$n = 2$	$l = 1$	$R_{21}(r) = 1(r/a_0)\exp\{-r/2a_0\}/\sqrt{3}(2a_0)^{3/2}$

TABLE 1.2: Hydrogenic wavefunctions: radial part.

For the radial and angular equations to have physically accepted solutions the quantum numbers must fulfill the following conditions [27]:

$$n = 1, 2, 3, \dots , \tag{1.1}$$

{I} The lowest allowed energy state of an atom

{II} Lower with respect to the transition energies in other atoms

$$0 \leq l \leq n-1\,, \tag{1.2}$$

$$-l \leq m \leq l\,. \tag{1.3}$$

These physically acceptable solutions describe the conserved quantities in our atomic system. The n is the **principal quantum number** and it determines the allowed energy levels (which are infinite but distinct). The angular momentum of an electron is defined by l, called the **azimuthal quantum number** and m is the **magnetic quantum number**. These quantities are conserved and precisely known.

1.2.1 Fine structure

The careful reader will notice at this point that there is a last important number missing, in order to be able to fully describe the quantum state of an electron: the spin, the intrinsic angular momentum of (in our case) an electron. This is not derived from the Schrödinger's equation, but was first added experimentally and then the Dirac equation theoretically explained.

When talking about angular momenta (spin and orbital) we have to keep in mind that these produce magnetic fields and as a result there is also a magnetic moment $\boldsymbol{\mu}$ associated to those angular momenta. We can imagine the magnetic moment to be a vector perpendicular to the surface the current loop is defining.

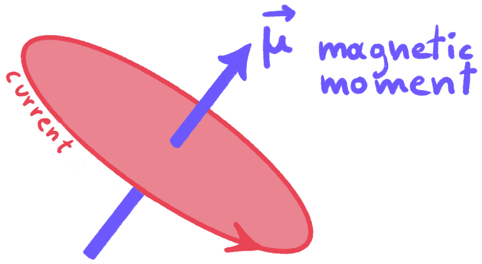

FIGURE 1.2: Classical view of a magnetic moment produced by an electric current.

An electron can thus can have a magnetic moment associated with its orbital angular momentum $\boldsymbol{l}$[I]:

[I] **Bold** letters represent vectors

$$\boldsymbol{\mu}_l = -g_l \mu_B \frac{\boldsymbol{l}}{\hbar} \tag{1.4}$$

with magnitude [28]:

$$|\boldsymbol{\mu}_l| = \frac{|e|}{2m_0} \hbar \sqrt{l(l+1)}\,, \tag{1.5}$$

and it also has its own angular momentum $\boldsymbol{s}$ (spin) with magnitude:

$$|\boldsymbol{s}| = \hbar \sqrt{s(s+1)}\,, \tag{1.6}$$

with the z-component equal to:

$$s_z = m_s \hbar\,, \tag{1.7}$$

and a magnetic moment associated with spin:

$$\boldsymbol{\mu}_s = -g_s \mu_B \frac{|\boldsymbol{s}|}{\hbar}\,. \tag{1.8}$$

In an external magnetic field the spin takes two values as depicted in Figure 1.3, where V is the potential energy of the magnetic dipole, $\boldsymbol{B}_0$ is the external magnetic field, m_s is the magnetic quantum number, g_s is the g-factor[I] of the electron (also called electron spin g-factor) characterizing the magnetic moment and the angular momentum of the electron and μ_B is the Bohr magneton – a quantum unit of magnetic dipole moment equal to:

$$\mu_B = \frac{|e|}{2m_0} \hbar \approx 9.27 \cdot 10^{-24} \frac{J}{T} \approx 0.93 \cdot 10^{-20}\, \mathrm{erg}\ \mathrm{G}^{-1} \tag{1.9}$$

The spin takes only two values and we can observe the z component, but not the x and y. We will get back to this fundamental principle in the following Sections.

In our experiments we work with multi-electron atoms and not with Hydrogen. Since no two electrons in an atom can have an identical set of quantum numbers only a specific number of electrons occupy each of the n electron shells. The total angular momentum of the completed shells[II] is zero. This is why we are interested in the outermost shells that contain valence electrons[III] and their quantum numbers, which luckily for us, in alkali atoms is only one electron–with a non-zero angular momentum, since the shell is not completed.

[I] Measured to be g_s = -2.00231930436092(36) [29]

[II] A complete shell contains the maximum allowed number of electrons

[III] Valence electrons are in the outermost shell of an atom

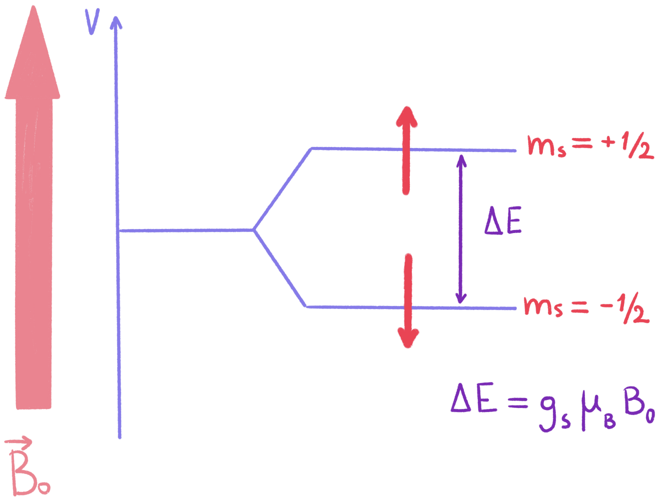

FIGURE 1.3: The projection of the electron spin in an external magnetic field takes one of two values.

The quantum numbers for multi-electron atoms are written with capital letters. The interaction of the outer electron's spin **S** with its orbital momentum **L** is called **spin-orbit coupling** and leads to the **fine structure** splitting of the excited state. The fine structure can be experimentally observed by the splitting of the spectral lines of an atom due to the spin-orbit coupling.

If we want to be scientifically precise we have to talk about the angular momentum states as probability distributions (more about this can be read in [30]). Luckily for us, there is an easier way to understand and picture the coupling of angular momenta and this is their representation as vectors, where the total angular momentum equals to:

$$\boldsymbol{J} = \boldsymbol{L} + \boldsymbol{S}\,, \tag{1.10}$$

with its magnitude being:

$$|\boldsymbol{J}| = \sqrt{J(J+1)}\,\hbar\,, \qquad |L-S| \leq J \leq L+S\,, \qquad J_z = m_J\hbar\,, \qquad m_J = J, J-1\ldots -J\,, \tag{1.11}$$

where $\boldsymbol{J}$ is the total angular momentum, $\boldsymbol{L}$ is the orbital angular momentum and $\boldsymbol{S}$ is the internal angular momentum (spin). In Quantum Mechanics it is impossible to know the exact direction in space of the angular momentum. The maximal information we can have is one projection of the electron's angular momentum on an axis; we call that axis the **quantization axis** [30]. Traditionally it is chosen along z and we denote the projection on it as J_z.

An energy level of an atom can now be described by its own **term symbol** which describes all the quantum numbers and is given by:

$$n^{2S+1}L_J\,. \tag{1.12}$$

A small, but important, note: If the spin-orbit coupling is weak, we can make the assumption that the orbital angular momenta of the individual electrons can add to the total orbital angular momentum **L**. This case is called LS-coupling and is not valid for heavier elements where the J-J coupling approximation is used. J-J coupling becomes a better approximation as the electrons become more relativistic.

1.2.2 Hyperfine structure

We have known for more than 100 years, that an atom consists not only of electrons, but also a nucleus –and you can rest assured that the nucleus affects the spectral lines as well. There is an even smaller splitting than the fine structure occurring due to the interaction of the nuclear angular momentum (nuclear spin) **I** and the electronic angular momentum **J**: their coupling leads to the total angular momentum **F**, which can also be depicted in a vector form with:

$$\boldsymbol{F} = \boldsymbol{J} + \boldsymbol{I}\,. \tag{1.13}$$

If the nuclear spin is smaller than or equal to the electron angular momentum, then the number of possible values of F is $2I + 1$. If the nuclear spin is larger then the angular momentum, the number of possible values of **F** is $2J + 1$ [30].

In this thesis we used three types of alkali atoms: ^{87}Rb, ^{85}Rb and ^{133}Cs. As an example, the ^{87}Rb ground state can be written as:

$$5^2S_{1/2} \tag{1.14}$$

We know that ^{87}Rb has nuclear spin $I = 3/2$ and hence it splits into two F hyperfine energy levels: $F = 1$ and $F = 2$.

It is important to note that there is another shift happening that we have not talked about so far that is, however, a QED effect. The fine structure does not predict different energies between states with the same J, but such a difference was experimentally seen in the Hydrogen atom [31]. The Lamb shift is what causes this split and is an effect arising from the quantization of the electromagnetic field: In addition to interacting with the proton the electron interacts with vacuum fluctuations. As a result, distribution of the electron's position gets blurred over some particular scale, meaning the electron gets slightly pushed away from the nucleus, lowering their interaction energy. As a result electrons closer or further from the nucleus will experience energy shifts from this effect differently and hence the difference between s and p.

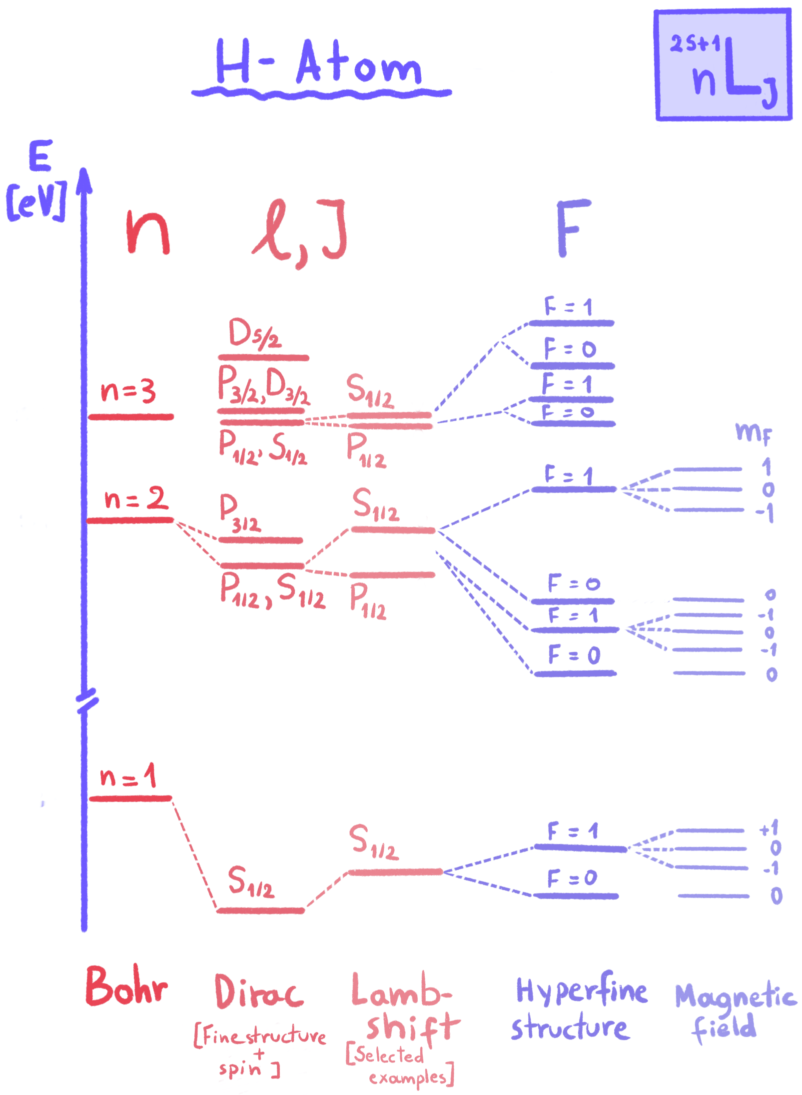

FIGURE 1.4: Illustration of the energy-levels shift due to the different quantum numbers: each line represents a specific energy. Each column shows the energy levels explained by models and corrections of them: Bohr introduced the n principal quantum number. Dirac predicted the electron spin; when applied to the hydrogen atom, Dirac's equation contained a potential energy term $L \cdot S$, resulting to the fine structure energy shift. The Lamb shift accounts for a small "push" of the electrons position away from the nucleus and is related to quantum field theory. The Hyperfine-structure energy difference is arising from the interaction between I and J. Finally, an external magnetic field will shift the F states (Zeeman effect).

1.3 Atoms in a magnetic field

1.3.1 Zeeman effect

The next step in our understanding of light-atom interactions would be to look at how an external magnetic field affects the energy states of an atom inside of it.{I}. This step would conclude our picture of how the energy levels of an atom shift due to different quantum numbers, see Figure 1.4.

In 1896 Zeeman noticed that the spectral lines of atoms are split when the atoms are placed inside a static magnetic field [27]. The (potential) energy ΔE that an atom gets from an external magnetic field $\boldsymbol{B} = B\hat{z}$ is given by [30]:

$$\Delta E = -\boldsymbol{\mu} \cdot \boldsymbol{B} \,. \tag{1.15}$$

Let us for simplicity assume that $\mathbf{S} = 0$; then the total angular momentum $\mathbf{J}$ coincides with the orbital angular momentum $\mathbf{L}$ [30].

There are a few magnetic moments associated with angular momentums, for example μ_L with the orbital angular momentum, μ_S with the spin angular momentum, μ_J with the total magnetic moment J and the μ_F related to the total angular momentum F.

Let us calculate this acquired energy shift: For the equation $\gamma = e/(2m_e c) = \mu_B/\hbar$ and from equation 1.5 we get that the magnetic moment associated with L is:

$$\boldsymbol{\mu}_L = \gamma \boldsymbol{L} = -\frac{\mu_B}{\hbar}\boldsymbol{L} \,, \tag{1.16}$$

where γ is the gyromagnetic ratio and μ_B is the Bohr magneton.

If the magnetic field is along z, knowing that

$$L_z = m_L \hbar \,, \tag{1.17}$$

and rewriting $(\mu_L)_z$ as $-\mu_B m_L$, the energy shift is:

$$\Delta E_{m_L} = -(\mu_L)_z B = \mu_B B m_L \,, \tag{1.18}$$

Eventually we want of course to know the energy splitting of the magnetic sublevels, so for the above case the energy difference between the initial i and final f state is given by:

[I] Atomic states are also split when the atom is under the influence of a static electric field. The system then behaves as if it has an electric dipole moment that can orient itself to the field. This is called the **Stark effect**. It can and does to some extend affect our experiments due to our CW lasers, but not as much as the Zeeman effect

$$\Delta E^f - \Delta E^i = \mu_B B(m_L^f - m_L^i)\,. \tag{1.19}$$

Other examples include the magnetic energy shift of a magnetic sublevel m_J for a fine-structure state, that would now be [30]:

$$\Delta E_{m_J} = -(\mu_J)_z \cdot B\,, \tag{1.20}$$

and for a hyperfine-structure state the Zeeman shift would be:

$$\Delta E_{m_F} = -(\mu_F)_z \cdot B\,. \tag{1.21}$$

How do we measure this energy shift? As we will see in Section 2.3 there are rules that determine which sublevels couple by electric-dipole transitions, called **selection rules**. To reveal a small teaser on what the selection rules for the magnetic quantum numbers are:

$$\Delta m_L = m_L^f - m_L^i = 0, \pm 1\,, \tag{1.22}$$

which give three (3) possible values for the energy split. This effect is the **normal Zeeman effect**.

Remember that we assumed the spin to be zero, so this effect can be described and predicted by non-relativistic quantum mechanics– hence the name *normal* in contrast to the anomalous Zeeman effect that takes the spin into account. Section 5.1 will provide a more detailed look into the Zeeman effect as well as the nonlinear Zeeman (NLZ) effect that appears for higher magnetic fields and is significant for Earth-field magnetometry.

1.4 Polarized Atoms

So far we have described the atomic states of a single atom. In the lab, however, we use an ensemble of atoms: one of our cells contains, in room temperature, about 10^{10} atoms per cm^3. If now we want to model such an ensemble using wave functions we would have to know the wave function of each atom and add them up, since every atom is described by a different wave function (assuming the atoms are not all in the same state). This is not only impossible computationally, but most importantly, we have no way of measuring experimentally each wave function [30]. In our context we call such a sample **unpolarized**, meaning there is equal probability to find an atom in any Zeeman sublevel. In contrast to that, an unequal distribution of different Zeeman levels is called **polarization**. A sample can have different degrees of polarization, but a sample with all its atoms having the same internal quantum state would be in a **pure state** or else would be **fully polarized**.

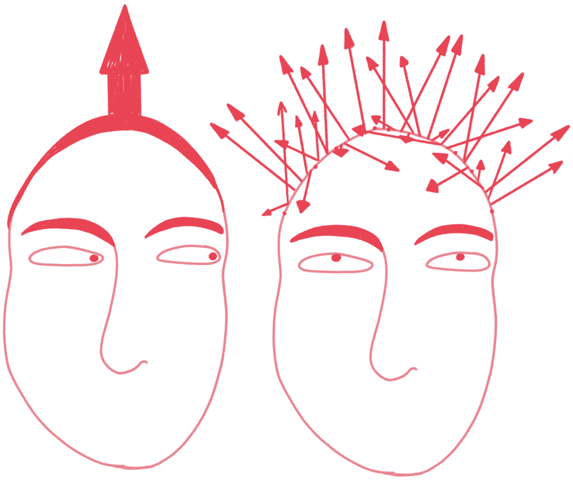

FIGURE 1.5: Spin states in a fully polarized (left) and unpolarized ensemble (right).

1.4.1 Density Matrix

To be able to describe an unpolarized sample we need to generalize the wave function. We introduce a new operator called the **density operator** represents an average over the wave functions [30]:

$$\rho = \frac{1}{N}\sum_{i=1}^{N} |\psi_i\rangle \langle\psi_i| \ , \tag{1.23}$$

where N is the number of atoms and ψ_i the atomic wave function of an atom i. The matrix elements n, m of the density operator form the **density matrix**:

$$\rho_{mn} = \langle m| \rho |n\rangle \ . \tag{1.24}$$

The density matrix describes both the polarized and unpolarized ensembles as well as the partially polarized which, unsurprisingly, is also the real case for our experiments. We get the expectation value of an observable A by calculating the expectation value: $< A >= Tr(\rho A)$. The density matrix satisfies also the conditions: $Tr(\rho) = 1$ and $\rho = \rho^{\dagger}$.

Two extremely important properties arise from the density matrix: coherences and populations. The diagonal elements of a matrix represent the probability of populations found in specific sublevels. As **population** of a state we define the probability of finding an atom in that state. The off-diagonal elements are called coherences which means they represent **superpositions** between the basis states of the density matrix[I].

[I] A quantum superposition of states happens when a system is in all of these states at the same time, meaning the sum of these states is a state of its own [32]

The properties of the density matrix can help us identify the state of polarization of our ensemble of atoms: If it is unpolarized– and considering for simplicity the two spin states –there is equal probability to find an atom in any of the two states, up or down. That would translate in "density-matrix" terms as both diagonal elements being equal to 1/2. The off-diagonal elements would be zero since there is no connection between the states; the phase between them is random[I] [30]:

$$\rho_{mn} = \begin{bmatrix} 1/2 & 0 \\ 0 & 1/2 \end{bmatrix} . \tag{1.25}$$

Note that the basis of the density matrix is the one that determines whether the coherences are zero or not zero (while populations are left unchanged). In Chapter 5 we will get back to that property which is the key to some of our experiments.

Two-level system

At this point it is useful to introduce the **two-level system**: “Consider a physical system having two states whose energies are close together and very different from those of all other states of the system. Assume that we want to evaluate the effect of an external perturbation (or of internal interactions previously neglected) on these two states. When the intensity of the perturbation is sufficiently weak, it can be shown that its effect on the two states can be calculated, to a first approximation, by ignoring all the other energy levels of the system. All the calculations can then be performed in a two-dimensional subspace of the state space” [33]. In short, a two-level system consists of two (2) discrete energy states–usually called the ground and the excited state– separated by a certain energy/frequency gap ω_0. Two parameters that are important here are the detuning $\Delta = \omega - \omega_0$ and the Rabi frequency Ω_R which describes the strength of the atom-field coupling (See Section 2.3.1). It is a useful and simple model for understanding and studying important phenomena that are characteristic of quantum mechanical systems. We will later see examples of two-level systems relevant for this thesis.

1.4.2 Liouville equation

The systems we study are evolving in time either due to internal (atoms move and collide, internal structure) or external interactions (electric or magnetic fields, initial conditions). The rate of change of the density matrix is often described by a first order differential equation called the **Liouville equation** [34]:

$$(\partial/\partial t)\rho = (1/i\hbar)[\mathscr{H}, \rho] + L(\rho) . \tag{1.26}$$

The term $(1/i\hbar)[\mathscr{H}, \rho]$ is following from the time-dependent Schrödinger equation. The term $L(\rho)$ represents the interactions between our system and the environment. These interactions are the **relaxation** and the **pumping** mechanism.

[I] Population represent a real physical property so the diagonal elements have to be positive or zero

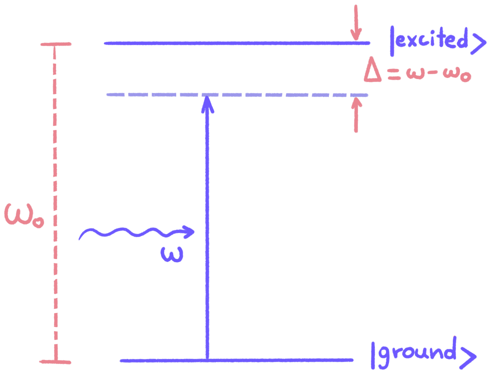

FIGURE 1.6: Illustration of a two-level system.

Relaxation– coming to equilibrium with the surroundings –can happen when the system gets depolarized when atoms collide with the walls or with each other, due to field gradients, and local field-differences. We will get back to that in Chapter 3. As far as pumping is concerned, it is the process by which one polarizes or depolarizes a system and we will talk about it in more detail in Chapter 2.

1.4.3 Angular momentum probability surface

It is notoriously hard to visualize quantum mechanics. To put it in Heisenberg's words: "Quantum theory provides us with a striking illustration of the fact that we can fully understand a connection though we can only speak of it in images and parables." I dare to say that images are usually not included in our understanding of quantum mechanics (QM). The visualization often reduces the scientific accuracy and researchers try to avoid it all-together, but, on the other hand, it also helps simplifying and understanding difficult concepts.

Luckily for us, there is a precise technique to visualize angular quantum polarization states of a density matrix, called **angular momentum probabilities**. For that, we calculate the probability of finding a magnetic sublevel along the quantization axis. If we want to find this probability along another axis we have to rotate the total angular momentum state. If we now plot this probability as a function of the direction of the quantization axis we get the **angular momentum probability surface**, as is illustrated in Figure 1.7 below (the illustration is based on the computated probability in [30]).

We can see directly from the plot what the rotational symmetry properties of the density matrix are. For example, in this case, the only preferred direction is along the quantization axis z. The only direction we can measure the maximal component of the angular momentum is $-z$ with a probability equal to 1. The symmetry axis might change, but not the symmetry of the surface around that axis.

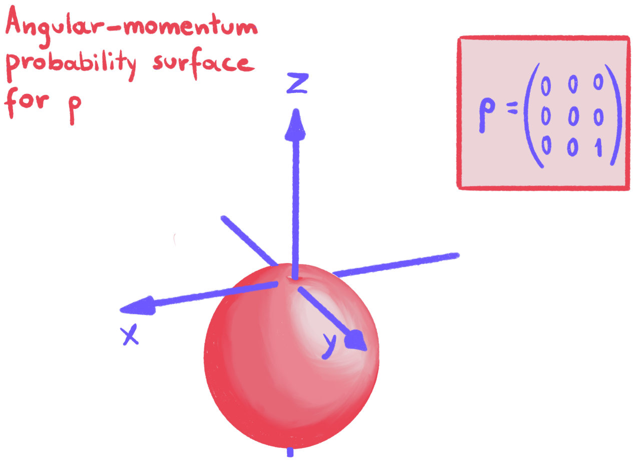

FIGURE 1.7: Illustrated angular-momentum probability surface of the density matrix ρ. The probability to measure the maximal component of the angular momentum along $-z$ is one (1).

The symmetry arising from these visualizations plays an important role– as we will see in Chapter 2 and 5 –in our experiments.

1.4.4 Quantum beats

Coherences between quantum states are represented by the off-diagonal elements of the density matrix and can be understood as quantum superposition between the basis states. In our case, it is often useful to work with coherences and hence we choose our quantization axis to be along the magnetic field. Of course this is a matter of convention, so it should not make a difference in the experiment what axis we choose. Interestingly though, if the quantization axis is chosen to be along the magnetic field, there is no change in the populations: what is oscillating then, is the *coherence* between two states. So why do we bother with the more complicated idea of coherences? At this point it is useful to introduce into the discussion the idea of **quantum beats**.

Quantum beats is the general term used to describe the time evolution of a coherent superposition of non-degenerate energy eigenstates at a frequency determined by their energy splittings [35], for example, the splittings happening in the NLZ effect (see Section 3.4.1).

This phenomenon happens if, for example, we have a pump that stretches atoms along y and a leading magnetic field along z that causes NLZ splitting. We apply a probe beam also polarized along y that drives an oscillation modulated at the difference of the frequencies between the magnetic sublevels: it is modulated at different *beats*. If we choose the quantization axis along the leading field (z direction) we will have coherences oscillating between the Zeeman sublevels which are, in this case, the energy eigenstates{I}. What this practically means is that, when we drive a resonance between two states, this resonance has a clear oscillating frequency, which we can simply imagine as a rotating polarization surface whose rotation we detect as our signal.

{I} Along the quantization axis the angular momentum eigenstates are also the energy eigenstates

Using the language of superposition between different energy eigenstates (here, different m_F states along the magnetic field), helps to work with coherences which will oscillate at a single frequency and that makes it is easier for us to count the number of oscillations produced by the NLZ effect.

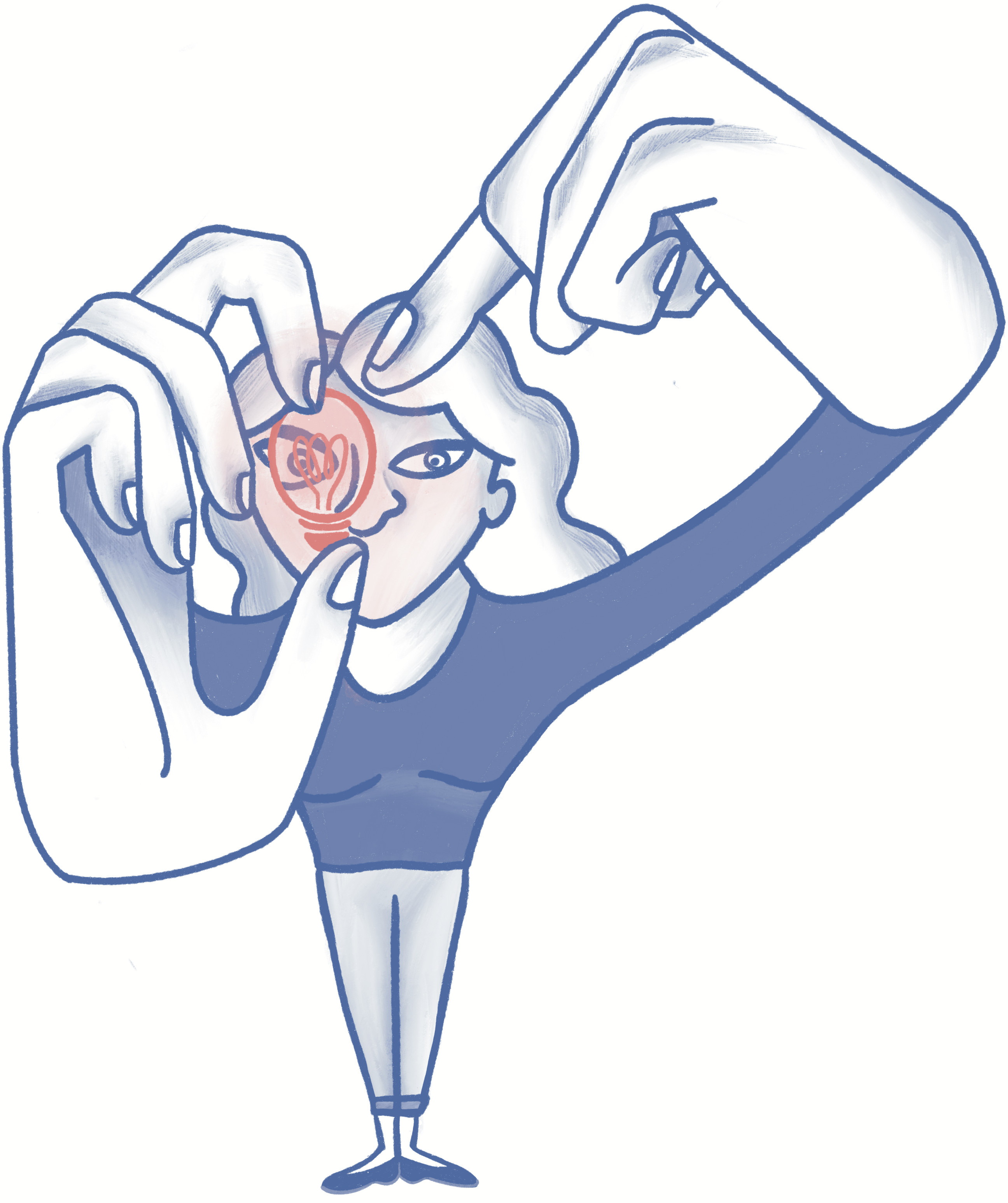

ich
denke ***ist***
etwas

("Ich" = I, "denke" = think, "ist" = is, "etwas" = something)
Max Bense, Cartesian concrete, 1966

2

Nonlinear light-atom interactions

So far, we talked about atoms, their energy levels, how these shift with magnetic fields and how we can describe an ensemble of many atoms. We also defined and visualized atomic polarization, but did not explain *how* it could be achieved. We surely can make an educated guess: We know that magnetic and electric fields influence atoms in a plethora of ways and we know that light is an electromagnetic wave. It comes as no surprise therefore that we use light-atom interactions to manipulate atoms in a way that suits our research goals.

In this Chapter we will discuss about nonlinear interactions, one of which is the mechanism called optical pumping that allows us to polarize atoms, and other nonlinear interactions between light and atoms that are key to the various effects studied throughout this thesis. Keep in mind that in this Chapter we switched to the International System of Units (SI) due to the nomenclature commonly used throughout the literature of nonlinear light-atom interactions.

2.1 Linear magneto-optical rotation

2.1.1 Faraday effect

In order to talk about nonlinear effects, it is intuitively helpful to first explain linear effects between atoms and light. One of the pioneers in electromagnetism was Michael Faraday. He studied a great amount of phenomena around electromagnetism and electrochemistry, the **magneto-optical Faraday effect** being one of them.

A **magneto-optical** effect is a phenomenon that appears when an electromagnetic wave (in our case light) propagates through a medium (in our case atoms) whose properties have been altered by an external magnetic field.

The Faraday effect is one of the most well known linear magneto-optical effects. It occurs when linearly polarized light that is transmitted through a medium undergoes rotation of its polarization plane, while a magnetic field is applied along the direction of propagation. Polarization[I] is a property of light's wave nature that describes the orientation of the oscillations in space. In **linear polarization**, the electric- and magnetic-field vectors are oscillating in a specific plane along the direction of propagation. The angle of rotation ϕ is proportional to the strength of the magnetic field $\mathbf{B}$, the length of the sample l and the properties of the medium [36]:

$$\phi = V \int_0^l B dl = VlB \,, \tag{2.1}$$

where V is wavelength, medium and temperature dependent [37]. Figure 2.1 visualizes the Faraday effect. If the magnetic field is perpendicular to the light's direction the effect is called **Voigt effect** in a gas and **Cotton-Mouton** effect in liquids [38].

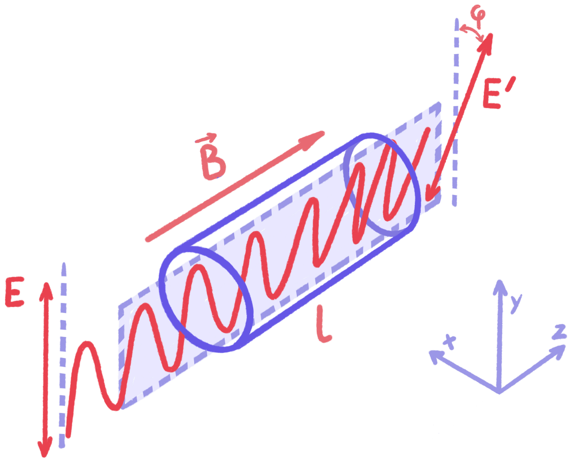

FIGURE 2.1: Linearly polarized light with electric field E enters the cell from the left. Its polarization plane rotates after it propagates through the medium with length l, that is inside a magnetic field along the light's propagation direction. The polarization of the field E' is now rotated by an angle ϕ.

What causes the Faraday effect is the difference of complex refractive indices of the polarization eigenmodes [II] that light can be decomposed into. For example, two polarization eigenmodes of light can be left (σ^-) and right (σ^+) circularly polarized waves [38]. If the refractive index of these two eigenmodes is different, then they also propagate with different velocities through the medium;

[I] Not to be confused with atomic polarization

[II] In general decomposing a field into eigenmodes is a well established technique in physics. As an example, electron orbits are eigenmodes of the energy, angular momentum, and spin operators [39]. Polarization eigenmodes, in particular, is a state of light that during its propagation through a medium can experience other changes, but its polarization is always invariant.

this phase difference leads to the rotation of the polarization plane. Polarization of light plays a great role in our systems and we will talk about it in more detail in Section 2.4.1.

2.1.2 Macaluso-Corbino effect

Macaluso and Corbino studied the Faraday effect around the turn of the 19th century. They discovered that the Faraday effect had a distinct resonant character close to the resonance of absorption lines[I]. That means that a strangely large Faraday rotation is observed when the frequency of the transmitted light is close to that of two energy states of the atoms in our medium. The main mechanism of the linear Macaluso-Corbino effect is illustrated in Figure 2.2:

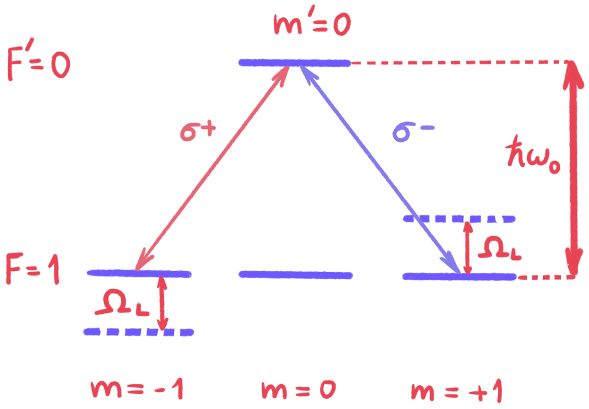

FIGURE 2.2: Illustration of the Macaluso-Corbino effect.

When linear light– which consists of the two circular components σ^+ and σ^-– interacts with a two-level system in zero field, the resonant frequency for the two components is the same. When we apply a magnetic field however, the ground-state-sublevels' degeneracy is lifted and now there is a difference of Ω_L between the sublevels. The difference between the two refractive indices, associated to the polarization, as we will see next, gives a difference in the phase velocities of the two components which is responsible for the rotation of the plane of polarization of the light and gives a characteristic spectral shape, [40], see Figure 2.3.

The Maculuso-Corbino effect is not linear in the magnetic field when the splitting of the Zeeman sublevels becomes comparable to the spectral width of the absorption line, in this case: when $\Omega_L \propto \hbar\,\Gamma$. We will discuss later in more detail about spectral widths.

[I] An atom can absorb photons with energies equal to the difference between two energy states; this energy difference we call absorption line.

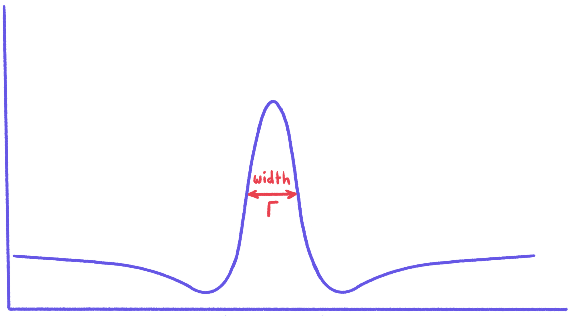

FIGURE 2.3: Illustration of the characteristic spectral shape of Malacuso Corbino effect and its width.

2.2 Nonlinear optical effects

A **nonlinear light-atom interaction** is an interaction between a medium and light in which the behaviour of the medium (its induced polarization P) depends non-linearly to the electric field E of the light. We will next investigate how to relate the microscopic theory for a single atom to the macroscopic observations that we make in the lab by using large ensembles of atoms [41].

2.2.1 Classical formalism – macroscopic

In a medium we can not only talk about one atom, so when we mention polarization P of a medium with N atoms this equals to the dielectric polarization density or electric dipole moment per unit volume (P=Np) i.e. the redistribution of charges polarizes the medium. In a material that is dielectric[I] the two charges in it (nucleus and electrons) can get displaced by applying an electric field $\mathbf{E}$ [42].

This creates an electric dipole moment with the electric displacement field –for the whole material– defined as:

$$\mathbf{D} = \epsilon_0 \mathbf{E} + \mathbf{P}\,, \tag{2.2}$$

where ϵ_0 is a constant that represents the ease by which electric field lines are formed in vacuum. If our medium is linear[II], homogeneous[III], nondispersive[IV] and isotropic[V] then:

$$\mathbf{P} = \epsilon_0 \chi \mathbf{E}\,, \tag{2.3}$$

[I] Material that can be polarized by an electric field.

[II] $P \propto E$

[III] Properties are independent of the position in space.

[IV] Speed of a wave does not depend on frequency of wave.

[V] Properties are independent of the direction in space.

where χ is the constant of proportionality called **electric susceptibility** of the medium. That is, if the assumptions me made about the behaviour of the medium hold true. If the medium is anisotropic– changes properties based on the direction $\overrightarrow{r}$ – then the susceptibility χ is a tensor.

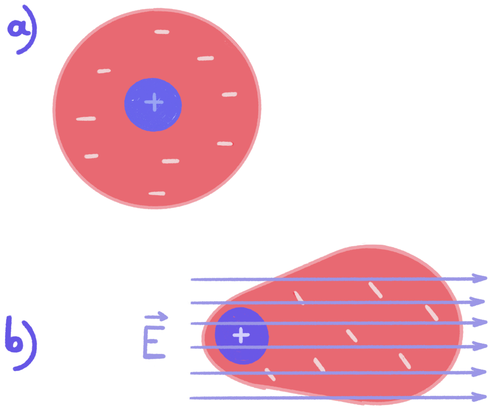

FIGURE 2.4: A simple illustration depicting the polarization of an atom without a field (a) and the induced polarization p of an atom when an electric field is applied (b): the minus stands for the electrons and the plus for the nucleus.

As the electric field $\mathbf{E(t)}$ becomes stronger the polarization becomes bigger as well. However, after the applied field becomes too large or when its frequency is close to a resonance, it starts to be comparable to the the intra-atomic electric field of the medium [42]. When this happens the electron cannot follow the oscillation of the electric field E anymore and it responds in an unharmonic way [43]. The medium's properties change and its behaviour (susceptibility) is no longer linear, but depends on the applied light field [44]. We can describe this nonlinearity by a Taylor series expansion in the electric field:

$$P = \epsilon_0 \sum_{n=1}^{\infty} \chi^{(n)} E^n = \epsilon_0 [\chi^{(1)} E + \chi^{(2)} E^2 + \chi^{(3)} E^3 + ...] , \tag{2.4}$$

where the expansion coefficients correspond to the $\chi^{(n)}$ nth order nonlinear **susceptibility**, a $n+1$ rank tensor.

The $\chi^{(1)}$ processes are linear processes. The $\chi^{(2)}$ processes and above are nonlinear, but there is another important distinction here: $\chi^{(2n)}$ processes are not existing in centrosymmetric media, where all directions are equivalent, because $\chi^{(2n)}$ processes require that the sign of $\chi^{(2n)}_{ijk}$ changes when the axis reverses to -i-j-k. Homogeneous gases, such as our atomic gases, fall into this category. Hence, in our experiments we work with 3rd order nonlinear processes such as the nonlinear magneto-optical rotation. This approach is useful for understanding the beginning of a given effect with increasing light power and works well when we deal with nonresonant light. However, when we have resonant laser excitation it makes no sense to distinguish between different perturbative orders once the transition is saturated, since the Series 2.4 is non-converging and all orders of the expansion are coupled [40].

The electric displacement **D** can now be rewritten as:

$$\mathbf{D} = \epsilon_0 \mathbf{E} + \mathbf{P} = \epsilon_0 \mathbf{E} + \epsilon_0 \chi \mathbf{E} = \epsilon_r \epsilon_0 \mathbf{E} \, , \tag{2.5}$$

where the **relative permittivity** $\epsilon_r = 1 + \chi$ and the **refractive index** is equal to:

$$\eta = \sqrt{\epsilon_r \mu_r} = \sqrt{\epsilon_r} = \sqrt{1 + \chi} \, , \tag{2.6}$$

if we ignore magnetic effects. The refractive index has an imaginary and a real part which are associated to two physical properties [45]: The imaginary part describes the absorption of the photons (scattering in all/random directions) and the real part describes the dispersion of the light (its speed propagation). The susceptibility{I} is related to the refractive index through the above formula and, as a result, we can infer the absorptive and dispersive properties of the medium by knowing the susceptibility of a medium.

2.2.2 Quantum mechanical formalism – from microscopic to macroscopic

For an atom in an electric field $E(t)\hat{e}_E$, with $\hat{e}$ being the unit vector along the light-polarization direction and amplitude E_0, the Hamiltonian is given by

$$H = -\boldsymbol{d}\hat{e}_E \boldsymbol{E_0} \, , \tag{2.7}$$

where **d** is the **electric-dipole operator** that is written for a charge q as

$$\mathbf{d} = q\mathbf{r} \, , \tag{2.8}$$

where **r** is position vector from the charge to a point around it and whose matrix elements are important for the light-atom interactions and **atomic transitions**. In our case, q is equal to $-e$ (the electron-charge magnitude) and **r** is the position of the electron with respect to the nucleus.

The expectation value of the dipole operator is $\langle d \rangle = Tr(\rho d)$ (see 1.4.1) and the polarization **P** of a medium with atomic density n (number of atoms per unit volume of that material) is:

$$\mathbf{P} = nTr\rho(E)\mathbf{d} = \hat{e}_E \sum_{g,e} d_{ge}\rho_{eg} + c.c. \, , \tag{2.9}$$

and

[I] The susceptibility is frequency dependant and this dependence is related to the dispersion properties of the material

$$d_{ge} = \langle e|\, d \,|g\rangle \ , \tag{2.10}$$

where d is the electric dipole moment operator, d_{ge} is the dipole matrix element related to a transition from the ground state $|g\rangle$ to the excited state $\langle e|$, $\rho(E)$ is the light-dependent density matrix, ρ_{ge} refers to the the optical coherence, E_0 is the amplitude of the applied electric field, and $\hat{e}_E$ is the unit vector [38].

We have talked about electric dipoles so far, but other kinds of multipole moments may be created, such as magnetic dipoles and electric quadrupoles. In order to distinguish between linear and nonlinear effects, we looked at how the properties of our medium P change with the electric light field E. In order to create a more systematic way of classifying these effects and including all types of atomic polarization we solve the density matrix with the pertubative approach [30]. We expand the density matrix $\rho(E)$ in a power series:

$$\rho(E) = \sum_{0}^{\infty} \rho^{(n)} E_0^n \, . \tag{2.11}$$

the term $\rho^{(0)}$ describes the density matrix in the absence of light. The terms $\rho^{(1)}$ and $\rho^{(2)}$ are associated with optical effects that are linear and hence are called linear processes. All higher-ranking terms are called nonlinear processes. The $\rho^{(2)}$ order of perturbation is responsible, amongst other effects, for the *quantum beats*. Due to $\rho^{(2)}$ the density matrix is quadratic in the electric field, but the optical coherences within the ground and exited states through this order are linear in the electric field. The optical properties of the ensemble are determined by these coherences and so we consider the effects of this term to be linear. In general, $\rho^{(n)}$ with n odd describe optical coherences, for example $\rho^{(1)}$ could describe linear absorption. Optical coherences are coherences between the opposite-parity lower and upper states of the optical transition[I]– see next Section 2.3.1. A $\rho^{(n)}$ with even n describes density matrix elements with the same parity. More about it can be read in [30] *Chapter 10: Light-atom interaction observed in transmitted light.*

This approach is useful if we want to understand the nonlinear optical phenomena, but it is not applicable in every case. If we have light strong enough to saturate a transition (see Section 2.4.2) or resonant light, then we need to solve the Liouville equation 1.4.2 which would make our solution more precise, but computationally and conceptually harder [38]. Keep in mind that the phenomena and effects that are going to be studied in this thesis are often complicated as they are a combination of processes of different ρ orders.

[I] If the orbital angular momentum is L, then the parity of the energy level is $(-1)^L$ for single-electron atoms.

2.3 Atomic transitions

2.3.1 Rabi frequency

We saw in Chapter 1 that the density matrix describes both polarized and unpolarized ensembles and two important properties arising from it are populations and coherences. In this Chapter we go back to the microscopic level in order to describe some important mechanisms of light interacting with an atom and more specific with a **two-level system**. The populations and coherences of the energy states of an atom can change through light-atom interactions and these changes are described by atomic transitions. In atomic physics generally, as well as our experiments in particular, we care immensely about the evolution of an atomic system under the action of a periodic perturbation. For us this plays a huge role, since we study light-atom interactions, which means we couple a two-level system with an optical field— an *oscillating* field.

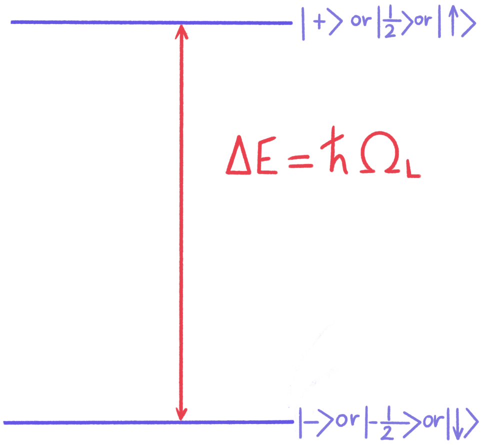

FIGURE 2.5: A two-level spin-1/2 system.

To be able to study such a system and define some important concepts we will consider the simplest case of a spin–1/2 system. This two-level system has two energy levels (two independent quantum states): spin projection 1/2 and spin projection −1/2. We now put this system inside a static magnetic field $B_0\hat{z}$. Now this system has a lower state and an upper state that correspond to the two angular-momentum projections on z. The energy difference between the lower state and the upper state corresponds to an energy interval of:

$$\Delta E = \hbar\Omega_L = g\mu_B B_0 \, . \tag{2.12}$$

We consider next a weak oscillating magnetic field with frequency ω transverse to the leading field $\boldsymbol{B_0}$ that we will call $\boldsymbol{B_1}$ and want to see how the state of this system will change with time. The trick to remove the time-dependence is to make a frame rotation to a frame where B_1 is stationary along y (or x). In the rotating frame the time evolution of the spin state is just Larmor precession around the effective field along $\hat{z}$ [30].

In the resonant case, where B_1 rotates at the Larmor frequency Ω_L, we practically don't care about the leading field $\boldsymbol{B_0}$ and the system's evolution is just Larmor precession around $\boldsymbol{B_1}$. If $\omega \neq \Omega_L$ (and assuming $\boldsymbol{B_1} = B_1\hat{y}$) then we have Larmor precession around:

$$\left(B_0 - \frac{\hbar\omega}{g\mu_B}\right)\hat{z} + B_1\hat{y}\,, \tag{2.13}$$

where $(B_0 - \frac{\hbar\omega}{g\mu_B})$ is the effective field along z. Let us go back to the resonant case again, where the spin state just rotates around y. At time t, we define the Rabi frequency as the frequency of Larmor precession in the field B_1:

$$\Omega_R = g\mu B_1/\hbar\,, \tag{2.14}$$

If we apply the rotation matrix to our system's wavefunction $\psi(t=0) = \begin{bmatrix}0\\1\end{bmatrix}$ we get:

$$\psi(t) = \begin{bmatrix} cos(\frac{\beta}{2}) & -sin(\frac{\beta}{2}) \\ sin(\frac{\beta}{2}) & cos(\frac{\beta}{2}) \end{bmatrix} \begin{bmatrix}0\\1\end{bmatrix} = \begin{bmatrix} -sin\Omega_R t/2 \\ cos\Omega_R t/2 \end{bmatrix}\,, \tag{2.15}$$

where the rotation angle around $\hat{y}$ is $\beta = \Omega_R t$. The probability to find the spin in the 1/2 state is:

$$P_{1/2} = \frac{1 - cos\Omega_R t}{2}\,, \tag{2.16}$$

and in the -1/2 state:

$$P_{-1/2} = \frac{1 + cos\Omega_R t}{2}\,. \tag{2.17}$$

These probabilities are oscillating as a function of time with a period equal to the inverse of the **Rabi frequency**.

We can generalize this problem for any two-level system under the influence of a periodic perturbation. In the case that interests us, where light couples to a two-level system, the Rabi frequency is $\Omega_R = dE_0/\hbar$, where E is the electric field and d is the electric-dipole matrix element.

2.3.2 Stimulated emission

Rabi oscillations cause the system's population to transition periodically between the two states. The atoms will be in the energetically lower state initially, but the Rabi oscillations will cause them to periodically go to the excited state, gradually increasing the probability of the system being found in the excited state. This happens through the mechanism of *absorption*: the system absorbs the energy of a photon and undergoes a transition from a lower energy state to a higher energy state. Under Rabi oscillations, the probability of the quantum system being in the excited state gets increased

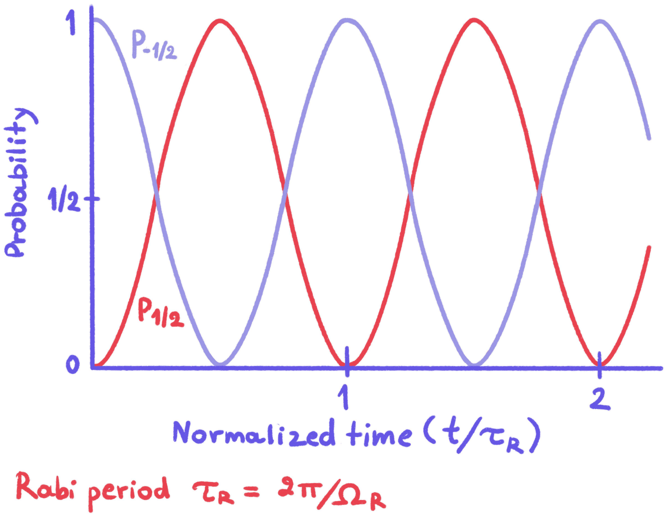

FIGURE 2.6: The probability of finding the spin in the 1/2 or -1/2 state oscillates with time.

and absorption occurs less and less with time. There are two important processes that can happen next: **spontaneous emission** and **stimulated emission**.

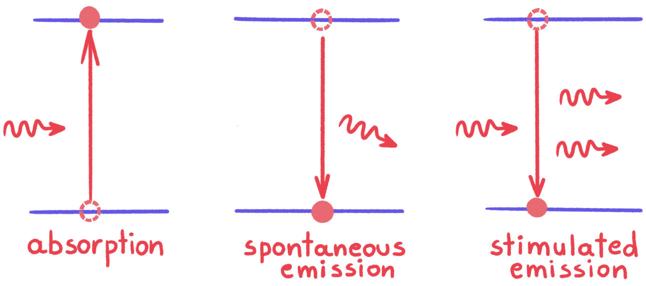

FIGURE 2.7: Absorption, spontaneous and stimulated emission from left to right.

Spontaneous emission is an important relaxation mechanism in which an atom goes from a higher energy state to a lower energy state, and in this process it emits a photon that corresponds to the difference of the two energy levels. For this to happen there is no external light-field required, but the excited states are unstable and tend to decay to lower energy states with a certain decay rate{I}. The time it takes for an excited atom to go from the excited to the ground state is an intrinsic physical property related to Heisenberg's energy-time uncertainty and is called the lifetime τ of the transition.

{I} Excited states with a longer lifetime are called metastable

This results always in broadening of a spectral line that we call **natural linewidth** of a transition $\Gamma_0 \propto 1/\tau$ and it is not related to other sources of broadening like collisions or the Doppler effect.

In the process of stimulated emission, same as in spontaneous emission, an atom goes from a higher energy state to a lower energy state, but this time this effect is "stimulated" by an electromagnetic field with a frequency that matches the energy difference between the excited state and a lower energy state. If our system is in the Rabi cycle in the upper state (not taking into account stimulated emission) then it will emit photons from the upper (excited) state to the (lower) ground state in the same direction and with the same phase as the field through the process of stimulated emission. The resulting light is coherent[I]. Lasers are the prime example of light coherence, which is one of the properties responsible for their unique properties.

2.3.3 Optical Bloch equations

Section 1.4.2 introduced the Liouville equation as the rate of change of the density matrix. The full equation of motion for the density matrix, including the Hamiltonian part due to the interaction with the external field and the spontaneous emission, is [41]:

$$(\partial/\partial t)\rho = (1/i\hbar)[\mathscr{H}, \rho] + \begin{bmatrix} -\Gamma\rho_{mm} & \frac{\Gamma}{2}\rho_{mn} \\ \frac{\Gamma}{2}\rho_{nm} & \Gamma\rho_{nn} \end{bmatrix} . \tag{2.18}$$

Keep in mind that the diagonal elements of the density matrix ρ correspond to populations and the non-diagonal to coherences of the corresponding levels. The diagonal elements of the last term show the time evolution of the populations with a decay rate Γ and the non-diagonal elements show the effect of the spontaneous emission on the coherences. We can view n as the ground state and m and the excited state in a two-level system.

The above matrix equation can be written in the form of four (4) differential equations known as the **optical Bloch equations**. The equations describe the time evolution of the populations and coherences in a two-level system. In addition to these equations, the elements of the density matrix must obey two other constraints: the sum of the populations must be equal to one (1), and the off-diagonal matrix elements must be complex conjugates [41]. These conditions can be written as three (3) independent components $\{u, v, w\}$ of a vector called the **Bloch vector** and are proportional to:

u: the in-phase component of the atomic dipole moment,

v: the quadrature component of the atomic dipole moment,

w: the populations of the ground and excited states .

The reason we use this geometrical language is, once again, for visual comprehension: The three (3) vector components of the Bloch vector are used as three dimensional coordinate system that defines a sphere called the **Bloch sphere**. The Bloch sphere is a tool that allows us to see the evolution of the

---

[I] The phase relationship between different parts of the wave remains constant over time and space i.e. the wave has a well-defined and stable phase

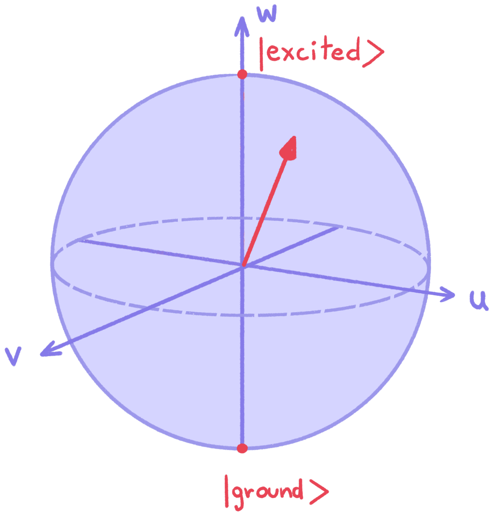

FIGURE 2.8: An illustration of the Bloch sphere.

system as a trajectory and represent a state with a vector from the origin to a point on that sphere. The radius of the Bloch sphere has a length of one (1)– if we don't consider spontaneous emission [41]. The diametrically opposite points of the north and south pole of the sphere correspond to the ground and excited states of our system (w axis). Whenever the vector rests on the equator of the Bloch sphere that corresponds to an equal superposition of the ground and excited state (50-50 probability for the system to be observed on either the ground or excited state).

2.4 Optical pumping

You might have noticed by now that we still have not introduced *how* one polarizes an atom and what happens with an ensemble of an enormous amount of atoms when light gets transmitted though it.

Pumping is a crucial *nonlinear light-atom interaction* [30] that allows us to manipulate atomic populations and coherences and create what is the basis for a huge range of applications and studies: magnetization of an ensemble. Through resonant excitation we can polarize enough atoms in an ensemble to create polarization that manifests as (macroscopic) magnetization.

2.4.1 Selection rules

As everything in Quantum Mechanics, the possible transitions of a system from one state to another are constrained, in this case by the angular-momentum **selection rules**. Light interacts with atoms that are in states called **bright states** by transferring to these atoms part of the angular momentum carried by the light beam [45]. The states that don't interact with the light are called **dark states**. Different states have different absorption rates based on the selection rules.

From the Equation 2.6 we know that the Rabi frequency of a driven transition is proportional to the electric-dipole operator $\mathbf{d}$ and the latter is, in turn, proportional to the matrix element of the position vector **r** of the electron. Therefore, the probability of an electric-dipole transition to be induced depends on the dipole moment of the transition, the amplitude of the electric field and the direction of the light field relative to the atomic dipole moment [30].

For the purposes of this thesis we will not go into the formalism of how to derive the selection rules or calculate the strength of the transitions. To establish these rules, one must study the non-diagonal matrix elements ($n \neq n'$) of the various atomic operators such as the electric and magnetic dipoles [33]. The selection rules have their origin in the **Wigner-Eckart theorem** which states that the matrix elements of a vector operator are a product of two factors: the first are called the **reduced matrix elements** and do not depend on the angular momentum projections m; the second are called the **Clebsch-Gordan coefficients**, are orientation dependent and show which states are coupled and with what probabilities. These coefficients will vanish, unless $J+1 \geq J' \geq J-1$, where J is the angular momentum of the given state. The above condition is the reason there is only one (1) unit of angular momentum added to the system when coupling vector operators [46]. A thorough quantitative approach can be found in the literature [47], [34].

The selection rules in an electric-dipole transition between initial and final states for a single-electron atom are:

$$\Delta S = 0\,, \tag{2.19a}$$

$$\Delta L = \pm 1\,, \tag{2.19b}$$

$$\Delta J = 0, \pm 1\,, \tag{2.19c}$$

$$\Delta F = 0, \pm 1\,, \tag{2.19d}$$

$$\Delta m_J = 0, \pm 1\,. \tag{2.19e}$$

Let us qualitatively explain these rules one by one:

- $\Delta J = 0, \pm 1$ is a strict rule that arises from angular momentum conservation. Since the photon spin is one (1), the case $\Delta J = 0$ is not allowed for single-photon transitions.
- $\Delta S = 0$ obeys the rule that the electron spin in an optical transition remains constant, meaning that the spin wave function is preserved– that case is true only for LS coupling.
- $\Delta L = \pm 1$ The electric dipole operator does not depend on the spin component S. These matrix elements (see 2.10) vanish unless $\Delta L = \pm 1$.
- $\Delta F = 0, \pm 1$ is similar to the J rule when the interaction involves an atom with nonzero nuclear spin I. As long as J is conserved in the system, the selection rule $\Delta J = 0, \pm 1$ applies as well.
- So far, the rules were related to the magnitude of the angular momenta, but they also concern their projections on the quantization axis which are related to the magnetic quantum numbers m. The selection rules in this case depend on the polarization of the light. As a convention

> in QED, the polarization is defined with respect to the quantization axis: right-circular (left-circular) polarization is a property of the light whose polarization vector rotates clockwise (counter-clockwise) as we look from the source towards the light propagation [30]. Later we will describe polarized light with respect to a fixed axis (the axis of our magnetic field, usually also the quantization axis). We call light that is linearly polarized along this axis *π-polarized* and light that rotates clockwise (counterclockwise) as viewed from source *σ_+ polarized* (σ_-) [48]. Polarized light can be decomposed into the above three polarizations. Now, photons that are right-circularly polarized (left-circularly polarized) have a projection of angular momentum of $+1$ (-1) on the quantization axis. The selection rules are [I]:
>
> For σ_+ (right-polarized): $\Delta m_J = +1$ and for σ_- (left-polarized): $\Delta m_J = -1$.
>
> Keep in mind here that in optics when we talk about right and left-circular polarization we usually define it in the opposite way to the above convention.

Besides the angular-momentum selection rules, there is another important rule related to parity. Remember that in atoms odd parity is defined when $(-1)^L = -1$ and the opposite is true for even parity. The *electric-dipole moment* has odd parity, which means that the initial and final states must have different parity in order for the matrix elements to not give a zero value. This means that electric-dipole transitions between states with the same parity are forbidden. We call this the parity-selection rule. In some of our experiments we are interested in *magnetic-dipole* transitions, because these are the ones that occur. In this case, some of the angular-momentum selection rules stay the same and some change. For example, regarding the parity-selection rule: the magnetic-dipole transitions couple states with the same parity.

2.4.2 Saturation parameters

Another way to distinguish between linear and nonlinear effects is the decay rate of the ground and excite states. Nonlinear effects start appearing when the light is resonant or strong compared to a characteristic saturation intensity. If, with the increase of the light intensity, the properties of the medium depend on the light, we talk about a nonlinear process. It is important to realize that the degree of nonlinearity strongly depends on atomic saturation by the light field as well as the relaxation rate of atomic polarization [40]. There is a gradual transition from the linear to the nonlinear that happens when the rate by which we excite atoms gets larger than the rate by which atoms spontaneously return to the ground state i.e the relaxation rate (see equation 1.26):

$$\kappa = \frac{\text{excitation rate}}{\text{relaxation rate}} . \tag{2.20}$$

To be more exact: The saturation parameter is the ratio of the rates of coherent light-atom interactions (responsible for Rabi oscillations) and incoherent relaxation processes (e.g., spontaneous decay) [40].

[I] We talk about J for an atom with zero nuclear spin I. If I is nonzero then these rules are the same for the total angular momentum F.

For a two-level system in which the upper state decays back to the lower state, when the light is resonant, the saturation parameter for the upper state is:

$$\kappa_1 = \frac{d^2 E_0^2}{\hbar^2 \gamma_0^2}\,, \tag{2.21}$$

where d is the dipole moment and γ_0 the relaxation rate of the upper state, which would make $\kappa_1 = d^2 E_0^2/\hbar^2\gamma_0$ the excitation rate. Remember from Section 2.3.1 that for a two-level system the Rabi frequency is $\omega_R = dE_0/2$. That would make κ_1:

$$\kappa_1 \propto \left(\frac{\omega_R}{\gamma_0}\right)^2\,. \tag{2.22}$$

We see that when $\kappa_1 \ll 1$ that means that the relaxation rate related to the spontaneous emission is dominating and atoms are in the lower state. When $\kappa_1 \gg 1$ the Rabi oscillation term dominates and the average population of the upper and lower state is 50–50; that is the nonlinear regime.

There is another case we need to study that is when the upper state decays predominantly to states other than the lower state of the transition. The light will keep exciting atoms to the upper state, while the excited state relaxes to the other states eventually leading all the atoms to these non-interacting states, called **dark states**. There are processes, such as collisions, that can redistribute atoms between the ground states at a rate γ.

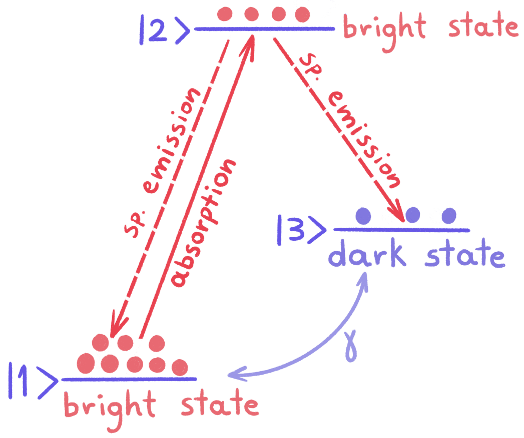

FIGURE 2.9: An illustration of a dark state $|3\rangle$ that does neither absorb nor emit photons. This is not a two-level system, but since it contains three levels it is called a three-level system. It interacts with the ground state $|1\rangle$ only indirectly through γ. For more details see 3.3.3.

In this case the saturation parameter is:

$$\kappa_2 = \frac{d^2 E_0^2}{\hbar^2 \gamma_0 \gamma}\,. \tag{2.23}$$

If γ is smaller than γ_0, which is the case sometimes in our experiments, then the denominator is small and the fraction gets much bigger, which means that in this system we can have a nonlinear effect with lower light intensities than in the case of κ_1. The decay rate of the upper state stays the same, but the population gets now redistributed back to the **bright state** at a slow rate determining the behaviour of the whole system.

If we have a dark state in the ground levels of our system we are in the case where the saturation parameter κ_2 is relevant. This is the case when for example one pumps with circularly polarized light or if the right- and left-circularly polarized light have different transition frequencies due to an external magnetic field. As we will see next, these cases are relevant for this thesis as our experiments are operating under similar principles.

Optical pumping that creates ground-state population imbalance such as is the case in many atomic magnetometers, creates also atomic polarization by definition. And any process that depends on atomic polarization is a nonlinear process since atomic polarization changes the properties of a medium. The saturation parameter κ_2 describes the generation of this polarization and the nonlinearities arising from it [30].

2.4.3 Mirrorless lasers

In this context, we can describe an effect that we will comprehensively discuss in Chapter 6 and 7 called **degenerate mirrorless lasing**. Both saturation parameters play a role in this effect. The principal idea is that optical pumping redistributes the population among the ground-state Zeeman sublevels – κ_2 is the relevant saturation parameter here. At sufficiently high light powers, as κ_1 reaches 1, the population is partially transferred to the excited state, which, in the case of an $F \rightarrow F+1$ transition may result in population inversions between certain sublevels of the ground and excited states. This inversion may, under right circumstances, result in directional emission from the sample.

In the case of degenerate mirrorless lasing, amplified spontaneous emission is produced along or opposite to the pump-beam direction, with polarization orthogonal to that of the pump. The pump field interacts with the Zeeman-sublevels (m_F) of a specific atomic transition and population inversion is produced between certain magnetic sublevels.

Amplified Spontaneous Emission (ASE)

We already talked about spontaneous emission, a quantum process in which an atom in an excited state spontaneously de-excites into a lower energy state by emitting a photon (the photon being emitted into one of the modes of the vacuum). One could also understand this process as stimulated emission by vacuum noise fluctuations.

Amplified spontaneous emission (ASE) is a phenomenon that occurs often in lasers and optical amplifiers as a result of stimulated emission processes that amplify the spontaneous radiation field that propagates in a medium with gain [49]. When the contribution from optical gain processes is greater than that of absorption and radiation that scatters away in a gain medium, we reach the threshold for ASE.

In atomic gas systems, the spatial coherence and beam divergence of ASE are affected by the geometry of the laser setup (the optically active part of the system) and the internal degrees of freedom (atomic populations, coherences and spectral lineshape) allowing for higher ASE spacial coherence. When one also assumes a pencil-like geometry for the pump laser (only a narrow cone of wavevectors contributes to the ASE modes), large enough atomic density and after calculating the rate of radiative transfer of the light field one can model the dynamics of an ASE field in a cold random atomic gas, under the approximation that inter-atomic scattering plays little to no effect. For more details read also [49].

We will delve experimentally into this fascinating topic in Chapters 6 and 7.

I write these words in steel,
for anything not set in metal cannot be trusted.
Brandon Sanderson, The Well of Ascension

3

Atomic magnetometers

3.1 Simple model of an optical magnetometer

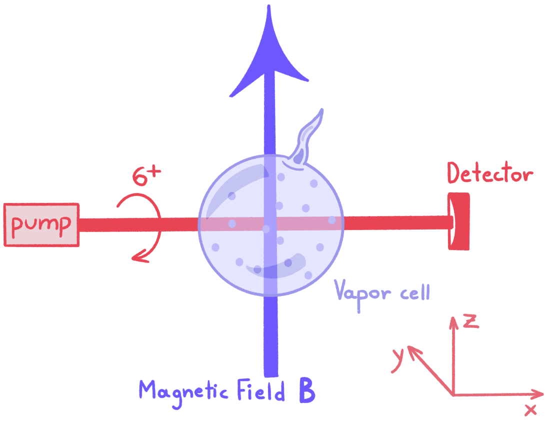

FIGURE 3.1: Illustration of a basic setup of an atomic magnetometer.

This Chapter is all about atomic magnetometers: what they are, how they work, their types and properties. After having discussed about the Rabi frequency, relaxation mechanisms, the time evolution of a two-level system, what optical pumping is and how nonlinear effects appear, we reached the point in which we can illustrate the basics of an optical magnetometer or OPM (optically pumped magnetometer).

3.1.1 Atomic structure

Many optical magnetometers are based on alkali atoms. A typical structure of the ground state S and the first excited states of such an atom– in this case ^{87}Rb –can be seen in Figure 3.2. The transitions from S to the two excited states $P_{1/2}$ and $P_{3/2}$ form a fine-structure doublet, and each of these transitions additionally have hyperfine structure [50].

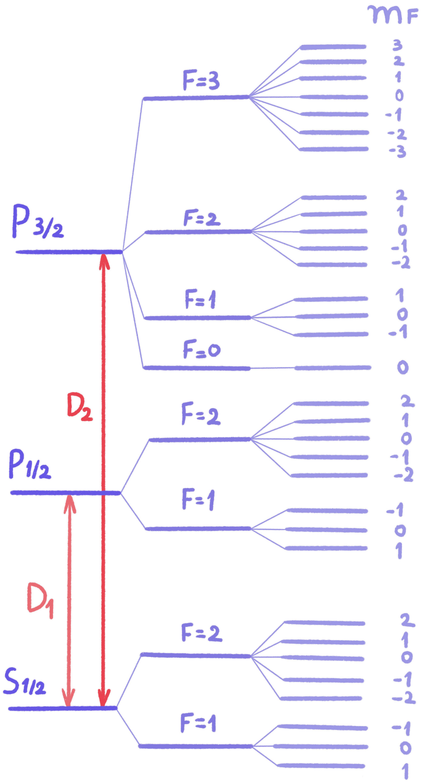

FIGURE 3.2: Transition structure of an alkali atom with nuclear spin $I = 3/2$ such as ^{23}Na, ^{41}K or ^{87}Rb [19].

We call the transitions between the magnetic (Zeeman) sublevels Δm_F, that belong to the same hyperfine level F, **Zeeman transitions**. The energy difference between them corresponds to frequencies in the radio-frequency range, while the hyperfine-structure transitions ($\Delta F = 0, \pm 1$) are in the microwave range. The transitions from S to the two excited states $P_{1/2}$ and $P_{3/2}$ are optical and are used for pumping [19]. This is why later we refer our laser lights as D_1 and D_2, where often D_1 is used for pumping and D_2 for probing.

Note here that, for some sublevels, the $m_F = -1$ has a higher energy the $m_F = 1$. Remember that we calculate the Zeeman energy shift for the hyperfine F states from: $\Delta E_{m_F} = g_F \mu_B B m_F$. The Lande factors g_F[I] for the two hyperfine components of the ground state $S_{1/2}$ play a role in these energy shifts. Considering that $F = I \pm J$ and because the Lande factor depends on $\boldsymbol{J}$ and $\boldsymbol{F}$, when electronic angular momentum J points in the same direction as the total angular momentum

---

[I] Lande factor is the g-factor for an electron

F, g_F is positive, and when they are directed in opposite directions g_F is negative. This creates this asymmetry of the signs between various m_F sublevels.

3.1.2 Vapor Cells

When we talk about atom-light interactions we know that we use lasers for the light-part of the interaction (see more in Section 3.5.3). How do we use atoms? We have a piece of alkali-metal that is placed inside a sealed glass cell, round or cylindrical. Inside the cell a small amount of the solid alkali evaporates into the gas phase, so that the cell is filled with alkali-vapor. We need to polarize the atoms/alkali-vapor which in turn should stay polarized for as long as possible.

In order to keep the atoms polarized for a longer time many cells use another gas called **buffer gas** inside the cell to prevent the atoms from diffusing away from the pump beam and towards the walls. Some cells have paraffin coating on the glass walls, so that, when the polarized atoms bounce at the walls they don't lose their polarization [51, 52]. In the magnetometer experiments of this thesis we used paraffin-coated cells.

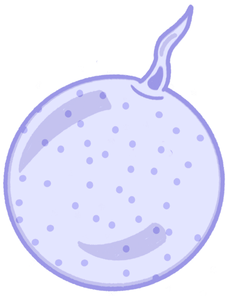

FIGURE 3.3: Vapor cell illustration: atoms are not to scale.

3.1.3 Pump

Let's now present the basics of an optical magnetometer. We have alkali atoms in a two-level system in a alkali vapor gas, as seen in Figure 3.4, with total angular momentum $F = 1/2$ for the ground state and $F' = 1/2$ in the excited state. The ground state, according to the angular-momentum rules 1.11, has two m_F sublevels $1/2$ and $-1/2$. In Figure 3.4 in ① we see the system and its population before we pump.

Next, we shine light to these atoms which is right-circularly or σ_+ polarized, according to our convention. The pump light is propagating along x and its frequency is near-resonant to the $F \rightarrow F'$ transition. When we apply the pump we drive Rabi oscillations, as detailed in Section 2.3.1. Based on the selection rules 2.19e if we pump with σ_+ light, we can only pump between sublevels that differ by $+1$. As a result, and as we see in ②, we have a dark state in our Zeeman ground sublevels which makes our system similar to the three-level system in Section 2.4.2 and so the saturation parameter κ_2 applies [40]. For now the magnetic field $\mathbf{B}$ is zero. We choose our quantization axis along the light propagation x and we see that, because of the way we can pump, with time, the probability of an

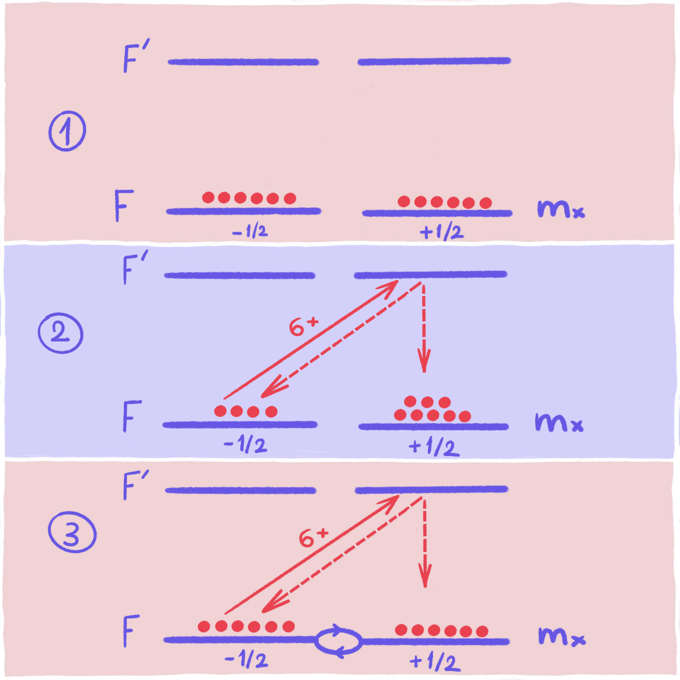

FIGURE 3.4: 1. Before pumping 2. Light depletes population at B=0 3. Optical detection when B≠ 0.

atom to be found in the state 1/2 is increasing since the 1/2 sublevel cannot interact with our light due to the selection rules and hence its population cannot be excited to higher levels. This creates a net angular momentum along x [19].

3.1.4 Probe

After we pumped, we suddenly add a uniform magnetic field $B_{\hat{z}}$ and we reduce the intensity of the light so that now the light beam pumps slowly. This is the case of ③ in Figure 3.4 and now the Zeeman sublevels are not degenerate anymore, due to $B_{\hat{z}}$. If we choose our quantization axis now along z we get reminded of the concept of *quantum beats*. What seemed abstract in Section 1.4.4 is now tangible; the states $|1/2\rangle_x$ and $|-1/2\rangle_x$ are now rotated to be written in the z coordinate system as:

$$|1/2\rangle_x = \frac{|-\rangle_z + |+\rangle_z}{\sqrt{2}}\,, \tag{3.1a}$$

$$|-1/2\rangle_x = \frac{|-\rangle_z - |+\rangle_z}{\sqrt{2}}\,, \tag{3.1b}$$

with $m_z = 1/2$ ($m_z = -1/2$) undergoing an energy shift of $\hbar\Omega_L/2$ ($-\hbar\Omega_L/2$), in other words *the superposition of the m_F states along the axis z of the magnetic field is oscillating at a frequency Ω_L*. The probability of finding the state in $m_x = 1/2$ which is the state which can interact with the light is also a sinusoidal function of Ω_L. The light that reaches now the detector interacts with the medium in a sinusoidal manner as well, since it gets absorbed more when the light state has more atoms. This change is what we detect and is what we call **Larmor precession** in a magnetic field **B**.

We can find magnetometers in a variety of configurations, some quite different to the example we described above. However, at its heart optical magnetometry remains the same: we induce a change in the opto-magnetic properties of the ensemble through pumping, which we then detect through a change in the light absorption or its polarization rotation corresponding to a Larmor-precession frequency.

Optical detection

The moment comes now to talk about detection in optical magnetometers. It is useful, once again, to start with the linear case of the Macaluso-Corbino effect as seen in Section 2.1.2, where linearly polarized light, composed of σ_+ and σ_- interacts with an atom. The frequencies of σ_- and σ_+ between the ground sublevels and the excited state are the same if the system is in zero field. When an external magnetic field is added, the ground-sublevels energy is shifted and σ_- and σ_+ now interact differently with the excited state. To explain this better we need to get back to the complex refractive index of the atomic medium η introduced in 2.2.2:

$$\eta = n + i\kappa\,. \tag{3.2}$$

In the above relationship, n is the real index of refraction, that has a dispersive behaviour as a function of the angular frequency of the light ω and κ is the imaginary part related to absorption. A change in the refractive index would result in a change in absorption or dispersion of light passing through the medium. Absorption can be detected through transmission of light, while dispersion is related to optical rotation. The change in the behaviour we detect, has its cause to the added magnetic field which creates **birefringence** {I} and/or **dichroism** {II}: the polarization components σ_- and σ_+ interact now differently with the medium and, as a result, they have a different refractive index η_- and η_+ whose difference creates the measured rotation. The rotation angle ϕ of the polarization of the light, in an atomic sample of length l, is given by:

$$\phi = \frac{\omega l}{2c}\,\mathrm{Re}(\eta_+ - \eta_-)\,. \tag{3.3}$$

For one refractive index value, the curve we detect is close to Lorentzian as seen in Figure 3.5. Generally in magneto-optical effects, and without getting into details about the formalism, optical rotation is, in the resonant case, dependent on the magnetic field in a way that resembles a dispersive Lorentzian. This is intuitively understood by considering that the relaxation of the atomic coherences in

---

{I} Refraction of light depends on its polarization

{II} Absorption of light depends on its polarization time is an exponential decay and the Fourier transformation of an exponential decay is a Lorentzian function.[I]

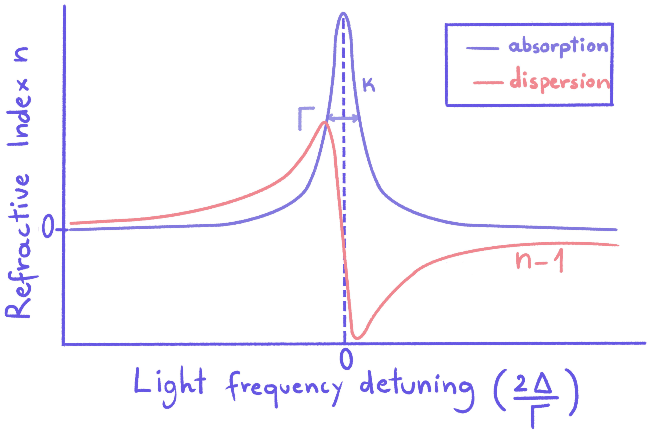

FIGURE 3.5: Lorentzian shape of the refractive-index change of light due to the Macaluso-Corbino effect.

The transitions driven by the light induce absorption with a Lorentzian shape and a phase shift with a dispersive shape [30]. These curves have a characteristic width Γ, while the curve of the absorption is an even function[II] with maximum at zero (0) light-detuning from resonance $2\Delta/\Gamma$ (or else has a maximum on resonance). The curve of dispersion is an odd function[III] that crosses zero (0) at no detuning/on-resonance.

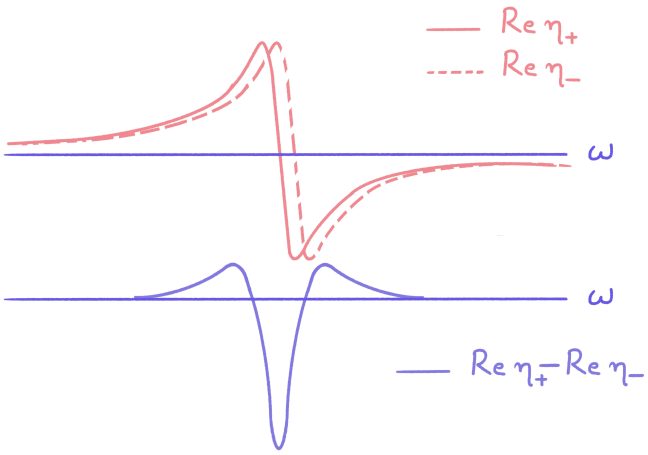

FIGURE 3.6: The real parts of the refractive indices are creating dispersive curves that are shifted in frequency due to the external magnetic field. Their difference is proportional to the linear optical rotation ϕ of the light passing through the medium.

[I] This is not a very accurate model, because the light beam interacts with the atoms in a finite time. However, to a first approximation the shape is qualitatively similar to a dispersive Lorentzian.

[II] $f(-x) = f(x)$

[III] $f(-x) = -f(x)$

We are in the linear case still, and here the optical rotation signal in a system with circular birefringence is a phase shift between σ_- and σ_+ when linear light propagates through an atomic medium. Based on Equation 3.3 , the angle is given by the difference between the dispersive (phase-shift) curves as seen in Figure 3.6.

The above description helps understanding linear effects, but nonlinear effects make the system much more sensitive to changes of the magnetic field. In linear effects we have shifts in the sublevels due to a magnetic field, but nonlinear effects are related to the evolution of created atomic polarization and Larmor precession. We will take a closer look at throughout the next Chapters, and especially in Section 3.3.3.

3.1.5 Shielding

In order to place the atoms inside zero (0) field, one needs to find a way to zero the external magnetic fields first. Sometimes, as is the case for many experiments in this thesis, we might want to work on the Earth's field (about 0.5 G) and not in zero field. One might think that this would solve our shielding problem, but, alas, the lab has an unexpected amount of items that can produce magnetic fields, from screwdrivers and waveplates to the moving elevator in the corridor above. Thankfully for us, we can work inside a shield and control this way magnetic fields. One can roughly divide the way to shield the atoms in two categories: **active** and **passive shielding**.

In active shielding, pairs of coils are used to cancel out the external fields. Biot–Savart's law states that constant electric current creates a magnetic field and hence by adding current through these coils we create opposite magnetic fields to the ones we want to eventually cancel.

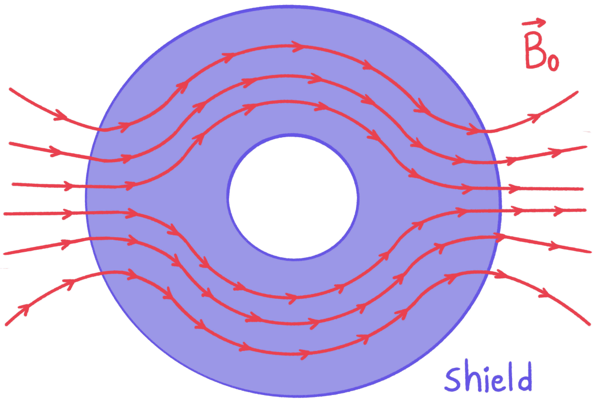

FIGURE 3.7: Magnetic shield with high permeability.

In passive shielding, we take advantage of materials with high magnetic permeability{I} to reduce the ambient magnetic noise. In our experiments we used four-layer magnetic shields from the company Twinleaf made out of a nickel–iron alloy called mu metal. This material does not allow the magnetic lines to pass through to its center where are cell is located, but rather it diverts the magnetic flux

---

{I} The magnetic permeability of a material is equal to the magnetic flux density B in a material created by a magnetic field, divided by the magnetic field strength H of this field. We can consider it to be a measure of how much magnetic flux can be concentrated inside a material.

and the magnetic field lines are now inside the material. Figure 3.7 shows a representation of the divergence of the path of the magnetic field lines due to a material with high permeability.

One might ask themselves why we use multiple thin layers for a better shielding effect and not one very thick piece. Our shielding ratio T (which needs to be as small as possible) would in that case scale proportionally to the increase of thickness. For example, if we add a $3x$ thicker shield, we get a shielding ratio of $T/3x$. If, however, we add different layers/shells separated by air in between, shielding becomes more efficient. By taking an approach for which the layers are magnetic circuits, one can calculate that for separate shells, T is proportional to the product of the thickness, meaning that, if we add a $3x$ thicker shield, we get a shielding ratio of $T/(x^3)$. The shell shape and the gap between the layers play a role as well. Adding to the fact that from time to time the residual magnetization inside the shielding layers can be increased, it becomes quickly clear that good magnetic shielding is not a trivial task.

3.1.6 Noise and Sensitivity

The concept of magnetic-field sensitivity is central to atomic magnetometry and it is often used to qualitatively compare different types of magnetometers. The units of sensitivity are often $\mathrm{T}/\sqrt{\mathrm{Hz}}$ in SI and it shows what the minimum detectable magnetic field is– i.e. a field that can be distinguished from noise. This noise depends on the frequency bandwidth and this is why we need to normalize sensitivity by dividing by frequency.

What we practically do in order to measure sensitivity is to measure the response of the magnetometer for some time t. Since the noise changes for different frequencies, we are interested in looking at this response in the frequency domain, so we perform a Fourier transform (FFT). In order to characterize noise, power spectral densities (PSD) are used instead of an FFT. To calculate a PSD each frequency bin in an FFT is multiplied by its complex conjugate and this results in an amplitude value (in our case B^2 normalized to the frequency bin width to get the units of T^2/Hz. This way our signal does not depend on bin width. To make comparisons easier we then take the root-mean-square (RMS) of the T^2/Hz and we calculate the amplitude spectral density. This is how we report the sensitivity in $T/\sqrt{\mathrm{Hz}}$.

Another way to calculate sensitivity is by using the fundamental limits set by quantum mechanics. There are two fundamentals limits: **projection noise (PN)** and **photon shot noise (PSN)**.

Projection noise (PN)

Let us think of an atom that is polarized along a particular direction. From the uncertainty principle we know that if we measure the angular-momentum projection on an orthogonal direction we get a random result [18]. In this case, the sensitivity is:

$$\delta B_{PN} \propto \frac{1}{\sqrt{N t_2 T}}\,, \tag{3.4}$$

where t_2 is the **spin-coherence time** related to transverse spin relaxation and N is the number of atoms in the ensemble. This equation is derived from the fact that one atom has an uncertainty of 1 rad in the Larmor precession angle for a measurement of time t_2. If we consider N times this atom and repeating T times we reach the above formula.{I}

Photon shot noise (PSN)

The other limitation to sensitivity is the photon shot noise. This is related again to Heisenberg's uncertainty principle and the detection of light. When light is detected by a photodetector, the number of photons arriving at any given time is random, and so the electrons produced by the photodetector– and hence our signal– is also fluctuating in time. In this case, sensitivity scales as:

$$\delta B_{PSN} \propto \frac{1}{\sqrt{\Phi T}}, \tag{3.5}$$

where Φ is the probe-photon flux (photons/second).

From the above we can conclude that in order to improve the sensitivity of a magnetometer (to make it smaller) we need to either improve the spin-relaxation time or increase the number of atoms that participate in the interactions. The first can be done by, for example, using coating and the latter by increasing the density inside the cell through higher temperatures.

3.1.7 Polarimetry

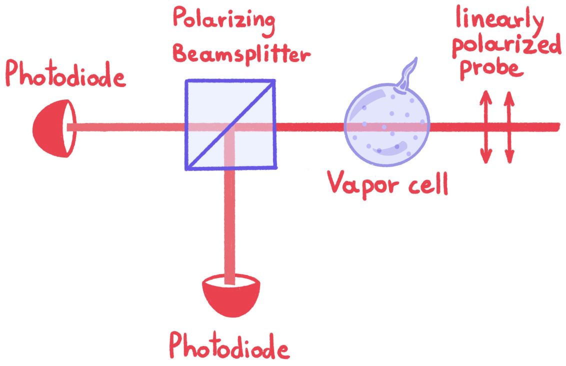

FIGURE 3.8: Balanced polarimetry setup.

There are several methods that we can use to detect optical rotation ϕ. We will here introduce the one used mostly in our experiments, since we detect at high-frequencies. This is called the **balanced**

{I} A way to overcome this limit is through spin squeezing

polarimetry technique which, as seen in Figure 3.8, consists of a polarizing beamsplitter which is set at 45° to the probe's polarization axis. This configurations splits the beam's intensity I_0 in two parts with intensities I_1 and I_2:

$$I_1 = I_0 sin^2(\phi - \frac{\pi}{4}) \,, \tag{3.6a}$$

$$I_2 = I_0 cos^2(\phi - \frac{\pi}{4}) \,, \tag{3.6b}$$

where $I_0 = I_1 + I_2$. The two intensities are equal, or in our case balanced, when $\phi = 0$ (no rotation). When the probe beam rotates, its optical rotation ϕ is given by:

$$\phi = \frac{I_1 - I_2}{2(I_1 + I_2)} \,, \tag{3.7}$$

and is valid for a small angle $\phi << 1$.

3.1.8 Spin relaxation

Spin-exchange collisions

In our efforts to reduce noise through heating, we come across a new obstacle: if we increase the temperature too much, collisions between the atoms are dominating the spin-relaxation time. In this case, the total spin is preserved, but the direction of the spin can change– see Figure 3.9. The nuclear spin I is not affected, but the atoms might change hyperfine states and get redistributed among other unobserved hyperfine Zeeman sublevels. The change in m_F states results in a change in the angle of the spin and hence its precession, leading to loss of atomic polarization in the ensemble (decoherence).

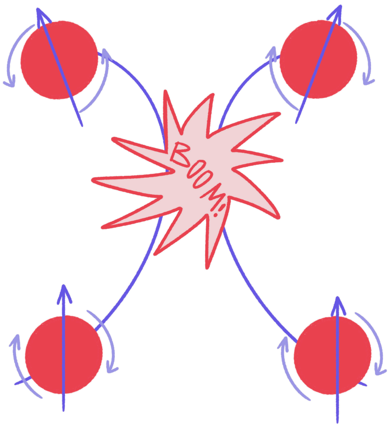

FIGURE 3.9: Spin-exchange mechanism. Red spheres are atoms that collide and after the collision precess in different directions as indicated by the purple arrows.

Note here that the total angular momentum is conserved: the vector sum of the spins after the collision should be the same as that before the collision. The spin-exchange collisions contribute to t_2 time and as a result can become important for a magnetometer's sensitivity.

Magnetic–field gradients

Many projects that are included in this thesis have been conducted in a magnetic field of the order of the Earth's field. Earth-field magnetometry can be very useful, since it does not require heavy and expensive shields or complicated instrumentation to cancel out magnetic fields. To test our theories in a controlled environment we have used shields which can attenuate DC fields below nT and have a sensitivity of few $fT/\sqrt{Hz}$. Unfortunately this is not the end of the story. Our cells are quite long, with a radius of a few cm up to a length of 14 cm for the cylindrical cells. Since we zero the field at a small area in the centre of the cell (and the shield), this means that the atoms experience different magnetic fields along the cell. In a paraffin-coated cell the atoms average the magnetic field to a large extent, but in cells with buffer gas the atoms diffuse slowly and the differences are much bigger. This magnetic-field gradient along the cell is broadening our linewidths and reduces our sensitivity.

3.2 Polarization moments

It has become quite obvious so far that the polarization of an atom and its symmetry plays a crucial role in atomic magnetometry and it can be useful to classify the symmetries that appear in a given atomic state. To do that, we decompose the density matrix into components that have the symmetries of the spherical harmonics, because these symmetries help us describe the polarization in a visual language. We therefore expand the density matrix over a set of irreducible tensor operators T_q^κ, with the rotational symmetries of the spherical harmonics. We call them polarization operators. The density matrix ρ can now be written as:

$$\rho = \sum_{\kappa=0}^{2F} \sum_{q=-\kappa}^{\kappa} \rho^{\kappa q} T_q^\kappa \, . \tag{3.8}$$

The *polarization moments (PM)* $\rho^{\kappa q}$ are characterizing the anisotropy of a state with total angular momentum F. These are the coefficients in the expansion of the density matrix into the irreducible tensor operators of rank $\kappa = 0$,...,2F and projection $q = \kappa$,...κ [53]. The covariant coefficients ρ_q^κ for a state with total angular momentum F in the $|m\rangle$, $\langle m'|$ basis are given by:

$$\rho_q^\kappa = \sum_{m,m'=-F}^{F} (-1)^{F-m'} \langle F, m, F, -m' | \kappa q \rangle \rho_{m'm} \, , \tag{3.9}$$

where $\langle ...|...\rangle$ indicate the Clebsch-Gordan coefficients [54].

The names we give to the polarization moments depending on their κ–rank sound familiar to a conversant in physics: they are borrowed from the multipole moment expansion of a static electric field. As such, ρ^0 is monopole moment or population, ρ^1 is dipole moment or **orientation**, ρ^2 is quadrupole moment or **alignment** etc.

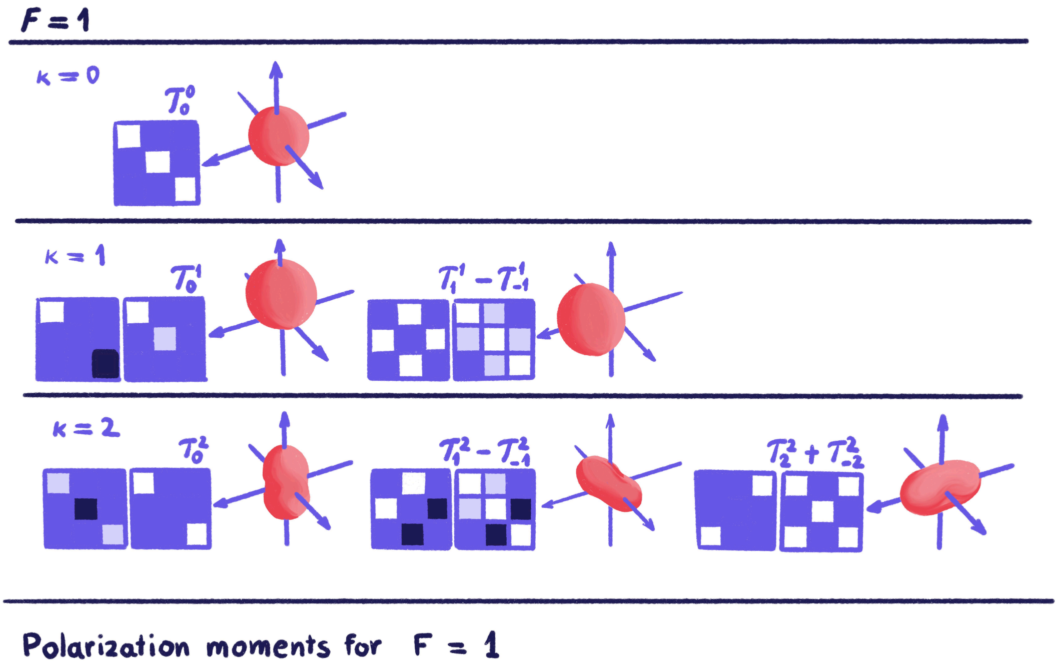

FIGURE 3.10: Polarization moments for a total angular momentum of $F = 1$. For spin $\vec{s} = 1$ we have three (3) projections 0, 1, and -1 which results in a 3x3 density matrix. On the bottom left are the nonphysical and on their right side are the physical density matrices representing the PM's [30]. Mathematically both are correct, however physically a diagonal with negative numbers or all zero (0) has no meaning, since the diagonal elements represent the probabilities of finding the the populations in a state. This is why we transform the density matrix to one where the diagonal makes physically sense and this new density matrix might also consist of linear combinations of T_q^κ. For each polarization moment the angular-momentum probability surface that corresponds to a physical density matrix is illustrated. The values indicated by color are: the middle value of purple is zero, dark purple are negative values and white and lighter purple correspond to positive values. In the case of $\kappa = 2$, for example, we see that κ defines the type of polarization (alignment) and q describes the axis of polarization. For $\kappa = 2$ we have three (3) possible axes for $q > 0$.

Let us give some examples to understand the properties of the PM. For $\kappa > 0$ we describe an ensemble that has any moment. The polarization moments ρ_0^κ (with $q = 0$) represent a polarization along the quantization axis{I} which corresponds only to populations and, accordingly, ρ_q^κ with q$\neq$ 0 describes transverse polarization to the quantization axis and coherences between the sublevels. An example of the polarization moments that could exist in the F=1 state is illustrated in Figure 3.10.

{I} In quantum mechanics we cannot know all the information of an operator. The maximum amount of information we could have is a projection on an axis. For the electron's angular momentum this projection is called the quantization axis and equals to $l_z = m\hbar$. We often use the magnetic field direction as reference so the m is called the magnetic quantum number. We choose the quantization axis according to what is convenient for our experiment.

For a specific κ we get -κ...κ components that oscillate with q times the Larmor frequency Ω_L. The measured signals are proportional to the real-valued sum and difference of these components.

Important note: We use a very similar notation– $\rho^{(n)}$ –to distinguish between linear and nonlinear effects in a medium (in Section 2.2.2). In this Section we use $\rho^{\kappa q}$ to classify the polarization moments that can be created in an atom and their symmetries. These two things are not the same.

3.3 Important types of atomic magnetometers

3.3.1 Mx and Mz magnetometers

The M_x and M_z magnetometers are based on magnetic-resonance phenomena. Typically, we have our atoms placed inside a bias (static) magnetic field $\mathbf{B_0}$. The atomic transitions are excited by a resonant oscillating (**RF**–radio frequency) magnetic field $\mathbf{B_1}$ with frequency ω. Optical pumping occurs with a resonant circularly-polarized light beam that creates magnetization of the ensemble of atoms. Macroscopically, the pumping of the medium creates atomic magnetization $\mathbf{M}$ which evolves around $\mathbf{B_0}$ due to **Larmor precession**.

To visualize the movement of $\mathbf{M}$, we can use the **Bloch sphere**– see Section 2.8 –to visualize the time evolution of the atomic magnetization including relaxation parameters.

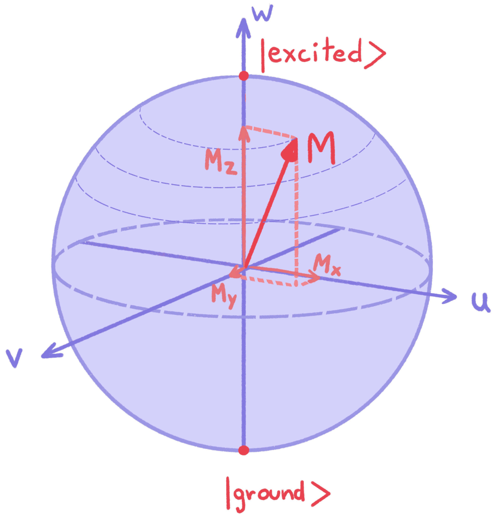

FIGURE 3.11: The Block sphere visualizes the possible solutions of the Bloch equations. The thin purple dashed line shows a possible path of the magnetization M.

Let us assume that for $t = 0$ the initial magnetization is M_0 and is along w. Both magnetic fields act on it and now magnetization M starts precessing around the effective field in a similar manner as explained in Section 2.3.1, where we talked about how an oscillating magnetic field makes our spin system evolve in time under Rabi frequency (or Larmor frequency in the resonant case, where ω is close to the resonant frequency ω_0).

Relaxation has to be considered as well: when the system returns to equilibrium, the longitudinal and transverse magnetization relax differently. There are two important time constants to consider here: $\mathbf{t_1}$ and $\mathbf{t_2}$. The longitudinal component returns to M_0 value (the value at t=0) with t_1 time and the transverse component becomes zero (there is no transverse component initially) with t_2. Generally, M_z and M_x magnetometers are distinguished by the method we use to detect/probe the signal [19]:

For M_z: we detect a component proportional to the longitudinal component of the magnetic moment and so t_1 time plays a role. In particular, t_1 limits the temporal response of the magnetometer to changes in the magnetic field.

For M_x: we detect the phase of the transverse component of the magnetic moment and the t_1 and t_2 times are not limiting how fast the magnetometer responds to changes in the magnetic field. T2 limits does limit however the sensitivity of the magnetometer.

Mz magnetometer

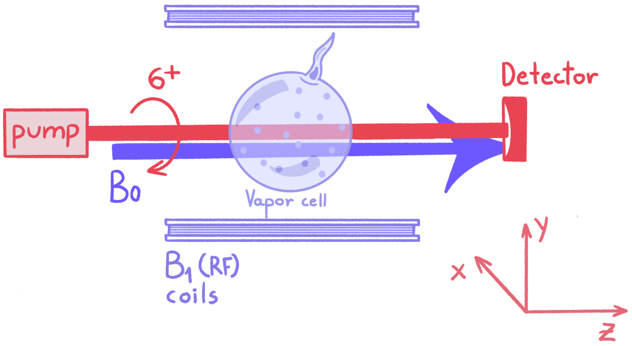

FIGURE 3.12: M_z magnetometer illustration.

In this magnetometer, we employ circularly polarized light in order to optically pump the atoms and create spin polarization in the ensemble and as a result magnetization. The bias magnetic field B_0 is along the pump direction, let's say z. Let's now apply an oscillating (RF) magnetic field B_1 transverse to B_0 with frequency close to the magnetic-resonance frequency ω_0. This frequency is related to the energy difference of the magnetic sublevels due to $\mathbf{B_0}$, in other words it is resonant to their Zeeman splitting. In classical-physics terms, when applying the RF field the magnetization vector gets tilted and now we do not only have longitudinal magnetization which is smaller than before, but also a transverse magnetization that is rotating. Longitudinal magnetization is related to a population difference created by the pump light along z and since now the projection of the magnetization vector along z is smaller than the original magnetization, this means that the $\mathbf{B_1}$ field reduced the created population difference. By modulating the frequency of the $\mathbf{B_1}$ field we can detect changes in the absorption of the pump light depending on how much population is left to be absorbed [19]. In other words, there is a periodic change of population on the magnetic sublevels along z due to the RF field that affects the absorption of the pump light which we detect.

Mx magnetometer

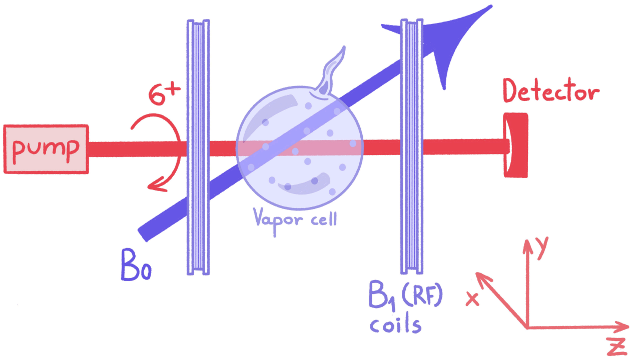

FIGURE 3.13: M_x magnetometer illustration.

In this magnetometer we use, as in the M_z case, circularly polarized light to pump. The bias field $\mathbf{B_0}$ is in this case oriented at 45° with respect to the pump light [55]. Equivalently, one can use two beams, a pump beam along $\mathbf{B_0}$ and a probe beam perpendicular to it. Here again, we have a change of coordinate system and the concept of coherences (see 1.4.4) apply: while the rate of change of the populations is limited by t_1 and t_2 times, the oscillation frequency of the coherences reacts almost immediately to the changes induced by the field and hence M_x magnetometers are faster than other types. [19]. Because M_x magnetometers respond fast to magnetic-field changes, they are usually used when one needs a movable device that responds fast, is sensitive and robust. They can also be good vector magnetometers, meaning they can measure the magnetic-field vector component. For some applications, M_z magnetometers are preferred, especially when one needs high accuracy.

3.3.2 Bell-Bloom magnetometer

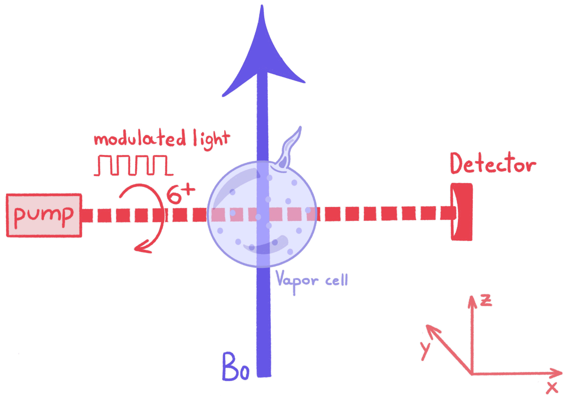

FIGURE 3.14: Bell-Bloom magnetometer illustration.

In the example we gave about the basics of the operation of a optical magnetometer in Section 3.1.3, we pumped under zero magnetic field and we probed under a bias magnetic field $\mathbf{B_0}$. In order to simplify the process or to be able to employ a magnetometer in the earth's-field– without a shield –it would be useful to be able to enable pumping and probing at the same time. This is possible in the Bell-Bloom magnetometric scheme.

In this type of magnetometer, the setup is the same as in Section 3.1.3 except for the fact that the bias field $\mathbf{B_0}$ stays on for the whole process and the intensity of the pump-light is modulated at a frequency Ω_m. **Modulation** of light, (or a laser beam in our case) is a process by which the output of the light, may it be phase, intensity, frequency, or polarization, is changing in time. In our experiments we use external modulation, which means that we take the laser-light output and we pass the light through a modulator, for example an Acousto-Optic Modulator or **AOM**, that outputs light with our desired modulation (see also 3.5).

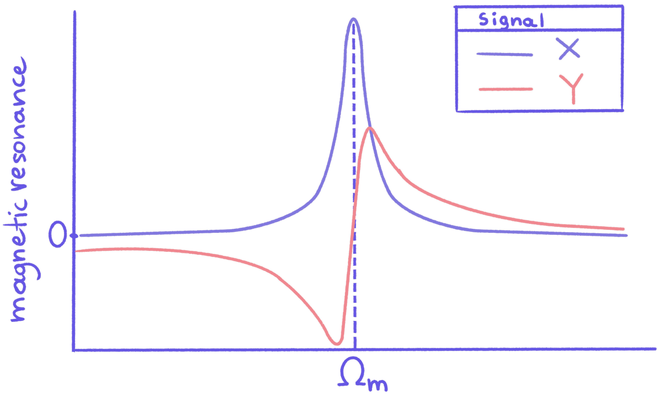

FIGURE 3.15: Magnetic Resonance. The X signal is the amplitude of the signal in-phase with Ω_L and Y is the signal amplitude out-of-phase with Ω_L.

If $\Omega_m = \Omega_L$ then pumping occurs at the same time as Larmor precession. The pump light acts here as a driving force in a driven harmonic oscillator at time $t - 2pi/\Omega_L$, $t - 4pi/\Omega_L$, ... [19]. We can look at it also from a different perspective: Since the intensity goes from 0 (zero) to maximum, we can say that only at the maximum intensity the spins are pumped along x and the spin-state is stationary in the rotating frame that rotates with frequency Ω_L. In order to keep Ω_m in resonance, we use often a voltage-controlled oscillator or function generator– a device that produces a waveform. Often, the **self-oscillating** mode is used, where the spin-precession signal is producing the frequency for the pump modulation.

What we detect is a characteristic resonance when we scan either the modulation frequency Ω_m or the magnetic field strength– see Figure 3.15. In the "stroboscopic" picture, if the spin-state that is stationary in the rotating frame is a dark state, the light does not interact with it and hence we see a peak in light transmission. If it is a bright state, we see a peak in absorption. Based on these measurements we can determine the magnitude of the field $\mathbf{B_0}$.

3.3.3 Nonlinear magneto-optical rotation (NMOR)

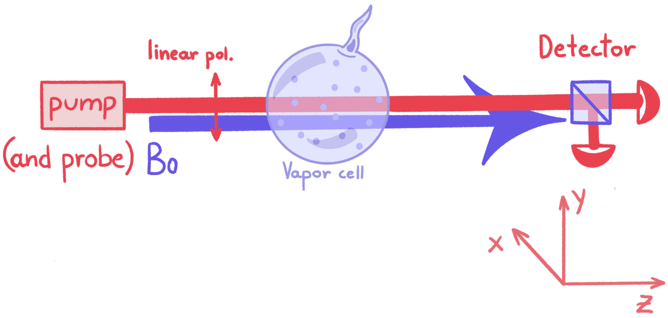

FIGURE 3.16: NMOR-based magnetometer illustration.

Nonlinear magneto-optical rotation or nonlinear Faraday rotation was first discovered in 1974 [56] and has since been extensively studied. Nonlinear magneto-optical rotation happens when linearly polarized light propagates through a medium placed inside a magnetic field $\mathbf{B_0}$ and its polarization plane rotates, with the rotation being dependent on the light-intensity. This effect produces a non-linear rotation that is– for small magnetic fields– about 10^4 times larger than the rotation produced by linear effects in a buffer-gas vapor cell [30]. As we will discover later, we can produce even bigger rotations by using paraffin-coated cells, making our magnetometers super **sensitive**, that is, able to detect extremely small changes in magnetic fields.

Three-level Λ-type system

Sometimes the two-level system is not sufficient to describe a system, for example in the case where we have linearly polarized light. We are specifically interested in the Three-level Λ-type system which will be briefly discussed in Section 2.4.2 and Figure 2.9 in order to be able to discuss about NMOR.

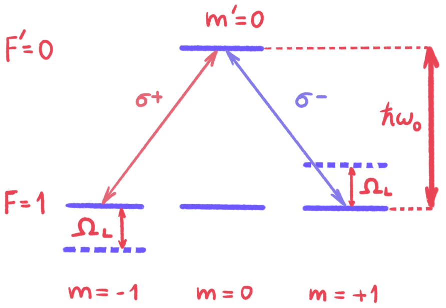

FIGURE 3.17: Three-level Λ-type system. Linearly polarized light couples the ground states to the excited state.

An approximation of such a system is the $F = 1 \rightarrow F' = 0$ with the ground sublevels $m = 1$ and $m = -1$ coupling to the excited state $m' = 0$ through the σ_+ and σ_- components of the linearly polarized light, as was the case in Figure 2.2 of the Macaluso-Corbino effect [38] reproduced in Figure 3.17. This system cannot be viewed as two independent two-level systems and coherences of the ground levels need to be taken into account.

Since we have a magnetic field along the light, the field $\mathbf{B_0}$ splits the Zeeman sublevels and now the coherences on the ground sublevels depend on $\mathbf{B_0}$.

Ground-state-coherence effects

An important feature, in NMOR experiments, are the narrow lines observed in paraffin-coated cells which are related to the lifetime of the ground-state atomic polarization– since our linearly polarized light creates coherences between those states**{I}**. Longer ground-state polarization times lead to higher sensitivity.

In Section 2.2.2, we talked about the pertubative expansion of the density matrix in orders $\rho^{(n)}$ and their use in classifying linear and nonlinear effects. Odd orders of $\rho^{(n)}$ ($\rho^{(1)}$, $\rho^{(3)}$,... etc) describe optical coherences, while even orders of $\rho^{(n)}$ ($\rho^{(2)}$, $\rho^{(4)}$,... etc) describe density-matrix elements between states with the same parity**{II}**. For transition between F levels, these density-matrix elements are level populations and Zeeman coherences.

In the case of NMOR, we could use two beams instead of one**{III}**: the first to pump and the second to probe. It helps also to look at the process of NMOR as a three-step process: In the first step, the linearly-polarized light creates ground-state polarization through pumping within the ground Zeeman sublevels, which is a $\rho^{(2)}$ order effect. This creates an aligned state– along the light-polarization axis– which is dark for one polarization of the pump– let's assume for y-polarized light– and it is bright for the other, in this case, x-polarization**{IV}**. Now linear dichroism was created, meaning that the absorption of the light that consists of orthogonal linear polarizations depends on these polarizations: the atomic medium absorbs one polarization and transmits the other.

Now comes the second step of the NMOR process. Alignment has been created along the light-polarization axis that rotates in the bias magnetic field $\mathbf{B_0}$ rotating also the axis of dichroism. This can be visualized with the peanut shape as seen in Figure 3.10.

For the final stage, the probe beam produces optical coherences and these are influenced by the ground-state polarization at first order $\rho^{(1)}$. This means that the probe beam interacts with the

---

{I} The effects in which the nonlinear rotation depends on the relaxation rate of the excited state are called Bennett-structure effects. In this case the light interacts only with a specific velocity subgroup and in the velocity distribution "peaks" and "holes" appear due to optical pumping

{II} As we found out in Section 2.4.1 these are magnetic-dipole transitions. In contrast, optical coherences are coherences between states of the opposite parity

{III} One-beam experiments work similarly

{IV} It is not always the case that the states are dark for one of the pump polarizations. For example, when we pump with $F \rightarrow F + 1$, the pumping happens in a bright state, but it is brighter for one polarization than the other dichroic medium in a linear way[I]. In this case we can also use, instead of a second probe beam, just the pump beam in a one-beam configuration.

Let us describe mathematically the rotation of the polarization by using the Λ system (see Section 3.3.3) to illustrate this process. If we use y-polarized light to polarize the atoms, they get polarized into the state:

$$|y\rangle = (|{+1}\rangle - |{-1}\rangle)\,. \tag{3.10}$$

By solving the time-dependent Schrödinger equation we find that the state $|y\rangle$ evolves in time inside a magnetic field as:

$$|\phi(t)\rangle = -\frac{i}{\sqrt{2}}(|{+1}\rangle\, e^{i\Omega_L t} - |{-1}\rangle)e^{-i\Omega_L t}\,, \tag{3.11}$$

where Ω_L is, as usual, the Larmor frequency and the initial state $|y\rangle$ rotates with Ω_L. The system $\phi(t)$ reproduces itself every half of the Larmor period, so $|\phi(\varphi + \pi/\Omega_L)\rangle = |\phi(\varphi)\rangle$, where φ is the relative phase. The axis of the alignment also rotates. When the polarization of the probe light and the atomic-alignment axis are parallel, or at 90° we have no rotation. At any other angle there is rotation. As a result, the probe light gets modulated at $2\Omega_L$ [38]. We will talk in more detail about this in Section 3.3.4 and in Chapter 5.

In reality, the above three processes, which can be thought of as a model of a rotating polarizer, happen all at the same time and the NMOR corresponds to a $\rho^{(3)}$- or $\chi^{(3)}$-order effect. The CW (continuous-wave) pump continuously creates polarization and the relaxation processes destroy it at $1/\gamma$ time, where γ is the **transit rate**. This is the rate at which atoms interact with the light beam and is a source of ground-state relaxation. The lineshape produced in this process– if we calculate the expectation value of the optical polarization and make assumptions about the relaxation rates γ and Γ– is a dispersive Lorentzian antisymmetric around zero field, as we saw in previous Sections [30].

High light power

The above model is working for low light power, but for higher-enough power we need to take **AC-Stark shifts** into account. AC-Stark shifts are energy shifts of atomic energy levels due to an oscillating light field. AC-Stark shifts together with a magnetic field can lead to optical-alignment that oscillates and gets converted to orientation, perpendicular to both the alignment and electric-field axis, in a process called **alignment-to-orientation conversion (AOC)** [57]. This effect needs to be taken into account, since it can also create optical rotation due to the orientation creating circular birefringence in the material. For an AC-Stark shift to produce AOC, it has to have a non-zero detuning between the optical frequency and the resonance [30] and so in a Doppler-free[II]

[I] This is true if the probe is not strong enough as we will see in the next Section

[II] Doppler broadening happens in all experiments, since atoms have a velocity along the light-propagation direction that makes them “experience” different frequencies. We can create a setup in which Doppler broadening does not play a role, if we manage to only “talk” to a group of atoms with a specific atomic velocity and we call it Doppler-free experiment where the light is on resonance AOC is not relevant. Another effect related to the high power of the light is **power broadening**, which is the effect of the magnetic resonance broadening due to effective relaxation induced by pumping. This happens when the pumping rate Γ_p (Ω_R^2/Γ) is bigger than the transit rate γ, or else, if $\Gamma_p/\gamma = \kappa_2 \geq 1$. In NMOR y-polarized light polarizes the atoms along y which is now a dark state. Under a magnetic field, the aligned atoms rotate and fast pumping would align atoms into y before a full rotation could happen, while an even faster pump could completely destroy NMOR.

3.3.4 NMOR with modulated light

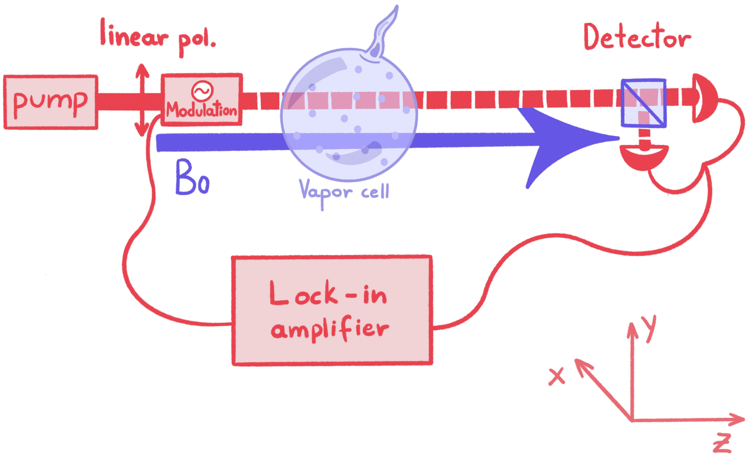

FIGURE 3.18: Setup of NMOR with modulated light. The linearly-polarized pump light gets modulated through a function generator. The modulated, detected, signal gets demodulated through a lock-in amplifier.

NMOR in antirelaxation-paraffin-coated cells offered unprecedentedly narrow resonances, related to ground-state atomic polarization that lives long, hence the name “antirelaxation”. As we will see later, this fact plays an important role in how sensitive our magnetometers can be. The width of this resonance is, in polarization-dependent effects such as NMOR, depending on the relaxation rate of the atomic polarization. This practically means that these magnetometers can be sensitive, but only in a small range of magnetic fields.

An experimental arrangement that can utilize the sensitive NMOR measurements with the efficient Bell-Bloom pumping scheme, is a type of NMOR magnetometry that uses modulated light in order to pump. One can modulate either the frequency (FM NMOR) [58] or the amplitude (AM NMOR) [59] of the light. This simple modification of modulating our pump and detecting at this frequency can allow us to get a magnetic resonance not only around zero field, but also at other values of magnetic field, allowing us, by definition, to extend the **dynamic range** of our magnetometers. We will talk here more about AM since this method is more often employed throughout the experiments of my thesis.

Amplitude modulation

Let us think of a linearly polarized pump beam that gets modulated at a frequency Ω_m. This modulation leads to higher harmonics of Ω_m appearing in the spectrum of the light with which the atoms can interact. What the response of the polarized atoms in a magnetic field looks like, is a short-lived signal that depends on time. The signal looks like a decaying oscillation: when we pump once we have the maximum optical rotation and then we see the signal relaxing towards zero.

What happens if we use more than one pulse to pump and polarize our atoms? If we pump with pulses that repeat themselves at a random rate, these will create phase differences between the precession of atoms pumped at different times this way destroying atomic polarization. There is a way, however to enhance our pumping process through modulation, if we pump every time a precession is full, in other words, when atomic polarization returns to its original state. Remember here, that linearly polarized light creates alignment, a polarization moment of rank $\kappa = 2$, symmetrical along an axis, as shown in Figure 3.19.

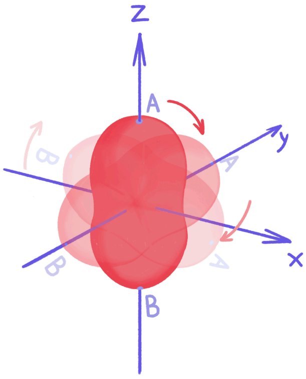

FIGURE 3.19: Angular-momentum polarization surface or alignment, produced by linearly polarized light and its rotation along the z axis.

When point A rotates from the positive axis z and reaches point B on the negative axis z, the surface has regained its symmetry. However a full rotation happens when point A reaches again the positive axis. This means that for the polarization to return to its original state, half a Larmor period is needed (or two times the Larmor frequency). For this reason, we synchronize the modulation of the pump with two times the Larmor frequency and we get a resonance in the oscillating signal (See also Figure 3.20.)

The length of the pulse of the modulation is defined by a quantity called **duty cycle** defined as:

$$D = \frac{W}{T} 100\% , \tag{3.12}$$

where D is the duty cycle, W the pulse width and T the period of the signal. For a Doppler-broadened transition, we achieve the best pumping with relatively short pulses of about 20% duty cycle [19].

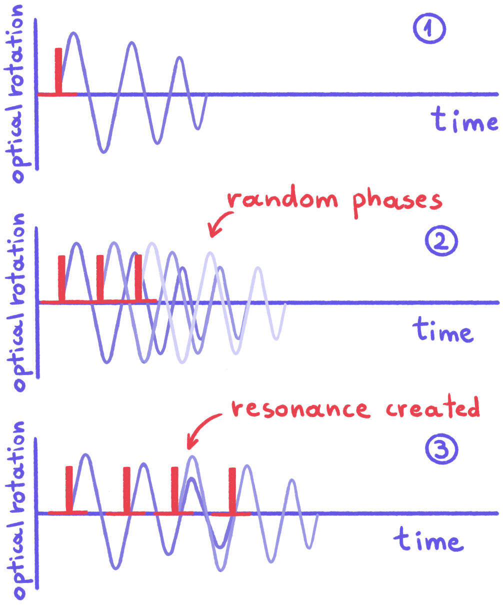

Figure 3.20: Optical-rotation signal in AM NMOR. In 3. the modulation is already at twice the Larmor frequency so the pulses are at the modulation frequency.

For probing we use CW light– which is the same as saying 100% duty cycle. This is one of the reasons that a two-beam setup is better for optimization, we can separately optimize the pump and probe beams: their duty cycle, their frequency and their power.

3.3.5 Spin-exchange-relaxation-free (SERF) magnetometer

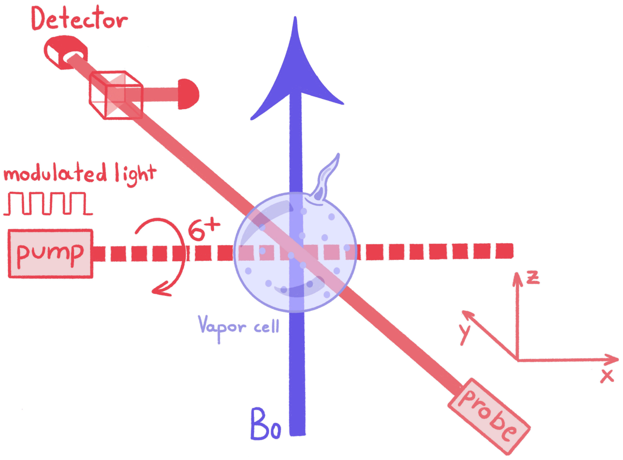

Figure 3.21: SERF-magnetometer illustration. In the SERF regime the atomic spins are rapidly kicked between the two ground-state hyperfine levels and this averages the oppositely signed precession.

For this overview to be complete, the spin-exchange-relaxation-free (SERF) magnetometer could not be missing. Since it is out of the scope of this thesis I will only briefly introduce its characteristics. As the name already hints, this is a magnetometer that is free of spin-exchange collisions. In Section 3.1.6 we outlined how spin-exchange collisions redistribute atoms among the Zeeman sublevels of the ground hyperfine states and this makes them precess in opposite directions [60]. These collisions contribute a lot to the t_2 relaxation thereby limiting our sensitivity. However, in 1973, Happer and Tang discovered very narrow (about 200 Hz) magnetic resonances in alkali vapors at high-densities and inside magnetic fields close to zero [61]. This is what we know today as the **SERF regime**: In Liouville's equation plus the relaxation terms (see Equation 1.4.2), when the term for spin-exchange is much smaller than the hyperfine term, *but* larger than any other term, spin-exchange does not contribute to spin relaxation. This means that when spin-exchange collisions happen faster than the precession frequency, which is the case in high density and small magnetic fields, the atoms sample all the Zeeman sublevels in both ground-state hyperfine levels fast enough for the collective, average spin to experience an effective precession frequency. The spin-exchange broadening factor depends on the how small the magnetic field is and how dense the atomic ensemble, this is why the SERF regime is around zero field and heating of the cell is needed.

Figure 3.21 illustrates a classic SERF-magnetometer setup. The circularly polarized pump creates orientation along its propagation direction. The magnetic field (perpendicular to both beams) rotates the spins and we detect a rotation of the linearly polarized probe beam along the third axis. The atomic densities required for SERF demand a cell temperature of the order of 200^oC.

In order to prevent atoms from colliding with the glass walls of the cell and to prevent spontaneous emission– both mechanisms would destroy polarization– a buffer gas is added, usually a noble gas like He and a diatomic molecule like N_2.

3.4 NLZ in Earth-Field magnetometry

3.4.1 Nonlinear Zeeman effect

Most of our experiments have been done with a vapor cell in a magnetic field that is of the order of the Earth field and so it is important to understand how a field of this order of magnitude can affect the states of our atoms differently than what we saw in Section **??**. So far we saw the effects of small magnetic fields, where the energy levels are changing in a linear way in the applied field. Now we are going to take a look at how a sufficiently large magnetic field can affect the level splitting in a *nonlinear way*.

The ground-state Hamiltonian for an atom in a magnetic field **B** for states with electronic angular momentum $J = 1/2$[I], is:

$$\hat{H} = A_J \mathbf{I} \cdot \mathbf{J} + g_s \mu_B \mathbf{S} \cdot \mathbf{B} - g_I \mu_N \mathbf{I} \cdot \mathbf{B}\,, \tag{3.13}$$

where A_J is the hyperfine coupling constant, **I** is the nuclear spin, g_s and g_I are the electron-spin and nuclear Landé factors of the atom, μ_B is the Bohr magneton, and μ_N is the nuclear magneton. The

---

[I] The multipole series that describes the hyperfine interaction consists of multiple terms from which the most important are A_J and B_J. A_J characterizes the strength of the magnetic-dipole interaction and B_J the strength of the electric-quadrupole interaction. However B_J is zero when I and J are both larger than $1/2$, such as in the case presented here.

first term describes the hyperfine interaction and the second and third terms the interactions with the magnetic field– i.e., Zeeman interactions.

In a atom that has one valence electron in an $S(J = 1/2)$ level, the analytical solution for the eigenvalues of the Hamiltonian is given by the Breit-Rabi formula 3.14. This gives us the energy shifts E_m of the magnetic sublevels $|m\rangle$ for a state with a total angular momentum F in a magnetic field of strength B [30, 62]:

$$E_m = \frac{\Delta_{hf}}{2(2I+1)} - g_I \mu_B m B \pm \frac{\Delta_{hf}}{2}\left(1 + \frac{4m\xi}{2I+1} + \xi^2\right)^{1/2}, \tag{3.14}$$

where $\xi = (g_J + g_I)\mu_B B/\Delta_{hf}$, Δ_{hf} is the hyperfine-structure interval and the ± sign refers to the $F = I \pm 1/2$ hyperfine levels, $g_J \approx 2$, while we neglect the Zeeman energy of the nuclear spin (last term in Eq. (3.13)= since $\mu_N \ll \mu_B$). The first two terms are linear to $\mathbf{B}$ and the third is nonlinear. The nonlinear term can be neglected if we operate the magnetometer in low-field, but it becomes important on the order of the Earth's magnetic field. If we plot these energies as a function of applied field, we get what we call **Breit-Rabi diagrams**, as illustrated in Figure 3.22. We chose cesium (Cs) as an example, since it will be relevant to our first experiment presented in the next Chapter.

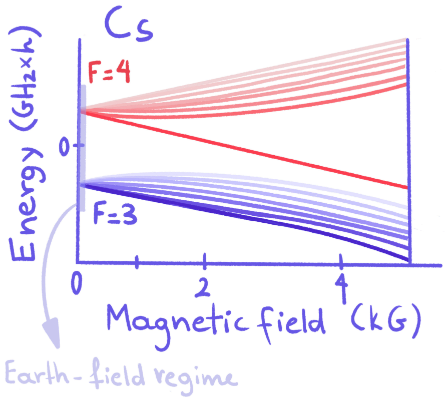

FIGURE 3.22: Breit-Rabi diagram of Cs. At the bottom of the illustration one can see that on Earth field, although 0.5 G is small in magntiude, the energy levels in this regime are behaving nonlinearly as a function of magnetic field.

If we expand the eigenenergies as a series in B around zero, the transition frequencies corresponding to $\Delta m = 1$ for the Cs $6^2\mathrm{S}_{1/2}\, F = 4$ system are

$$E_{m+1} - E_m \approx \frac{\mu_B B}{4} + \frac{(\mu_B B)^2}{16\Delta_{hf}}(2m-1)\,. \tag{3.15}$$

The quantity $\omega_{rev} = (\mu_B B)^2/(16\hbar\Delta_{hf})$ is the previously mentioned quantum-beat revival frequency. If we are on Earth field (50 µT or 0.5 G), the revival frequency after calculations is $\omega_{rev} = 2\pi{\cdot}3.3\,\mathrm{Hz} \propto 20\,\mathrm{Hz}$ [30]. Remember, from Section 1.4.4, that "quantum beats" is the general term used to describe the time evolution of a coherent superposition of non-degenerate energy eigenstates at a frequency determined by their energy splittings [35], for example, the splittings happening in the NLZ effect. It is exactly this frequency that we have calculated here and that is comparable to the magnetic resonance linewidth which makes the system strongly affected by the nonlinear Zeeman effect. The Cs magnetic resonance is split into eight peaks and as a result it is broadening the linewidth and the magnetometer sensitivity.

3.4.2 Heading error

A noise source that plays a role in scalar magnetometers, such as the ones studies in this thesis, is the so-called **heading error**. This describes the error of a measurement due to its dependence on the orientation of the sensor. There are a few applications, usually involving airborne or marine system, where the sensor is not at a constant angle and, as a result, heading error can affect the measurement. Sources of heading error involve magnetic materials inside the sensor, ferromagnetic electronics, but also reasons related to the physics of the sensor, such as different gyromagnetic ratios of hyperfine states and the nonlinear Zeeman effect. In Chapter 5, we will address heading errors pertaining to the second category.

3.5 Experimental devices

For the biggest part of my PhD journey, I worked hands-on in the lab with various optical and electronic devices. Since these are a predominant part of an experimentalist's life, I would like to briefly explain how some of them work.

3.5.1 Beam modulation

Modulation our light beam is vital for many of our experimental setups, as was demonstrated in Chapter 3. In our experiments we use EOM and AOM to externally modulate our beams.

Electro Optic Modulator – EOM

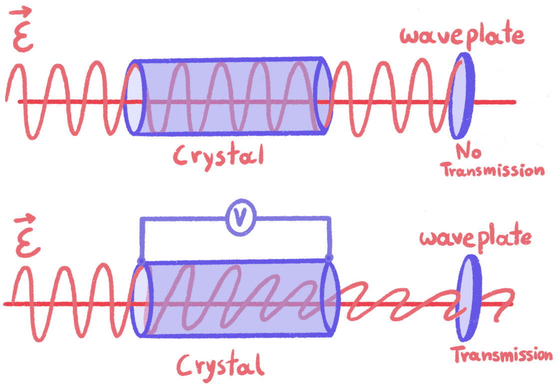

FIGURE 3.23: Simple example of an EOM's function, with voltage on and off.

An electro-optic modulator (EOM) works as an electrically-actuated polarising beamsplitter and waveplate, meaning it changes the birefringence of a nonlinear crystal through applying a Voltage and distorting the electrons in its internal structure. It can reach modulation speeds up to about 20MHz[I] and requires high driving voltages and special amplifiers to reach the hundreds of Volts needed for affecting the crystal.

As an example, when one does not apply a Voltage, the light passes through the crystal and then a polarizer at the output can allow full or zero transmission depending on how we aligned the polarizer.

If you apply voltage across the crystal, along one direction of it, it creates birefringence along this axis and it creates a phase difference between the two polarizations of an incoming linearly polarized light. Typically, an EOM relies on a linear electro-optic effect, which is known as the Pockels effect. This effect explains the change of the refractive index of a nonlinear (non-centrosymmetric) crystal by an electric field that is proportional to the strength of the field.

One can now control through the applied voltage the rotation of the polarization and the amount of the transmitted light and, as a result, control the power, phase or polarization of a beam. If one applies a varying voltage, the EOM frequency-shifts the light and so a very common use of EOMs is to generate sidebands on the central frequency of the light.

Acousto Optic Modulator – AOM

An acousto-optic modulator (AOM) diffracts the light beam that passes through it into several orders. It utilizes the acoustic waves causing an acousto-optic effect in which a material's permittivity changes due to mechanical strain, in this case using sound waves.

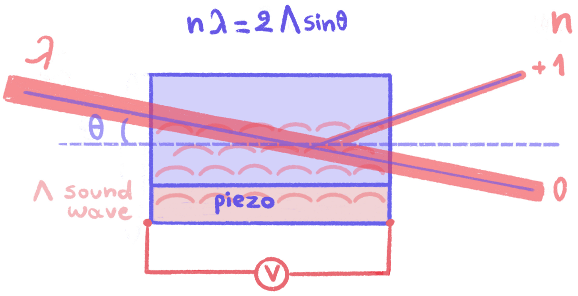

FIGURE 3.24: Simple example of an AOM's function.

As in the EOM, the key element in this case is a crystal through which light passes. On the crystal, there is a piezoelectric transducer attached which is connected to a source that provides to it an oscillating electrical signal. The piezo creates a sound wave that produces an oscillating mechanical strain through the material. The mechanical stress creates a medium density which is also periodic, with regions of high and low density and so it induces a periodic change of the refractive index in the crystal. The periodic refractive index in the crystal behaves like a grating creating constructive or destructive interferences. Light passing through the AOM scatters off the created periodic grating

---

[I] We use less than 1MHz modulation in our experiments and experiences something like Bragg diffraction, as seen in Figure 3.24, operating under the Bragg condition $n\lambda = 2\Lambda sin\theta$, where n = order of diffraction, λ = wavelangth of light, Λ = wavelength of the acoustic wave and θ = angle of incidence.

When considering cost, the AOM is generally a more affordable option than the EOM and is usually used for intensity modulation. In our case we were sometimes limited by the power output of the AOM and used an EOM instead. On the other hand the AOM's electronics are cheaper and it allows high enough modulation, so that we used AOMs more often in our setups than EOMs. AOMs also frequency shift the output beams, but these frequency shifts are generally smaller than for the case of the EOMs.

3.5.2 Lock-in amplifier – LIA

For atomic-magnetometer experiments we need to be able to measure the Larmor frequency of our system. However, this is not the only frequency present in our signal: in a lab we have a broad range of white noise consisting of lower and higher frequencies than the one we want to detect. In order to extract our signal from the noise, we use a device called the lock-in amplifier (LIA). A simple explanation follows of how a LIA works in the time domain.

A LIA requires a frequency reference to detect the response of the experiment at this frequency. The LIA amplifies the signal and multiplies it by the reference signal. After using a low pass filter and in the case where the reference frequency equals to the signal frequency, the single-phase LIA output is a signal proportional to the signal amplitude V_0 and the phase φ of the reference:

$$Signal \propto V_0 sin(\omega t)\,, \tag{3.16}$$

$$Reference \propto V_0 sin(\omega t + \varphi)\,, \tag{3.17}$$

$$LIA_{output} = \frac{1}{2} V_0 cos(\varphi)\,. \tag{3.18}$$

From the above equations, we can easily see that, since the cosine component can be either negative or positive, the output can also be either negative or positive. For $\varphi = 0$, the $LIA_{output} = \frac{1}{2}V_0$ and usually the calibrated output is $LIA_{output} = \frac{1}{\sqrt{2}}V_0$. The peak-to-peak amplitude is $V_{pp} = 2V_0$, so the final LIA output is:

$$LIA_{output} = \frac{V_{pp}}{2\sqrt{2}}\,. \tag{3.19}$$

The lock-in amplifiers that I refer to in this thesis are dual-phase LIA, which means that we get two outputs X and Y with the reference oscillator shifted by 90°. By calculating the magnitude R of the vector (X,Y) one gets rid of the phase dependence as follows:

$$X = \frac{1}{\sqrt{2}} V_0 cos(\varphi)\,, \tag{3.20}$$

$$Y = \frac{1}{\sqrt{2}} V_0 sin(\varphi)\,, \tag{3.21}$$

$$R = (X^2 + Y^2)^{\frac{1}{2}} = V_0\,. \tag{3.22}$$

We can see that the R, contrary to the output of the LIA, is always positive and does not depend on the phase between the signal and lock-in reference.

3.5.3 Laser

The word laser has become part of everyday language over the past few decades. It is however an acronym which stands for Light Amplification by Stimulated Emission of Radiation. The light emitted from a laser is monochromatic{I}, collimated{II} and coherent{III}.

In order to create a laser usually three processes are needed:

1. Inversion of population: More atoms or molecules exist in a high-energy level than in lower-energy levels, as is usually the case in nature. Inversion happens by transferring energy from external sources to the system (pumping).

2. Optical amplification based on stimulated emission: This process creates photons of the same frequency and phase. When an atom is in an excited state, it can be stimulated by a passing photon with a frequency $\nu_{\Delta E}$ that corresponds to the energy gap ΔE of the transition from the excited state to the ground state. The excited atom returns to the ground state and emits a second photon with the same frequency ν resulting in two photons with the same frequency. This process creates photons of the same frequency and phase.

3. An optical resonator{IV}: two mirrors are positioned on the two ends of a cavity, so that the photons created by the stimulated emission are reflected between the mirrors repeatedly, while a small part of the laser light gets emitted from one side.

Diode Lasers

Although the work of this thesis belongs to the field of atomic physics, we have solid-state physics to thank for a fundamental part of our setups: diode lasers are affordable, robust and compact.

In order to start talking about semi-conductors and diodes we need to start by describing the probability of electrons occupying different energy levels. In solid-state physics a band structure is often

---

{I} Light of a narrow wavelength, close to a single wavelength

{II} The light's waves are parallel to each other, and hence the beam is not diverging or converging for a long distance

{III} The light's waves are in phase with each other in time and space

{IV} Or is it? See Chapter 6 and 7

used to describe the range of electron energy levels within the bands, and the probability of electrons filling the bands is determined by the Fermi-Dirac distribution:

$$f(E) = \frac{1}{1 + e^{(E-E_f)/kT}} \,, \tag{3.23}$$

where T is the absolute temperature and k is Boltzmann's constant. The **Fermi level** with Fermi energy E_f is the highest filled energy level at 0° K. The valence electron band is formed by the lower energy orbitals (which are always filled), and the conduction band is formed by the higher energy bands. There is a gap in energy between the valence band and the conduction band, in other words, there aren't energy levels there in the gap: the smaller this gap is, the less energy is needed for electrons to transfer between the two bands and the closer the material is to a conductor.

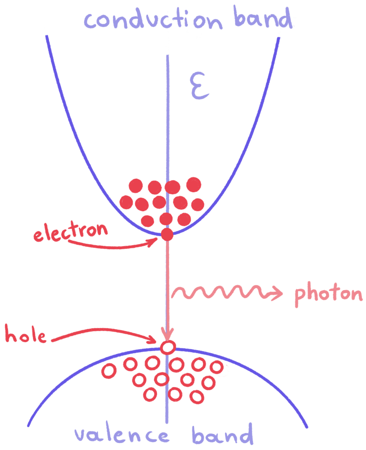

FIGURE 3.25: Photon emitted when electrons and holes are recombined in a direct-band-gap structure. One can determine what the conductivity of a material is by looking at the material's band structure. In semi-conductors the conduction and the valence bands are not overlapping, but the gap is also small enough for an electron to gain energy and make the transition.

The population at the Fermi level is 50% and so it lies between the two bands and its distance from the conduction band determines the material's conduction properties. It can also change if one heats the material or adds impurities to it, such as by introducing donor or acceptor atoms (n-type or p-type). A laser diode is a p–n diode semi-conductor, which is a semi-conductor consisting of a p-type semi-conductor and an n-type semi-conductor. When free holes are added in a semiconductor (doping) this one is then called **p-type**, and when it is doped with free electrons, it is called **n-type**. The population inversion is happening along the p-n junction. To have stimulated emission, the electron population in the conduction band must be higher than in the valence band and the current required for lasing to happen is called the threshold current. Similar to electrons changing atomic states, when holes and electrons are in the same region, an electron may transition from its area (the conduction band) to the valence band and emit a photon, see Figure 3.25. This process is called recombination. In order to initiate it, an external voltage source is used causing electrons to move through the junction and fall into holes.

The cavity of the laser is formed by two high reflective mirrors, with one of them having less than 100% reflectivity so that the laser beam can exit through it. The laser light coming out of the laser diodes is linearly polarized along the junction, but their polarization is varying and depending on temperature or optical power.

ECDL – Extended-Cavity Diode Laser

In order to fine-tune and stabilize parameters of a diode laser, such as power and wavelength, often an optical and electronics system is used after the output of the diode-laser beam.

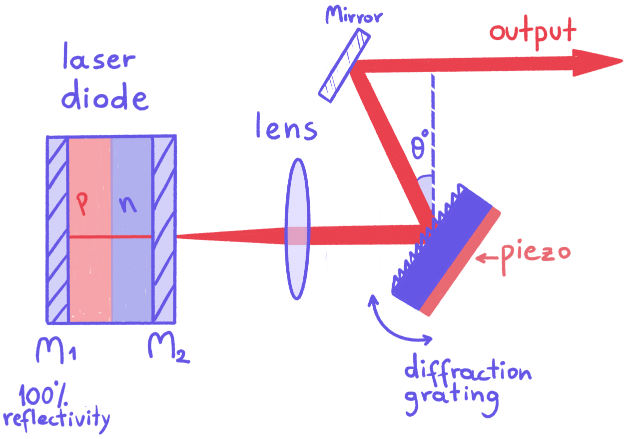

FIGURE 3.26: ECDL Littrow configuration.

One of these systems is the extended-cavity diode laser (ECDL) which consists of a laser diode inside a larger cavity and other optical elements. A common configuration for the optical system of an ECDL is the Littrow configuration: this consists of the external cavity defined between the 100% rear reflective mirror of the diode and the grating few *cm* away, a collimating lens, and a diffraction grating attached to a turning lever and a piezo element [63], [64]. Often a mirror is attached after the grating so that, when the grating is moved to adjust the wavelength, the output beam does not change direction. The external cavity's length can also be controlled by changing the temperature and hence stabilizing this temperature is crucial. The broad tuning range of the laser is determined by rotation or translation of the grating, while smaller changes in the laser's wavelength are made by using a piezo actuator.


N
W
E
S

You spin me right 'round, baby, right 'round
Like a record, baby, right 'round, 'round, 'round

Dead or Alive

4

All-optical spin locking in alkali-vapor magnetometers

The text presented in this section is part of a paper that has been published as [65]. For the work presented in this Chapter, I build upon the idea conceived by Dmitry Budker. Together with Guzhi Bao we constructed the setup needed for the experiment. I took part of the data and analyzed part of them. Together with the rest of the co-authors, I co-wrote and edited the manuscript.

4.1 The idea

In the first Chapters of my thesis, the theoretical basis was set for understanding nonlinear magneto-optical effects and atomic magnetometry. By the end of Chapter 3, in Section 3.4.1 we took a look at the non-linear Zeeman (NLZ) effect and how it affects our resonances in atomic magnetometry. The NLZ effect is the biggest limitation when aiming for the high sensitivities achieved by OPMs operating in Earth's magnetic field. It causes two important problems in accurate measurements: first, the splitting and, as a result, the broadening of the magnetic resonance which causes in turn loss in sensitivity [30]. The second issue, is the measurement errors related to the orientation between the lasers and the magnetic field, the so-called heading-error [66].
There have been several techniques proposed for canceling out the NLZ effect: tensor light shift effects [67], double-modulated synchronous optical pumping [68], polarization modulation [69] and frequency modulation [70] and more recently **spin locking (SL)** [71].

In the latter scheme, an oscillating magnetic field (RF field) or short magnetic-field pulses applied in the laboratory frame results in an effective static magnetic field along the atomic magnetization in the rotating frame (in the rotating frame the oscillating field looks like a static magnetic field). The atomic spin state then precesses about this static field, rather than evolving into a different state, as it would under the action of the nonlinear Zeeman effect alone. As a result, the spin-locking field prevents splitting, shifts, and line-shape asymmetries from occurring.

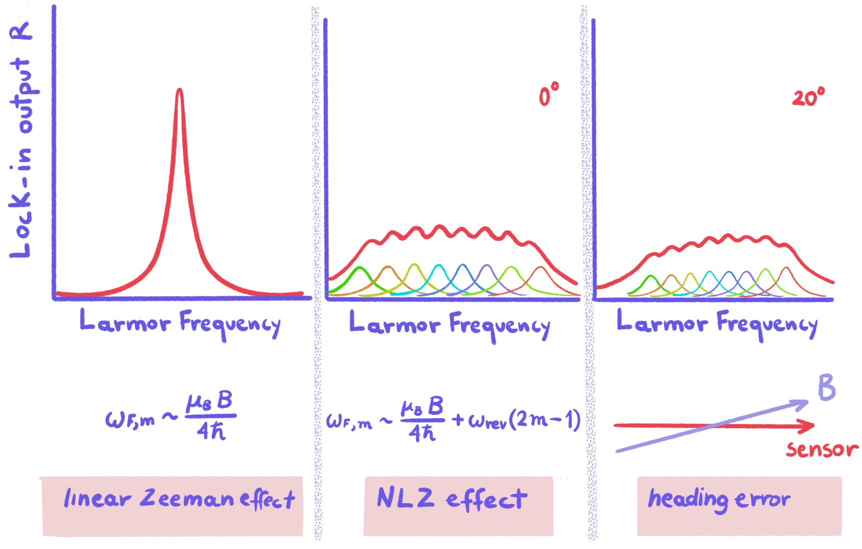

FIGURE 4.1: NLZ effect in Cs. (From left to right) Figure 1: The Zeeman effect allows us to polarize our atoms and get a magnetic resonance. Figure 2: The Nonlinear Zeeman effect is splitting the resonance depending on the number of m levels. Figure 3: When the magnetic field and the beams are not perpendicular to each other (for example, here they are at 20°), the already split resonance get an asymmetry.

A potential drawback to this approach is that applied magnetic fields may lead to crosstalk between closely located sensors (for example in a gradiometric configuration). This would limit the applicability of this technique to sensor networks, which are important in biomedical applications, such as imaging the human heart or mapping brain activity [72–76], as well as magnetic field monitoring in experiments searching for a permanent electric dipole moment of the neutron [77, 78]. Additionally, in remote magnetometry applications, spin-locking magnetic fields cannot be directly applied to the atomic sample [79–81]. The all-optical spin locking technique applied in this work is used to bypass such difficulties.

4.2 Spin locking

Spin locking, as demonstrated in [71], was generated by the use of a small magnetic field applied in the rotating frame along the main magnetization of the spins of Cs atoms. Spin locking could in theory be induced by using a fictitious magnetic field– in the form of a light field– rather than a real magnetic field. In the presence of light, the energies of Zeeman sublevels are subject to AC Stark shifts, or “light shifts” [82–85].

Linearly polarized light causes scalar and tensor shifts, while circularly polarized light can cause a vector shift. The scalar component shifts the Zeeman sublevels all together [86]. The effect of the vector light shift (VLS) is analogous to a fictitious magnetic field: it acts like the Zeeman effect on the atomic structure [83,87]. VLS have been studied in the context of all-optical magnetometry [18], [85]; in particular, light was used as a substitute for RF (radio frequency) fields [86,88] in optically pumped RF-driven magnetometers.

Here, we demonstrate all-optical compensation of the nonlinear Zeeman shift in a magnetometer using spin locking by replacing the RF field with an intensity- and polarization-modulated laser beam. With this method we can build a highly sensitive multi-sensor magnetometer array capable of working in the magnetic-field range of the Earth.

To describe the physics of spin locking, we start with a total angular momentum $F = 1$ system interacting with a leading magnetic field along $\hat{\mathbf{z}}$ and an oscillating magnetic field along $\hat{\mathbf{x}}$. The atomic spins are initially prepared in the $m_F = 1$ state along the $\hat{\mathbf{x}}$ direction by a circularly polarized pump field, and we assume that the probe-light power is sufficiently low to be neglected for the dynamics. With the quantization axis along $\hat{\mathbf{z}}$ and in the rotating frame (applied field is co-rotating with the angular-momentum vector) the initial state is:

$$\psi(0) = \frac{1}{2}\begin{pmatrix} 1 \\ \sqrt{2} \\ 1 \end{pmatrix}. \tag{4.1}$$

The Hamiltonian for the system under the rotating-wave approximation (RWA)[I] for the RF field is [71]

$$\hat{H}_{RWA} = \hbar \begin{pmatrix} \omega_{rev} & -\frac{\Omega_{RF}}{2\sqrt{2}} & 0 \\ -\frac{\Omega_{RF}}{2\sqrt{2}} & 0 & -\frac{\Omega_{RF}}{2\sqrt{2}} \\ 0 & -\frac{\Omega_{RF}}{2\sqrt{2}} & \omega_{rev} \end{pmatrix}, \tag{4.2}$$

where ω_{rev} is the "revival" frequency characterizing the strength of the NLZ effect (See 3.4.1) and Ω_{RF} is the Larmor frequency induced by the oscillating field and is proportional to its amplitude.

We write the state $\psi(t)$ of F as a superposition of energy eigenstates Ψ_k with eigenvalues E_k:

$$\psi(t) = \sum_k \Psi_k e^{-iE_k t/\hbar}. \tag{4.3}$$

[I] An oscillating field with linear polarization is a superposition of rotating fields: one rotating in a clockwise sense and the other rotating in a counter-clockwise sense. In the rotating frame on resonance, the co-rotating field is static and the counter-rotating field appears to rotate at twice the frequency. The terms of the Hamiltonian that are rapidly oscillating are then neglected and this approximation is called the rotating-wave approximation (RWA). When the driving field is strong enough, the counter-rotating field could produce a shift in the resonance frequency of the system: the Bloch-Siegert shift.

The probability $P(t,0)$ for an atom to be found in the initial state, $|\langle\psi(t)|\psi(0)\rangle|^2$, can be written as

$$P(t,0) = \frac{\omega_{lock}^2 + \Omega_{RF}^2 + \omega_{rev}^2 \cos(\omega_{lock} t)}{2\omega_{lock}^2}, \tag{4.4}$$

where $\omega_{lock} = (\omega_{rev}^2 + \Omega_{RF}^2)^{1/2}$ is the spin-locking oscillation frequency. With an increase in the spin-locking field amplitude, the oscillating component of $P(t,0)$ decreases in amplitude and the frequency of the oscillation increases (see Figure 4.2). In this simplified model, it appears that spin locking improves with the amplitude of the applied field. However, when the RF field is large enough so that the rotating-wave approximation is not valid anymore, the presence of the spin-locking field leads to power broadening of the magnetic resonance. Under this condition the optimal amplitude of the field is when Ω_{RF} is comparable to ω_{rev}.

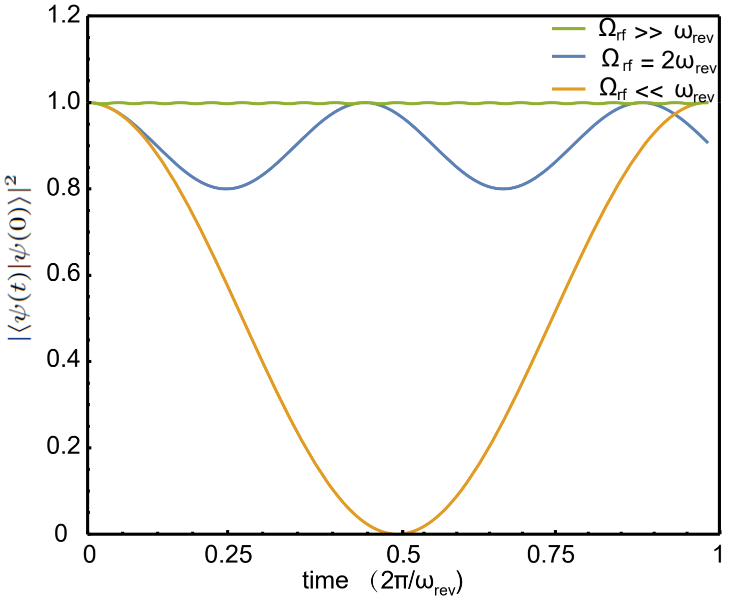

FIGURE 4.2: Probability $P(t,0)$ for an atom to be found in the initial state. For small amplitudes of the spin-locking field ($\Omega_{rf} \ll \omega_{rev}$), the probability undergoes quantum beating. If the amplitude of the spin-locking field is much larger than the NLZ parameter ($\Omega_{rf} \gg \omega_{rev}$), the atoms remain in the initial state. If the amplitude of the spin-locking field is equal to the NLZ parameter ($\Omega_{rf} = 2\omega_{rev}$), the atoms are partially locked in the initial state and the populations undergo oscillation with frequency ω_{lock}.

4.2.1 Spin Locking with AC Stark shift

The vector component of the light shift induced by circularly polarized light can be interpreted as a fictitious magnetic field along the light propagation direction, with magnitude [89]

$$B_{\text{fict}} = \frac{-c(\Delta)\mathcal{I}\epsilon}{\hbar\gamma_{\text{Cs}}}, \tag{4.5}$$

where $c(\Delta)$ is a proportionality constant that depends on atomic parameters and the frequency detuning Δ from an atomic resonance, $\mathcal{I}$ is the light intensity, $\gamma_{\mathrm{Cs}} = 2.2 \cdot 10^{10}$ rad/(s · T) is the Cesium gyromagnetic ratio and $\epsilon = \left[\mathcal{I}(\sigma_+) - \mathcal{I}(\sigma_-)\right]/\mathcal{I}$ is the Stokes parameter specifying the degree of circular light polarization ($\epsilon = +1$ for σ_+-polarized light, $\epsilon = -1$ for σ_--polarized light and $\epsilon = 0$ for linear polarization).

Consider the same system as in the previous section– an $F = 1$ system with a leading magnetic field along $\hat{z}$ and a circularly polarized pump beam propagating along $\hat{x}$. Now, rather than an RF field, we apply a modulated, circularly polarized light beam propagating in the same direction as the pump, near-resonant with a transition to an $F = 0$ state, in order to induce vector light shifts. Next, let's calculate what the effective Stark-shift Hamiltonian is.

Effective Hamiltonian of Stark Shift

We will, here, calculate the light shift due to a circularly polarized field that is near-resonant with an $J = 1 \to J' = 0$ atomic transition. The detuning from the atomic resonance is called Δ and we assume the light is σ_+ polarized and propagating along the x-direction. If we use the x-basis $\{|1,-1\rangle_x, |1,0\rangle_x, |1,+1\rangle_x, |0',0'\rangle_x\}$, the light is only affecting one transition $|1,-1\rangle_x \leftrightarrow |0',0'\rangle_x$ due to the selection rule for σ_+ polarized light (see Figure 4.3). The dipole interaction $H = -\mathbf{d} \cdot \mathbf{E}(t)$ can be used to describe the interaction between the atom and the light. The Hamiltonian in rotating wave approximation (RWA) with rotating frequency $\omega_0 + \Delta$ is

$$H = \hbar \begin{pmatrix} 0 & 0 & 0 & 0 \\ 0 & 0 & 0 & 0 \\ 0 & 0 & 0 & -\frac{\Omega_R}{2\sqrt{3}} \\ 0 & 0 & -\frac{\Omega_R}{2\sqrt{3}} & -\Delta \end{pmatrix}_x , \tag{4.6}$$

where Ω_R is the Rabi frequency and $|\Omega_R|^2$ is proportional to the intensity of the light. The effect of oscillating fields with frequency $2\omega_0 + \Delta$ is ignored by the RWA. The energy eigenvalue E_{J,m_J} of this system is:

$$\begin{aligned} E_{1,-1} &= \frac{\hbar}{6}(-3\Delta + \sqrt{9\Delta^2 + 3\Omega_R^2}) \approx \frac{\hbar\Omega_R^2}{12\Delta} , \\ E_{1,0} &= 0 , \\ E_{1,1} &= 0 , \\ E_{0',0'} &= \frac{\hbar}{6}(-3\Delta - \sqrt{9\Delta^2 + 3\Omega_R^2}) \approx -\frac{\hbar\Omega_R^2}{12\Delta} . \end{aligned} \tag{4.7}$$

Since the light is detuned from atomic resonances, it is possible to derive an effective Hamiltonian for the ground states only. In the x-basis for the ground states $\{|1,-1\rangle_x, |1,0\rangle_x, |1,+1\rangle_x\}$, this Hamiltonian reads

$$H_{\text{eff}} = \frac{\hbar\Omega_R^2}{12\Delta}\begin{pmatrix} 1 & 0 & 0 \\ 0 & 0 & 0 \\ 0 & 0 & 0 \end{pmatrix}_x . \tag{4.8}$$

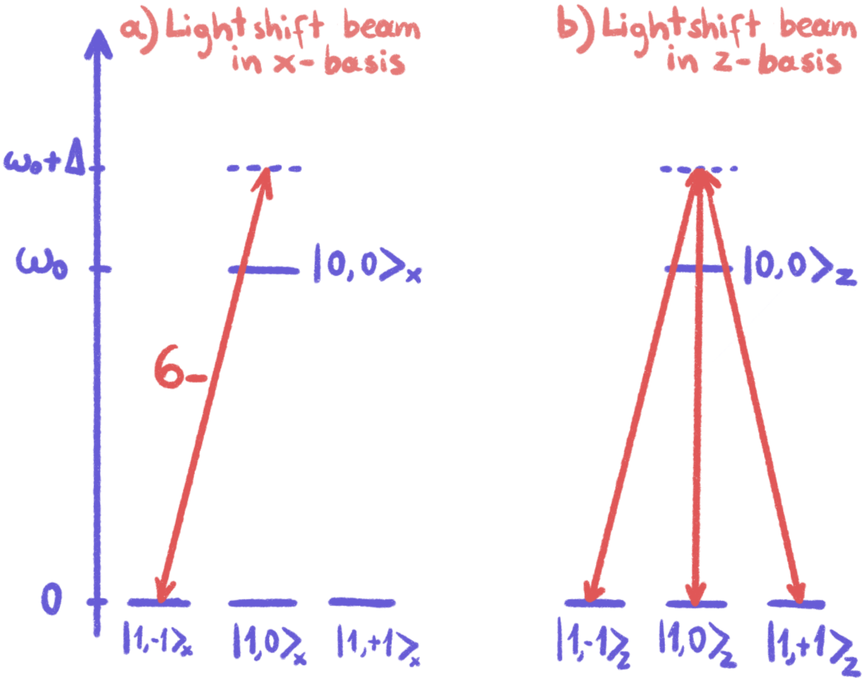

FIGURE 4.3: (a) Schematics for atomic levels $J = 1$ and $J' = 0$ coupled by circularly polarized light propagating in the x-direction. Only two levels are coupled in the x-basis. (b) All levels are coupled if one used the z-basis.

We are now interested in finding the Hamiltonian in the z-basis. In order to do so, we notice that a $\pi/2$ rotation about the y-axis rotates the x-axis into the z-axis. This rotation matrix can be written as

$$R(\hat{y}, \pi/2) = \exp\left[-i\left(\frac{\pi}{2}\right)\hat{J}_y\right] = \begin{pmatrix} \frac{1}{2} & -\frac{1}{\sqrt{2}} & \frac{1}{2} \\ \frac{1}{\sqrt{2}} & 0 & -\frac{1}{\sqrt{2}} \\ \frac{1}{2} & \frac{1}{\sqrt{2}} & \frac{1}{2} \end{pmatrix}_x , \tag{4.9}$$

We can now find the effective Hamiltonian in the z-basis as

$$\begin{aligned} \hat{H}^{+}_{eff} &= R(\hat{y}, \pi/2) H_{\text{eff}} R(\hat{y}, \pi/2)^{\dagger} \\ &= \frac{\hbar\Omega_R^2}{12\Delta}\begin{pmatrix} \frac{1}{4} & -\frac{1}{2\sqrt{2}} & \frac{1}{4} \\ -\frac{1}{2\sqrt{2}} & \frac{1}{2} & -\frac{1}{2\sqrt{2}} \\ \frac{1}{4} & -\frac{1}{2\sqrt{2}} & \frac{1}{4} \end{pmatrix}_z . \end{aligned} \tag{4.10}$$

For σ_- polarized light, the effective Hamiltonian in the z-basis is:

$$\hat{H}^{-}_{eff} = \frac{\hbar\Omega_R^2}{12\Delta}\begin{pmatrix} \frac{1}{4} & \frac{1}{2\sqrt{2}} & \frac{1}{4} \\ \frac{1}{2\sqrt{2}} & \frac{1}{2} & \frac{1}{2\sqrt{2}} \\ \frac{1}{4} & \frac{1}{2\sqrt{2}} & \frac{1}{4} \end{pmatrix}_z . \tag{4.11}$$

With this we arrive at the effective Hamiltonian in the form of Eq. (4.12). The effective Stark-shift Hamiltonian for σ_+ and σ_- beam can be represented as:

$$\begin{aligned} \hat{H}^{+}_{eff} &= \hbar\frac{(\Omega^{+}_{LS})^2}{\Delta}(K_1 - K_2), \\ \hat{H}^{-}_{eff} &= \hbar\frac{(\Omega^{-}_{LS})^2}{\Delta}(K_1 + K_2), \\ K_1 &= \frac{1}{48}\begin{pmatrix} 1 & 0 & 1 \\ 0 & 2 & 0 \\ 1 & 0 & 1 \end{pmatrix}, \\ K_2 &= \frac{1}{48}\begin{pmatrix} 0 & \sqrt{2} & 0 \\ \sqrt{2} & 0 & \sqrt{2} \\ 0 & \sqrt{2} & 0 \end{pmatrix}, \end{aligned} \tag{4.12}$$

where $\Omega^{\pm}_{LS}$ is the Rabi frequency of $\sigma_\pm$- polarized light, $|\Omega^{\pm}_{LS}|^2$ is proportional to the intensity of the light $\mathcal{I}(\sigma_\pm)$, and Δ is the detuning. The light-shift beam can be intensity- and/or polarization-modulated as we will see in the details in the experimental section below. The intensity of $\sigma_\pm$-polarized light in Figure 4.6(c) is:

$$\begin{aligned} \mathcal{I}(\sigma_-) &= I_0\frac{\cos(\omega_{RF}\,t) + |\cos(\omega_{RF}\,t)|}{2}, \\ \mathcal{I}(\sigma_+) &= I_0\frac{-\cos(\omega_{RF}\,t) + |\cos(\omega_{RF}\,t)|}{2}, \end{aligned} \tag{4.13}$$

where ω_{RF} is the light-shift-field modulation frequency. By substituting Eq. (4.13) into Eq. (4.12), we get the total Stark-shift Hamiltonian:

$$\hat{H}_{LS} = \frac{\hbar(\Omega^{m}_{LS})^2}{\Delta}\left[K_1|\cos(\omega_{RF}\,t)| + K_2\cos(\omega_{RF}\,t)\right], \tag{4.14}$$

where Ω^{m}_{LS} is the amplitude of the modulated Rabi frequency. The first term is an unwanted perturbation caused by the light shift beam. The second term describes a pure fictitious RF field $B_{\text{fict}} \propto I_0\cos(\omega_{RF}\,t)$ which is used to perform all-optical spin locking.

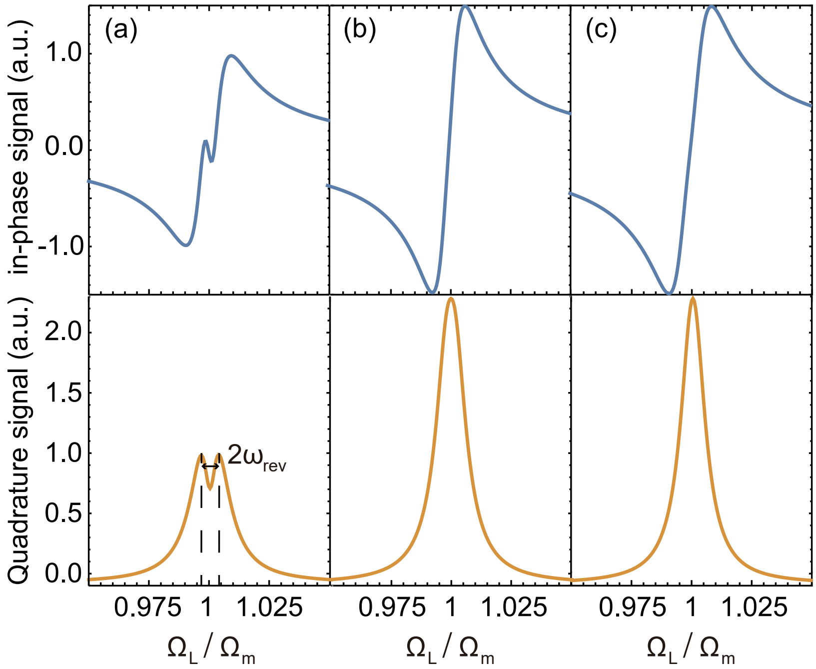

FIGURE 4.4: Theoretical calculations of signal. Theoretical calculated in-phase (top row) and quadrature (bottom row) first-harmonic amplitudes of optical rotation signal. The NLZ effect splits the magnetic resonance into two peaks: (a) without the the spin-locking field (b) with RF field (c)with intensity modulated light-shift field. For these plots, the parameters $\Omega_{pr}/\gamma = 100$, $\delta_{pr}/\gamma = 10^6$, $\Omega_p/\gamma = 10^4$, $\delta_p/\gamma = 10^3$, $\Delta_m/\gamma = 10^3$, $\omega_{rev}/\gamma = 1.5$, $\Omega_{RF}/\gamma = 0.02$, $\Omega_{LS}^m/\gamma = 0.02$, $\Delta/\gamma = 10^5$ are chosen.

4.2.2 Optical Rotation Signal

Let's assume that probe light that is linearly polarized along $\hat{x}$ with detuning δ_{pr} and Rabi frequency Ω_{pr}, is used to measure the atomic state of Cs during its evolution. The propagation direction $\hat{\mathbf{y}}$ of the probe is perpendicular to both the propagation direction of the pump light $\hat{\mathbf{x}}$ and the direction of leading field $\hat{\mathbf{z}}$. The pump field with central detuning δ_p and Rabi frequency Ω_p is periodically modulated with frequency Ω_m. To simplify the calculations, we assume that the frequency of the pump is sinusoidally modulated, with modulation amplitude Δ_m.

When $\Omega_m = \omega_{RF}$ (when the pump modulation frequency is equal to the light-shift-field modulation frequency), we can solve the time-periodic evolution equation using Floquet theory [90,91]. Results of numerical calculations with the AtomicDensityMatrix (ADM) package [30] are shown in Figure 4.4 to illustrate the in-phase and quadrature first-harmonic amplitudes of the optical-rotation signal. Here, we consider each sublevel to undergo relaxation (for example, due to spin-depolarizing collisions) at a rate γ. In addition, the upper state undergoes spontaneous decay at a rate $\Gamma = 10^6\gamma$. Without the light-shift beam [4.4(a)], the magnetic resonance is split due to the NLZ effect. Figures 4.4(b) and (c) show the magnetic resonance with RF field and amplitude-modulated light-shift field, respectively.

The NLZ splitting apparent in 4.4(a) is no longer visible in 4.4(b) or 4.4(c) as in both cases spin-locking is achieved, either through an RF field or through the modulated light shift, demonstrating that theoretically both approaches achieve the desired effect.

Up to now, we show the theoretical simulation of all-optical spin locking in $F = 1$ to $F' = 0$ system. For a real atomic system, there are many hyperfine levels that need to be taken into account its modeling, something that would increase the computational complexity. Hence, for this case, we present only experimental results.

4.3 Experimental setup

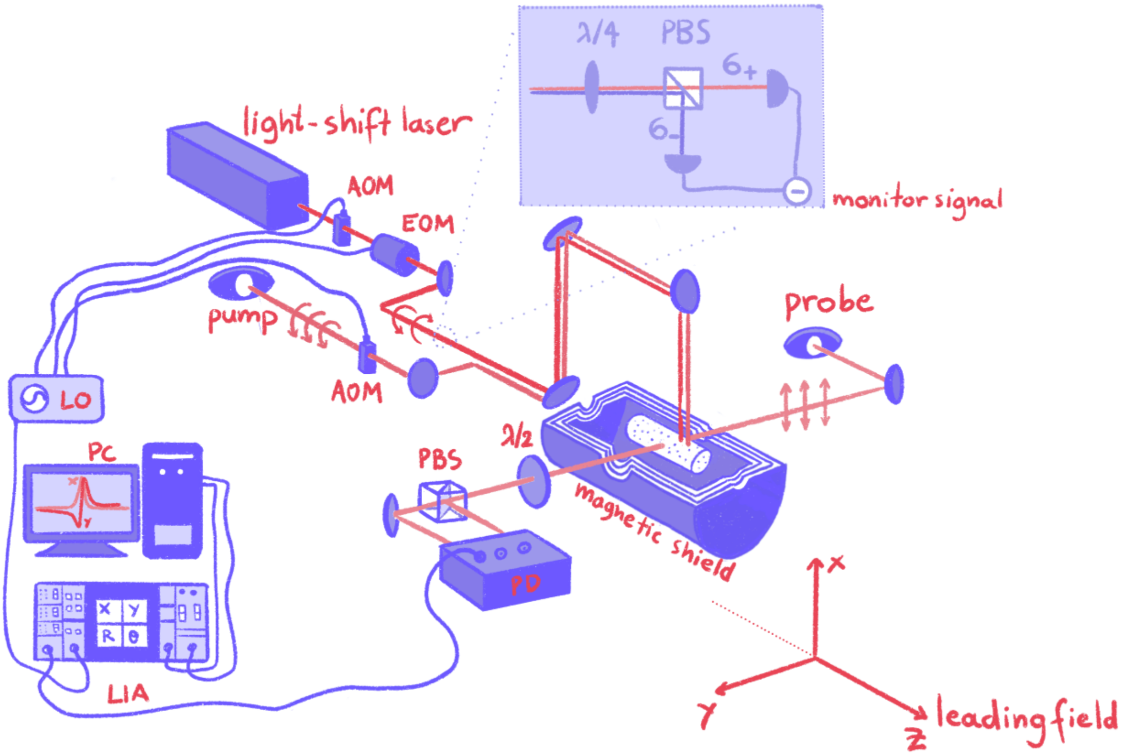

FIGURE 4.5: Experimental setup for all-optical spin locking: AOM: acousto-optic modulator; EOM: electro-optic modulator; HWP: half-wave plate; QWP: Quarter-wave plate; PBS: polarizing beam splitter; PD: balanced photodetector; LIA: lock-in amplifier; LO: local oscillator. A partial view of the magnetic shield is shown in the figure. Atoms are contained in a glass cell positioned in the center of the magnetic shield and are pumped (along $-\hat{\mathbf{x}}$) and probed (along $\hat{\mathbf{y}}$) by laser beams under a static magnetic field (along $\hat{\mathbf{z}}$). The intensity of the light-shift laser beam is sinusoidally modulated with an AOM at a frequency Ω_m, while its polarization is switched between the σ_+ and σ_- states every π/Ω_m, using an EOM. Inset shows the monitor setup for polarization and amplitude of the light-shift beam.

Figure 4.5 shows the experimental apparatus. A paraffin-coated cylindrical cell with a length of 5 cm and a diameter of 4 cm containing ^{133}Cs at room temperature, is enclosed within a four-layer mu-metal magnetic shield.

The atoms are pumped in the stretched state along the $-\hat{\mathbf{x}}$ direction with a circularly polarized, $-\hat{\mathbf{x}}$-directed laser beam. The **pump-laser** frequency is locked to the Cs D2 $6^2S_{1/2}\,F=3 \rightarrow 6^2P_{3/2}\,F'=4$ transition at 852 nm with a dichroic atomic vapor laser lock (DAVLL) [92]. The beam is pulsed (3% duty cycle) with an acousto-optic modulator (AOM). The time-averaged light power– while the AOM is on –is 50 µW[I].

The polarization rotation of a 10 µW, $\hat{\mathbf{y}}$-directed **probe beam** induced by the polarized atomic vapor is measured with a balanced polarimeter after its transmission through the cell. The beam is linearly polarized along the x axis and detuned by about 4 GHz towards higher frequencies (blue detuned) from the D2 $F=4 \rightarrow F'=5$ transition.

A circularly polarized **light-shift beam** produced with a Ti:sapphire laser propagates parallel to the pump beam. The intensity of the beam is modulated with an AOM and its polarization is modulated with an EOM in order to provide a time-varying light shift. The setup for monitoring the modulation of the light-shift beam is shown in the inset of Figure 4.5. A quarter-wave plate is used to convert the circular σ_+ and σ_- components into orthogonal linear polarization components the intensities of which are monitored with two photodetectors. The waist of the collimated laser beam in the vapor cell is 1.5 mm. The frequency of this laser can be widely tuned and is, for most of the experiments presented here, detuned by 10 GHz from the $6^2S_{1/2}\,F=4 \rightarrow 6^2P_{3/2}\,F'=5$ D2 transition towards lower frequencies (red detuned). Its frequency is stabilized to the internal reference cavity of the laser. A detuning of 10 GHz was chosen to minimize optical pumping by the light-shift beam, while maintaining a sufficient fictitious-magnetic-field amplitude (~14 nT for 250 mW power) for spin locking.

To measure the **magnetic resonance**, we fix the modulation frequency Ω_m of both the pump and light-shift beams at a particular value (corresponding to the Larmor frequency for a magnetic field of up to 100 µT). We scan the leading $\hat{\mathbf{z}}$-directed magnetic field and observe the polarization of the probe beam. The signal from the balanced polarimeter is fed into a lock-in amplifier and is then demodulated at the modulation frequency. The magnetic resonance can be observed in the polarization rotation amplitude and phase of the probe beam.

4.4 Results

We employed three different methods to modulate the light-shift beam and achieve spin locking. Figure 4.6 shows the amplitude of the lock-in output as a function of the leading magnetic field around 60 µT and with the pump-laser modulation frequency fixed at 216,620 Hz. The magnetic resonance spectra are shown without and with application of the light-shift beam (black and red curves, respectively), as well as without the pump beam (blue curve).

In the method depicted in Figure 4.6(a,b), either the intensity or the polarization of the light-shift beam is modulated, to provide a sine-modulated light shift, as in Refs. [85,86]. In the **polarization-modulation scheme**, the fictitious magnetic field is oscillating around zero. However, in this

---

[I] Our power meter takes a specific amount of samples per second and averages the values in this range

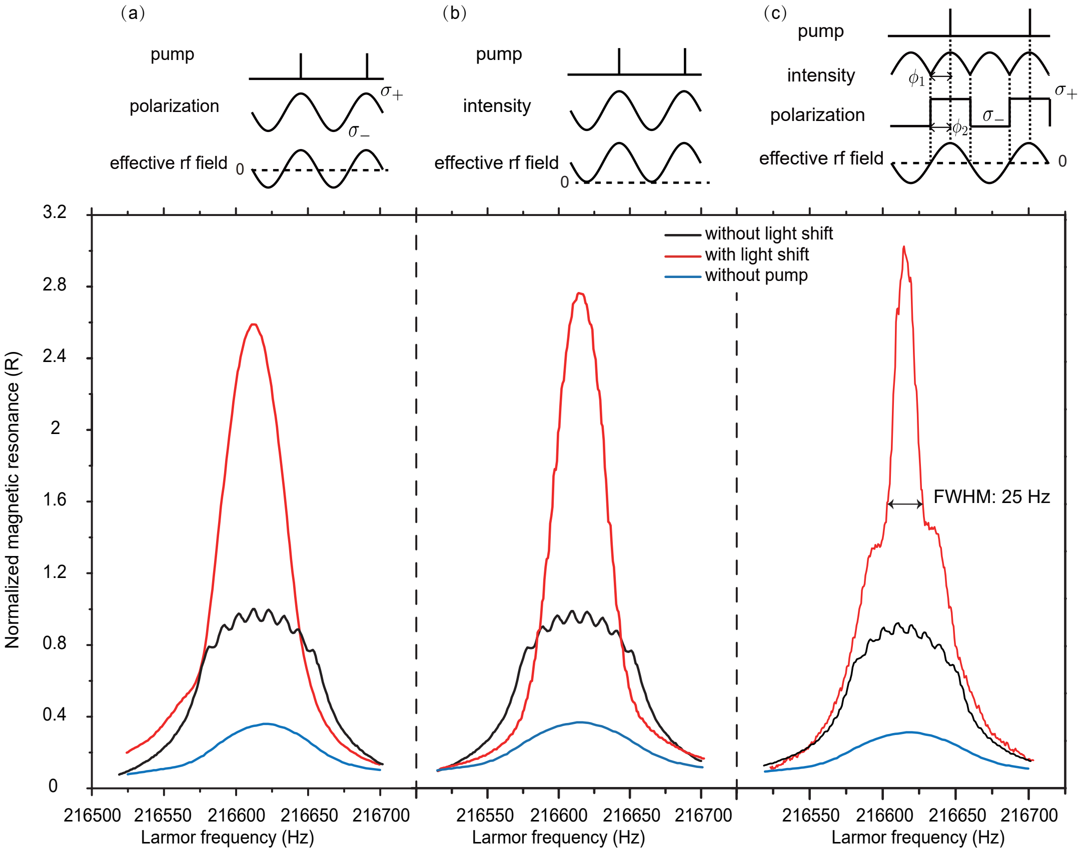

FIGURE 4.6: (Experimental data) Magnetic-resonance line shape for a modulation frequency of 216,620 Hz as a function of the leading magnetic field along the z axis with applied light-shift field and pump (red line), without light-shift field and pump (black line), and without pump field (blue line). The amplitude of magnetic resonance without light shift is normalized to unity. The power in (a) and maximum power in (b,c) of the light-shift beam is 200 mW. The inset shows the polarization modulation (a), intensity modulation (b) and both modulated (c) schemes for the pump and light-shift field.

scheme, the light is only purely circularly polarized when $\epsilon = \pm 1$ (see formula 4.5); the presence of the other polarizations causes tensor-light shifts that broaden the transition. In the **amplitude-modulation scheme**, the VLS produces a fictitious magnetic field of magnitude $B_{\text{fict}} \propto [1 + \cos(\Omega_m t)]$. The oscillating term of the fictitious field locks the spins. The static term of the fictitious field plays no role in spin locking, but the constant light leads to broadening of the linewidth due to residual optical pumping and heading error. In the absence of the light-shift beam, the magnetic resonance is split into eight partially-resolved Lorentzian peaks, due to the NLZ effect. When we apply the modulated light-shift beam we get a narrower full-width-half-maximum (FWHM) central peak and an amplitude increase.

In Figure 4.6(c), the direction of the fictitious magnetic field is modulated by switching the polarization of the light-shift beam from σ_+ to σ_- using an EOM. In addition, the intensity $\mathcal{I}$ of the light-shift beam is modulated with an AOM as $\mathcal{I} \propto |\cos(\Omega_m t)|$. In this modulation scheme, neglecting the counter-rotating component, the fictitious RF field co-rotates with the precessing spins in the laboratory frame. Since the polarization and propagation direction of the light-shift beam and the

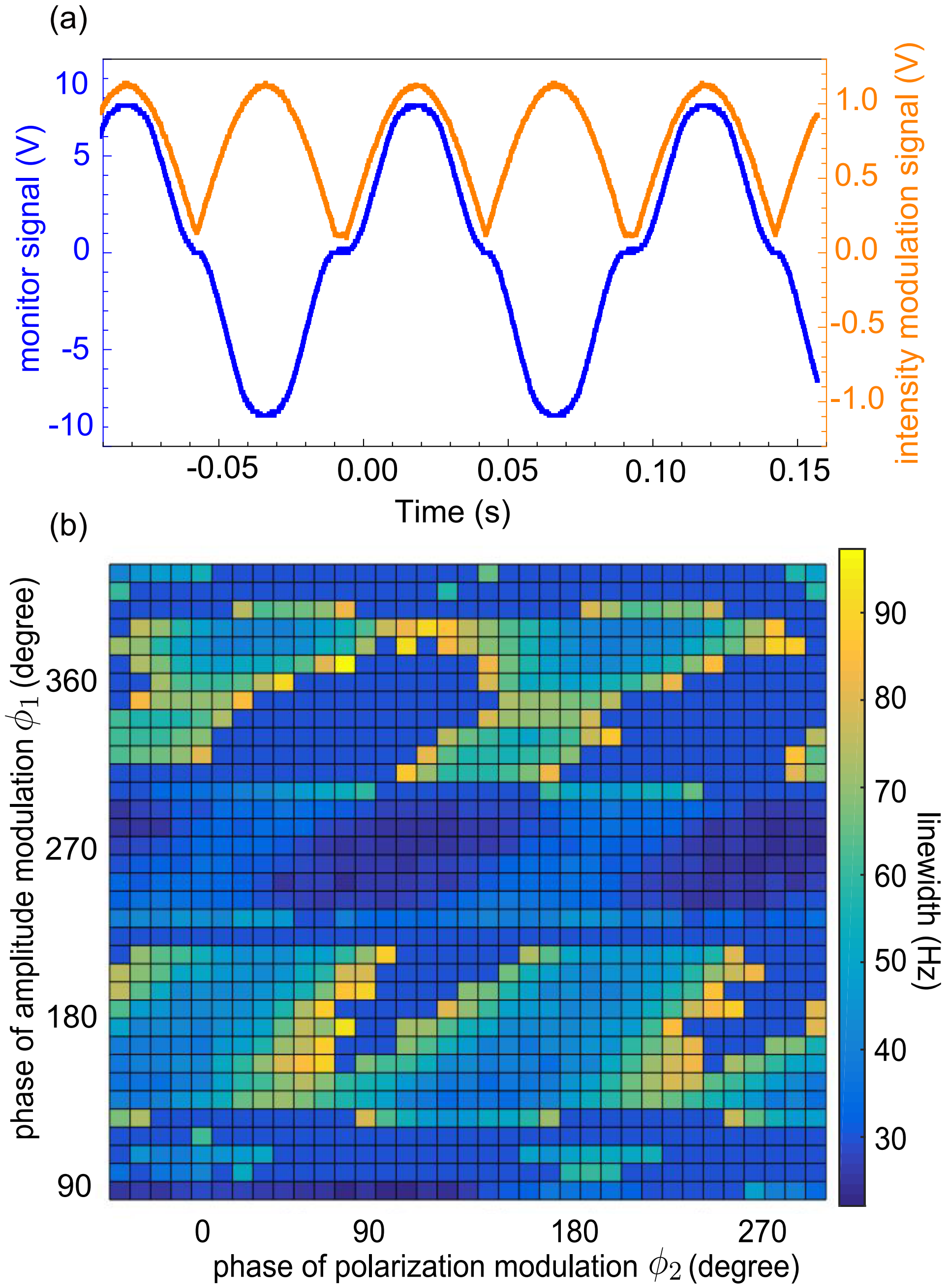

FIGURE 4.7: (a) Observed monitor signal and input intensity modulation signal. Here $\phi_1 = -\pi/2$ and $\phi_2 = -\pi/2$. The distortion of fictitious RF field is mainly caused by nonlinear response of the AOM. (b) Phase scanning of ϕ_1 and ϕ_2.

pump beam are the same, the light-shift beam also pumps the atoms. The blue lines in Figure 4.6 show the magnetic resonance with the light-shift beam on but without a pump beam. The stochastic nature of the optical pumping leads to a decrease in atomic-coherence and results in broadening of the magnetic resonance.

The phase of the intensity and polarization modulation needs to be chosen carefully to ensure that the spin-locking field points along the direction of the precessing spins [71]. To create a fictitious

RF field that changes smoothly, the polarization should be switched when the intensity is modulated to zero. Additionally, the fictitious RF field has to be in-phase with the pump pulse. We show the monitor signal (produced by subtraction of the σ_+ and σ_- recorded powers) for $\phi_1 = -\pi/2$ and $\phi_2 = -\pi/2$ in Figure 4.7(a), as a fictitious RF field. Here ϕ_1 is the phase of the intensity modulation and ϕ_2 is the phase of the polarization modulation. Figure 4.7(b) displays the magnetic-resonance line width for different ϕ_1 and ϕ_2. Some of the best results are achieved around $\phi_1 = 3\pi/2$ and $\phi_2 = \pi/2$.

Figure 4.8 shows the effective linewidth of the magnetic resonance in Earth-field range (60 µT) as a function of the applied light-shift beam power and its detuning. When the light-shift beam has low power and is detuned far off resonance, there is no spin locking and the effective line width is ≈100 Hz. When the light-shift beam is near resonant with the atomic transition, the effect of optical pumping is much stronger than that of the VLS. As a result, the line width of the magnetic resonance is even broader than that observed in the absence of the light-shift beam. When the light is far-off resonant from the optical transition, the optical pumping is negligible and the VLS dominates the interaction. We observe a minimum of the line width for a 220 mW light-shift beam, 10 GHz detuned below the D2 $6^2S_{1/2}\,F = 4 \rightarrow 6^2P_{3/2}\,F' = 5$ transition. Note, however, that spin locking works well also for the opposite sign of detuning, corresponding to a sign reversal of the effective RF field. We could not apply higher powers because of the available laser.

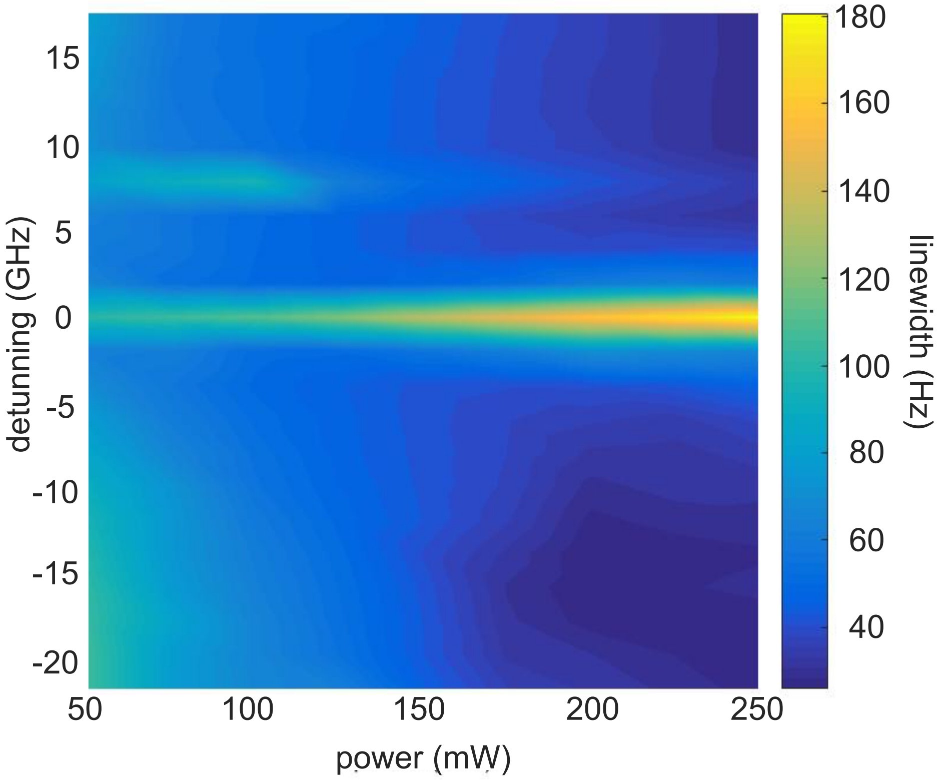

FIGURE 4.8: Map of the magnetic-resonance linewidth as a function of the applied light-shift-field power and detuning. The minimum linewidth is 25.25(6) Hz.

4.5 Conclusions

In Chapter 3.1.6 the sensitivity of a magnetometer is explained and studied and it becomes clear that the smaller the linewidth and the bigger the amplitude the higher the sensitivity of our magnetometer. Here we have demonstrated an all-optical method to suppress the NLZ effect in the range of the Earth's magnetic field by using spin locking, which effectively manifests by reducing the linewidth or our magnetic resonance.

A polarization and intensity-modulated light-shift beam is applied which suppresses NLZ-related broadening of the magnetic resonance. This method works with either application of intensity modulation or polarization modulation, but the combination of both yields the best results.

In contrast to other techniques, this method does not cause crosstalk in sensor networks and does not interact with samples close to the sensor. The Larmor frequency induced by the optimally effective spin-locking field in the rotating frame is one order of magnitude larger than the spin-revival frequency; the phases (ϕ_1 and ϕ_2) are chosen such that the corotating part of the fictitious RF magnetic field is colinear with the precessing spins.

We note that the method improves the sensitivity of Earth-field-range magnetometers for two reasons: **the increase in the magnetic-resonance signal amplitude** and **the reduction in the effective linewidth**.

Intuitively, the area under the black and red curve in Figure 4.6 should be of equal size since spin locking would combine the 8 peaks to one. We observe however a larger under-the-curve area for spin locking compared to no spin locking. That could be due to residual optical pumping by the light-shift beam, which could be improved if we detuned the beam even further and used higher powers.

Another interesting finding is the resonance lines look more noisy from left to right as we look at Figure 4.6. This is speculated to be a result of magnetic noise, which we could find out if we calculate the sensitivity. Since the slope of our resonance increases, the quantum limit of the sensitivity is improved, but there is also magnetic noise in our shield because of the noisy current source we are using. If the quantum noise is bigger than the magnetic noise we won't notice the latter, but when the sensitivity improves the magnetic noise emerges. In better words: a more sensitive magnetometer is also responding more to magnetic noise, hence the difference in the noise between our different resonances.

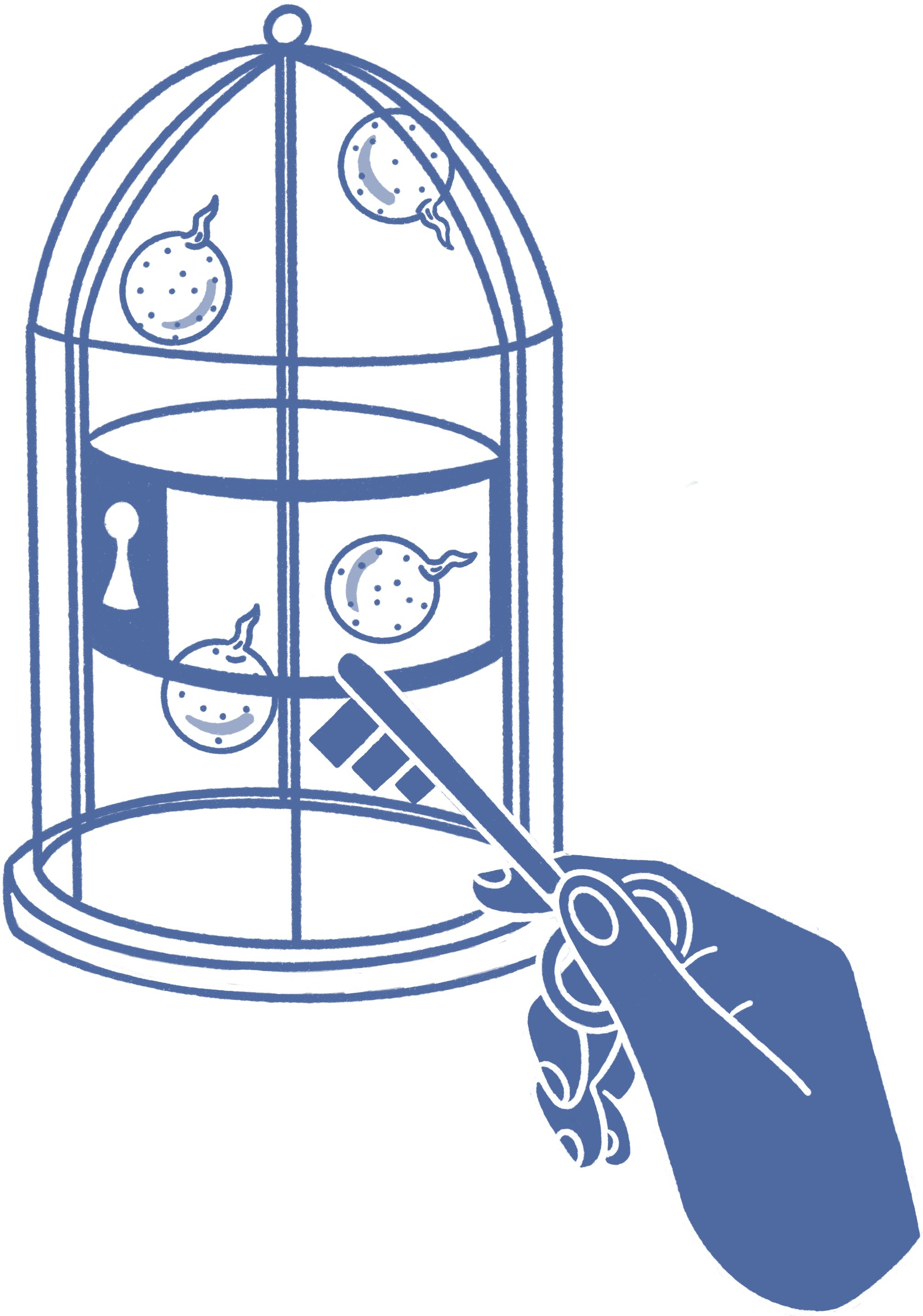

The real voyage of discovery consists,
not in seeking new landscapes, but in having new eyes.

Marcel Proust

5

Rb magnetometry free from NLZ-effect-related heading error in Earth-field range

The text presented in this section is part of a paper that has been published as Ref. [93]. For the work presented in this Chapter, I build upon the idea conceived by Rui Zhang and we constructed the setup needed for the experiment together. I took a big part of the data and analyzed part of them. Together with the rest of the co-authors, I co-wrote and edited the manuscript.

5.1 The idea

Very sensitive and low-cost magnetometers that work on Earth-field, in an unshielded environment have been the holy grail of optical magnetometry for many decades. We discussed in Chapter 3 that such devices would be of great importance for the production of inexpensive and sensitive sensors or imaging devices that can operate in many environments. This appealing perspective has been the motivation for a collective effort of thinking and testing ways to tackle the biggest limiting factor for scalar Earth-field magnetometers, namely the **heading error**.

In Section 3.4.2 one can find a more detailed description of the effect, but to freshen up the reader's memory, heading error is the dependence of the scalar magnetometer's reading on the direction of the magnetic field [19]. There are mainly three physical sources of heading error: the **nonlinear Zeeman effect (NLZ)** due to the coupling between electron spin and nuclear spin [94–96], the **different gyromagnetic ratios of two ground hyperfine states** due to the linear nuclear Zeeman effect (NuZ) [96,97], and the **magnetic-field-direction-dependent light shift** (LS) [95]. The first two effects lead to the orientation-dependent asymmetry of the magnetic resonance curve, and the third leads to the orientation-dependent shift of the magnetic resonance frequency. These changes of our measured magnetic resonance lead to a loss of sensitivity (see Chapter 3). Since atomic magnetometry is famous for its unmatched sensitivity the heading error is posing a serious problem in the field. We will in this Chapter occupy ourselves with a strategy to suppress NLZ-related heading error. To paraphrase John F Kennedy, “Ask not what your magnetometer can do for you, ask what you can do about its heading error”.

5.1.1 Strategies to suppress the NLZ-related heading error

Traditionally there are three (3) strategies to deal with NLZ-related heading error:

1. **Physical or theoretical compensation**, including compensation with tensor light shift [98], compensation with spatially separated pumping beams of opposite circular polarizations [95], and using a high-power pump and correcting with theoretical predictions [96]{I}.

2. **Using modulation schemes to address atomic spins** in states less sensitive to direction-related magnetic resonance asymmetry, including synchronous optical pumping with double modulation [68], push-pull pump [99], and spin-locking with synchronous optical pumping and radio-frequency (RF) [94], such as our project covered in Chapter 4 or modulated optical [65] field.

3. **Using transitions intrinsically free from NLZ-related splitting**, for example, excitation of high-order atomic polarization moments [53]. Compared with the first two strategies whose performance relies on careful adjustment of experimental parameters, theoretically, the latter strategy should give a better heading-error suppression, as it is intrinsically free from the NLZ effect, and it does not require special hardware or additional modulation, which is especially welcome for mobile or wearable systems. However, these approaches suffer from dramatic decrease of signal amplitude in the geomagnetic field range, which precludes their applications in high-sensitivity magnetometry.

Our idea belongs to the last category since we tried to take a more fundamental approach to the problem by asking ourselves the question: What makes the magnetic resonance split in the first place? And, what if, we could only have one resonance and conceptually avoid the asymmetry that would arise from multiple peaks? In the following pages I will shed some light into how we dealt with these questions and how we came up with the idea of a simple heading-error-free atomic magnetometer.

5.2 The Physics behind the idea

This section introduces briefly the physics needed to understand how we built our magnetometer and why it works. For a more fundamental understanding one should start by reading Chapters 1 and 2 of this thesis.

To prompt the reader’s memory, the density matrix describes polarized states, as well as unpolarized, since not all atoms in a physical system can be described by the same wave function. The diagonal

---

{I} In some cases, heading errors due to NuZ [96] or LS [95] effect are suppressed together with the NLZ-related effect at the same time.

elements of the density matrix represent the probability of finding the atom in a state $|m\rangle$ or else, their **population**. The off-diagonal elements are called **coherences** and they are at the heart of many nonlinear and quantum optical phenomena including our very own nonlinear magneto-optical rotation (NMOR) [100].

Let us remember polarized atoms—*atoms described by the same wave function.* A visually easy but precise way to imagine polarized atoms, is the visualization of the probability of finding the maximum projection of the angular momentum of a polarized ensemble along a direction. The **angular-momentum probability surfaces**, as they are called, reveal the symmetry of the polarization state. This anisotropy **{I}** of the atomic states is caused by population differences and coherences between Zeeman sublevels. [53].

At this point we need to bring into the discussion the quantum beats and realize that here lies the essence of our idea: in the quantum-beats picture, the superposition of the Zeeman m_F states along the magnetic field is oscillating at a frequency Ω_L that we can directly measure. We would ideally build a magnetometer in a way that we have only one coherence oscillating at one frequency, because if we have more than one these will be different because of the NLZ effect. If an atom is prepared in the superposition of two m_F states and if these two states have different energies, then the superposition will evolve at a frequency corresponding to the energy difference between these two states divided by $\hbar$. We will then have only a *single alignment magnetic resonance* in a ground hyperfine state (in $F = 1$), corresponding to the transition between these m_F states. A magnetometer based on this resonance would be free from the NLZ-related splitting and asymmetry of the magnetic resonance curve, and thus would be intrinsically free from NLZ-related heading error.

5.3 Experiment

Let us make the basic idea behind our magnetometer concrete. The energies of the Zeeman sublevels are nonlinearly dependent on the magnetic field strength and so the frequency intervals between the Zeeman sublevels are unequal and the differences become bigger as the field increases—up to a certain field (see Section 5.1 for more).

As we mentioned before, if we pump with circularly polarized light we create orientation which is an asymmetric polarization surface on one half of the polarization axis and, if we pump with linearly polarized light, we create alignment, which creates a symmetric surface along the polarization axis (see Figure 3.10). For an orientation experiment, the coherences or populations will evolve between $\Delta m = 1$ Zeeman sublevels and for an experiment based on alignment they evolve between $\Delta m = 2$ Zeeman sublevels; remember here, that the sublevels are separated by unequal intervals due to the NLZ effect.

For the orientation experiment, in the $F = 2$ ($F = 1$) hyperfine state, there are four (two) different $\Delta m = 1$ magnetic resonance frequencies, which lead to asymmetric broadening or splitting of the

---

[I] Anisotropy is the quality of exhibiting properties with different values when measured along axes in different directions. [101]

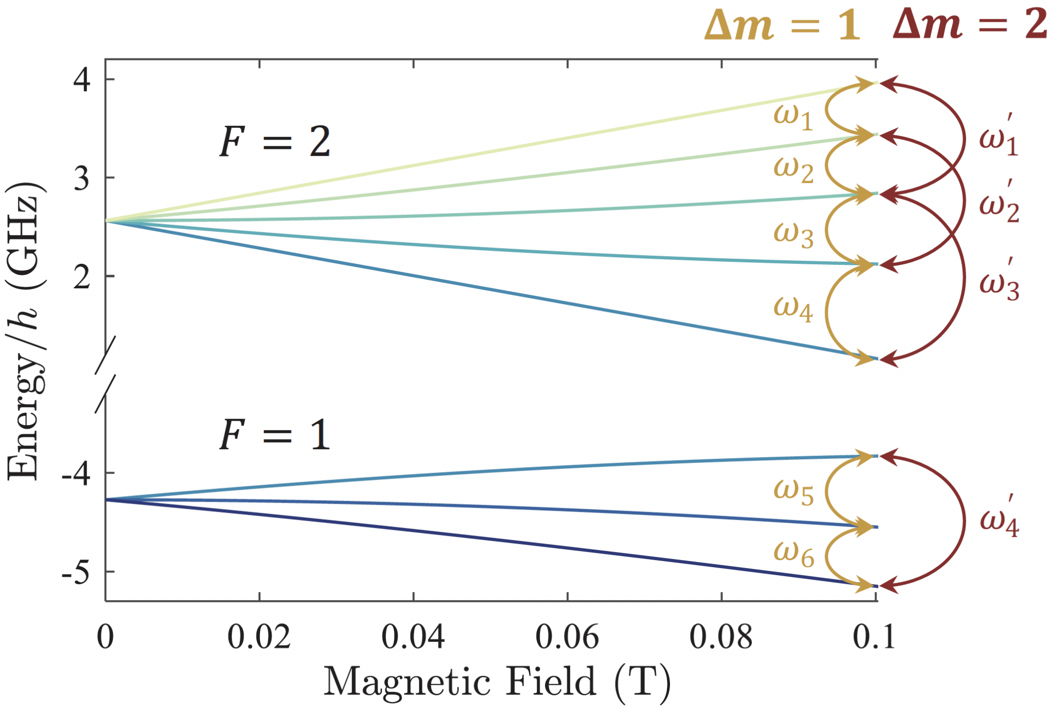

FIGURE 5.1: Schematic of NLZ-heading-error-free magnetometer. Nonlinear Zeeman effect of ^{87}Rb ground state $5^2\mathrm{S}_{1/2}$ and corresponding magnetic resonance frequencies. In the $F = 2$ ($F = 1$) hyperfine state, there are four (two) different $\Delta m = 1$ magnetic resonance frequencies, labelled with ω_1 to ω_4 (ω_5 to ω_6), respectively, and 3 (1) different $\Delta m = 2$ magnetic resonance frequencies, labelled ω_1' to ω_3' (ω_4'), respectively.

magnetic resonance curve when the background field is in the Earth-field range [94–96]. The populations and the matrix elements of the different Zeeman sublevels change with the magnetic field direction. This means that the amplitudes of the different components of the magnetic resonance change also with the magnetic field direction, which leads to the magnetic-field-direction-dependent asymmetry of the magnetic resonance and gives rise to heading errors [94–96]. In contrast to the $\Delta m = 1$ magnetic resonance in orientation, there is **only a single** $\Delta m = 2$ resonance in the $F = 1$ hyperfine state for alignment. This would mean that our resonance will have only *one peak* and is then by default free from heading error; Figure 5.1 explains visually this process.

5.3.1 Pumping and probing

An important parameter for the success of our experiment was the pump-probe scheme (illustrated in Figure 5.2) used to generate and respectively detect atomic polarization in the $F = 1$ hyperfine state. We pump with a 795 nm laser with a frequency resonant with the ^{87}Rb D1 transition ($5^2\mathrm{S}_{1/2}F = 2 \rightarrow 5^2\mathrm{P}_{1/2}F' = 2$) and we probe with a 780 nm laser light, red shifted about 0.5 GHz from the ^{87}Rb D2 transition $5^2\mathrm{S}_{1/2}F = 1 \rightarrow 5^2\mathrm{P}_{3/2}F' = 0$ transition.

In Figure 5.3 we show the spectrum of our pump and in Figure 5.4 the spectrum of our probe and it is noted where we pump and probe accordingly. The spectra show Bennett structures related to Doppler-free saturated absorption as well as Doppler-broadened resonances. Important note: these

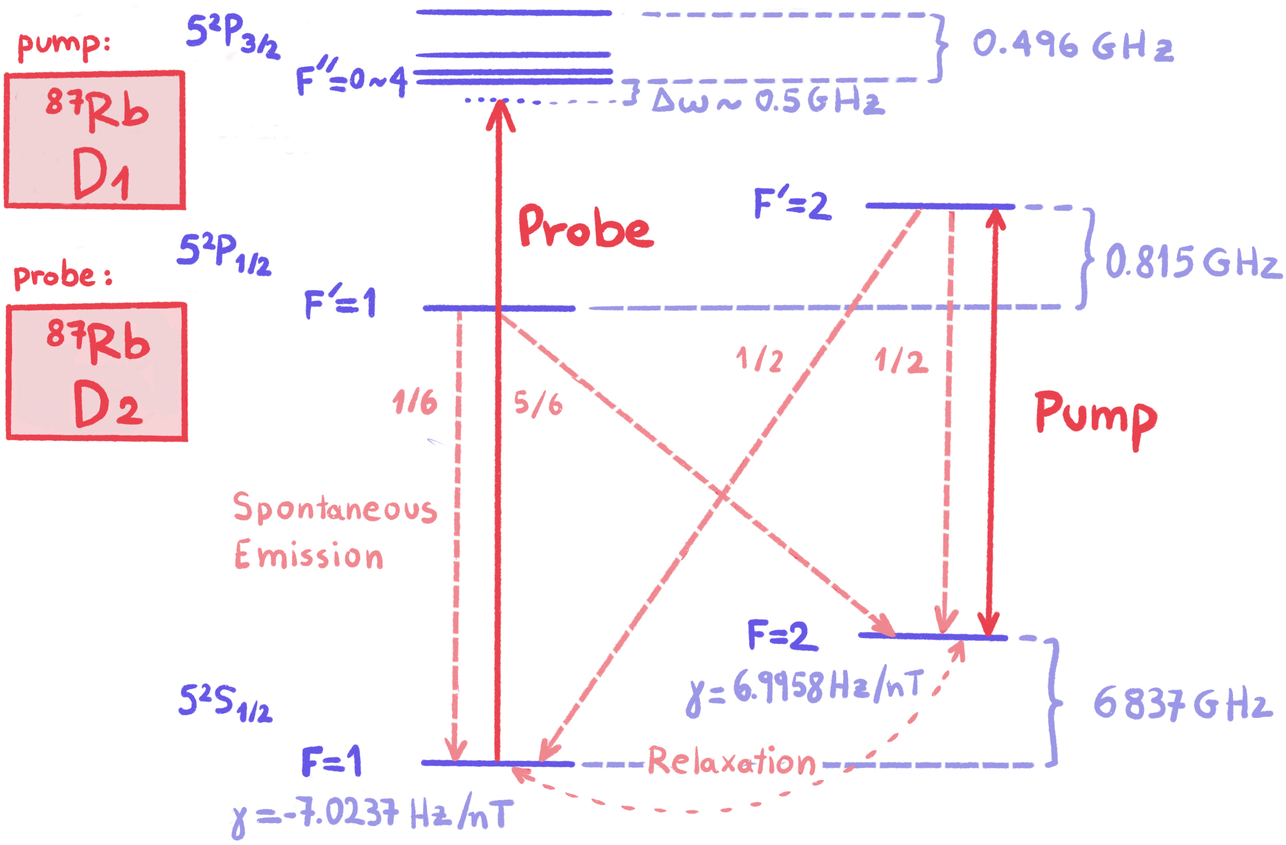

FIGURE 5.2: Pump and probe scheme of alignment magnetometer. Energy levels of ^{87}Rb atoms and excitation scheme (not to scale). Pump beam is a 795 nm laser beam exciting the $5^2\mathrm{S}_{1/2}F = 2$ to $5^2\mathrm{P}_{1/2}F' = 2$ transition, which generates atomic spin polarization in the $5^2\mathrm{S}_{1/2}F = 1$ state via repopulation pumping; the probe beam is a 780 nm laser tuned to the low frequency side relative to the $5^2\mathrm{S}_{1/2}F = 1$ to $5^2\mathrm{P}_{3/2}F'' = 0$ transition.

spectra are produced by a cell we call **reference cell** and it is different than the main cell we use for our experiments which produces the magnetic resonance and that contains only ^{87}Rb. We use the Doppler-free saturated absorption spectrum of the reference cells containing both ^{87}Rb and ^{85}Rb for stabilizing our laser frequencies.

Both lasers propagate along the leading magnetic field and quantization axis z and are linearly polarized along y, the same way as we explained in the example in 1.4.4. The pump beam generates atomic polarization in the $F = 1$ state via repopulation pumping [102] {I} (Figure 5.2) and the polarization is monitored by detecting optical rotation of the probe light.

In the Earth-field range, the difference between the $F = 1$ and $F = 2$ resonance frequencies is in the kHz range, see Figure 5.9. This frequency difference is much larger than the relaxation rate of the ground-state polarization and, as a result, the $F = 2$ state will not be trapped in the dark state and the pumping process is efficient. The pump and probe are resonant with transitions that start from

---

{I} In repopulation pumping a large fraction of the atoms is prepared in a coherent superposition of ground states non-coupled with the applied laser radiation ("dark state") [103]

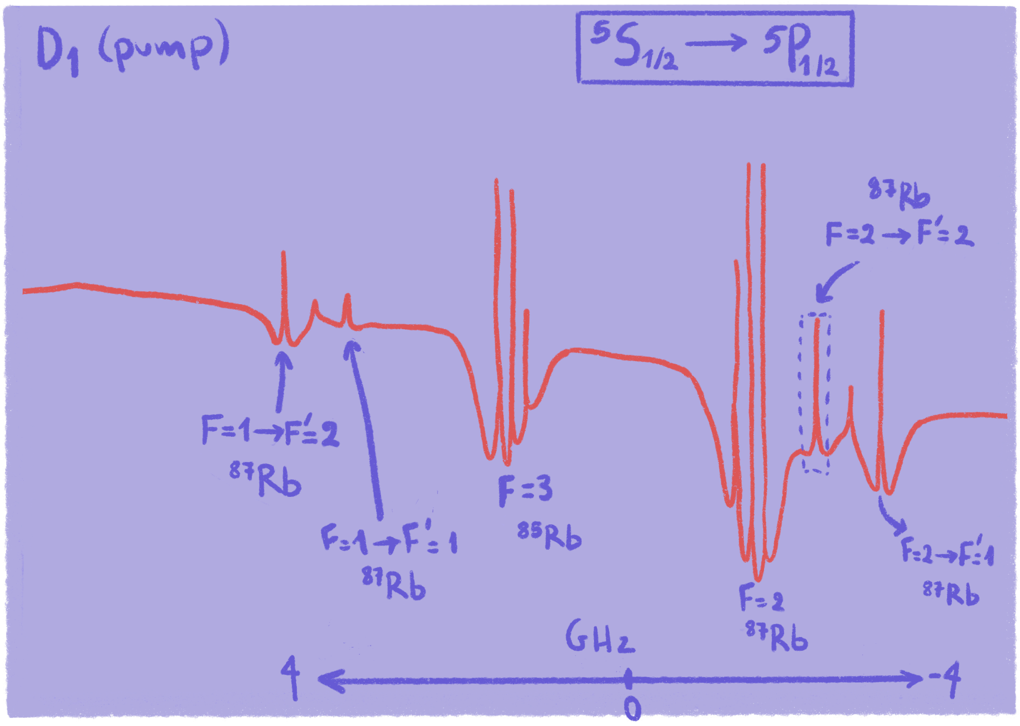

FIGURE 5.3: D1-line spectroscopy of rubidium. Frequency decreases from left to right. In the alignment-based magnetometer experiment the pump light is tuned to the line marked with a dashed box.

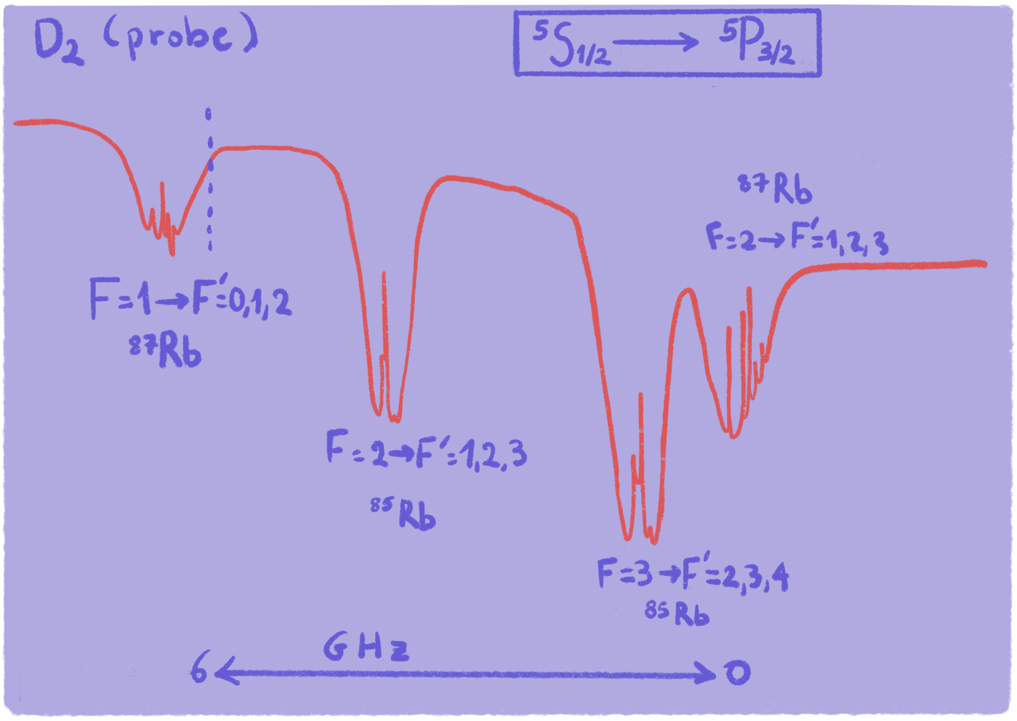

FIGURE 5.4: D2-line spectroscopy of rubidium. The dashed line indicates the probe tuning in the magnetometry experiment.

different ground hyperfine states, and as a result this technique constitutes indirect pumping, which does not cause power broadening of the magnetic resonance [104, 105].

In an NMOR magnetometer that uses circularly polarized light to pump, we modulate the pump light with the Larmor frequency (See Chapter 3). In our case, to produce a magnetic resonance, the pump beam is modulated at two times the Larmor frequency of the $F = 1$ hyperfine state. This interesting requirement can be explained by taking a look at the polarization surfaces.

5.3.2 q-fold symmetry

As already mentioned, by choosing the quantization axis along z, we are producing coherences, which correspond to non-diagonal density matrix elements $\rho_{n,m}$, where $n - m = q$ and the medium has *transverse polarization*. Remember, that each PM has the symmetry of a particular spherical harmonic. The q-th PM component has a q-fold symmetry, which means that when the angular-momentum probability surface is rotated by $2\pi/q$ around the polarization axis, it coincides with itself (see also *density matrix rotation* in [30]). When we pump with linear light, we get polarization with 2-fold symmetry around the light-polarization direction. We can easily understand this by looking at the polarization surfaces. In our case we would have a peanut shaped surface (quadrupole) polarized transverse to the magnetic field (and quantization axis). What kind of rotation around the field would make the surface turn back to its original state? That would be a rotation by $2\pi/q = \pi$, which corresponds to $q = 2$. It would therefore make sense to pump with light that is modulated at $2\Omega_L$.

The signal that we detect will be the optical rotation of the probe beam oscillating at this frequency and as a result we will need to demodulate it at $2\Omega_L$.

5.3.3 Apparatus

Our experimental arrangement is built in such a way that we can switch between an orientation and an alignment magnetometer. This way, we can use the exact same experimental conditions to compare the two resonances with regards to the NLZ effect and heading error.

The experimental arrangement for measuring the alignment magnetic resonance is shown in Figure 5.5 and for the orientation magnetic resonance in Figure 5.6.

The cylindrical anti-relaxation-coated atomic vapor **cell** has a diameter of about 4 cm and length of about 5 cm, filled with isotope-enriched ^{87}Rb.

For the **alignment magnetometer** both the pump and the probe beam are linearly polarized and propagate through the atomic vapor cell along the z direction. The pump beam is square-wave modulated with an AOM at $2\Omega_L$ with a duty cycle of 20%.

For the **orientation magnetometer** The pump (probe) beam is circularly (linearly) polarized and propagates through the atomic vapor cell along the y (x) direction. In this case, the pump beam is modulated at the Larmor frequency.

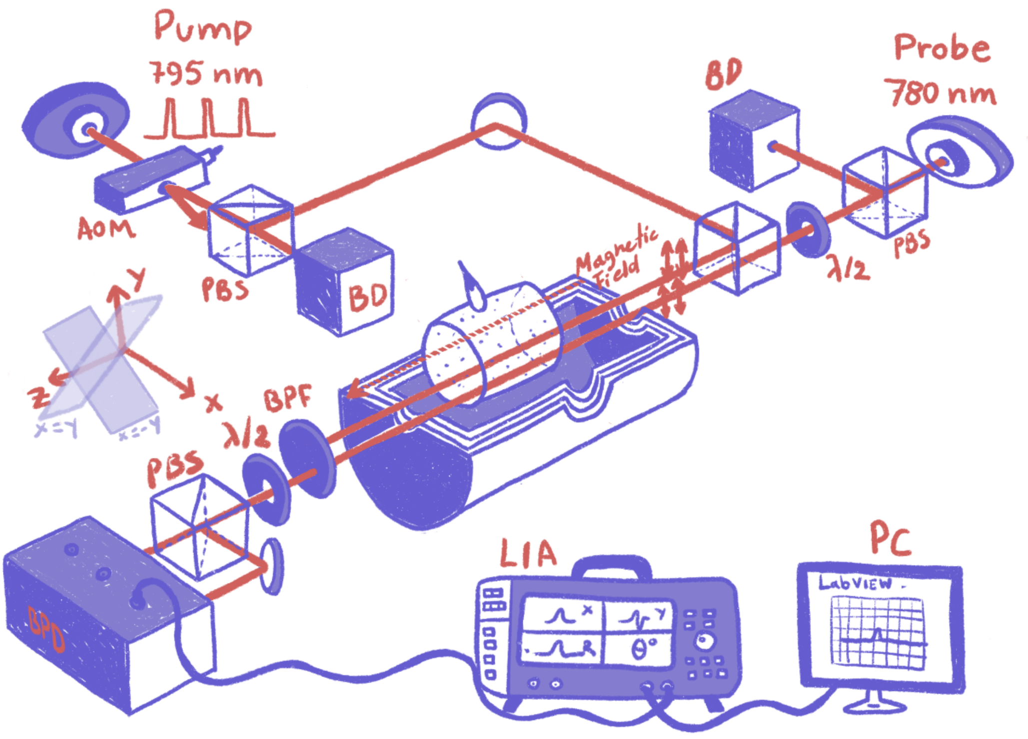

Figure 5.5: Alignment resonance setup. Pump, a linearly polarized 795 nm laser beam used to generate the atomic alignment polarization; Probe, a linearly polarized 780 nm laser beam used to detect the Larmor precession of the atomic alignment polarization via optical rotation; AOM, acousto-optic modulator used to pulse the pump beam; PBS, polarizing beam splitter; BS, beam splitter; $\lambda/2$, half-wave plate; $\lambda/4$, quater-wave plate; BPD, balanced photodiode; BPF, bandpass filter with central wavelength of 780 nm, which is used to prevent pump from entering the BPD; BD: beam damp; LIA, lock-in amplifier; PC, personal computer.

In order to maintain the consistency of experimental conditions, the two setups share the same vapor cell, shield, electronics and the pump and probe lasers. During the alignment or orientation experiment, only the corresponding pump and probe beams are allowed to pass through the vapor cell, while the other two beams are blocked.

The leading magnetic field is produced by applying current to the internal coil within the innermost magnetic shield. We used a Thorlabs current source with an accuracy of 0.1 mA. We detected resonances by scanning a small range around the modulation frequency and demodulating that signal at the modulation frequency by using a lock-in amplifier.

5.4 Comparison to an orientation magnetometer

5.4.1 Resonances

A comparison of the alignment and orientation magnetic resonances is shown in Figure 5.7 in which the background magnetic field is set along the z direction, with the field strength ranging from 20 μT to 50 μT (data are shifted vertically for clarity).

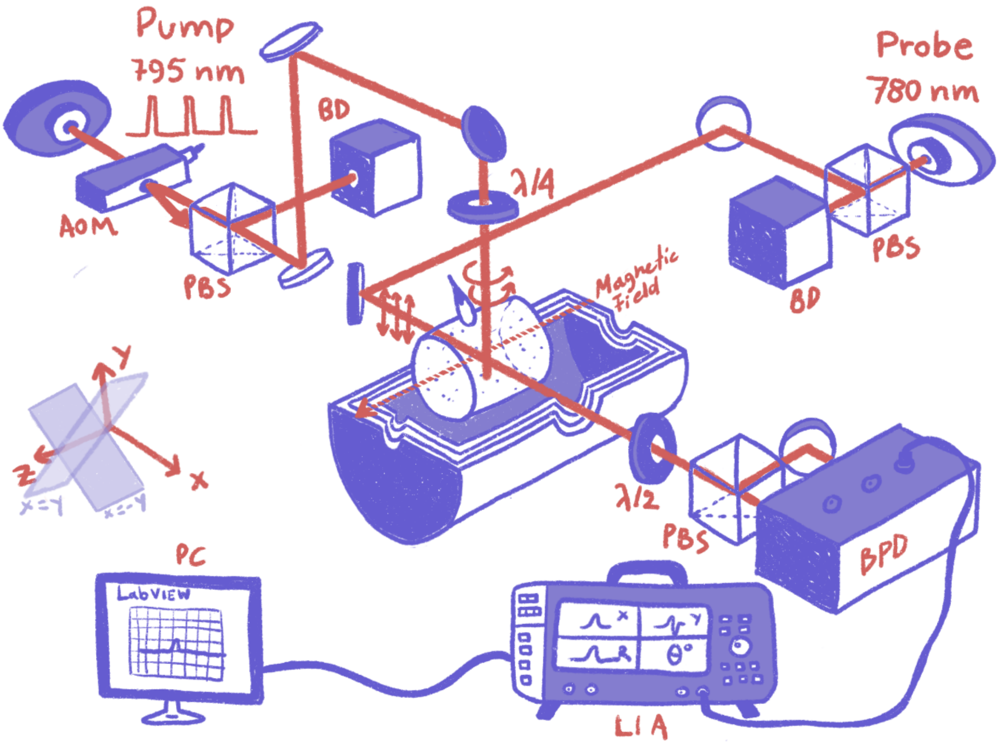

FIGURE 5.6: Orientation resonance setup. Pump, a circularly polarized 795 nm laser beam used to generate the atomic orientation polarization; Probe, a linearly polarized 780 nm laser beam used to detect the Larmor precession of the atomic orientation polarization via optical rotation; AOM, acousto-optic modulator used to pulse the pump beam; PBS, polarizing beam splitter; BS, beam splitter; $\lambda/2$, half-wave plate; $\lambda/4$, quater-wave plate; BPD, balanced photodiode; BPF, bandpass filter with central wavelength of 780 nm, which is used to prevent pump from entering the BPD; BD: beam damp; LIA, lock-in amplifier; PC, personal computer.

The time-averaged optical power of the pump and probe beam in the alignment (orientation) experiment is 100 μW (50 μW) and 300 μW (15 μW), respectively. These parameters were chosen to produce relatively strong signals with minimal power broadening of the magnetic resonances.

The shield is equipped with a $\partial B_z/\partial z$ gradient coil which was used to compensate the magnetic field gradient by connecting it to a Throlabs current source with an accuracy of 0.01 mA. The gradient was large enough to affect the resonance lines, but compensating only this first-order gradient was sufficient to make it low enough as to not affect the sensitivity.

5.4.2 Heading error

The alignment signal is always a single Lorentzian peak. Its central frequency at $2\omega_L$, corresponds to the $\Delta m = 2$ magnetic resonance between the $F = 1, m_F = -1$ and $F = 1, m_F = 1$ state. The orientation signal has always two peaks, corresponding to the $\Delta m = 1$ magnetic resonances between $F = 1, m_F = -1$ and $F = 1, m_F = 0$ and $F = 1, m_F = 1$ states and is split as the magnetic field increases. This result shows that our expectations of a NLZ-free alignment magnetic resonance

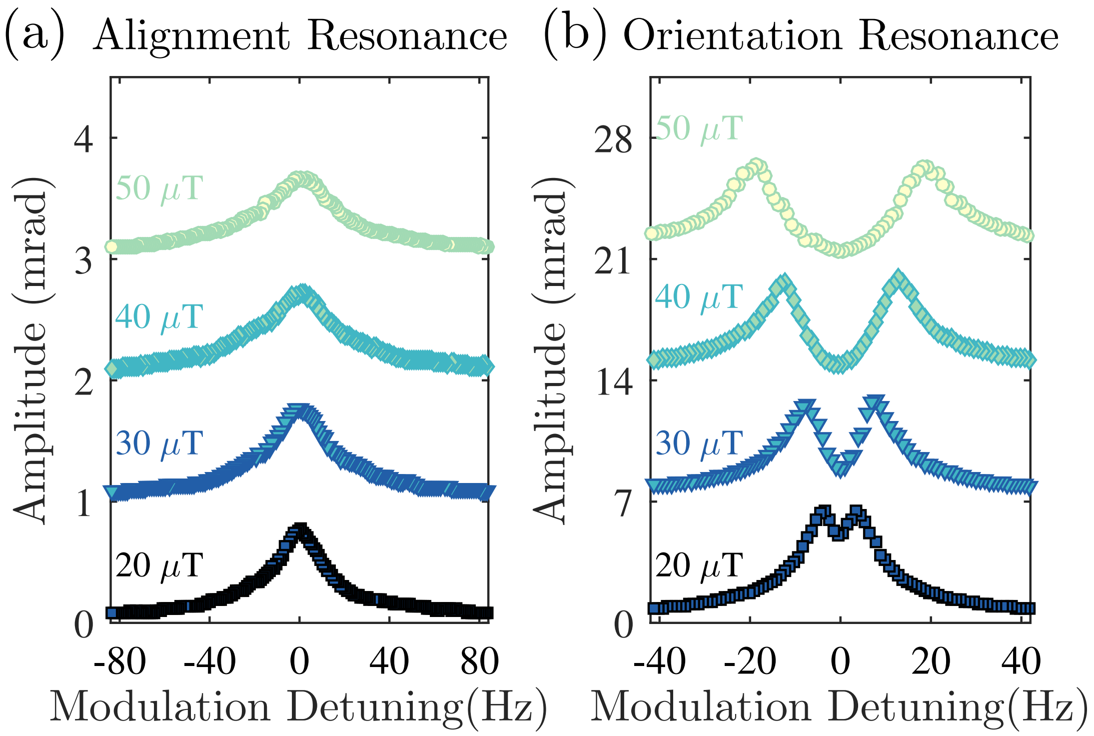

FIGURE 5.7: Magnetic resonances of alignment and orientation polarization with background magnetic field of different strengths. **(a)** Alignment resonance. **(b)** Orientation resonance. Background magnetic field is set along z direction, with strength ranging from $20\,\mu$T to $50\,\mu$T. Different magnetic resonances are shifted vertically for clarity. Since the alignment-resonance frequency is about twice that of orientation, the scale of detuning in (a) is also twice that of (b). The amplitude of the alignment signal is smaller than that of the orientation signal for the reasons explained in [25].

on Earth-field are confirmed. Both the alignment and the orientation resonances are broadened at stronger magnetic fields due to residual magnetic gradients.

In the geomagnetic field range, the estimated photon-shot-noise-limited sensitivities [106–110] of the alignment-based magnetometry are in the tens of fT/$\sqrt{\text{Hz}}$ range. Our best sensitivity is about $9\,$fT/$\sqrt{\text{Hz}}$ (See Section 5.4.3). When the background field gets larger, there is a degradation of the sensitivity. One possible reason for this is the increased magnetic field gradient, since image currents in the shields may not be perfectly symmetric and thus there are induced gradients from the coils and shields that scale with the applied magnetic field.

The magnetic-field-direction dependence of the alignment and orientation resonances is shown in Figure 5.8.

The magnetic field strength is kept at $30\,\mu$T and the angle between the field direction and the z axis is scanned in a 120 degrees range, during which we keep $B_x = B_y$ or $B_x = -B_y$, respectively. In that process, the magnetic field behaves as a vector rotated in a plane defined by the equation $x = y$ or $x = -y$, which contains the z axis and is 45 degrees from the x-z plane and the y-z plane, as shown in Figures 5.5 and 5.6 as light purple parallelograms nearing the coordinate system. When the field angle is 0 degree, the magnetic field is along the z axis.

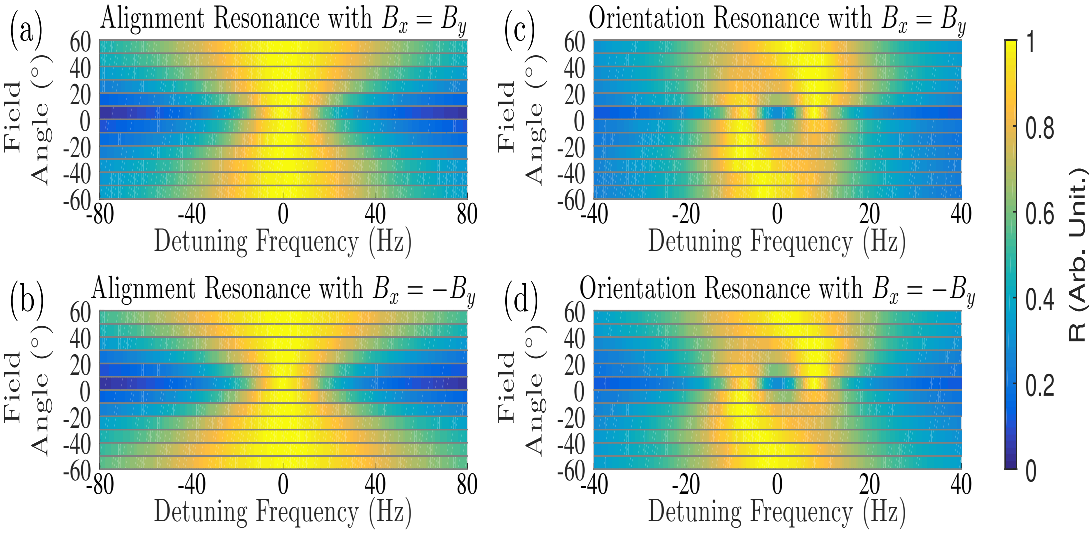

FIGURE 5.8: Magnetic resonances of alignment and orientation polarization with background magnetic field along different directions. **(a)** Alignment resonance with $B_x = B_y$. **(b)** Alignment resonance with $B_x = -B_y$. **(c)** Orientation resonance with $B_x = B_y$. **(d)** Orientation resonance with $B_x = -B_y$. The strength of the background magnetic field was kept at 30 μT. The angle between the background magnetic field and the z direction is represented as the vertical axis. The broadening of the magnetic resonances at larger field angle is due to the increased magnetic field gradients. Since this broadening does not affect our conclusion about resonance symmetry, and that the compensation of such gradients along different directions is complex, these gradients are not compensated during this experiment. Gradients are not compensated.

The relative heights of the two Lorentz peaks in the orientation magnetic resonance are dependent on the magnetic field direction, which leads to an asymmetry and a central-frequency shift of the magnetic resonance when the field is not along the z direction. This gives rise to the NLZ-related heading error. In contrast, the alignment resonance is always symmetric. This means that magnetometry based on this (alignment) resonance is free from the NLZ-related heading error. The broadening of both the orientation and the alignment magnetic resonance at a larger field angle is due to the increased magnetic gradient, as the x and y-directed magnetic field produced by the magnetic coil is less uniform than the z-directed magnetic field.

Another source of heading error comes from the different Larmor frequencies of the $F = 1$ and $F = 2$ ground hyperfine states (their difference is around 27.9 Hz/μT and lies in the kHz range in the geomagnetic field). The tails of the nearby $F = 2$ magnetic resonance change in size depending on the magnetic field direction and that introduces magnetic-field-direction-related error to the measurement of the $F = 1$ Larmor frequency. If we take a magnetic resonance at 20 μT for example, as shown in Figure 5.9, the $F = 1$ Larmor frequency can be determined from either the peak frequency of the demodulated X signal or the zero-crossing frequency of the demodulated Y signal. These frequencies, however, are shifted by the $F = 2$ resonance, because the X contribution from the $F = 2$ resonance leads to a sloping background and the Y contribution from the $F = 2$ resonance leads to a residual background at around the $F = 1$ resonance frequency. Since the efficiency of producing and detecting atomic spin polarization is dependent on the orientation of the pump/probe laser beam

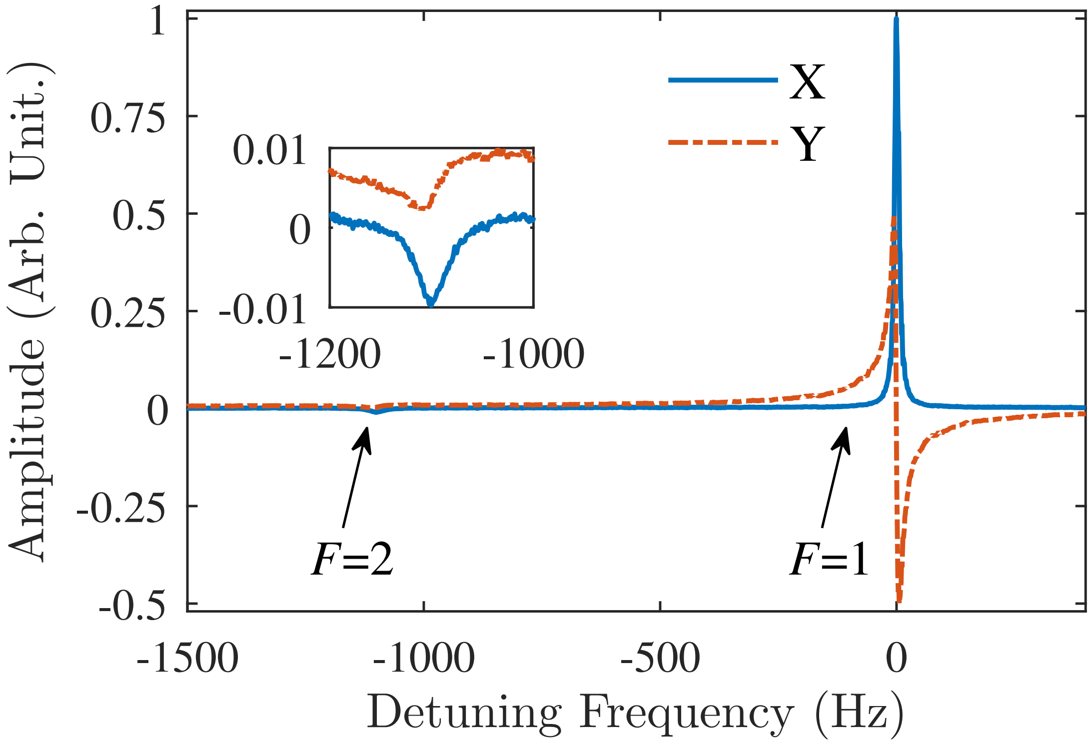

Figure 5.9: Typical $F = 1$ and $F = 2$ alignment magnetic resonance. Background magnetic field is set to 20 μT along the z direction. The insertion shows details about the $F = 2$ resonance. This magnetic resonance is averaged from four scans.

relative to the magnetic field, the amplitude of the $F = 2$ resonance depends on the field direction as well and thus leads to heading error. What we can do is reduce the relative amplitude of the $F = 2$ resonance because this way its tails will be also reduced around the $F = 1$ resonance and as a result the heading error. Due to the fully resolved ground hyperfine states in the buffer-gas-free antirelaxation-coated cell, the probe beam is far detuned from the transitions involving the undesired $5^2S_{1/2}\,F = 2$ hyperfine state, suppressing the amplitude of the $F = 2$ resonance to about 100 times more than that of the $F = 1$ resonance, as shown in Figure 5.9. Considering the large frequency difference between these two resonances, the influence from the $F = 2$ resonance on the $F = 1$ Larmor frequency only leads to heading error on the order of tens of fT.

The light shift due to the probe beam is also a source of heading error. When the background magnetic field is not aligned with the polarization of the probe beam, a linearly polarized (probe) beam can generally be viewed as three linearly polarized components. The one is the π component, a linearly polarized light whose polarization aligns with the magnetic field, given that the quantization axis is set along the background magnetic field. The other two consist of again linearly polarized light with its polarization perpendicular this time to the magnetic field, also viewed as a σ^+ and σ^- combination with equal strength. Because these two optical components are of equal strength, and their frequency detunings relative to the atomic transitions are almost the same, their light shifts on the $(F = 1)$ $m = -1$ and $m = 1$ states are almost identical. [111]. Since the alignment resonance frequency corresponds to the energy difference between the $(F = 1)$ $m = -1$ and $m = 1$ states the light shift of the alignment resonance is largely suppressed.

The frequency detuning of σ^+ and σ^- are slightly different, because of the Zeeman shift of the atomic transitions– σ^- and σ^+ have the same optical frequency, but the Zeeman effect leads to different atomic-transition frequencies, so they end up with a different detuning. As a result, there is still residual light shift due to the Zeeman-effect-related unbalanced detuning of optical transitions involving, respectively, the $(F = 1)$ $m = 1$ and $m = -1$ states, which is on the order of several pT, according to simulations based on the ADM package [112]. If the optical polarization of the probe beam is actively rotated to make it always perpendicular to the magnetic field, then the light shift will only lead to a constant bias, rather than a heading error. This method will also help to build a dead-zone-free magnetometer [113].

Finally, there is another effect that can lead to a systematic error in our magnetometric system. We use a 4-level system to pump and probe in which interference effects can arise: In such a system a resonance between two states can be affected by another resonance between two different states although the latter do not share common final or initial states with the first two states (See Figure 5.2) [114, 115]. In our case a coherence between the pump states will be transferred to the $F = 1$ ground state which eventually leads to a frequency shift of the $F = 1$ resonance.

The presence of such effects can be identified by measuring the heading error as a function of the light power (particularly, the pump power) and completely eliminated using a “free-decay” protocol, where atomic evolution occurs in the absence of applied light between pump and probe light pulses– or simpler, we measure the Larmor frequency while the pump and probe are off.

5.4.3 Estimation of NuZ-related Heading Error

As shown in Figure 5.9, the $F = 1$ resonance frequency at $20\,\mu$T can be determined from either the peak frequency of the demodulated X signal or the zero-crossing frequency of the demodulated Y signal. The peak frequency of X (zero-crossing frequency of Y), however, is also influenced by the $F = 2$ resonance, because the X (Y) contribution from the $F = 2$ leads to a sloping background (residual background) at around the $F = 1$ resonance frequency. Since the $F = 2$ resonance amplitude is influenced by the magnetic-field direction, this background is also magnetic-field-direction related and thus is a source of heading error. Assuming the contributions of $F = \alpha$ resonance (α=1 or 2) to the demodulated X and Y data have the Lorentzian form of

$$\begin{aligned} X_\alpha &= \mathrm{Re}\Big(\frac{A_\alpha \delta\nu_\alpha}{i(\nu_\alpha - \nu_\mathrm{m}) + \delta\nu_\alpha}\Big) = \frac{A_\alpha \delta\nu_\alpha^2}{(\nu_\alpha - \nu_\mathrm{m})^2 + \delta\nu_\alpha^2}\,, \\ Y_\alpha &= \mathrm{Im}\Big(\frac{A_\alpha \delta\nu_\alpha}{i(\nu_\alpha - \nu_\mathrm{m}) + \delta\nu_\alpha}\Big) = \frac{A_\alpha \delta\nu_\alpha(\nu_\alpha - \nu_\mathrm{m})}{(\nu_\alpha - \nu_\mathrm{m})^2 + \delta\nu_\alpha^2}\,, \end{aligned} \tag{5.1}$$

where A_α, ν_α and $\delta\nu_\alpha$ are the amplitude, central frequency and the half width at half maximum (HWHM) linewidth of the $F = \alpha$ resonance, while ν_m is the modulation frequency of the pump beam. [I]

The presence of the X_2 and Y_2 terms lead to a shift of the effective central frequency of the magnetic resonance around ν_1.

Taking the X signal as an example, the effective peak frequency is the modulation frequency ν_m at around ν_1 which leads to a zero slope of the overall X signal, e.g.,

$$\left(\frac{\partial X_1}{\partial \nu_\mathrm{m}} + \frac{\partial X_2}{\partial \nu_\mathrm{m}}\right)\Big|_{\nu_\mathrm{m}\sim\nu_1} = 0\,. \tag{5.2}$$

According to Eq. (5.1), the slopes of the X_1 and X_2 measured data close to the resonance, i.e., $\nu_1 = \nu_\mathrm{m}$, have the form of

$$\begin{aligned}\frac{\partial X_1}{\partial \nu_\mathrm{m}}\Big|_{\nu_\mathrm{m}\sim\nu_1} &\approx \frac{2A_1(\nu_1-\nu_\mathrm{m})}{\delta\nu_1^2}\,,\\ \frac{\partial X_2}{\partial \nu_\mathrm{m}}\Big|_{\nu_\mathrm{m}\sim\nu_1} &\approx \frac{2A_2\delta\nu_2^2}{(\nu_2-\nu_1)^3}\,,\end{aligned} \tag{5.3}$$

so the shift of the peak frequency of X is

$$\Delta\nu_{1X} \approx \frac{A_2\delta\nu_1^2\delta\nu_2^2}{A_1(\nu_2-\nu_1)^3}\,. \tag{5.4}$$

As for the Y signal, the effective zero-crossing frequency is the modulation frequency ν_m at around ν_1 which leads to a zero value of the overall Y signal, e.g.,

$$(Y_1 + Y_2)\big|_{\nu_\mathrm{m}\sim\nu_1} = 0\,. \tag{5.5}$$

According to Eq. (5.1), the Y_1 and Y_2 data in the vicinity of the resonance, i.e., $\nu_1 = \nu_\mathrm{m}$, have the form of

$$\begin{aligned}Y_1\Big|_{\nu_\mathrm{m}\sim\nu_1} &\approx \frac{A_1(\nu_1-\nu_\mathrm{m})}{\delta\nu_1}\,,\\ Y_2\Big|_{\nu_\mathrm{m}\sim\nu_1} &\approx \frac{A_2\delta\nu_2}{(\nu_1-\nu_2)}\,,\end{aligned} \tag{5.6}$$

so the shift of the zero-crossing frequency of Y is

$$\Delta\nu_{1Y} \approx \frac{A_2\delta\nu_1\delta\nu_2}{A_1(\nu_2-\nu_1)}\,. \tag{5.7}$$

[I] Note that the lineshape for the Y_2 case is not perfectly dispersive in practice as seen in Figure 5.9; One possible reason is that the measured Y_2 is a combination of a dispersive curve and an absorptive curve. When the modulation frequency is far detuned, the dispersive (absorptive) curve scales as 1/*detuning* (1/*detuning*^{2}). Because the absorptive component decreases much faster with larger detuning than the dispersive component, the far-detuned behavior of the Y_2 will be dominated by its dispersive component. Hence, it is safe to use inverse-detuning scaling to estimate the upper limits on the $F = 1$ resonance shift, even though in practice Y_2 is not ideally dispersive.

5.5 Sensitivity

The sensitivity of an optically pumped magnetometer is limited by two fundamental quantum noises: **the spin-projection noise**–in measuring the pointing angle of the atomic spins and **the photon shot noise**–in measuring the polarization angle of the probe beam [19]. The spin-projection-noise-limited sensitivity measured in noise spectral density is given by [108, 116]

$$\delta B \approx \frac{1}{\gamma_1\sqrt{2F}}\frac{1}{\sqrt{N\tau_2}}\,, \tag{5.8}$$

where $\gamma_1 \approx -7\,\mathrm{Hz/nT}$ is the gyromagnetic ratio of the $F = 1$ ground state, $F = 1$ is the total angular momentum of the system, N is the atoms in the vapor cell and τ_2 is the lifetime of the atomic polarization. Given that the atoms N are $\approx 9 \times 10^{10}$ in room temperature in a vapor cell with a radius of 4 cm and a length of 5 cm and τ_2 about tens of ms, the spin-projection-noise-limited sensitivity is in the $\mathrm{fT}/\sqrt{\mathrm{Hz}}$ range, which is one or two orders of magnitude smaller than the photon-shot-noise limited sensitivity of our current setup. As a result, we focus on the photon-shot-noise limited sensitivity, as shown below.

The photon-shot-noise limited sensitivity of an optical-rotation-based magnetometer is given by [106, 107]

$$\delta B \approx \Big(\frac{\partial\phi}{\partial B}\Big|_{\nu_\mathrm{m}=\kappa\gamma_1 B}\Big)^{-1}\delta\phi\,, \tag{5.9}$$

where ϕ is the optical rotation amplitude of the probe beam and is a function of B (magnetic field) and ν_m (modulation frequency of the pump beam), κ is the rank of atomic polarization (2 for alignment), $\gamma_1 \approx -7\,\mathrm{Hz/nT}$ is the gyromagnetic ratio of the $F = 1$ ground state, $\partial\phi/\partial B|_{\nu_\mathrm{m}=\kappa\gamma_1 B}$ is the resonant slope of ϕ with respect to the magnetic field B, which could be read from the Y component of the magnetic resonance, and $\delta\phi$ is the sensitivity to the optical rotation angle of the probe beam, measured in $\mathrm{rad}/\sqrt{\mathrm{Hz}}$.

In the present magnetic resonance scanning, we scan the modulation frequency of the pump beam ν_m rather than the magnetic field B. As a result, $\partial\phi/\partial\nu_\mathrm{m}|_{\nu_\mathrm{m}=\kappa\gamma_1 B}$ can be directly measured from the magnetic-resonance data. Considering the relation $\phi(B,\nu_\mathrm{m}) = \phi(B+\Delta B, \nu_\mathrm{m}+\kappa\gamma_1\Delta B)$ when $\Delta B \ll B$, which indicates

$$\begin{aligned}\frac{\partial\phi}{\partial B} &= \lim_{\Delta B\to 0}\frac{\phi(B+\Delta B,\nu_\mathrm{m})-\phi(B,\nu_\mathrm{m})}{\Delta B}\\ &= \lim_{\Delta B\to 0}\kappa\gamma_1\frac{\phi(B,\nu_\mathrm{m}-\kappa\gamma_1\Delta B)-\phi(B,\nu_\mathrm{m})}{\kappa\gamma_1\Delta B}\\ &= -\kappa\gamma_1\frac{\partial\phi}{\partial\nu_\mathrm{m}}\,,\end{aligned} \tag{5.10}$$

we have

$$\begin{aligned}\frac{\partial\phi}{\partial B}\Big|_{\nu_\mathrm{m}=\kappa\gamma_1 B} &= -\kappa\gamma_1\frac{\partial\phi}{\partial\nu_\mathrm{m}}\Big|_{\nu_\mathrm{m}=\kappa\gamma_1 B}\\ &= -\kappa\gamma_1\frac{A}{\delta\nu} = 2\pi\tau_2 A|\gamma_1|\,,\end{aligned} \tag{5.11}$$

where A is the optical rotation amplitude on resonance, $\delta\nu$ is HWHM linewidth of the resonance, and $\tau_2 = \kappa/(2\pi\delta\nu)$ is the lifetime of the atomic polarization. Now, the sensitivity is given by

$$\delta B \approx \frac{\delta\phi}{2\pi\tau_2 A|\gamma_1|}\,. \tag{5.12}$$

The photon-shot-noise-limited angular sensitivity $\delta\phi$ is estimated to be $1/\sqrt{P}$ [106], where P is the photon flux entering the polarimeter. In the present experiment, the power of the 780 nm probe beam entering the vapor cell is about 300 μW, and about one third of it is gathered with the polarimeter. Considering that the energy of a photon with wavelength of 780 nm is about 2.55×10^{-19} J, a 100 μW optical power gathered with the polarimeter means that there are about 3.9×10^{14} photons entering the polarimeter per second, or photon flux $P\approx3.9\times10^{14}\,\mathrm{s}^{-1}$. So $\delta\phi$ is about $5.1\times10^{-8}\,\mathrm{rad}/\sqrt{\mathrm{Hz}}$.

The estimated photon-shot-noise-limited sensitivities of the alignment magnetometry as a function of magnetic field strengths are shown in Figure 5.10(a), with the field kept along the z direction.

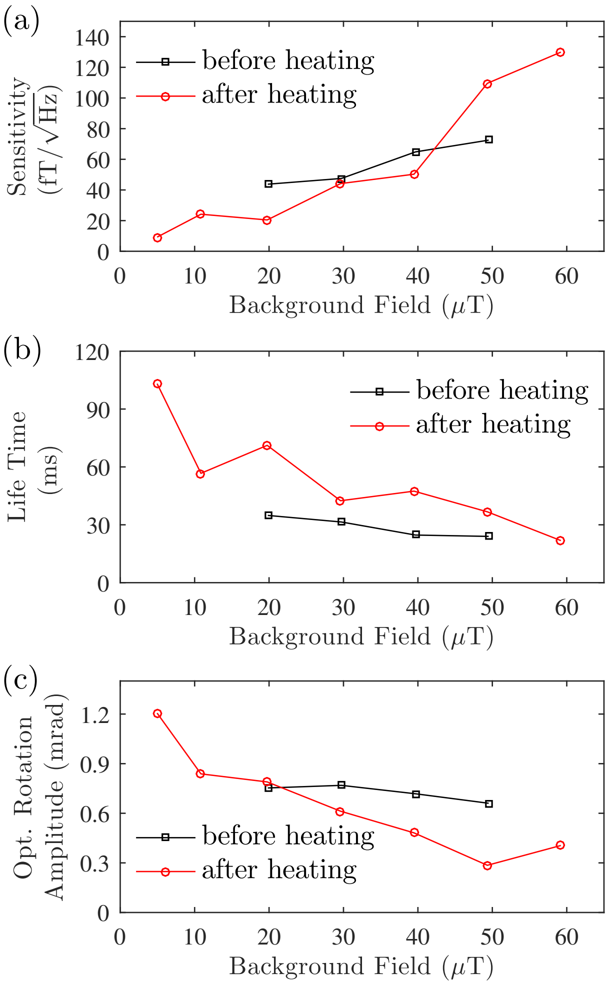

FIGURE 5.10: **(a)** Photon-shot-noise-limited sensitivity, **(b)** Life time and **(c)** optical rotation amplitude of alignment-based magnetometry as a function of background magnetic field. The background magnetic fields are kept along the z direction. The black squares (red circles) represent data taken before (after) vapor cell heating.

We present two sets of results, one of which is measured before the vapor cell heating, and the other is measured after the heating, during which the vapor cell body was heated to about 60 °C for several hours and the cell stem was kept as the coldest place of the cell. The sensitivities are in the tens of $\mathrm{fT}/\sqrt{\mathrm{Hz}}$ range, with the best sensitivity reaching about $9\,\mathrm{fT}/\sqrt{\mathrm{Hz}}$. Generally, the sensitivities degrade with the increased background field. This is possibly due to the increased magnetic field gradient, which in turn decreases the lifetime and amplitude of atomic polarization and thus the optical rotation amplitude, as shown in Figure 5.10(b) and (c). The overall performance of the magnetometer is improved after heating, which is due to the increased spin lifetime [117]. These results suggest that such an alignment resonance is promising for highly sensitive magnetometry in the geomagnetic field range.

To achieve shot-noise-limited sensitivity in practice, there are some technical issues to tackle. The first one is magnetic field fluctuations, which may be much larger than the shot-noise-limited sensitivity. In the geomagnetic field range (5×10^{-4} T level), a sensitivity for 1 Hz bandwidth of about 10 fT (10^{-14} T) means that the relative noise of the magnetic field should be about 2×10^{-10}, which is beyond the stability of commercial current sources (we use current sources to drive magnetic coils and generate magnetic field). It is possible to achieve such sensitivity in the geomagnetic field range in differential measurements by subtracting the common-mode signal or by actively stabilizing the magnetic field with atomic magnetometers [118]. Besides, one should make sure that the contributions from electronic noise of the detector and technical noise due to laser frequency/power fluctuations to the measured optical rotation noise is smaller than that of shot noise. Careful optimization of detectors, lasers, and experimental parameters including optical power and demodulation frequency are needed for this purpose [109, 110].

5.6 Conclusions

In conclusion, we have demonstrated a sensitive scalar magnetometer free from NLZ related heading error in the Earth-field range. This magnetometer is based on the $\Delta m = 2$ magnetic resonance in the ^{87}Rb $F = 1$ ground hyperfine state. In contrast to conventional alkali-metal magnetometry, where the magnetic resonance curve is split and distorted in the Earth field, the magnetic resonance demonstrated here is only a single Lorentzian peak, which is thus free from NLZ induced splitting and asymmetry. For our magnetometer, the photon-shot-noise limited sensitivity reaches tens of $\mathrm{fT}/\sqrt{\mathrm{Hz}}$ in the Earth field range, with the vapor cell at the room temperature. The sensitivity could be further improved by heating the cell to increase the atomic vapor density [117]. This scheme is also effective at suppressing the heading error due to the NuZ and LS effects. Due to the fully resolved ground hyperfine states in the antirelaxation-coated cell, the residual signal from $F = 2$ is relatively small and thus its influence is at most at the tens of fT level, which is on the limit of the sensitivity of this magnetometer. Moreover, as there is only linearly polarized light used in this magnetometer, it is free from the vector light shift [111], which is another possible source of heading error[I]. Considering that the remaining tensor light shift will not change the frequency difference

---

[I] Although, cells can have birefringent windows which induce elliptical polarization of the light and thereby accidentally cause nominally linearly polarized light to generate vector light shifts [119] between $m = \pm 1$ magnetic sublevels in the ground $F = 1$ system, i.e., the central frequency of the desired $\Delta m = 2$ magnetic resonance, this scheme is promising for more accurate magnetometry. It should be noted that the magnetic resonance frequency itself still has cubic correction in the strength of the magnetic field. Finally, a similar method can be implemented with other alkali metals that have a $F = 1$ ground level, such as ^{39}K, ^{41}K and ^{23}Na.

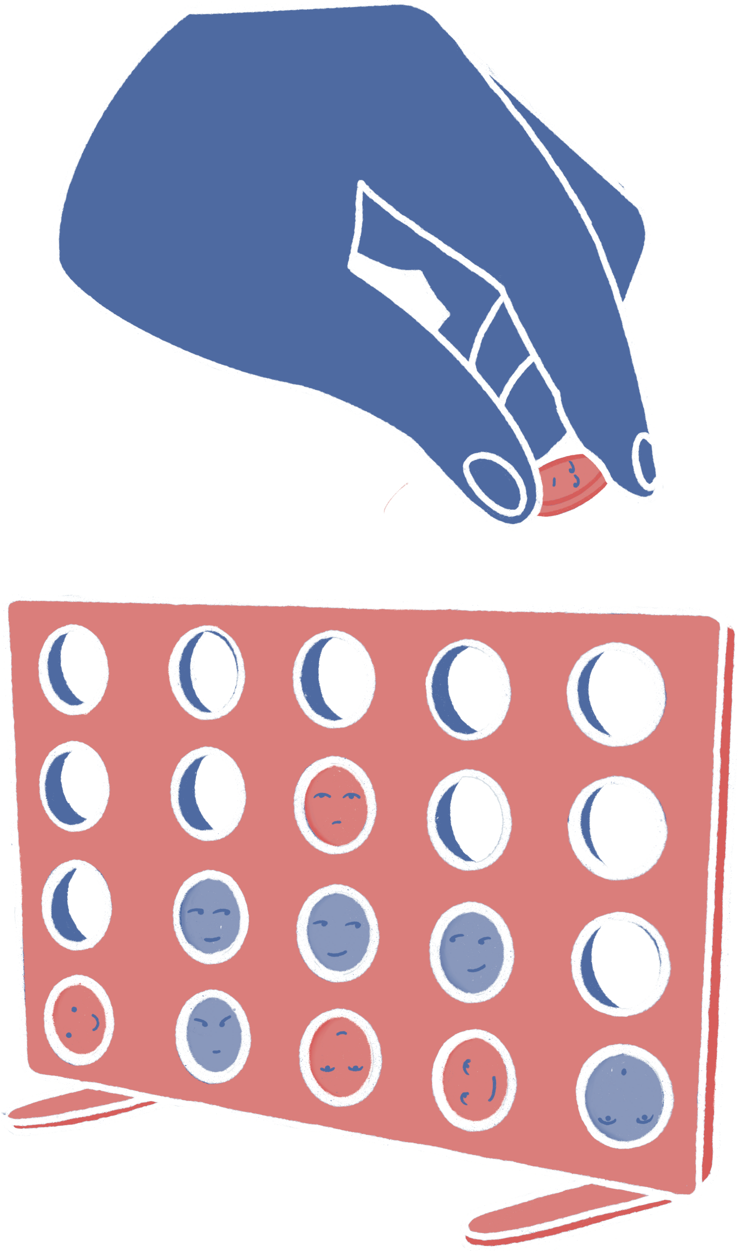

Instead of obtaining a mirror,
Obtain a person.
Look into him.
Use different people.
Old, young, fat, small, etc.

Mirror Piece, Yoko Ono

6

Degenerate mirrorless lasing–Forward beam

Some of the text presented in this section is part of a paper that has been published as [120] and [49]. For the work presented in this Chapter, I build upon the idea conceived by Prof. D. Budker and Aram Papoyan in Ref. [120]. I constructed part of the setup needed for the experiment in Mainz together with Guzhi Bao. I took part of the data and analyzed them and together with the rest of the co-authors, I co-wrote and edited the manuscript.

6.1 The idea

Until now, the focus of our work has been on nonlinear magneto-optical rotation, or else, nonlinear Faraday rotation. We have extensively talked about this phenomenon and studied it in Chapters 2, 4 and 5. In the last two Chapters of this thesis we will discuss about another nonlinear phenomenon called mirrorless lasing, broadly defined here as directed monochromatic emission from an ensemble of atoms or molecules excited with pump laser light.

In the cases studied throughout my thesis so far, the pump beam was never polarized parallel to the transverse magnetic field. This is intuitively understood, because in the case where the laser field **E** with wave vector **k** is polarized parallel to the transverse magnetic field ($\mathbf{E} \parallel \mathbf{B}$, $\mathbf{B} \perp \mathbf{k}$) [121], there is no Larmor precession of polarized atoms around the magnetic field, since they would all be polarized along the magnetic field. This seems, at first sight, to eliminate any possibility to generate narrow lines and thus makes such a configuration unattractive for spectroscopic studies.

Nevertheless, narrow magnetic resonances with high signal-to-noise ratio may arise due to coherence effects related to partial **inversion of population**. This can happen on transitions between magnetic sublevels belonging to the excited and ground-state levels under intense excitation by linearly polarized light of cycling transitions of an alkali-atom D_2 line ($F_e > F_g$) [122, 123].

In this project, we observed narrow, high-contrast, magneto-optical resonances, when irradiating a Rb cell with a single laser beam under specific conditions: it is a continuous wave single-mode linearly polarized laser beam at relatively high intensity, with its frequency tuned to the $^{85}\mathrm{Rb}$ $F_g{=}3 \rightarrow F_e{=}4$ or $^{87}\mathrm{Rb}$ $F_g{=}2 \rightarrow F_e{=}3$ transitions of the D_2 line.

The magnitude and width of the resonances exhibit a strong nonlinear dependence on the laser-light intensity and on the magnetic field, as well as a sub-natural linewidth. We called this observation *mirrorless lasing* since the detected beam exhibits characteristics similar to a laser beam, but with a single beam-pass through the cell/medium and of course without any mirrors existing to add to the stimulated emission.

The results of this work were the fruits of our collaboration with the Institute for Physical Research, NAS of Armenia, Ashtarak. for a clear overview of the experiment I will present in Chapters 6 and 7 the Sections into parts based on the experiments conducted in Mainz and Ashtarak respectively.

6.2 The Mechanism

Section 2.4.3 introduced the basic theoretical framework for mirrorless lasers. There are a few papers that deal with the phenomenon experimentally and motivated our own project. In [122, 123] it was demonstrated that interaction of linearly polarized light with an $F_e > F_g$ cycling D_2 transition of alkali atoms may result in amplified radiation between certain Zeeman sublevels, as shown in the illustration in Figure 6.1. This amplification occurs at intensities of light above $\sim 20\,\mathrm{mW/cm}^2$ in a steady-state regime, due to redistribution of population towards $m_F = 0$ [124, 125], which results in population inversion on $|m_{F_e}| = n \rightarrow |m_{F_g}| = n + 1$, where n is a natural number.

The population inversion has a strongly nonlinear dependence on the light intensity: above a threshold, the inversion increases reaching saturation followed by a decline. For $B = 0$ and *linearly* polarized pump light, there appears **optical gain** for polarization *orthogonal* to that of the pump light in the forward and backward directions [122]. When we apply an external magnetic field, this should influence the redistribution of population and the onset of population inversion.

Since we want to detect magnetic-field-induced changes in transmitted light due to gain, we need an environment that is very well magnetically shielded and a measurement which is not affected by other magneto-optical effects. For this reason, we chose the external magnetic field that will be applied to test our theory to be parallel to the laser field $\mathbf{B} \parallel \mathbf{E}$ and perpendicular to its direction $\mathbf{k}$. In this case, there is no optical rotation or ellipticity associated with the Faraday or Voigt effects [121].

In order to confirm our expectation that such a system can indeed produce an inversion of population, we used the Atomic Density Matrix (ADM) package [112]. We calculated, using a simple model, that

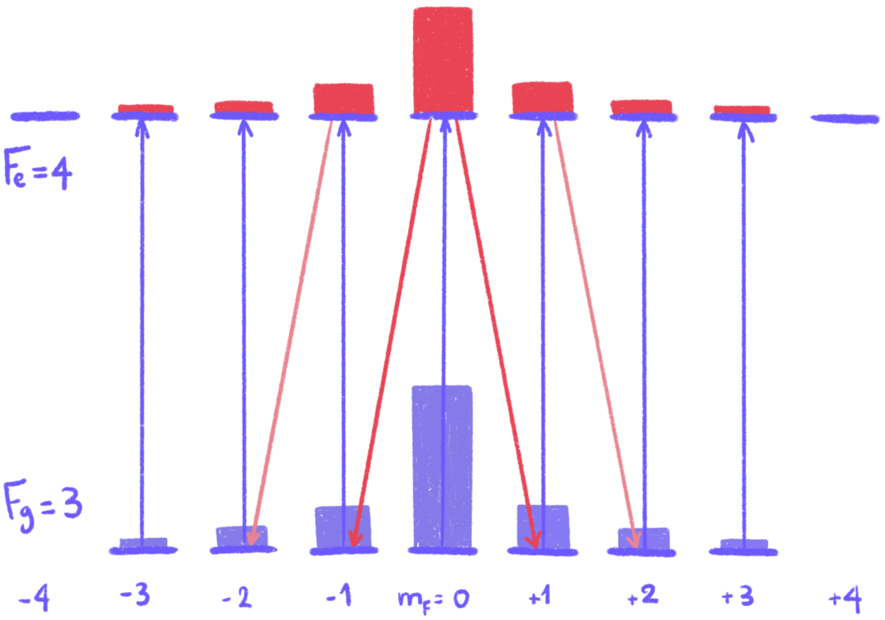

FIGURE 6.1: Inversion of population between magnetic sublevels. Onset of population inversion and amplified radiation corresponding to $\Delta m_F = \pm 1$ transitions under excitation of ^{85}Rb D_2 line with an intense linearly polarized laser radiation for zero magnetic field (the quantization axis Z is chosen to be along the laser light polarization). Bars: population of sublevels (not to scale). Red corresponds to population of excited states and purple population of ground states.

a magnetic field applied along the linear polarization of a laser beam establishes population inversion. We observe that the steady-state populations of particular Zeeman sublevels, when excited with linearly polarized light, depend on the magnetic field that is applied (when $\mathbf{B} \parallel \mathbf{E}$). For that, we calculated the steady-state solution of the Liouville equation for different transitions.

The results of the calculations of magnetic field dependencies of steady-state populations for different ground and excited state sublevels are shown in Figure 7.2.

Magnetic field dependencies of steady-state populations for the ground state sublevels (m_{Fg}) and excited state sublevels (m_{Fe}) of the "cycling" transitions F_g=3 → F_e=4 (^{85}Rb) and F_g=2 → F_e=3 (^{87}Rb) of the rubidium D_2 line ($5S_{1/2} \rightarrow 5P_{3/2}$), under excitation with linearly-polarized radiation with $S = 100$, are presented in Figure 7.2a and Figure 7.2b, respectively. S is the saturation parameter defined as:

$$S = \frac{|\Omega|^2}{\Gamma^2/4 + \delta^2}\,, \tag{6.1}$$

where Ω is the effective Rabi frequency, δ is the detuning from resonance, and Γ is the radiative decay rate.

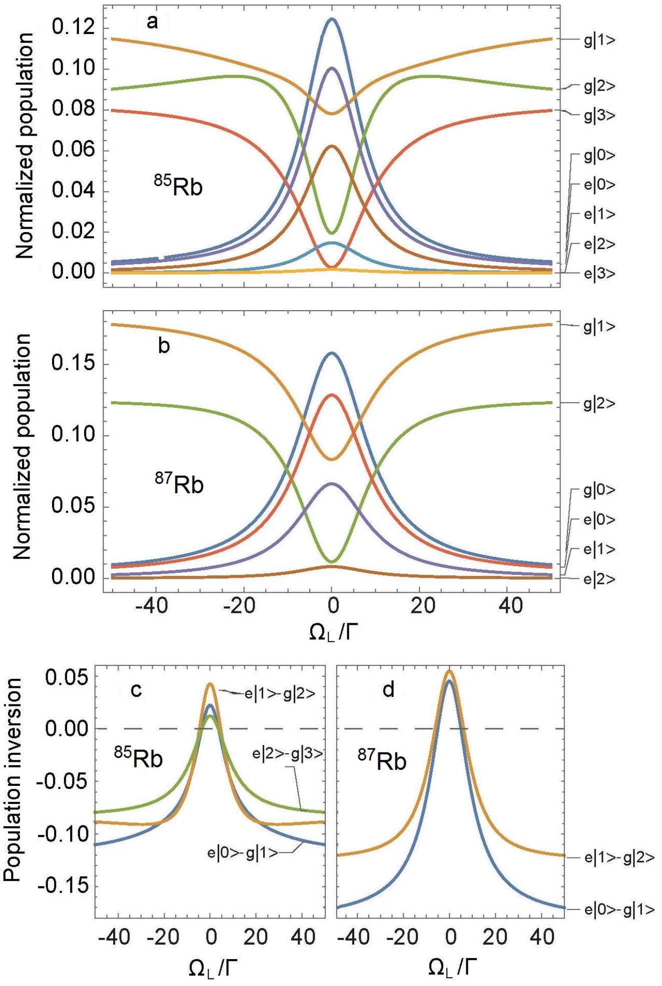

FIGURE 6.2: Numerical simulations with the ADM package for inversion of populations: **B** $\parallel$ **E** magnetic-field dependence of normalized steady state population of ground state ($g|m_{F_g}>$) and excited state ($e|m_{F_e}>$) Zeeman sublevels linked by $\Delta m_F = 0$ transitions ^{85}Rb F_g=3 $\rightarrow$ F_e=4 (a) and ^{87}Rb F_g=2 $\rightarrow$ F_e=3 (b), and population inversion on corresponding $m_{F_e} \rightarrow m_{F_g}$ transitions (c,d). The light power is sufficient to provide population inversion. Γ is the decay rate of excited state, Ω_L is the Larmor frequency. The width of the resonance is not affected by the ground state relaxation rate included in the model, which is much smaller than Γ.

The two axes of the simulated graph are: the population inversion versus the magnetic field, which is expressed in Ω_L/Γ normalized Larmor frequency units—$\Omega_L = g_F \mu_B B/\hbar$, g_F is a Landé factor, μ_B is the Bohr magneton, and B is the magnetic field strength—is shown in Figure 7.2c,d. The population inversion is practically calculated by the difference between the population of an excited m_F state and the population of a ground m_F state.

We can see from the simulation that population inversion establishes at zero magnetic field; it is stronger for the ^{87}Rb F_g=2 $\rightarrow$ F_e=3 transition. Application of a magnetic field corresponding to $\Omega_L/\Gamma \approx 5-10$ eliminates the population inversion.

An important point to note here is that we calculated population inversion but *not* gain. The model predicts a bigger population at the 0 excited level than in the -1 and +1 of the ground state which would create y linearly polarized light (orthogonal to the x polarized incoming light). However, we did not take into account the absorption of the ground-state populations to the excited states. This means that we might have population inversion, but no gain and this is very important to actually see amplification of our inputing light.

Below, we present experimental data which indicate that, in this system, a number of different nonlinear-optical effects take place, including degenerate four-wave mixing and mirrorless lasing. The latter is a particularly interesting case because, in contrast to most other works on cw mirrorless lasing in alkali atoms (see [126, 127] and references therein), in the our case lasing occurs at the same wavelength as optical pumping. The only feature that is different between the pump beam and the lasing beam is the polarization, that is why we call this effect **entirely degenerate mirrorless lasing**.

6.3 Evidence for degenerate mirrorless lasing in alkali metal vapor: forward beam magneto-optical experiment

6.3.1 Technique

This experiment, as simple as it might be from an experimental point of view, needs a lot of precision and care. This is of course due to the fact that one needs to detect the mirrorless lasing beam (our signal) on the same path as that of the beam that creates the inversion (our pump) and the two beams differ only in polarization. It also requires a well controlled magnetic-field environment as well as almost perfect blocking of reflections.

For these reason, we collaborated with our colleagues in Ashtarak. Experimental measurements were initially carried out in Ashtarak using the setup shown schematically in Figure 6.3 (A). In order to check the reproducibility of the results, carry out independent measurements with better control of the applied magnetic field, and providing the capability of precise measurements of the output-light spatial profile, another set of measurements was carried out in Mainz, with the setup seen in Figure 6.3 (B). In order to make sure that the reader understands the similarities and small, but—as will be discussed in Chapter 7—important differences between the two setups, I made a distinction between the Mainz and the Ashtarak experiments in the pages to follow.

6.3.2 Laser

In Ashtarak:

In the Ashtarak setup (Figure 6.3A), $a \approx 1.5$ mm-diameter beam from a single-frequency cw extended-cavity diode laser (wavelength 780 nm, linewidth 1 MHz, input intensity varies) was used.

In Mainz:

In the Mainz setup (Figure 6.3B), $a \approx 1.5$ mm-diameter beam from a single-frequency cw extended-cavity diode laser (wavelength 780 nm, linewidth 100 kHz, input intensity varies) was used.

6.3.3 Setup

In Ashtarak: The beam was purified of the initial linear vertical polarization with a Glan-Thomson polarizer and directed to a 135 mm-long sealed-off room-temperature (RT) glass cell with a side-arm containing natural rubidium. The cell had no coating or buffer gas.

The vapor-cell temperature was kept at 30 °C, which corresponds to a number density of $N = 1.16\times10^{10}\,\mathrm{cm}^{-3}$ of Rb atoms. It was verified that small changes in atomic density did not qualitatively influence the observed effects. The cell was surrounded with an assembly of mutually orthogonal pairs of calibrated Helmholtz coils with the axes carefully aligned along the X, Y, Z directions. The coils were used for canceling the magnetic field in two directions (X, Y), monitored to $\approx 10\,\mathrm{mG}$ with a Fluxmaster fluxgate-magnetometer, and scanning within up to ± 1 G in the third direction (Z).

In Mainz:

The Mainz setup (Figure 6.3B), contrary to the one in Ashtarak, includes a magnetic shield. The coils installed inside the Twinleaf MS-2 magnetic shield allowed to apply and scan the magnetic field in the X, Y, Z directions. The magnetic shield can zero the outside fields up to $10\,\mathrm{fT}/\sqrt{Hz}$ [128].

Separate measurements have been done to evaluate possible contribution from the inhomogeneity of the applied magnetic field. The contribution was found to be insignificant. In particular, the measured longitudinal (B_X) component was less than 1.5 % of the applied B_Z field. Two linear polarizers (LPVIS050) were used for purification of the input laser light polarization and selection of the orthogonally-polarized component in the output beam. The spatial distribution of the forward beam emerging from the cell was studied with a beam profiler DMK 41BU02.H from the company Imaging Source.

6.3.4 Detection

In Ashtarak:

The light transmitted through the cell was directed onto a polarizing beam splitter (PBS) decomposing the incident polarization into vertical and horizontal components that were simultaneously detected with two photodiodes. Diaphragms were placed in front of the photodiodes located 70 cm away from the cell in order to cut the most of the fluorescence of the Rb atoms that is a potential noise source. The two detection channels were adjusted to have the same sensitivity. A fraction of the laser light passed through an auxiliary room-temperature rubidium reference cell to monitor the spectrum.

A set of calibrated neutral-density filters was used to change the incident light intensity before the cell ("AT" in Figure 6.3 A). The filters from the set, which were not used for attenuation, were placed at the position of AT after the cell. With this configuration, the off-resonance signal did not change, so that there was no need to adjust the photodiode gain.

In Mainz:

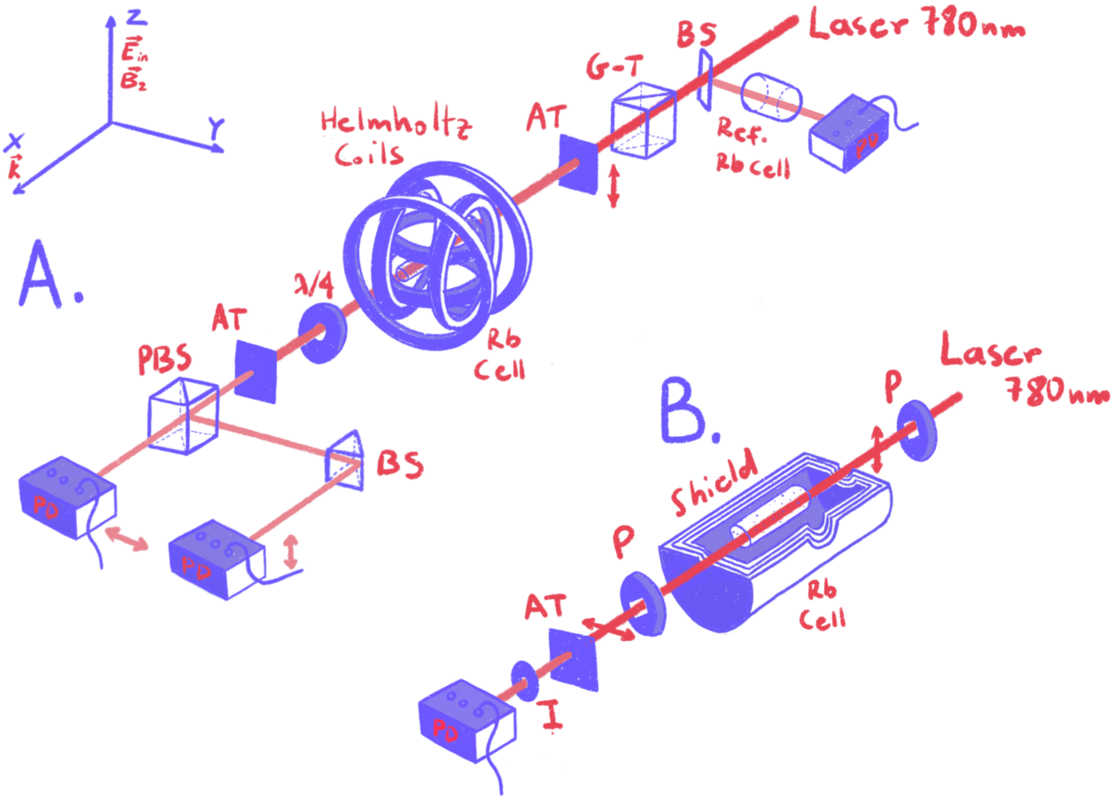

FIGURE 6.3: Experimental setup and the measurement configuration in Ashtarak (A) and Mainz (B). PBS: polarizing beam splitter; BS: beam splitter; $\lambda/2$: half-wave plate; $\lambda/4$: quater-wave plate; PD: photodiode; AT: attenuator; P: polarizer; G-T: Glan-Thompson Polarizer; Iris: I

The light transmitted through the cell was directed onto a polarizer and then through a filter (AT) and an iris directed to either a photodetector or to a camera depending on the data we took.

6.3.5 Results

In Ashtarak:

The first measurement was done by scanning the B_Z in the $\pm$ 0.12 G range. The frequency of the incident linearly polarized (E_Z) light was at the maximum of the Doppler-overlapped transition groups ^{85}Rb F_g=3 → F_e=2,3,4 or ^{87}Rb F_g=2 → F_e=1,2,3 of Rb D_2 line, and was monitored by the reference signal. The intensity of the output light (with orthogonal polarization E_Y) was recorded with Photodiode 1 (see Figure 6.3 A) for 12 values of incident laser intensity I_L ranging from 1 to 1100 mW/cm^2. This output orthogonal light is what is expected to be our lasing beam.

The output intensity normalized by the input intensity is presented in Figure 6.4a,b. Negligible output signal was recorded for low laser radiation intensity ($I_L < 1\,\mathrm{mW/cm^2}$). At $I_L \approx 1.5\,\mathrm{mW/cm^2}$ a (≈ 15 mG FWHM) resonance feature appears first on the ^{87}Rb F_g=2 → F_e=3 transition, centered around $B = 0$, and then also on the ^{85}Rb F_g=3 → F_e=4 transition (≈ 20 mG FWHM at $I_L \approx 3\,\mathrm{mW/cm^2}$). Further increase of intensity results in broadening and amplitude increase of the resonance feature to a maximum normalized value recorded at $I_L \approx 35$ and 85 mW/cm^2 for ^{87}Rb

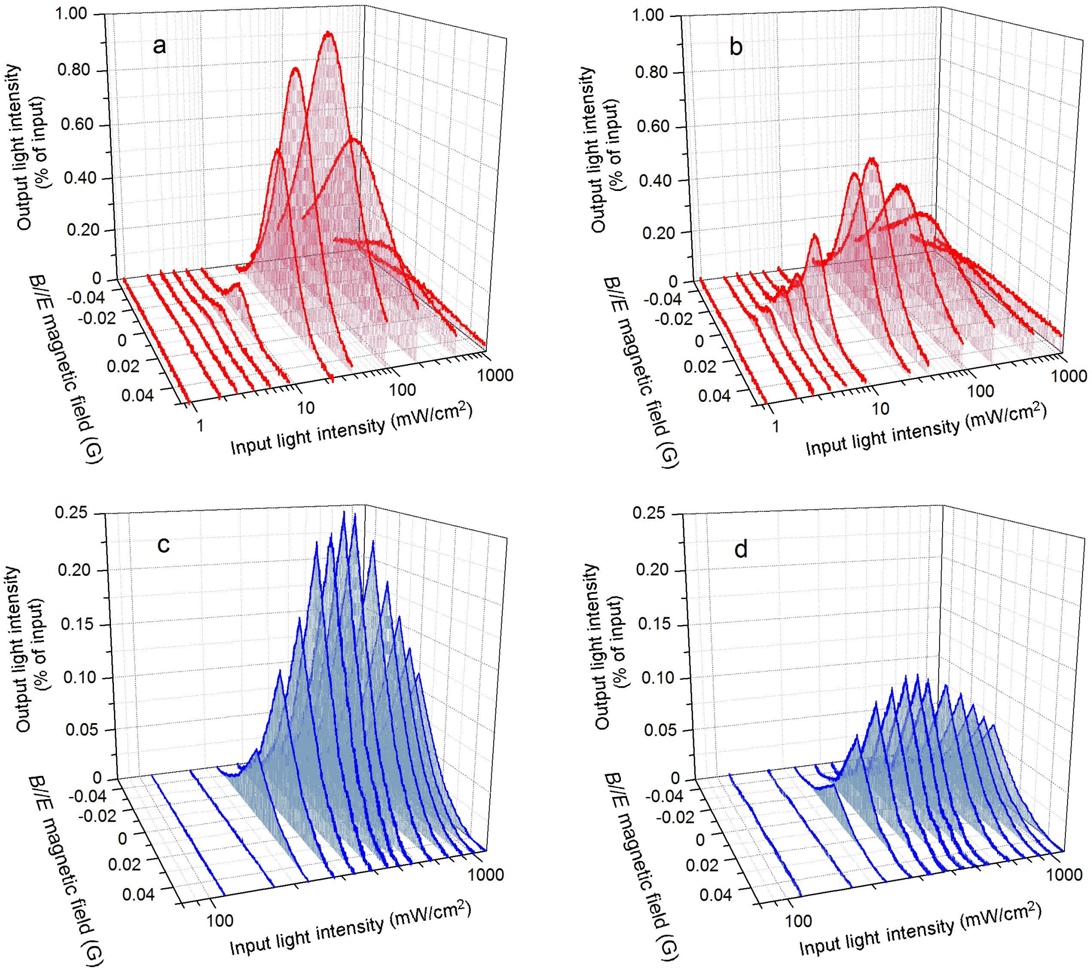

FIGURE 6.4: Dependences of normalized output intensity with orthogonal polarization (see text) on magnetic field ($\mathbf{B} \parallel \mathbf{E}$) for ^{85}Rb F_g=3 → F_e=4 (a,c) and ^{87}Rb F_g=2 → F_e=3 (b,d) D_2 transitions, measured in Ashtarak (a,b) and Mainz (c,d).

F_g=2 → F_e=3 and ^{85}Rb F_g=3 → F_e=4, respectively. By increasing the intensity even more we get a reduction of the transmitted intensity at $B = 0$ and further broadening of the resonance.

The scaled and absolute intensity values of $B = 0$ resonances, as well as their widths depending on the laser light intensity, derived from the Ashtarak measurements presented in Figure 6.4a,b are shown in Figure 6.5. As seen in the figure, the absolute output intensity reaches 10 mW/cm^2 (or 1 % of the incident-light intensity). The input-intensity dependence of the output signal is *strongly nonlinear* (note the log-log scale needed to present the data spanning several orders of magnitude). The low-intensity range for the absolute intensity dependence is magnified in the inset of Figure 6.5a in log-log scale, exhibiting *threshold behavior* of the output light. The resonance linewidth rises monotonically from ≈ 0.02 to 0.1 G when changing I_L (Input light intensity) by three orders of magnitude, from ≈ 1 to 1000 mW/cm^2, with a steeper slope for ^{87}Rb F_g=2 → F_e=3.

Measurements similar to those presented in Figure 6.4 were performed also for the output light with initial laser polarization (E_Z), recorded with the Photodiode on the right (see Figure 6.3a). A dip

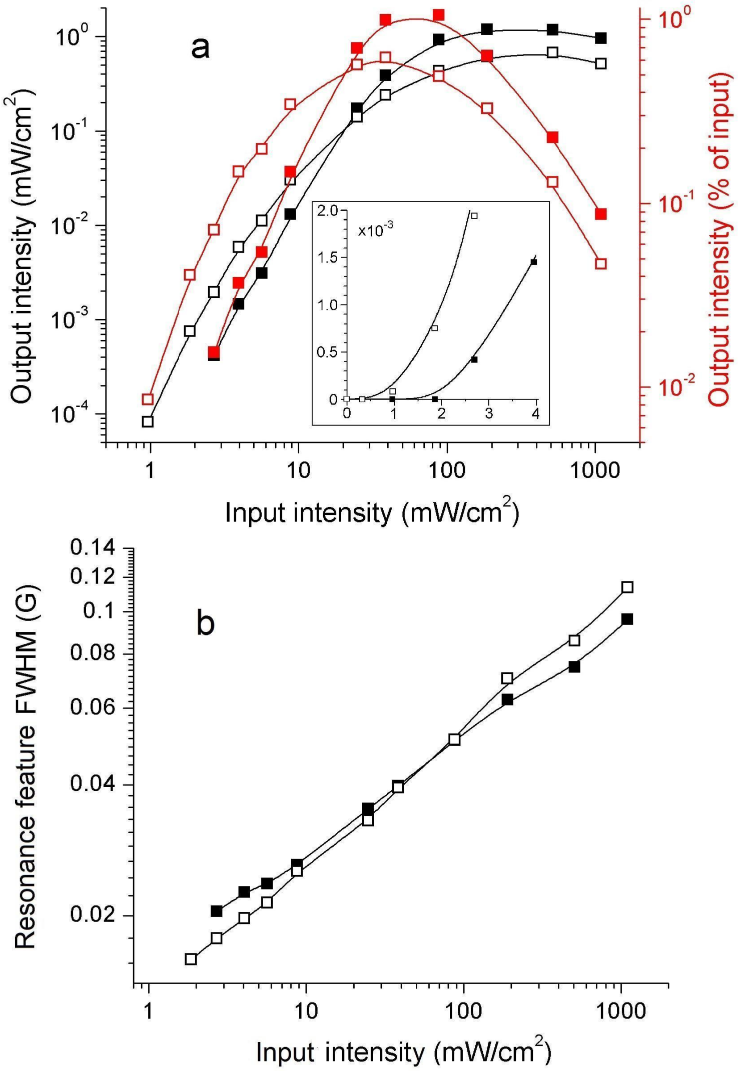

FIGURE 6.5: Input-intensity dependences of (a) absolute (black symbols, left axis) and normalized (red symbols, right axis) of the output intensity with orthogonal polarization for $B = 0$; (b) FWHM width of $B = 0$ resonance for the output orthogonally-polarized light, retrieved from the measurements presented in Figure 6.4a,b. Solid squares: ^{85}Rb F_g=3 $\rightarrow$ F_e=4; open squares: ^{87}Rb F_g=2 $\rightarrow$ F_e=3. Solid lines are drawn as a guide to the eye.

centered at $B = 0$ complementary to the peak for the orthogonal polarization was recorded for the same conditions and with nearly the same parameters (amplitude and width) as for the case of the orthogonal polarization. Unlike zero-background peaks for E_Y, the E_Z dip appears on top of a background resulting in an inconspicuous, low-contrast signal. For this reason, we do not present this graph here, but it will be explored below, when presenting the results of the double-scanning measurements.

Circular polarization analysis of the output light was also performed with the Ashtarak setup. Figure 6.6 presents the circular polarimeter output signal versus $\mathbf{B} \parallel \mathbf{E}$ for the case of ^{85}Rb F_g=3 $\rightarrow$ F_e=4 transition measured at different values of I_L corresponding to the conditions of Figure 6.4a,b. One can clearly see that ellipticity in output light polarization appears around $B = 0$ for $I_L \approx$

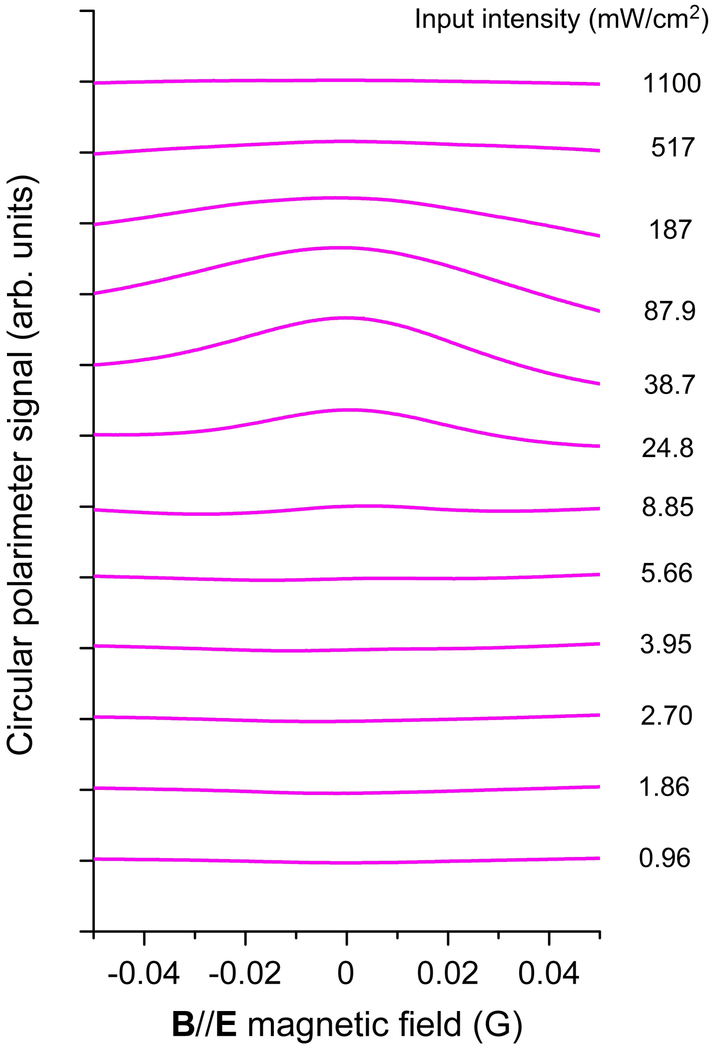

FIGURE 6.6: Ellipticity in output light: Magnetic-field dependence of the output signal for the ^{85}Rb F_g=3 → F_e=4 transition recorded with a circular polarimeter at different input-light intensities (same as in Figure 6.4a,b). No normalization; the curves are shifted vertically by equal amounts.

$10 - 500\,\mathrm{mW/cm^2}$, i.e. in the input-intensity range where the orthogonally polarized output light is significant. This is a signature of non-random phase of the generated light with respect to the excitation-light phase, which cannot be explained directly by mirrorless lasing that implies random phase relation between the generated and the pump radiation. The observed phase correlation may occur due to an accompanying wave-mixing process, which contributes to the detected signal because of insufficient spatial resolution. The results of further experimental studies of the generated beam profile performed with the Mainz setup indicating the presence of a concomitant four-wave mixing are presented below.

The next series of measurements carried out in Ashtarak were aimed at detailed studies of the **frequency dependence of the resonances across the whole spectral range of the Rb D_2 line**. Simultaneous double linear scanning of the laser frequency and the $\mathbf{B} \parallel \mathbf{E}$ magnetic field was performed by applying triangular control pulses with different repetition frequencies.

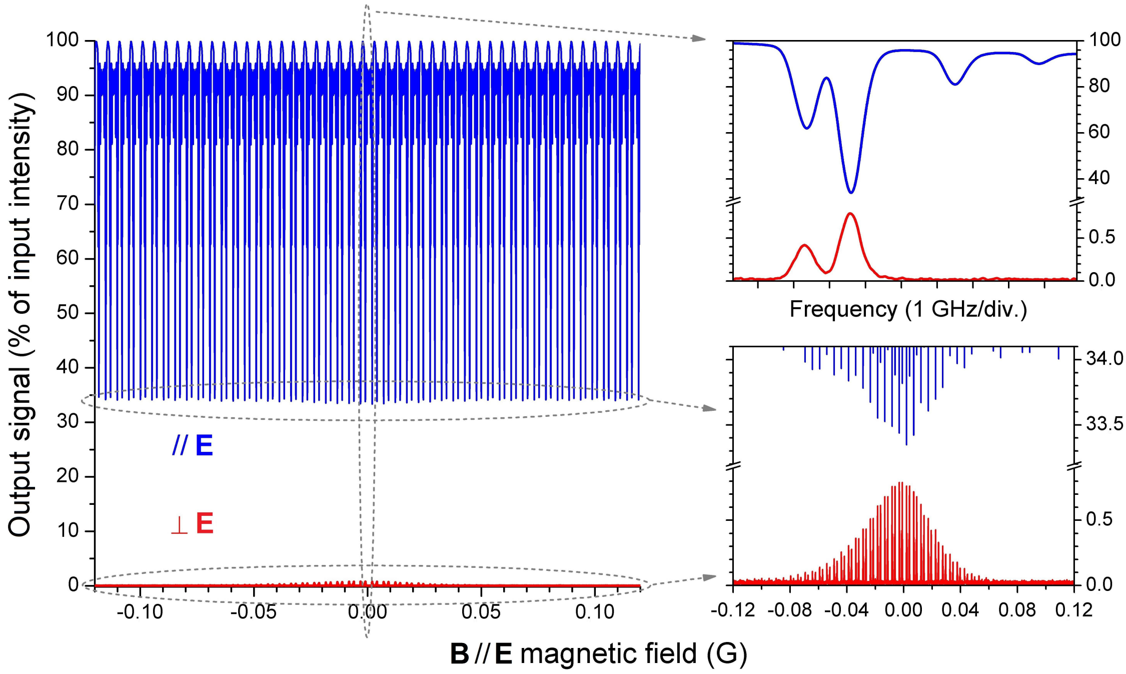

FIGURE 6.7: Double-scanning measurement for the output light with polarization parallel ($\|\mathbf{E}$) and orthogonal ($\perp\mathbf{E}$) to the input laser polarization for incident light intensity of $87.9\,\mathrm{mW/cm^2}$. A single slow (compared to the frequency of the spectral scanning) B-field scan ($\mathbf{B} \parallel \mathbf{E}$) in the range of $\pm 0.12\,\mathrm{G}$ is combined with fast laser-frequency scans over 10 GHz covering the Rb D_2 line. Upper inset: zoomed output light spectrum in the region of $B = 0$; lower inset: zoomed signals of $\perp\mathbf{E}$ output light (lower trace), and $\|\mathbf{E}$ output light in the region of the dip (upper trace).

The results of such measurements for the linear polarization components of the output light with simultaneous slow scanning of the B-field ($\mathbf{B} \parallel \mathbf{E}$) and fast scanning of the laser frequency across the D_2 line are presented in Figure 6.7 for an incident intensity corresponding to a maximum output signal with orthogonal polarization for the ^{85}Rb F_g=3 $\rightarrow$ F_e=4 transition. It can be seen from the upper zoomed-in inset that the $\perp$ $\mathbf{E}$ polarized-light spectrum (lower trace) does not contain the transition groups ^{85}Rb F_g=2 $\rightarrow$ F_e=1,2,3 and ^{87}Rb F_g=1 $\rightarrow$ F_e=0,1,2 unlike the $\parallel$ $\mathbf{E}$ polarized-light spectrum (upper trace), where these transitions are well pronounced. Note that the maximum amplitude of the resonance is observed when the laser frequency is tuned to the absorption maximum of the cycling transitions. It is noteworthy that for the $B = 0$ peak in the orthogonally-polarized output light there is a complementary dip in signal with unchanged input polarization. This is a direct signature of parallel-to-orthogonal polarization conversion in the output light.

In Mainz:

Similar measurements about **dependences of normalized output intensity with orthogonal polarization** on magnetic field were carried out in the Mainz setup. The cell length was the same, temperature was similar (RT), and the input beam diameter was of similar size. The resulting peaks exhibit ,qualitatively similar behavior, with somewhat higher threshold and maximum conversion values of input light intensity (Figure 6.4c,d). Among other quantitative distinctions from the

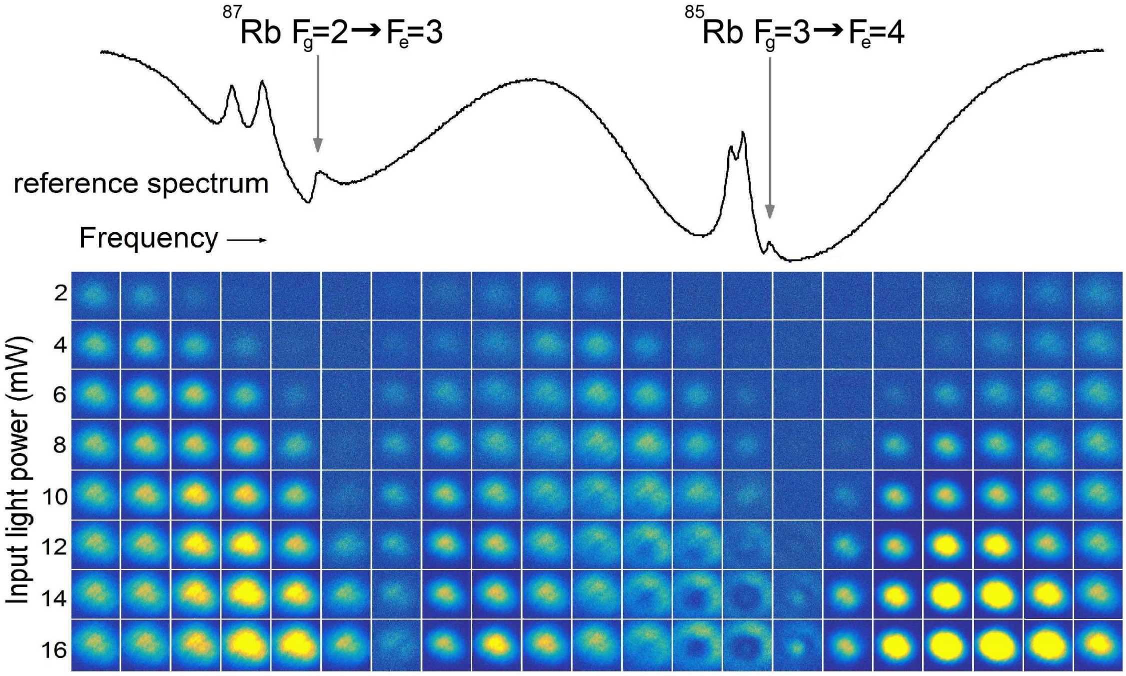

FIGURE 6.8: Spatial-profile measurements of the orthogonally polarized component of the forward beam at zero magnetic field. Upper curve: saturated-absorption spectrum for reference.

Ashtarak experiment are lower maximum conversion efficiency ($\approx 0.25\,\%$), and a sharper shape of the $B = 0$ peak.

We tried to study this quantitative discrepancy between the Ashtarak and Mainz results for the input beam intensity values where the orthogonally-polarized output beam is efficiently generated, as well as for the conversion efficiency (Figure 6.4). One could ascribe this to the different output-beam detection geometries used on the two setups. The detection angle in Ashtarak was about 15 mrad, while in Mainz it was 6 mrad. Another possible reason is the magnetic-field environment (different precision of the B-field control). In order to clarify this issue, additional measurements were done in Mainz using a beam profiler for spatial analysis of the output beam.

The spatial profile of the orthogonally polarized output beam versus frequency, covering the ^{85}Rb F_g=3 → F_e=2,3,4 and ^{87}Rb F_g=2 → F_e=1,2,3 transitions groups, is shown in Figure 6.8 for different values of input beam power. We are here at zero field. In these measurements, the extinction ratio for the crossed polarizers was somewhat worsened by a slight tilt of the analyzer, so that when the laser radiation frequency is off-resonance from the atomic transitions, some residual light remains in the transmitted beam, with intensity increasing linearly with input power. When the laser frequency is tuned closer to the atomic transition, the residual light gets absorbed. A bright beam emerges above the threshold input power of $\approx$ 10 mW. In the region of ^{85}Rb F_g=3 → F_e=4 transition, the emerging narrow axial beam is surrounded by a ring structure, which remains, even becoming stronger, with some blue frequency shift from the resonance. The threshold of the ring structure is somewhat different from the one of the central beam. The ring structure is not observed around the ^{87}Rb F_g=2 → F_e=3 transition.

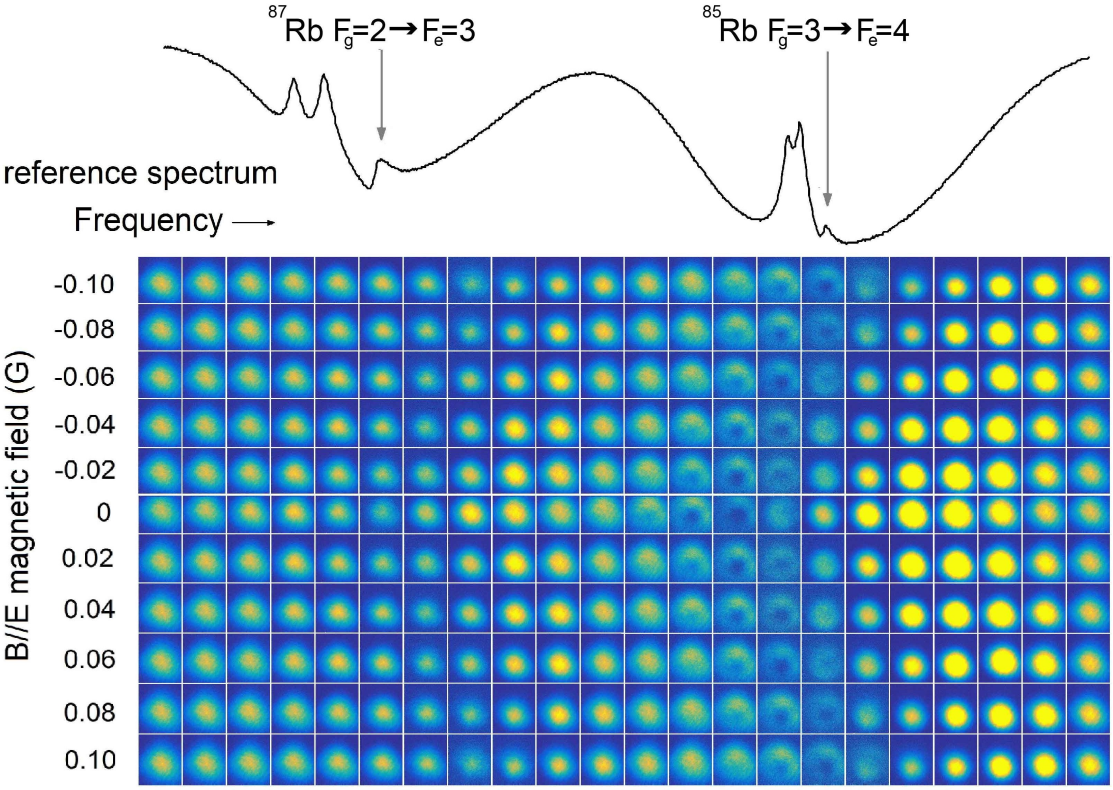

Figure 6.9: Spatial-profile measurements of the orthogonal component of the forward beam for different laser frequencies and different values of the magnetic field with a fixed input beam power of 12 mW. Upper curve: saturated-absorption spectrum for reference.

The same technique was employed for the study of the output beam profile versus laser frequency and $\mathbf{B} \parallel \mathbf{E}$ magnetic field. For this measurement, the value of the input light power was kept at 12 mW (above the observed threshold for the ^{85}Rb F_g=3 → F_e=4 transition). The results of this measurement are shown in Figure 6.9. One can see that the increase of the magnetic field leads to vanishing of the central bright beam, unlike the ring structure which becomes even more pronounced.

The results of these measurements indicate that the spatial profile of the beam and the detection angle (aperture) are of importance for the studied process, which may explain the quantitative distinction of Ashtarak and Mainz results observed in Figure 6.4.

6.4 Discussion

We explored a variety of experimental methods to be able to observe the mechanism described in the Introduction. These experiments provided a link between the observed features with the formation of amplified orthogonally polarized light (mirrorless lasing) under excitation of an $F_e > F_g$ atomic cycling system with intense linearly polarized light.

We believe the obtained experimental results are consistent with the mechanism described in the Introduction, sufficiently proving the link between the observed features with the formation of amplified orthogonally polarized light (mirrorless lasing) under excitation of an $F_e > F_g$ atomic cycling system with intense linearly polarized light. A short list of our results together with our interpretation follows.

Linearly polarized light induces polarization of the $F_e > F_g$ atomic system resulting in light-induced alignment, redistributing the ground state population towards the $m_{F_g} = 0$ Zeeman sublevel. In the weak-light-intensity limit, when we apply weak B_Z ($\mathbf{B} \parallel \mathbf{E}$) magnetic field the transmitted radiation is not influenced. However, when the excitation intensity of the laser beam is strong enough (above saturation), light is generated, which is orthogonally polarized with respect to the incident radiation and this gets influenced by magnetic fields. In particular the atomic polarization component that is created can undergo Larmor precession around B_Z, since it is orthogonal to that field. This precession redistributes the ground-state population among Zeeman sublevels, and eventually affects the conditions of population inversion. The characteristic strength of the magnetic field needed to destroy the amplification is consistent with time-of-flight broadened ground state coherence time (time-of-flight broadening for an atom traversing the laser beam $\gamma_c/2\pi \approx 100\,\mathrm{kHz}$).

In the results in Mainz, this whole process is evidenced by sharp $B = 0$ peaks in Figure 6.4, blue curves. Broader peak features observed in the Ashtarak experiment (Figure 6.4 a,b) could be caused by the absence of shielding, which results in residual ac components of the laboratory magnetic field, estimated to be about $10\,\mathrm{mG}$.

Note that the coherence time can be substantially increased (by orders of magnitude) using antirelaxation-coated cells, cells with buffer gas, or cold atoms [40], allowing a potential reduction of the magnetic resonance width down to $\sim 0.1\,\mathrm{mG}$.

There is yet another mechanism possibly responsible for effective broadening of the magnetic resonance with I_L. At high light intensity, the distribution of the ground-state Zeeman sublevel populations is dominated by light-induced polarization, thus diminishing the effect of Larmor coupling. As a result, the alignment remains preserved for a larger range of the B-field. This causes a continuous growth of the magnetic-resonance width as a function of light power (Figure 6.5b), as opposed to the output light intensity, which undergoes saturation at high values of I_L (Figure 6.5a). Comparison of Figure 6.4 a and b shows that the $B = 0$ peak signal appears at lower values of I_L for ^{87}Rb F_g=2 → F_e=3 as compared with ^{85}Rb F_g=3 → F_e=4. This result is in qualitative agreement with the calculations presented in [122], which give the values for inversion threshold intensity $S \approx 13$ and $\approx$ 25, respectively. The suppression of orthogonally polarized amplified radiation at $B = 0$ observed for $I_L > 100\,\mathrm{mW/cm^2}$ (Figure 6.5a) is in qualitative agreement with the experimental results obtained in [122]. This decline may be attributed to saturation effects.

About the overall polarization of the output beam measured in Figure 6.6: Generation of the orthogonally polarized output beam at $B = 0$ should cause ellipticity in the overall polarization of the transmitted beam. This is consistent with the measurements done with a circular polarimeter configuration (Figure 6.6) where the ellipticity is observed only in the conditions favorable for mirrorless lasing. When we apply a B_Z magnetic field, this tends to cease the generation of ellipticity, thus recovering linear polarization of the output beam. On the contrary, around $B = 0$, where we also expect mirrorless lasing to happen, a peak feature is observable.

For non-cycling transitions (^{85}Rb F_g=2 → F_e=2, F_g=2 → F_e=1 and F_g=1 → F_e=1 and ^{87}Rb F_g=1 → F_e=0 and F_g=1 → F_e=1) pumped with a linearly polarized laser light, practically no atoms remain in the excited state (see, for example, [125]). Consequently, no population inversion can develop. Indeed, no mirrorless lasing is observed on these transitions.

6.4.1 Ring structure

One point that we need to understand in this phenomenon is the ring structure observed in the spatial profile of the output beam in the conditions close to the optimal conditions for mirrorless lasing. This could be an indication for a **four-wave mixing (FWM)** process which can develop in a system of magnetic sublevels of degenerate two-level atoms pumped with intense linearly polarized light.

FWM is a nonlinear phenomenon related to phase-matching or simply put: momentum conservation. In our case, because of the degeneracy, we deal with degenerate four-wave mixing, a configuration in which three different light fields of same frequency are propagating in a nonlinear optical material to and a fourth beam [129].

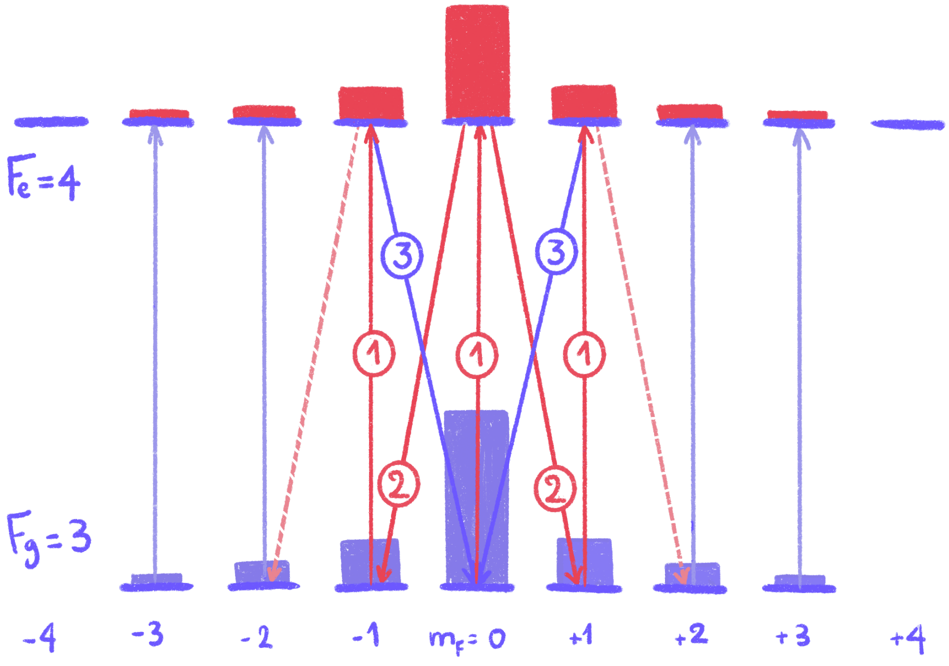

FIGURE 6.10: Schematic diagram of entirely-degenerate four-wave mixing process.

A schematic diagram of such a process is presented in Figure 6.10.

Excitation on transitions ① drives atoms from $m_{F_g} = 0$ sublevel to $m_{F_e} = 0$ and from $m_{F_g} = 1$ sublevel to $m_{F_e} = 1$, followed by transfer to $m_{F_g} = \pm 1$ by inversion-amplified radiation ② with subsequent laser excitation to $m_{F_e} = \pm 1$, and finally the loop is closing by emission of induced light ③. To make it more clear, the phase relationship would be $\vec{k1} + \vec{k1} = \vec{k2} + \vec{k3}$.

The figure shows only two symmetric FWM channels linked with $m_F = 0$, but the process can similarly occur also on neighboring magnetic sublevels. Again here, the distinction of this process from other known schemes is that it is *entirely* degenerate (all the four waves have the same frequency, they differ only by polarization).

Efficient generation of FWM requires phase-matching, the conditions for which are related to the dispersive properties of the nonlinear medium (in our case the Rb gas). Conical emission results from phase matching and can be straightforwardly separated from the axial mirrorless lasing, the latter having much lower divergence.We estimated the divergence in this experiment to be $\approx 10^{-3}$ rad. If all fields are having the same frequency and are co-linear, a non-collinear direction for the FWM-generated field could be only due to very different refractive index for the inversion-amplified radiation ②.

Being assisted by the population inversion, the FWM process competes with the direct mirrorless lasing, which results in different optimal conditions for their observation as is seen in Figs. 6.8 and 6.9. Four-wave mixing is related to Kerr nonlinearity effects: more about that in the next Chapter.

Summarizing, let us list the indications that support our claim that we observed degenerate mirrorless lasing:

1) The absence of magnetic resonance for B_Z ($\mathbf{B} \parallel \mathbf{E}$) below $I_L \approx 1.5\,\mathrm{mW/cm^2}$ (^{87}Rb F_g=2 → F_e=3) and $\approx 3\,\mathrm{mW/cm^2}$ (^{85}Rb F_g=3 → F_e=4); nearly exponential initial above-threshold growth of the $B = 0$ feature until it saturates (Figs. 6.4, 6.5a). This is an indication of a nonlinear effect.

2)There is a narrow resonance in the magnetic-field dependence of the generated light: this is our strongest evidence so far. In this configuration, there is **no such resonance** expected in this field range for non-lasing processes, because of symmetry reasons (B-field is directed along the light polarization). The big question here is, if any possibility of misalignment or self-induced ellipticity or birefringence of cell windows could break this symmetry.

3) Consistency of the laser-intensity range where the magnetic resonance is observed (Figure 6.4) with the results of [122]. In this paper amplification due to partial population inversion on ^{85}Rb F_g=3 → F_e=4 and ^{87}Rb F_g=2 → F_e=3 transitions was directly recorded in the backward direction.

4) Outright absence of any orthogonally polarized output light for ^{85}Rb F_g=2 → F_e=1,2,3 and ^{87}Rb F_g=1 → F_e=0,1,2 ($F_e < F_g$) transitions, independently of the B_Z value (Figure 6.7).

A comprehensive theoretical treatment and modeling of the problem is quite complex and would ideally include many processes such as propagation effects with partial depletion of the pump beam. The careful reader will have noticed that we are discussing about lasing only in the forward direction although the directionality did not seem important in the theoretical description of the problem. The absence of backward lasing will be discussed in the next Chapter.

6.5 Conclusions

In conclusion, we have experimentally observed effects consistent with degenerate mirrorless forward lasing in rubidium vapor contained in uncoated buffer-gas-free vapor cells under excitation with linearly polarized laser radiation tuned to the ^{85}Rb F_g=3 → F_e=4 and ^{87}Rb F_g=2 → F_e=3 D_2 transitions.

The generated beam is orthogonally polarized to the incident light polarization, and has low divergence ($\approx 10^{-3}$ rad). The lasing occurs above a certain threshold value of the incident light intensity ($I_L \sim 3\,\mathrm{mW/cm^2}$), and grows nonlinearly at least up to $\sim 0.3\,\%$ conversion efficiency at $I_L \approx 90\,\mathrm{mW/cm^2}$. Further increase of the pump power I_L results in a decrease of the generated light intensity, which almost completely vanishes at $I_L \sim 1000\,\mathrm{mW/cm^2}$. The generated light is sensitive to the application of a transverse ($\mathbf{B} \parallel \mathbf{E}$) magnetic field, forming a narrow ($\sim 20\,\mathrm{mG}$) resonance centered at $B = 0$.

Based on the analysis of the experimental results, the observed effect is attributed to the population inversion established on $|m_{F_e}| = n \rightarrow |m_{F_g}| = n + 1$ transitions between the Zeeman sublevels (where n is a non-negative integer), resulting in an orthogonally-polarized beam under excitation of a D_2 $F_e > F_g$ transition with linearly-polarized laser light. However other nonlinear effects seem to interfere with our forward lasing.

If we conduct the experiment with antirelaxation-coated or buffered vapor cells the obtained results may be of interest for optical magnetometry. For instance, mirrorless lasing in the backward direction, could be useful for remote mesospheric magnetic sensing using the sodium layer as a sensor [130].

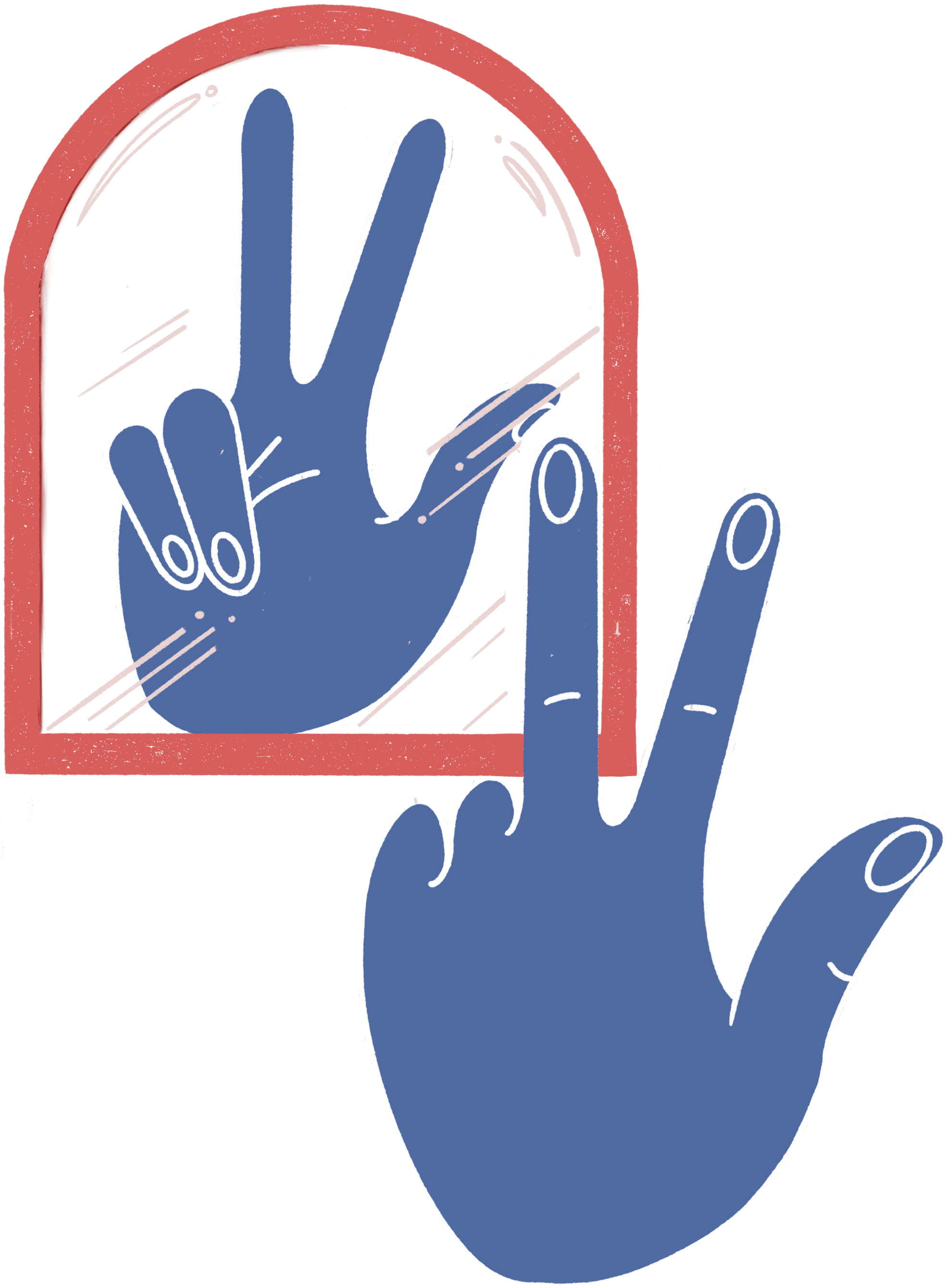

Refutations have often been regarded as establishing the failure of a scientist, or at least of his theory. It should be stressed that this is an inductivist error. Every refutation should be regarded as a great success. Even if a new theory should meet an early death, it should not be forgotten; rather its beauty should be remembered, and history should record our gratitude to it.

Karl Popper

7

Unsolved (lab) mysteries

7.1 Degenerate mirrorless lasing- Backward Beam

Some of the text presented in this section is part of a paper that has been published as [49]. For the work presented in this Chapter, I worked for part 1 experimentally together with my colleague Guzhi Bao to set up and test the experiment in Mainz and, for part 2, I rebuild the whole setup and analysed the data by myself.

7.1.1 The Idea

In Chapter 6 we introduced the idea of degenerate mirrorless lasing, a phenomenon in which amplified spontaneous emission is produced along the pump direction in a Rb vapor, with orthogonal polarization to that of the pump, when the pump beam has linear polarization under zero magnetic field. The pump field interacts with the Zeeman-sublevels (m_F) of a specific atomic transitions and population inversion is produced between certain magnetic sublevels. Specifically, the transitions in which we expected and observed the lasing are $F_e > F_g$ cycling transitions in the D2 line of rubidium and in particular ^{85}Rb F_g=3 → F_e=4 and ^{87}Rb F_g=2 → F_e=3.

What we have detected so far is nonlinear dependence between the incoming and outgoing beam as well as a narrow magnetic resonance when we scan the magnetic field around zero and when this field is parallel to our pump polarization. These are a strong indication of amplified emission in the forward direction or else *forward mirrorless lasing*. While forward mirrorless lasing can be an interesting phenomenon, *backward mirrorless lasing* can be of even more interest, since it can be used for distant magnetometry, for example in laser guide stars [130]. In the simple model we have so far it seems that there should not be a reason for not having backward amplified emission and only forward. To make things easier, in the backward direction, four-wave mixing processes and Kerr effect does not contribute. And yet, backward degenerate mirrorless lasing seemed to be a much harder case than we expected.

It is known that there is a difference between backward and forward emission, since the velocity distribution of atoms and light shifts can produce a forward-backward asymmetry [131]. Special in our case was that strong backward emission was observed in Armenia, and this could not be reproduced in Mainz, even with the same vapor cell and the same experimentalists.

I will give a side by side overview of the experiments made in Mainz and Ashtarak, although the timeline is quite nonlinear.

7.1.2 In Ashtarak, part I

Our collaborators in Ashtarak used the same setup as the one for forward lasing, with an additional part for backward detection. The cell, laser, the pumping/input frequency and the shielding coils are all the same as in the forward-beam experiment in Chapter 6. The experiment was conducted at room temperature (in Armenia during the summer).

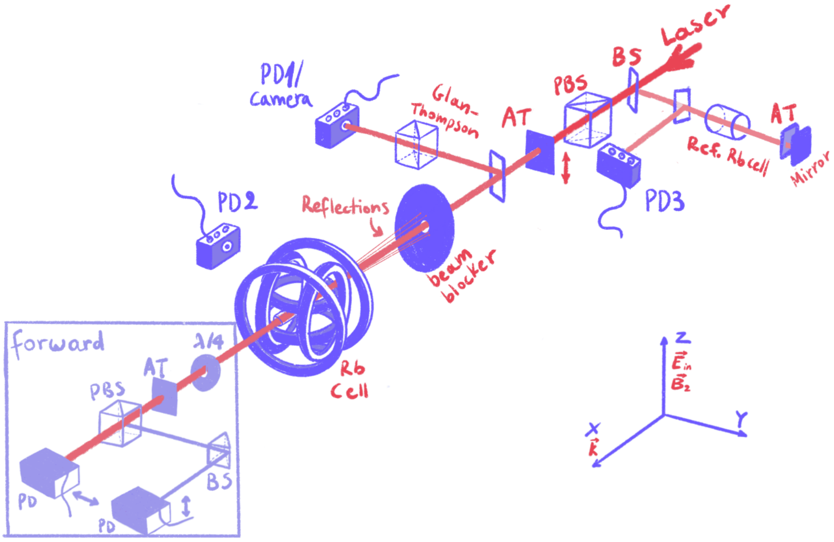

FIGURE 7.1: Backward lasing setup in Ashtarak. AT: Attenuator for controlling laser power; PD: Photodetector; PBS: Polarizing beam splitter; BS: Beam splitter; PD1 is used for detecting the orthogonal polarization of the backward beam, PD2 detects fluorescence and PD3 is monitoring the frequency of the laser to have a reference on which frequency we pump.

The 780 nm input laser beam has a 2 mm diameter and a linewidth of 15 MHz. Its frequency is tuned to the cycling transitions where we expect inversion of population to happen [(|F_g=3 → F_e=4 (^{85}Rb) and F_g=2 → F_e=3 (^{87}Rb) of the rubidium D_2 line: $5S_{1/2} \to 5P_{3/2}$].

The setup has three parts: the part on the right, monitored by PD3, is using spectroscopy on the reference cell in order to monitor the frequency of the laser beam that we also call pump, that will create the inversion of population. The beam afterwards reaches the middle part of the setup, goes through the cell and gets detected in the forward direction setup. For degenerate mirrorless lasing we expect a backward beam with a polarization orthogonal to that of the pump beam. This is why this part contains a beam blocker and a Glan-Thompson polarizer. The beam blocker acts also as a pinhole for the backward lasing to go through, but is blocking all four reflections coming from the four window surfaces of the cell (two from the faces of the window in the front and two of the back window of the cell). The backward beam is detected with PD1 or an IR digital camera. As a complementary measurement, the fluorescence from the cell was detected with PD2.

To monitor the nonlinear behavior of the backward beam, a magnetic field B was applied in the direction along z ($B_z \parallel E_{in}$)—where we do not expect nonlinear magneto-optical effects. The incoming pump beam had a 23 mW power and its frequency was linearly scanned across all the D2 lines to get the whole spectrum of the lasing beam and the fluorescence.

Results

Without revealing too much, since this paper has not been published yet, our collaborators *detected* in the backward direction, by scanning the magnetic field B_z from -0.5 to 0.5 G, a beam with the largest intensity at zero field.

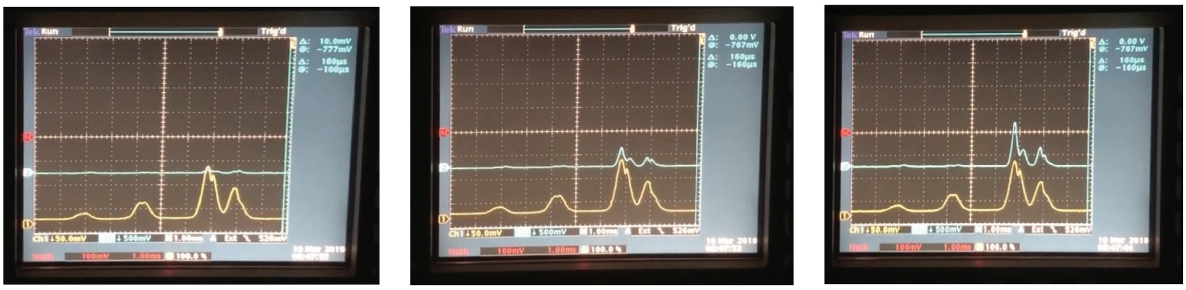

FIGURE 7.2: Backward-direction in Ashtarak for different magnetic fields. The blue line is the signal in the backward direction and the yellow line is the fluorescence. **Left**: Signal at 0.5 G, **Middle**: Signal around 0.2 G, **Right**: Signal at 0 G.

The backward signal develops only in the region of the cycling transitions ($F_e > F_g$) ^{85}Rb F_g=3 $\rightarrow$ F_e=4 and ^{87}Rb F_g=2 $\rightarrow$ F_e=3. Even after blocking the four main reflections of the cell, we see on zero field some scattering signal from the incoming laser beam that is not blocked but propagates freely until it is stopped by the wall a few meters away. The spectrum of the backward beam has some sub-Doppler features at the crossover resonances CO32 ^{87}Rb and CO43 ^{85}Rb.

When applying a longitudinal magnetic field (**Bx**//**k**), there is positive correlation between the magnetic field and the signal: at ±0.5 G we have an increase of 30 x in the backward signal. No data is provided for this observation in this thesis.

Discussion

Our collaborators in Armenia observed in the backward direction a beam that is appearing only at the same cycling transitions as we observed for the forward direction and has orthogonal polarization to the incoming beam. The beam appears around zero field (B parallel to the electric field of the incoming beam) with its highest amplitude at 0. Some important things to notice:

- The beam appears- after a threshold in input laser power.
- The cell is 8 cm long, sapphire windows, no buffer gas and no coating. In order to observe backward emission, the cell was being moved slowly by hand until we found a signal. The signal was then immediately appearing in full amplitude or not at all. This effect was attributed to residual birefringence of the cell.
- The smaller signal in the backward direction compared to the forward lasing we observed in Chapter 6 is hypothesized to exist due to the the atomic velocity distribution: The backward-emitted photons are absorbed by opposite-velocity atoms, so there is bleaching/saturation of the medium for the velocity group of atoms corresponding to forward transmission.

7.1.3 Mainz, part I

Back to Mainz, we initially built a setup to monitor possible backward lasing and at the same time we used another laser (probe) to detect whether there is gain in the backward direction.

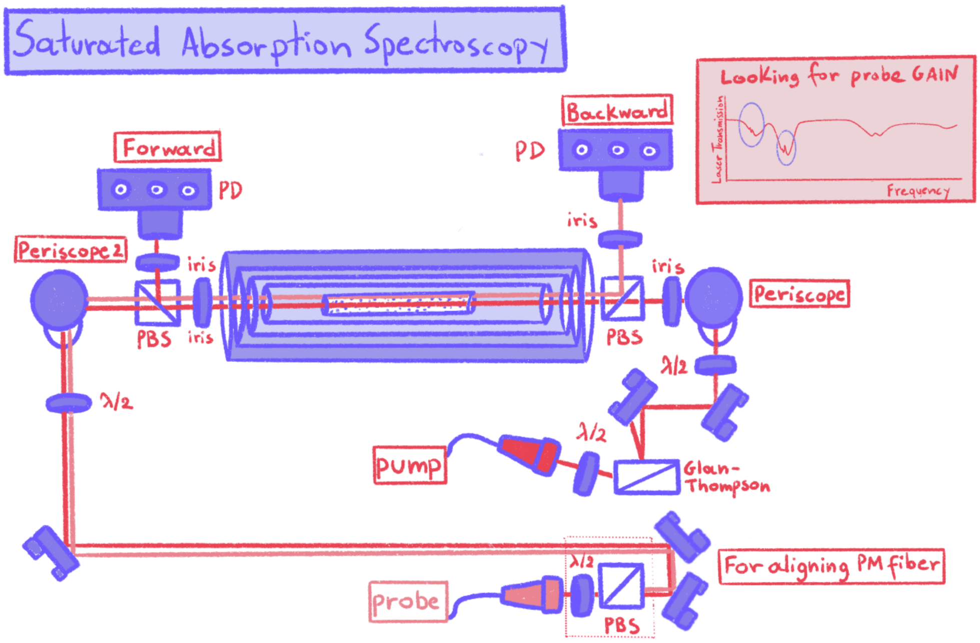

FIGURE 7.3: Saturation spectroscopy of probe beam. The dark-red line is the pump, the light-red line is the probe. We monitor both beams to see possible gain in the expected frequencies on the probe beam, as illustrated at the top right.

The idea was that, if there is a population inversion established, then the incoming probe beam, scanned through the frequencies at which we expect population inversion, will show some gain. This would be a direct observation of amplification happening in the backward direction. We tried many pump powers, ranging from a few μW to 22 mW. Our probe beam was ranging between $100-2\,\mu$W and but no gain was seen, including at the 10 times lower probe power than the beam seen in Ashtarak. The pump was equally strong as in Armenia (20 mW)and our beam size smaller, but we failed to see any gain on the probe beam.

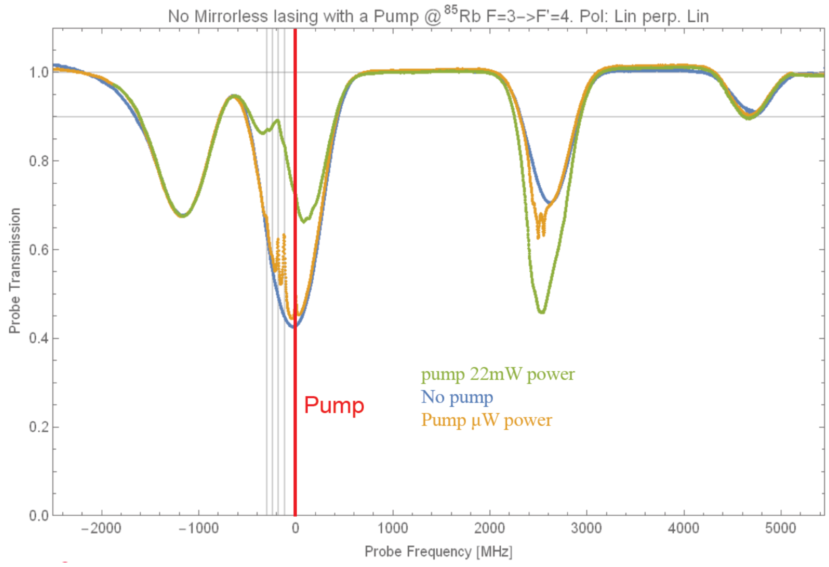

FIGURE 7.4: Setup for measuring probe gain in ^{85}Rb.

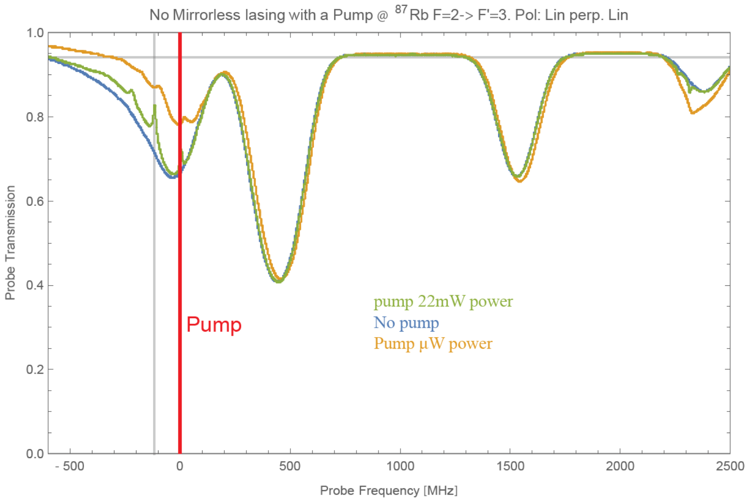

FIGURE 7.5: Setup for measuring probe gain in ^{87}Rb.

Since I did not see any signal in the backward direction, I decided to improve the forward-direction setup and check all the things that could be different from the Ashtarak setup. A list with the setup parameters that were studied follows.

Polarizers

Linear polarization of our incoming pump beam seems to be of importance to our experiment. I checked the extinction ratio of our polarizers in order to be able to have an estimation of how well the pump is polarized.

The extinction ratio of a polarizer is a measure of how well the light is polarized in a linear polarization mode. The two orthogonal linear polarization states related to transmission and reflection are **S** and **P**. The polarization that gets transmitted through a polarizer$_i$ is called P_i and is parallel to the incident surface, while the S$_i$ polarization is orthogonal to it and gets reflected. The extinction ratio is defined as the power of P_i to S_i, where S and P are always defined with respect to the plane of incidence. The plane of incidence is defined by the vector of the beam's direction and the vector of the incidence surface. Ideally a reflective polarizer will transmit only one of the two linear polarizations and reflect the other, reducing by half the incoming light intensity.

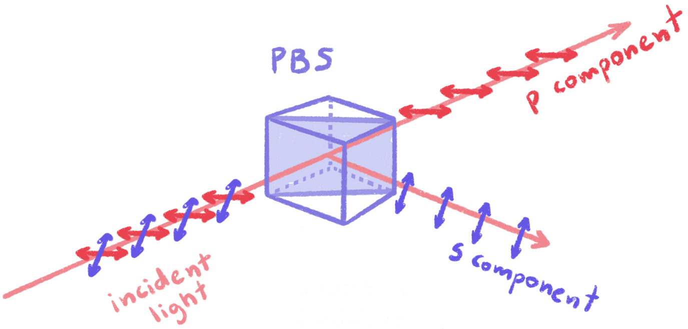

FIGURE 7.6: Example of S and P polarization of light. The incident light contains two types of polarization: S and P. The P component is parallel to the plane of incidence and the S component is perpendicular to it.

I tested the polarizers I was using with a good Glan-Thompson polarizer, with an extinction ratio of 100000 : 1. Figure 7.7 shows the setup used to test out polarizers by measuring the incoming and outcoming powers of a laser going through a good and already tested polarizer. The resulting extinction ratio was around 300 : 1 and was depending on the position of the polarizer: on the edges of the polarizing material there are more asymmetries than in the middle. This ratio was less than expected from the polarizers' specs and so we ordered new and better polarizers to replace the former with.

Temperature

Another parameter we needed to check was the temperature at which the experiment took place. In Ashtarak the work was conducted under RT. I started with RT and heated the cell with a heat gun up to 50 $°C$.

Laser Power

Since there seems to be a threshold in detecting a forward beam and a range of optimal powers, I tuned the power of our laser to the maximum I could which was around 22 mW before the cell. Lower

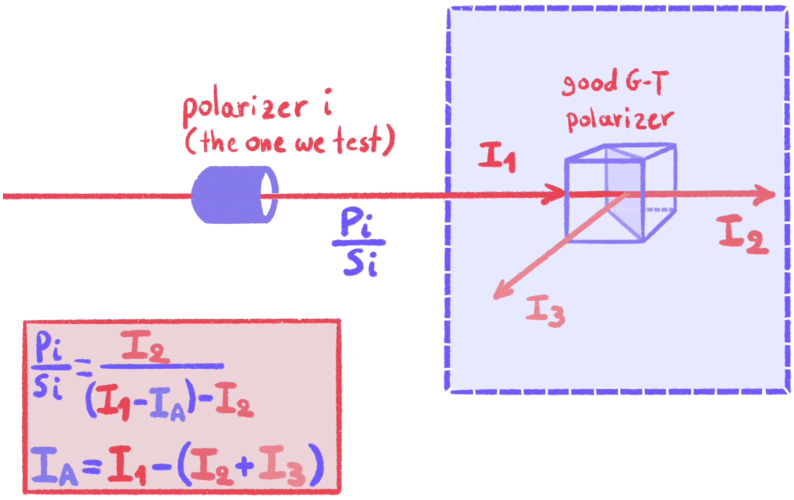

FIGURE 7.7: Measuring extinction ratio of PBSi. We test how well linearly polarized our laser with power I_1. I_2 is the power of the transmitted beam, I_3 the power of the reflected beam and I_A power of the possibly absorbed beam due to the G-T polarizer. The G-T polarizer is not a cube, but it is shown as such here for simplicity.

powers were also investigated in case we encountered a similar phenomenon as in Figure 6.4 where the forward magnetic resonance declines with higher powers. At no point between a few μW and 22 mW did we get a backward signal. One could assume that the laser power might not be enough to create all along the cell the conditions necessary for lasing. However the power after the cell is over the threshold for forward lasing, meaning we should have population inversion all along the cell.

Beam size

The beam diameter D in the improved setup was about 100 μm at the point of focus. The diffraction angle θ is $\theta \sim \frac{\lambda}{D} \sim 10^{-2}$. The cell was 14 cm long and we made sure that it focuses in the middle of the cell, so at the output of the cell the beam size is $70mm \cdot 10^{-2} = 0.7mm$. This makes it about half the size of the 1.5 mm beam size in Ashtarak.

Identify reflections

A very important background signal for backward detection are the reflections coming from the incoming pump beam getting reflected on windows of the Rb cell. The light reflects two times on the front and two times on the back of the windows covering the cylindrical cell. We can detect this way two strong and two weaker reflections on the backward direction which we must block. (The weaker ones are from the external antireflection-coated surfaces). It is also important to block the beam with a very black material after is passes the cell to avoid partial reflection back into the cell. As we will reveal later, the only signal we ever had in the backward direction in Mainz was due to the scattering of the pump beam on a wall 4 m away.

Cell birefringence

The initial guess about the discrepancy between Mainz and Ashtarak regarding the backward-direction was the possible birefringence of the cells we used. Normally glass does not induce birefringence, however stress caused by pressure or glue used to attach the windows to the cylindrical part of the cell can locally induce changes in the glass and make it birefringent. These local inhomogeneities can change the refractive index associated with a specific polarization going through the glass. If the first glass window alters the polarization of the pump beam it could be that the strict conditions for population inversion are not met.

The problem with testing this theory is that we cannot measure inside the cell to compare the possibly induced birefringence between the two setups. If we measure with crossed polarizers on the other side of the cell, the risk exists that the back window of the cell changes the output polarization as well and what we measure does not accurately reflect what the atoms see.

In order to detect backward signal in Ashtarak the cell was moved carefully and at a specific point; there was full signal detected, in contrast to zero signal when the cell was moved off this point. In Mainz it was much harder to move the cell carefully because it was inside a shield and we could move it only with a non-magnetic stick or string attached to the cell. However, we tried to compensate for birefringence by using either a quarter-wave plate and or a half-wave plate; this did not have any effect.

Scanning rate and function

Since we wanted to measure the backward signal and the fluorescence and compare to reference signals at any time, we scanned the laser frequency with a linear function from an external function generator (triangular pulses) and slow enough –between 20−0.5 Hz– for the population inversion to be established. The scanning rate was similar to the one in Ashtarak.

Magnetic field

A big difference between our two setups was the magnetic field compensation. The model we used in the forward-direction experiment requires zero field for the population inversion to be established. The compensation mechanism in Ashtarak however, were homemade Helmholtz coils with the distance of the inner smaller coils being almost equal to the length of their cell. That would create a big magnetic gradient along the cell with the sides of the cell being under a nonzero magnetic field.

Laser linewidth

Another difference was the linewidth of our pump laser. In Ashtarak it was between 15−10 MHz while our laser had sub-MHz linewidth. Later we tried to repeat the experiment with a broader laser but we still did not see backward lasing.

Forward Detection

After checking out and fixing some of the differences between our setups, I repeated parts of the forward beam experiment to detect possible changes.

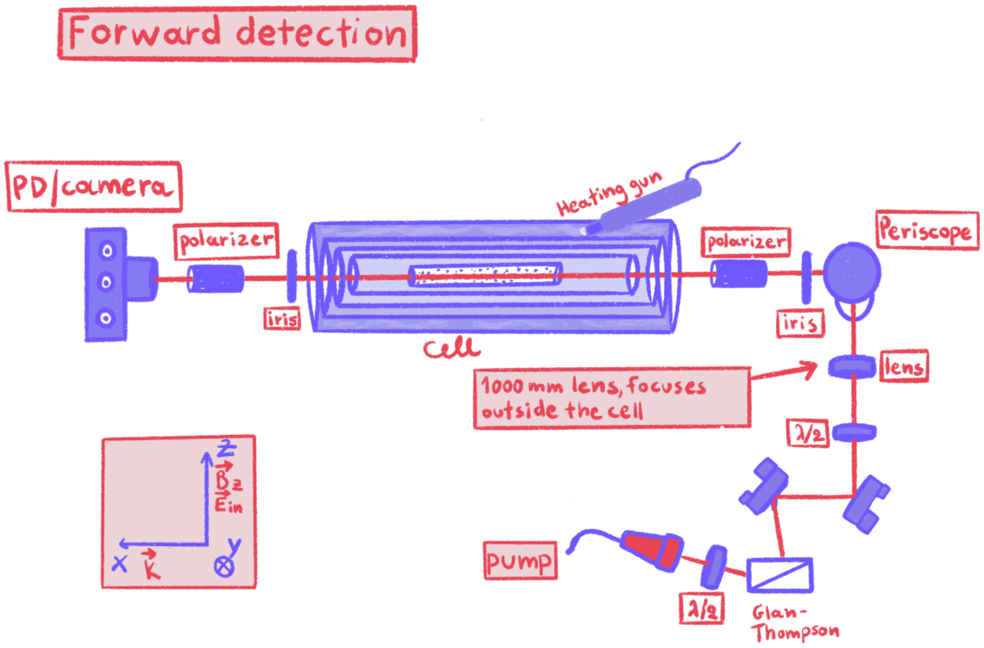

FIGURE 7.8: Forward beam experiment. We replaced all the polarizers with good ones and heated the cell starting from RT and up to 45°C. We detected either with a camera or with a photodetector to compare the data. We operated at zero(0) magnetic field.

The forward detection signal looks a lot like the results we had before. I scanned the laser at 10 mW over a 9 GHz range covering the D2 line and on the camera we can saw a bright spot appearing with a black ring in the middle for some frequencies, which seem to be shifted compared to our previous experiment. I wanted to study the ring effect a bit more. We had attributed this effect to FWM which required linear polarization, so I added a quarter-wave plate to see what happens with circular polarization. At low pump power (1.7 mW) the dark ring disappeared and re-appeared again at high power. Then, I removed the second crossed polarizer which means the detected polarization remained vertical and I could still see the ring. This phenomenon can be explained by the **Kerr effect**.

The Kerr effect is a 3rd order nonlinear effect related to the degenerate FWM effect as described in Chapter 6 only we do not need a specific polarization for it to happen. If we use a strong laser beam interacting with an atomic vapor, the latter behaves as a Kerr medium, meaning it has an intensity-dependent refractive index [132]. Our beam has a Gaussian intensity profile, meaning the intensity of the beam changes according to the Gaussian function and hence we have radial dependence of the index of refraction. The cross-section of the beam with the vapor causes nonlinearities. The high-intensity laser changes the refractive index of our vapor and the vapor acts as a lens to the beam. To better understand this process, I show Figure 7.9: the refractive index indicates how much light bends in a material. In our case, between the maximum and the minimum refractive index, we have maximum absorption, which creates the pattern of the black spot we see in the middle of the beam when we scan around a resonance with frequency ω_0.

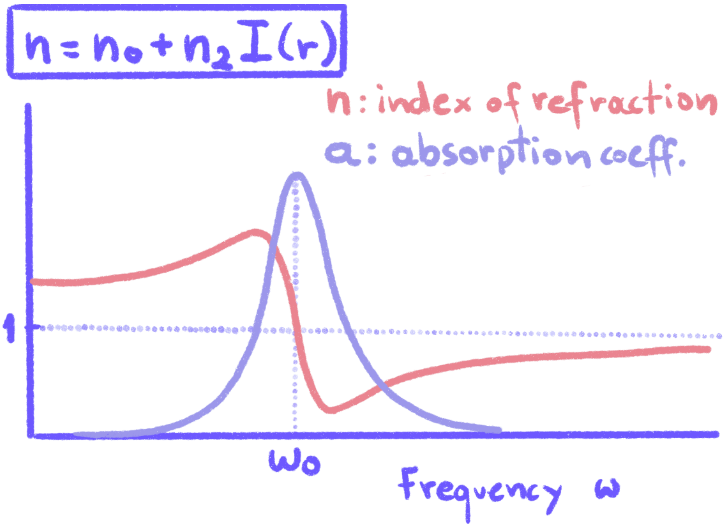

FIGURE 7.9: Kerr effect/self-focusing. The index of refraction n and the absorption coefficient in relation to frequency are illustrated for a better understanding of the Kerr/self-focusing effect. The phenomenon arises when a high-intensity laser beam propagates through a Rb vapor while the laser frequency is scanned around a resonant frequency ω_0.

I filmed the effect of self-focusing on our beam: in Figure 7.10 one can see how the beam evolves from 1-8 when we detect it using a laser-viewing card for near infrared light. In pictures 1 and 7 there is a small black ring in the middle of the beam, exactly where we have the beam maximally absorbed. Again, the beam shows this inhomogeneous behavior because its intensity in not evenly distributed and the refractive index depends on the intensity.

Backward detection

So far we have studied the forward beam in more detail. The next step was to build a setup for backward detection now that our system was better controlled and studied. Figure 7.11 shows the experimental setup.

At 50°C and at 500 mHz scanning rate across the first two resonances where we expect lasing to happen, we get faint light in the backward direction. The beam in the forward direction after the cell is at this point blocked with a black carton. The signal on the camera is two big (compared to the central spot) faint rings in the background and a flashing light in the center.

It seems that this signal arises entirely from scattering: the beam structure we see on the camera has a component that is frequency dependent (fluorescence from scattering on the carton) and one weaker and larger in the back, frequency independent (incoherent scattering on carton). When we block the beam in the forward direction with black aluminum foil, the backward signal completely disappears.

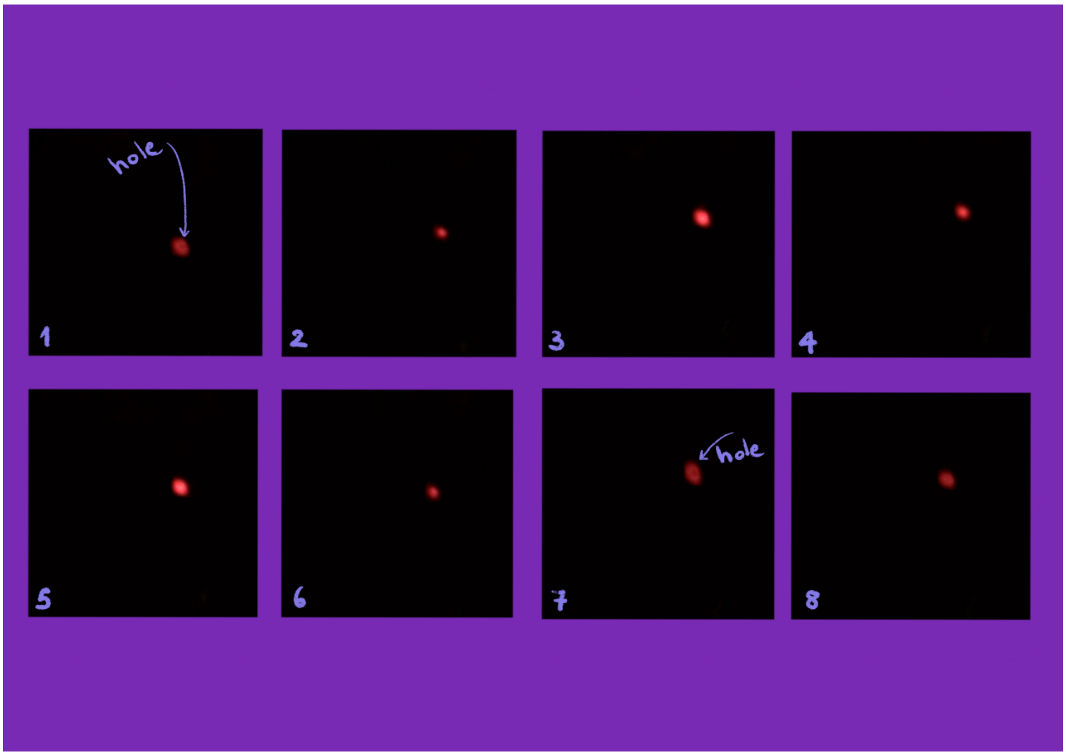

Figure 7.10: Kerr effect/self-focusing on a laser-viewing card. Pictures 1−8 show the time evolution of our detected beam without a crossed polarizer: size, shape and intensity are changing time. In picture 1 and 7 one can see a small black dot in the middle of the beam indicating self-focusing.

The next step was to put limits on backward detection: I calibrated the intensity on the camera to estimate how much power we detected. For attenuated pump, when we reflect it back with a mirror, we get 6 pW on the camera. When we block it with black carton, but not perfectly, we get 0,5 nW. When we block with good quality black paper the limit is set at 0,1 nW. Based on that and with a 30 mW beam, the estimated detected lasing efficiency is $3 * 10^{-9}$, meaning we can detect a beam that is more than 1 billion times weaker than our pump.

It is important to note here is that when I directed the beam 3 m away and focused it on the wall, I got a lot of frequency dependent light back (see above), a strong indication that scattering is important since it can create a false signal and should be checked thoroughly. The intensity we detect depends on the distance from the camera and focus of the beam as well as angle of the surface we use to block the beam with.

Discussion

The only signal in the backward direction that we were able to detect was due to scattering of the forward beam. The flashes on the camera that were frequency dependent were detected with a photodetector as well and coincided with the cross-over resonances.

This signal can arise from the system imperfections. The transmitted beam scatters on the impact surface and some of it is reflected back to the vapor cell. Due to imperfections such as window birefringence or residual magnetic field, the polarization of the back-scattered light can change so

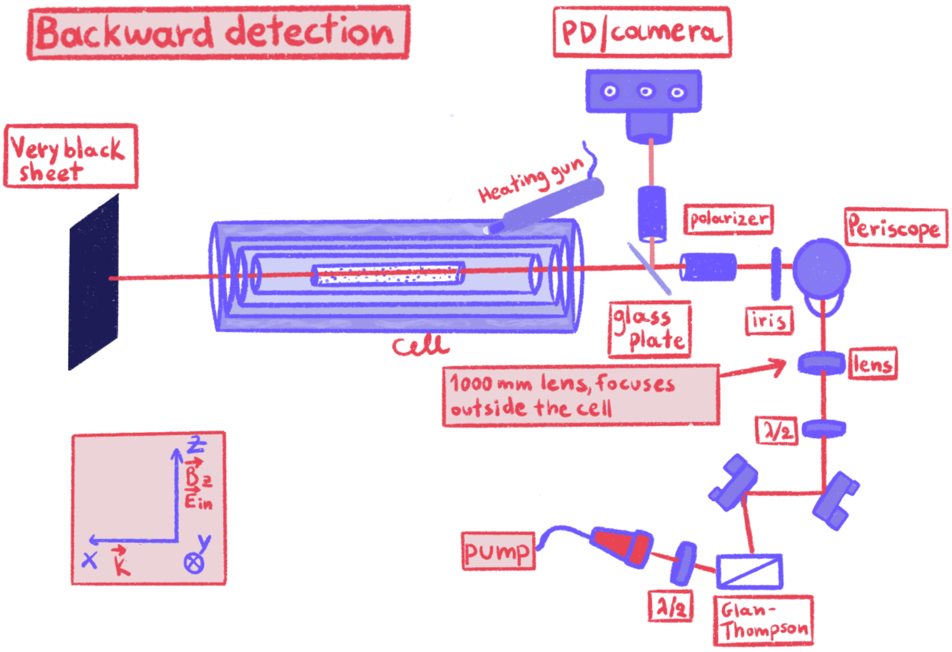

FIGURE 7.11: Backward beam experiment. We replaced all the polarizers with good ones and heated the cell starting from RT and up to 45°C. We detected either with a camera or with a photodetector to compare the data. We operated at zero(0) magnetic field. The beam in the forward direction is blocked with various materials.

that part of it would appear in the polarization channel where we expect mirrorless-lasing light, producing a Doppler-free signal. This might explain why the flashes on the camera coincide with the CO lines. At that point the scattering of the forward beam seemed to be a possible explanation for the signal seen in Ashtarak.

7.1.4 Ashtarak, part II

In order to better understand the disagreement of the results of the two setups, I took a trip to Armenia in Spring of 2019. By then, the possibles theories for the the discrepancy of our results were:

- The signal in Armenia is scattering from the wall.
- The laser in Ashtarak has a much broader linewidth of 16 MHz compared to the laser in Mainz (<100 kHz); however, we do not know why the linewidth would have such a crucial impact on the phenomenon and we can only speculate. Further experiments with a broader-linewidth laser in Mainz did not yield results.
- Difference in magnetic field compensation due to lack of a shield in Ashtarak or a much bigger gradient along the cell.
- The cell in Armenia inducing less birefringence because of the way it was made.

- Something else or a combination of the above.

With me I brought the Rb cell used in Mainz as well as the very black aluminum sheet with which I fully blocked the scattering of the forward beam.

After working on their existing setup and looking at the backward-detection signal, we replaced their cell with ours and we blocked the scattering with the black sheet. We had to move the cell from Mainz by hand a bit longer than Ashtarak's cell but we managed to get a signal with it. The black sheet suppressed the background, but not the entire signal. We also replaced the laser with an Extended Cavity Diode Laser of 1 MHz linewidth resembling our conditions a lot more. The results were the same as reported to us before: the signal appears in the region of the cycling transitions $(F_e > F_g)$ ^{85}Rb F_g=3 → F_e=4 and ^{87}Rb F_g=2 → F_e=3. We can see scattering signal from the wall which almost disappears when we later block it with the very dark sheet. There are also sub-Doppler features at the crossover resonances CO32 ^{87}Rb and CO43 ^{85}Rb. The power of the detected beam is about 10^4 times smaller than the input beam and the relation between input and output beam seems quite linear, while the input vs output intensity for the forward beam was highly nonlinear.

FIGURE 7.12: Backward beam experiment in Ashtarak. Backward-direction detection at zero field in Ashtarak. The blue line in the oscilloscope is the signal in the backward direction and the yellow line is the fluorescence.

Discussion

At this point the question remains: is this signal backward lasing?

Indications that this could be backward lasing:

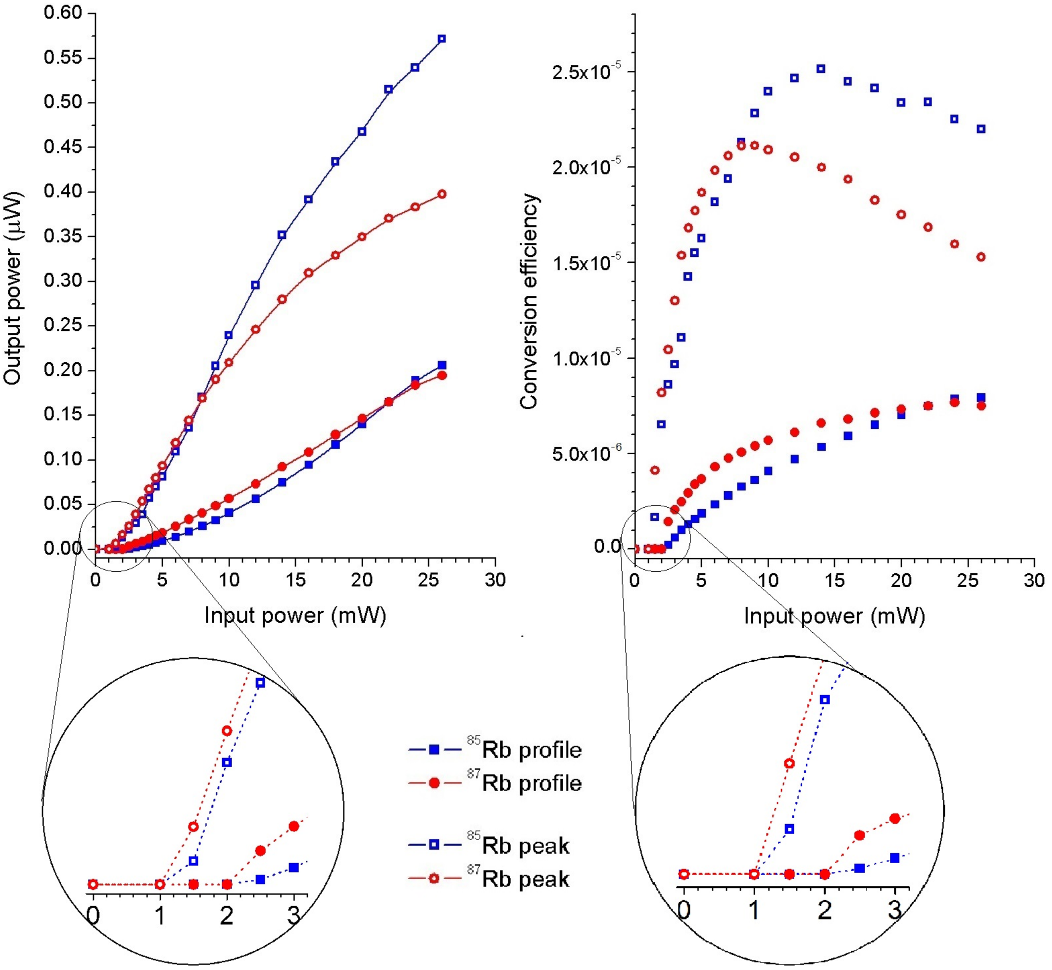

FIGURE 7.13: Data from Ashtarak, not yet published: Zero magnetic field input power dependence of the absolute (left panel) and normalized (right panel) backward radiation power. Solid symbols: amplitudes of Doppler-broadened contours of ^{87}Rb (circles) and ^{85}Rb (squares) transitions, Open symbols: amplitudes of the narrow peaks located at corresponding crossover resonances CO32 (circles) and CO43 (squares). Lines are drawn to guide the eye.

- When a random back reflection from the cell windows goes in the beam path, we get no signal.
- There is a magnetic field dependence of the backward signal when none is expected without mirrorless lasing, beam vanishes at ±0.5 G.
- Peaks are only seen at the expected transitions $F_e > F_g$ from our model in Chapter 6

Issues of concern:

- To get a backward signal there is always a back reflection from a window 1-3 beam diameters from the pinhole.
- The nature of the Doppler-free structure is not clear. It is usually created by a counter-propagating beam, so this enhances the idea that this might be a back reflection of some

sort. You can also have these nonlinear ellipticity effects, induced by cell birefringence that give quite similar signals even in zero field, see [133].

- The fact that the cell needs to be moved around in order to get a signal could indicate induced birefringence. However, the always sudden appearance of the effect implies that the conditions for the polarization have to be very strict, avoiding the tiniest ellipticity. It could also imply that there is seeding of the effect with the right ellipticity in some backward scattering.
- Could uncompensated magnetic fields create other effects? Or could the gradient field that is bigger in the Ashtarak experiment play a role in the creation of a backward-lasing beam? A strange effect in this experiment was that when applying a Bx field (along k) the backward signal grew from 0 to 0.5 .

7.1.5 Mainz, part II

The last part of the experiment took place in Mainz and some of our collaborators from Ashtarak visited as well. The two final parameters that struck us as most important were the possible birefringence of the cell and the different magnetic environment or gradient along the cell.

In order to be able to move the cell inside the magnetic shield, our collaborators designed a 3D printed plastic case which could be translated from outside. It was not as precise as moving the cell by the hand, but it was still a good enough motion for testing different input spots on the windows.

The next idea was to apply a magnetic field along the longitudinal direction which showed an increase in backward signal in Ashtarak. This did not give any signal back *with the exception* of adding a mirror after the crossed polarizer: When we had a back-reflection, and when we added magnetic field along x (parallel to $\mathbf{k}$), we got a signal in the backward direction that resembles the one seen in Ashtarak. However we could not get backward radiation in the way our collaborators seem to have detected. We have postponed further experiments until we have a more solid model that calculates the possible gain in this system. To this day, the mystery of backward degenerate lasing has not been solved.

7.1.6 Conclusions

Degenerate mirrorless lasing is an interesting phenomenon that has been experimentally observed in the forward direction. However, more experimental work needs to be done for backward directed emission and the theory behind needs to be better understood.

7.2 Spin locking in Rb

In this final part of the Section of unsolved lab mysteries, I will shortly describe a project that never came to an end due to discrepancies with previously published results. It serves more as a report, in the case that a future researcher wants to look into the topic of spin-locking.

7.2.1 The idea

The idea of this project was to take the method of spin locking as published in [94] and apply it on Rb in an unshielded environment. We worked on two levels in the case: We were building the equipment for working eventually on earth field without a shield and in parallel we were testing out how spin locking works in Rb inside a magnetic shield.

7.2.2 Experiment

We simulated the conditions of the spin locking paper in Cs [94]. We attempted to ask the following questions in ^{87}Rb:

- How does the resonance look at low fields and what is the linewidth?
- Are there residual fields in the shield?
- Is there a big gradient along the main magnetic field?
- How does the resonance change with higher fields?
- How does the resonance look at earth field and what is the width of each peak?
- Scan amplitude and phase of the RF field to find where and if there is a narrowing in the linewidth through spin locking

The setup is shown in Figure 7.16 and the experimental parameters follow in detail.

Cell

I used a Rb cell containing both ^{87}Rb and ^{85}Rb. In comparison the project we tried to reproduce was using Cs. Both the Rb and the Cs cell are 5 cm.

Pump-probe

The pump was locked to the ^{85}Rb D1 line $F = 3$ and the probe was D2 ^{87}Rb $F = 3$ detuned towards $F = 3$. The axes were the same as in [94]: The leading field along z (long axis of the shield and cell), the pump along y (from the top of the cell) and the probe along x.

Pump-probe powers

The light power of the pump during the “on” part of the cycle is $1\,mW$ and the probe power is at $20\,\mu W$. In [94]: the pump power was at $50\,\mu W$ and the probe at $10\,\mu W$.

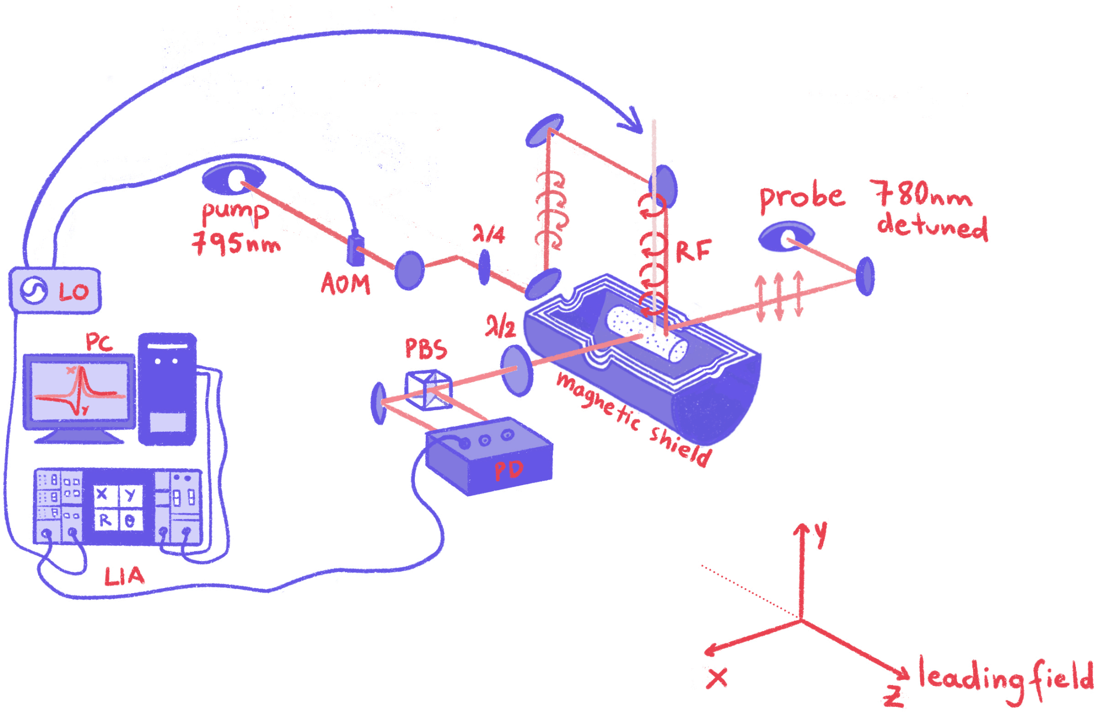

FIGURE 7.14: Spin-locking setup in ^{87}Rb.

Duty circle

The duty circle was 5% of the pump modulation in our case and 3% in the Cs spin-locking paper.

Leading field

The leading field was 55000 nT in our case and 98000 nT in [94].

RF (spin-locking) field

In both projects, the spin locking (RF) field is applied along the pump axis, is a sine wave and its frequency is equal to the modulation frequency. I tried out different RF-field strengths which we report in mV. The Voltage corresponds to a magnetic field of $41.2 * Voltage$. For example: $10\,mV \rightarrow 0.412\,nT$, $167\,mV \rightarrow 6.8\,nT$, etc.

7.2.3 Results

After setting up the experiment in Rb, as seen in Figure 7.14, I recorded the magnetic resonance without a spin-locking field on Earth field (in this case 30μT). As seen in Figure 7.15 the resonance splits in 4 peaks. The NLZ revival frequency for ^{87}Rb for 30μT is calculated to be 6.45 Hz, hence the split from one peak to the other should be about 12.9 Hz (2∗revival frequency). At a first glance, the split seems to fit the calculation. To be more precise, I fit the the X, Y and R components of the resonance with 4 different parameters for width and 4 for amplitude. The split the fit calculates agrees to what we roughly assumed and is around 11.6 Hz, the amplitudes vary quite a lot. The split we see comes from the NLZ effect, but there seem to be asymmetries in the shape and amplitude of the peaks possibly due to heading error or gradient.

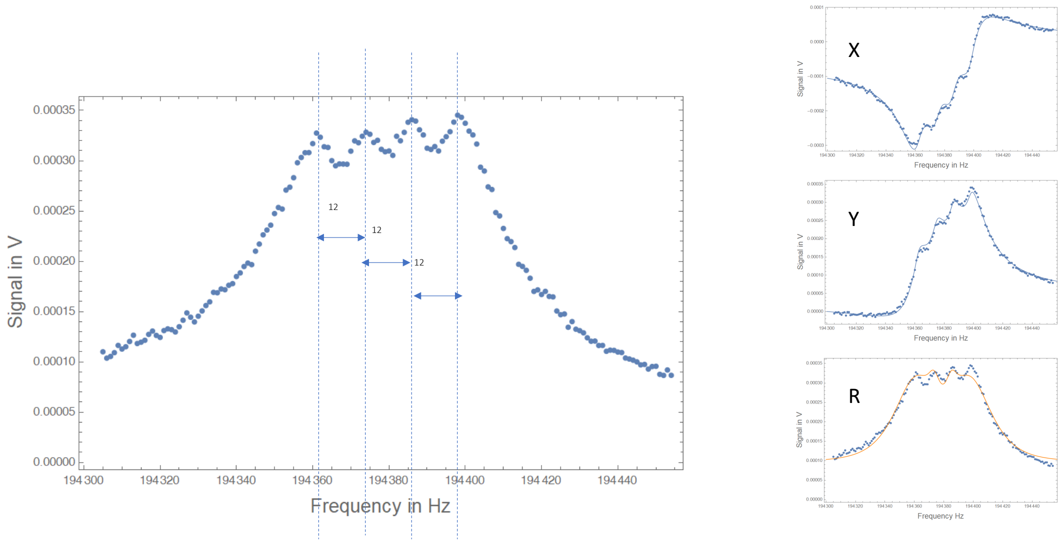

A

B

FIGURE 7.15: Rb Resonance under Earth field, at 30μT. The resonance and an estimation of the split is seen on the left and the right side shows the fitting of the X, Y and R components of the resonance.

I measured the residual field in the middle of the shield and cell– when all other fields are off – and I found along x: 16 nT, along y: 16 nT and along z: 30 nT. Next, while having the field on along z at 18.4 μT, I measured the magnetic field with a fluxgate (by hand) along the whole shield with a step of 1 cm, starting at 1 cm away from the inner coil. The gradient seems to be very roughly 100 nT along the cell (5 cm).

Another parameter we tested was the phase of the RF field; I choose the "best phase" based on which phase gives the maximum amplitude. This seems to change with different amplitudes of the RF field.

Figure 7.16 shows the Rb resonance at 55 μT for different RF-field amplitudes.

7.2.4 Discussion

It seems that in our Rb setup, the RF field makes the amplitude bigger and narrows the whole resonance, which is consistent to the results in Cs [94]. However, it does not decrease the signal's amplitude in the off-resonant case as seen in Figure 7.17 and marked by the dashed green lines. In our case, the RF field increases the signal, but in [94] the spin locking field dramatically decreases the signal.

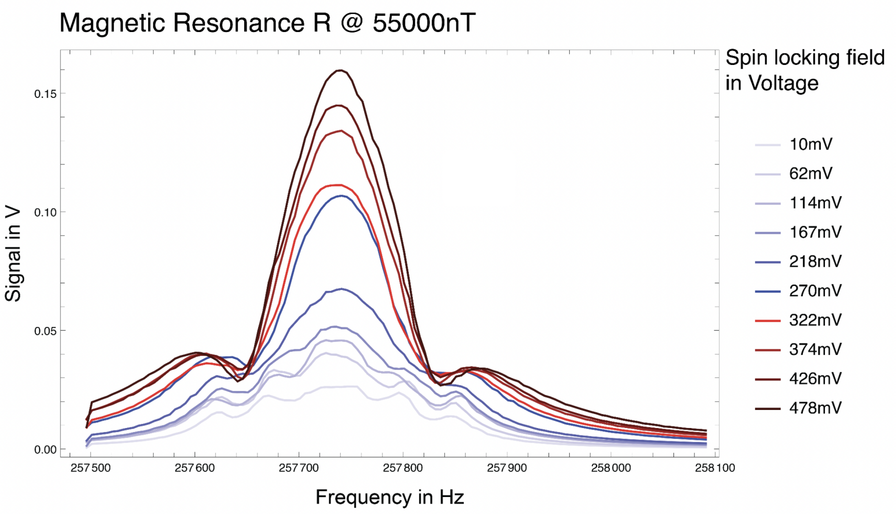

FIGURE 7.16: Spin locking in Rb at 55μT for different RF-field amplitudes.

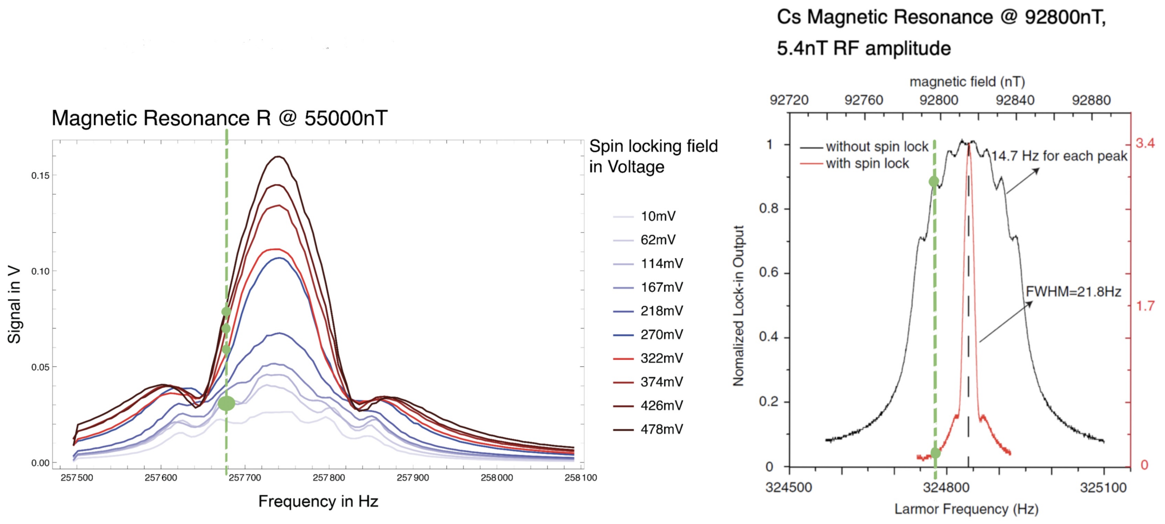

FIGURE 7.17: Comparison between spin locking in Rb (left) and Cs (right) and how it affects the off-resonant case.

7.2.5 Conclusions

Although narrowing is observed in both cases, there are differences between the two and one would need to make a direct "longitudinal" comparison between different signals in the two cases. There are also more subtle things to discuss such as asking ourselves if both cases should be called spin locking or if one of the two helps magnetometry more.

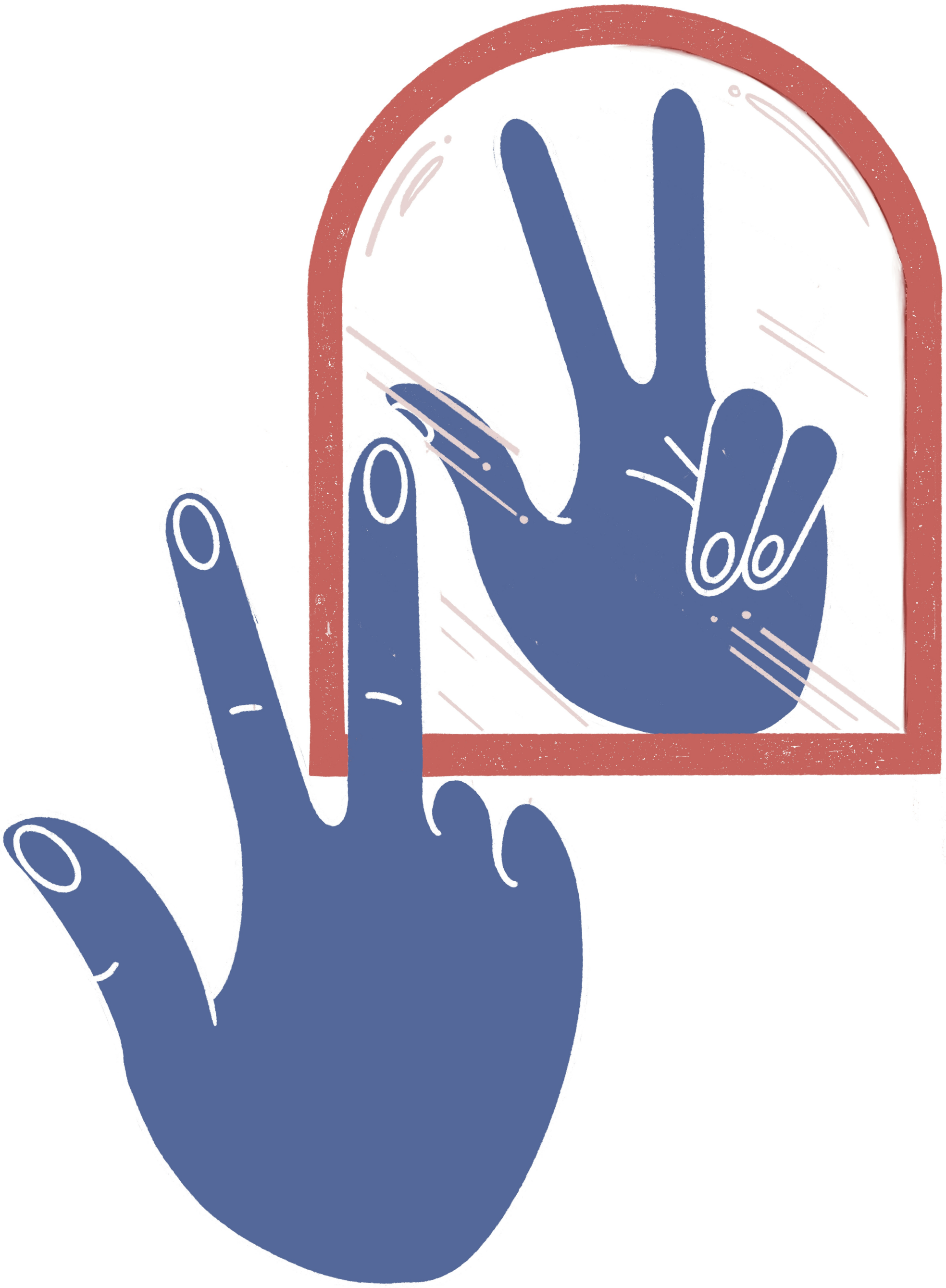

8

Conclusions

In this thesis, I describe the major projects that I worked on during my PhD research. Each chapter in the thesis provides a separate outlook for each project.

In particular, an important part of the work was focused on Earth-Field magnetometry and how to improve the sensitivity of the magnetometers working in the geomagnetic field range (Chapters 4, 5). Specifically, my first project was on all-optical spin locking, where we developed an all-optical magnetometer and demonstrated a method to suppress the NLZ effect in the range of the Earth's magnetic field. This method improves the sensitivity of earth-field-range magnetometers for two reasons: an increase in the magnetic resonance signal amplitude and a reduction in the effective linewidth. On the same topic, we came up with the idea of making a magnetometer that is completely free of heading error. Here, we presented a sensitive scalar magnetometer that is free from (NLZ) related heading error and has a sensitivity of tens of $\mathrm{fT}/\sqrt{\mathrm{Hz}}$ in the Earth's magnetic field range. Next steps in this field would include building these magnetometers without any kind of shielding and testing them on Earth-Field and in an environment that is not magnetically noisy.

In parallel to the Earth-Field magnetometer projects I was working on mirrorless lasing (Chapters 7, 6). We observed degenerate mirrorless lasing in the forward direction, but we had different results than our collaborators for the backward direction. More experimental work is needed on backward directed emission, and the theory behind it must be better understood through the construction of more accurate models.

Results presented in this thesis were first published in the following papers: [93], [65], [120], [49]

Bibliography

[1] M. W. McElhinny, R. Merrill, *The earth's magnetic field : its history, origin, and planetary perspective* (London ; New York : Academic Press, 1983).

[2] T. Gillian, *North Pole, South Pole : the epic quest to solve the great mystery of Earth's magnetism* (New York, NY: The Experiment, 2010).

[3] J. Osborne, J. Orton, O. Alem, V. Shah, *Proc. of SPIE* **10548**, 105481G (2018).

[4] J. Kitching, *Applied Physics Reviews* **5**, 031302 (2018).

[5] D. Sheng, A. R. Perry, S. P. Krzyzewski, J. K. S. Geller, S. Knappe, *Applied Physics Letters* **110**, 031106 (2017).

[6] H. Dehmelt, Modulation of a light beam by precessing absorbing atoms, *Phys. Rev.* **105**, 1924–1925 (1957).

[7] W. Bell, A. Bloom, Optical detection of magnetic resonance in alkali metal vapor, *Phys. Rev.* **107**, 1559–1565 (1957).

[8] W. Bell, A. Bloom, Optically driven spin precession, *Phys. Rev. Lett.* **6**, 280–281 (1961).

[9] I. K. Kominis, T. W. Kornack, J. C. Allred, M. V. Romalis, *Nature* **422**, 596–599 (2003).

[10] J.-H. Storm, P. Hömmen, D. Drung, R. Körber, *Appl. Phys. Lett.* **110**, 072603 (2017).

[11] H. B. Dang, A. C. Maloof, M. V. Romalis, *Applied Physics Letters* **97**, 151110 (2017).

[12] K. Jensen, M. A. Skarsfeldt, H. Stærkind, J. Arnbak, M. V. Balabas, S.-P. Olesen, B. H. Bentzen, E. S. Polzik, *Scientific Reports* **8** (2018).

[13] I. A. et al., *Phys. Rev. Lett.* **103** (2009).

[14] J. M. Higbie, E. Corsini, D. Budker, *Review of Scientific Instruments* **77** (2006).

[15] A. L. Bloom, *Applied Optics* **1** (1962).

[16] G. Bison, R. Wynands, A. Weis, *Optics Express* **11** (2009).

[17] M. D. et al., *Space Sci. Rev.* **114** (2004).

[18] D. Budker, M. Romalis, *Nature Physics* **3** (2007).

[19] D. Budker, D. F. J. Kimball, *Optical Magnetometry* (Cambridge University Press, 2013).

[20] A. E. Siegman, *Lasers* (University Science Books, 1986).

[21] T. Dudok, Y. Nastishin, Optically pumped mirrorless lasing. a review. part i. random lasing, *Ukrainian Journal of Physical Optics* **14**, 146-170 (2013).

[22] M. S. Malcuit, J. J. Maki, D. J. Simkin, R. W. Boyd, Transition from superfluorescence to amplified spontaneous emission, *Phys. Rev. Lett.* **59**, 1189–1192 (1987).

[23] H. Cao, J. Xu, Y. Ling, A. Burin, E. Seeling, X. Liu, R. Chang, Random lasers with coherent feedback, *IEEE Journal of Selected Topics in Quantum Electronics* **9**, 111-119 (2003).

[24] B. V. Zhdanov, R. J. Knize, Review of alkali laser research and development, *Optical Engineering* **52** (2012).

[25] M. Auzinsh, D. Budker, S. M. Rochester, Light-induced polarization effects in atoms with partially resolved hyperfine structure and applications to absorption, fluorescence, and nonlinear magneto-optical rotation, *Phys. Rev. A* **80**, 053406 (2009).

[26] J. Weiner, F. Nunes, *Light-Matter Interaction: Physics and Engineering at the Nanoscale, Second Edition* (Oxford University Press, 2017).

[27] E. Liarokapis, *Notes in Atomic and molecular physics* (School of applied mathematical and physical sciences, NTUA, Athens, 2012).

[28] T. Henrich, *Optisches Pumpen von 3He und Polarisationsanalyse, Basierend auf der wissenschaftlichen Prüfungsarbeit für die erste Staatsprüfung für das Lehramt an Gymnasien* (Johannes Gutenberg Universität, Mainz, 2008).

[29] E. Tiesinga, P. J. Mohr, D. B. Newell, B. N. Taylor, Codata recommended values of the fundamental physical constants: 2018, *Rev. Mod. Phys.* **93**, 025010 (2021).

[30] M. Auzinsh, D. Budker, S. Rochester, *Optically Polarized Atoms: Understanding Light-atom Interactions* (Oxford University Press, 2010).

[31] R. Coker, Physics 362l, `https://web2.ph.utexas.edu/~coker2/index.files/ch36pt2317L.htmaccessedon2022-11-24`.

[32] P. Dirac, *The principles of quantum mechanics* (Oxford University Press, 1947).

[33] C. Cohen-Tannoudji, B. Diu, F. Laloe, *Quantum Mechanics, Vol. 1* (Wiley-VCH, 1977).

[34] W. Happer, Optical pumping, *Reviews of modern physics* **44** (1972).

[35] E. B. Alexandrov, M. Auzinsh, D. Budker, D. F. Kimball, S. M. Rochester, V. V. Yashchuk, Dynamic effects in nonlinear magneto-optics of atoms and molecules, *Journal of the Optical Society of America B* **22** (2005).

[36] T. Haider, A review of magneto-optic effects and its application, *International Journal of Electromagnetics and Applications* **7**, 17-24 (2017).

[37] D. Vojna, M. Duda, R. Yasuhara, O. Slezák, W. Schlichting, K. Stevens, H. Chen, A. Lucianetti, , T. Mocek, Verdet constant of potassium terbium fluoride crystal as a function of wavelength and temperature, *Optics Letters* **45** (2020).

[38] S. Pustelny, Nonlinear magneto-optical effects, Ph.D. thesis, Jagiellonian University Krakow (2007).

[39] M. Mazilu, J. Baumgartl, S. Kosmeier, K. Dholakia, Optical eigenmodes; exploiting the quadratic nature of the energy flux and of scattering interactions, *Optics Express* **19** (2011).

[40] D. Budker, W. Gawlik, D. F. Kimball, S. M. Rochester, V. V. Yashchuk, A. Weis, Resonant nonlinear magneto-optical effects in atoms, *Rev. Mod. Phys.* **74** (2002).

[41] M. P. A. Jones, Atom-light interactions.

[42] F. X. Kärtner, O. D. Mücke, *Nonlinear Optics* (Center for Free-Electron Laser Science, DESY Department of Physics, University of Hamburg, 2016).

[43] R. Pool, Molecular orientation at biological interfaces, water and lipids studied through surface-specific vibrational spectroscopy, Ph.D. thesis, University of Amsterdam (2013).

[44] S. B. Mendes, P. Tandy, Advanced optics phys 545, `https://www.physics.louisville.edu/sbmendes/` (2010). Accessed on 2022-12-09.

[45] C. Cohen-Tannoudji, *Manipulating atoms with photons* (Nobel Lecture, 1997).

[46] J. A. McGovern, Advanced quantum mechanics i, lecture notes, `https://theory.physics.manchester.ac.uk/~judith/` (2012). Accessed: 2023–27-03.

[47] C. Cohen-Tannoudji, J. Dupont-Roc, G. Grynberg, *Photons and Atoms : Introduction to Quantum Electrodynamics* (Wiley-VCH, 1989).

[48] A. Fabricant, I. Novikova, G. Bison, How to build a magnetometer with thermal atomic vapors: A tutorial, *New J. Phys.* **25** (2023).

[49] A. Ramaswamy, J. Chathanathil, D. Kanta, E. Klinger, A. Papoyan, S. Shmavonyan, A. Khanbekyan, A. Wickenbrock, D. Budker, S. A. Malinovskaya, Mirrorless lasing: a theoretical perspective (2023).

[50] D. A. Steck, Rubidium 87 d line data, `http://steck.us/alkalidata` (2010). Revision 2.1.4, 23 December 2010).

[51] M. T. Graf, D. F. Kimball, S. M. Rochester, K. Kerner, C. Wong, D. Budker, E. B. Alexandrov, M. V. Balabas, V. V. Yashchuk, Relaxation of atomic polarization in paraffin-coated cesium vapor cells, *Phys. Rev. A* **72**, 023401 (2005).

[52] E. B. Alexandrov, M. V. Balabas, D. Budker, D. English, D. F. Kimball, C.-H. Li, V. V. Yashchuk, Light-induced desorption of alkali-metal atoms from paraffin coating, *Phys. Rev. A* **66**, 042903 (2002).

[53] V. M. Acosta, M. Auzinsh, W. Gawlik, P. Grisins, J. M. Higbie, D. F. J. Kimball, L. Krzemien, M. P. Ledbetter, S. Pustelny, S. M. Rochester, V. V. Yashchuk, D. Budker, Production and detection of atomic hexadecapole at earth's magnetic field, *Opt. Express* **16**, 11423–11430 (2008).

[54] V. V. Yashchuk, D. Budker, W. Gawlik, D. F. Kimball, Y. P. Malakyan, S. M. Rochester, Selective addressing of high-rank atomic polarization moments, *Phys. Rev. Lett.* **90** (2003).

[55] S. Groeger, G. Bison, J.-L. Schenker, R. Wynands, A. Weis, A high-sensitivity laser-pumped mx magnetometer, *Eur. Phys. J. D* **38**, 239–247 (2006).

[56] W. Gawlik, J. Kowalski, R. Neumann, F. Träger, Strong narrowing of the na forward scattering signals due to the interaction with an intense dye laser field, *Phys. Rev. A* **48**.

[57] D. Budker, D. F. Kimball, S. M. Rochester, V. V. Yashchuk, Nonlinear magneto-optical rotation via alignment-to-orientation conversion, *Phys. Rev. Lett.* **85**, 2088–2091 (2000).

[58] D. Budker, D. F. Kimball, V. V. Yashchuk, M. Zolotorev, Nonlinear magneto-optical rotation with frequency-modulated light, *Phys. Rev. A* **65**, 055403 (2002).

[59] W. Gawlik, L. Krzemień, S. Pustelny, D. Sangla, J. Zachorowski, M. Graf, A. O. Sushkov, D. Budker, Nonlinear magneto-optical rotation with amplitude modulated light, *Applied Physics Letters* **88**, 131108 (2006).

[60] S. J. Seltzer, Developments in alkali-metal atomic magnetometry, Ph.d. dissertation, Princeton University, Princeton, NJ (2008).

[61] W. Happer, H. Tang, Spin-exchange shift and narrowing of magnetic resonance lines in optically pumped alkali vapors, *Physical Review Letters* **31**, 273 (1973).

[62] G. Breit, I. I. Rabi, Measurement of nuclear spin, *Physical Review* **38**, 2082 (1931).

[63] MOGLabs, External cavity diode laser manual, `https://www.moglabs.com/products/tunable-lasers/littrow-lasers` (2014-2023).

[64] Vitawave, Technical description and instruction manual of an extended cavity diode laser ecdl-7830r, `http://vitawave.ru/eng/manuals/` (2014).

[65] G. Bao, D. Kanta, D. Antypas, S. Rochester, K. Jensen, W. Zhang, A. Wickenbrock, D. Budker, All-optical spin locking in alkali-vapor magnetometers, *Phys. Rev. A* **105** (2022).

[66] G. Oelsner, V. Schultze, R. IJsselsteijn, F. Wittkämper, R. Stolz, Sources of heading errors in optically pumped magnetometers operated in the earth's magnetic field, *Phys. Rev. A* **99** (2019).

[67] K. Jensen, V. M. Acosta, J. Higbie, M. P. Ledbetter, S. Rochester, D. Budker, *Phys. Rev. A* **79** (2009).

[68] S. J. Seltzer, P. J. Meares, M. V. Romalis, *Phys. Rev. A* **75** (2007).

[69] A. Ben-Kish, M. Romalis, *Physical Review Letters* **105** (2010).

[70] V. Acosta, M. P. Ledbetter, S. Rochester, D. Budker, D. F. J. Kimball, D. C. Hovde, W. Gawlik, S. Pustelny, J. Zachorowski, V. V. Yashchuk, *Phys. Rev. A* **73** (2006).

[71] G. Bao, A. Wickenbrock, S. Rochester, W. Zhang, D. Budker, *Physical Review Letters* **120** (2018).

[72] G. Bison, N. Castagna, A.Hofer, P. Knowles, J.-L. Schenker, M. Kasprzak, H. Saudan, A. Weis, A room temperature 19-channel magnetic field mapping device for cardiac signals, *Appl. Phys. Lett.* **95**, 173701 (2009).

[73] G. Lembke, S. N. Erné, H. Nowak, B. Menhorn, A. Pasquarelli, G. Bison, Optical multichannel room temperature magnetic field imaging system for clinical application, *Biomed. Opt. Express* **5**, 876–881 (2014).

[74] S. Groeger, G. Bison, A. Weis, Design and performance of laser-pumped cs-magnetometers for the planned ucn edm experiment at psi, *Journal of research of the National Institute of Standards and Technology* **110**, 179 (2005).

[75] E. Aleksandrov, M. Balabas, S. Dmitriev, N. A. Dovator, A. I. Ivanov, M. I. Karuzin, V. N. Kulyasov, A. S. Pazgalev, A. P. Serebrov, Quantum magnetometer for stabilization of the neutron magnetic resonance, *Tech. Phys. Lett.* **32**, 627–629 (2006).

[76] A. Borna, T. R. Carter, J. D. Goldberg, A. P. Colombo, Y.-Y. Jau, C. Berry, J. McKay, J. Stephen, M. Weisend, P. D. D. Schwindt, A 20-channel magnetoencephalography system based on optically pumped magnetometers, *Phys. Med. Biol.* **62**, 8909 (2017).

[77] T. M. Ito, the nEdm Collaboration, *Journal of Physics: Conference Series* (IOP Publishing, 2007), vol. 69, p. 012037.

[78] A. Kraft, H.-C. Koch, M. Daum, W. Heil, T. Lauer, D. Neumann, A. Pazgalev, Y. Sobolev, A. Weis, Development of a 3he magnetometer for a neutron electric dipole moment experiment, *EPJ Techniques and Instrumentation* **1**, 8 (2014).

[79] J. M. Higbie, , S. M. Rochester, B. Patton, R. Holzlöhner, D. B. Calia, D. Budker, Magnetometry with mesospheric sodium, *Proceedings of the National Academy of Sciences* **108**, 3522–3525 (2011).

[80] B. Patton, O. O. Versolato, D. C. Hovde, E. Corsini, J. M. Higbie, D. Budker, A remotely interrogated all-optical 87 rb magnetometer, *Appl. Phys. Lett.* **101**, 083502 (2012).

[81] F. P. Bustos, D. B. Calia, D. Budker, M. Centrone, J. Hellemeier, P. Hickson, R. Holzlöhner, S. Rochester, Remote sensing of geomagnetic fields and atomic collisions in the mesosphere, *arXiv preprint arXiv:1802.04686* (2018).

[82] B. S. Mathur, H. Tang, W. Happer, Light shifts in the alkali atoms, *Phys. Rev.* **171**, 11 (1968).

[83] C. Cohen-Tannoudji, J. Dupont-Roc, Experimental study of zeeman light shifts in weak magnetic fields, *Phys. Rev. A* **5**, 968 (1972).

[84] F. L. Kien, P. Schneeweiss, A. Rauschenbeutel, Dynamical polarizability of atoms in arbitrary light fields: general theory and application to cesium, *The European Physical Journal D* **67**, 92 (2013).

[85] B. Patton, E. Zhivun, D. C. Hovde, D. Budker, All-optical vector atomic magnetometer, *Phys. Rev. Lett.* **113**, 013001 (2014).

[86] E. Zhivun, A. Wickenbrock, B. Patton, D. Budker, Alkali-vapor magnetic resonance driven by fictitious radiofrequency fields, *Appl. Phys. Lett.* **105**, 192406 (2014).

[87] E. Zhivun, A. Wickenbrock, J. Sudyka, B. Patton, S. Pustelny, D. Budker, Vector light shift averaging in paraffin-coated alkali vapor cells, *Opt. Express* **24**, 15383–15390 (2016).

[88] Z. Lin, X. Peng, W. Li, H. Wang, H. Guo, Magneto-optical double resonance driven by fictitious fields, *Opt. Express* **25**, 7668–7676 (2017).

[89] B. Julsgaard, Entanglement and quantum interactions with macroscopic gas samples, Ph.D. thesis, Aarhus Universitetsforlag (2003).

[90] S. M. Rochester, Modeling nonlinear magneto-optical effects in atomic vapors, Ph.D. thesis, UC Berkeley (2010).

[91] S. Coop, S. Palacios, P. Gomez, Y. N. M. de Escobar, T. Vanderbruggen, M. W. Mitchell, Floquet theory for atomic light-shift engineering with near-resonant polychromatic fields, *Opt. Express* **25**, 32550–32559 (2017).

[92] V. V. Yashchuk, D. Budker, J. R. Davis, Laser frequency stabilization using linear magneto-optics, *Review of Scientific Instruments* **71**, 341–346 (2000).

[93] R. Zhang, D. Kanta, A. Wickenbrock, H. Guo, D. Budker, Heading-error-free optical atomic magnetometry in the earth-field range, *Phys. Rev. Lett.* **130** (2023).

[94] G. Bao, A. Wickenbrock, S. Rochester, W. Zhang, D. Budker, Suppression of the nonlinear zeeman effect and heading error in earth-field-range alkali-vapor magnetometers, *Phys. Rev. Lett.* **120**, 033202 (2018).

[95] G. Oelsner, V. Schultze, R. IJsselsteijn, F. Wittkämper, R. Stolz, Sources of heading errors in optically pumped magnetometers operated in the earth's magnetic field, *Phys. Rev. A* **99**, 013420 (2019).

[96] W. Lee, V. G. Lucivero, M. V. Romalis, M. E. Limes, E. L. Foley, T. W. Kornack, Heading errors in all-optical alkali-metal-vapor magnetometers in geomagnetic fields, *Phys. Rev. A* **103**, 063103 (2021).

[97] Y. Chang, Y.-H. Guo, S.-A. Wan, J. Qin, Asymmetric heading errors and its suppression in atomic magnetometers (2021).

[98] K. Jensen, V. M. Acosta, J. M. Higbie, M. P. Ledbetter, S. M. Rochester, D. Budker, Cancellation of nonlinear zeeman shifts with light shifts, *Phys. Rev. A* **79**, 023406 (2009).

[99] A. Ben-Kish, M. V. Romalis, Dead-zone-free atomic magnetometry with simultaneous excitation of orientation and alignment resonances, *Phys. Rev. Lett.* **105**, 193601 (2010).

[100] S. Pustelny, M. Koczwara, L. Cincio, W. Gawlik, Tailoring quantum superpositions with linearly polarized amplitude-modulated light, *Phys. Rev. A* **83** (2011).

[101] E. G. The Editors of Encyclopaedia Britannica, anisotropy. URL: `https://www.britannica.com/science/anisotropy`. Accessed on 2021-10-29.

[102] W. Happer, Optical pumping, *Rev. Mod. Phys.* **44**, 169–249 (1972).

[103] F. Renzoni, E. Arimondo, Depopulation and repopulation pumping in coherent population trapping, *EPL* **46** (1999).

[104] W. Chalupczak, R. M. Godun, S. Pustelny, W. Gawlik, Room temperature femtotesla radio-frequency atomic magnetometer, *Appl. Phys. Lett.* **100**, 242401 (2012).

[105] R. Gartman, W. Chalupczak, Amplitude-modulated indirect pumping of spin orientation in low-density cesium vapor, *Phys. Rev. A* **91**, 053419 (2015).

[106] D. Budker, D. F. Kimball, S. M. Rochester, V. V. Yashchuk, M. Zolotorev, Sensitive magnetometry based on nonlinear magneto-optical rotation, *Phys. Rev. A* **62**, 043403 (2000).

[107] V. Acosta, M. P. Ledbetter, S. M. Rochester, D. Budker, D. F. Jackson Kimball, D. C. Hovde, W. Gawlik, S. Pustelny, J. Zachorowski, V. V. Yashchuk, Nonlinear magneto-optical rotation with frequency-modulated light in the geophysical field range, *Phys. Rev. A* **73**, 053404 (2006).

[108] E. Zhivun, Vector ac stark shift in ^{133}Cs atomic magnetometers with antirelaxation coated cells, Ph.D. thesis, University of California, Berkeley, Berkeley, CA, USA (2016).

[109] C. Troullinou, R. Jiménez-Martínez, J. Kong, V. G. Lucivero, M. W. Mitchell, Squeezed-light enhancement and backaction evasion in a high sensitivity optically pumped magnetometer, *Phys. Rev. Lett.* **127**, 193601 (2021).

[110] V. G. Lucivero, P. Anielski, W. Gawlik, M. W. Mitchell, Shot-noise-limited magnetometer with sub-picotesla sensitivity at room temperature, *Review of Scientific Instruments* **85**, 113108 (2014).

[111] F. Le Kien, P. Schneeweiss, A. Rauschenbeutel, Dynamical polarizability of atoms in arbitrary light fields: general theory and application to cesium, *Eur. Phys. J. D* **67**, 1–16 (2013).

[112] S. Rochester, Adm package, `https://rochesterscientific.com/ADM`.

[113] T. Wu, X. Peng, Z. Lin, H. Guo, A dead-zone free ^{4}He atomic magnetometer with intensity-modulated linearly polarized light and a liquid crystal polarization rotator, *Rev. Sci. Instrum.* **86**, 103105 (2015).

[114] M. Horbatsch, E. A. Hessels, Shifts from a distant neighboring resonance, *Phys. Rev. A* **82**, 052519 (2010).

[115] A. Marsman, M. Horbatsch, E. A. Hessels, Interference between two resonant transitions with distinct initial and final states connected by radiative decay, *Phys. Rev. A* **96**, 062111 (2017).

[116] D. Budker, M. G. Kozlov, Sensing: Equation one (2020).

[117] W. Li, M. Balabas, X. Peng, S. Pustelny, A. Wickenbrock, H. Guo, D. Budker, Characterization of high-temperature performance of cesium vapor cells with anti-relaxation coating, *J. Appl. Phys.* **121**, 063104 (2017).

[118] K.-M. C. Fu, G. Z. Iwata, A. Wickenbrock, D. Budker, Sensitive magnetometry in challenging environments, *AVS Quantum Sci.* **2**, 044702 (2020).

[119] D. F. Jackson Kimball, J. Dudley, Y. Li, D. Patel, J. Valdez, Constraints on long-range spin-gravity and monopole-dipole couplings of the proton, *Phys. Rev. D* **96**, 075004 (2017).

[120] A. Papoyan, S. Shmavonyan, A. Khanbekyan, H. Azizbekyan, M. Movsisyan, G. Bao, D. Kanta, A. Wickenbrock, D. Budker, Evidence for degenerate mirrorless lasing in alkali metal vapor: forward beam magneto-optical experiment, *Journal of Physics B: Atomic, Molecular and Optical Physics* **52** (2019).

[121] G. Nienhuis, F. Schuller, Magneto-optical effects of saturating light for arbitrary field direction, *Opt. Commun.* **151**, 40-45 (1998).

[122] M. Movsisyan, S. Shmavonyan, A. Papoyan, Amplification of radiation in atomic vapor induced by a linearly polarized laser radiation, *Cent. Eur. J. Phys.* **9**, 948-955 (2011).

[123] E. Gazazyan, G. Grigoryan, A. Papoyan, Amplification of a weak circularly polarized light signal in a multilevel atomic medium, *J. Contemp. Phys. (Arm. Acad. Sci.)* **46**, 145–149 (2011).

[124] A. Taichenachev, A. Tumaikin, V. Yudin, An atom in an elliptically polarized resonant field: the exact steady-state solution for closed $j_g = j \to j_e = j + 1$ transitions, *J. Exp. Theor. Phys.* **46** (2011).

[125] G. Nienhuis, A. Taichenachev, A. Tumaikin, V. Yudin, Steady state of atoms in a monochromatic elliptically polarized light field, *Europhys. Lett.* **44** (1998).

[126] A. Sharma, N. D. Bhaskar, Y. Q. Lu, W. Happer, Continuous-wave mirrorless lasing in optically pumped atomic cs and rb vapors, *Appl. Phys. Lett.* **39** (1981).

[127] A. Akulshin, F. Bustos, D. Budker, Continuous-wave mirrorless lasing at 2.21 μm in sodium vapors, *Opt. Lett.* **43**, 5279-5282 (2018).

[128] https://twinleaf.com/shield/ms-2/ .

[129] B. Ghosh, P. Chakraborty, *Reference Module in Materials Science and Materials Engineering* (Elsevier, 2022).

[130] F. Bustos, D. Calia, D. Budker, M. Centrone, J. Hellemeier, P. Hickson, R. Holzlöhner, S.Rochester, Continuous-wave mirrorless lasing at 2.21 μm in sodium vapors, *Nature Commun.* **9** (2018).

[131] S. Reynaud, M. Himbert, J. Dupont-Roc, H. H. Stroke, C. Cohen-Tannoudji, Experimental evidence for compensation of doppler broadening by light shifts, *Phys. Rev. Lett* **42** (1979).

[132] W. S. Martins, H. L. D. de S. Cavalcante, T. P. de Silans, M. Oriá, M. Chevrollier, Two-beam nonlinear kerr effect to stabilize laser frequency with sub-doppler resolution, *Applied Optics* **51** (2012).

[133] S. M. Rochester, D. S. Hsiung, D. Budker, R. Y. Chiao, D. F. Kimball, V. V. Yashchuk, Self-rotation of resonant elliptically polarized light in collision-free rubidium vapor, *Phys. Rev. A* **63** (2001).